Numerical Investigation of Woven Wire Mesh Screens for Landing Gear Aerodynamic Flow and Noise Control

PATRICK NWOSA OKOLO

Supervisor: Prof. Gareth J. Bennett

Department of Mechanical & Manufacturing Engineering

Trinity College Dublin

Ireland

September 2017

A thesis submitted to the University of Dublin in partial fulfillment of the requirements for a Ph.D degree

Declaration

I declare that this thesis has not been submitted as an exercise for a degree at this or any other universities and it is entirely my own work. I agree to deposit this thesis in the Universitys open access institutional repository or allow the Library to do so on my behalf, subject to Irish Copyright Legislation and Trinity College Library conditions of use and acknowledgement.

Patrick Nwosa Okolo, September 2017

Abstract

Recently, acoustic engineers, researchers and relevant institutions seek to reduce noise levels associated with the aerodynamic complexities of an aircraft, particularly within close proximity to airport communities. The environmental and health effects caused by aircraft noise emission has increased the level of research in this area, with new policies aiming to address such negatives and to reduce noise levels associated with an aircraft. Aircraft landing gear contributes a major percentage to the overall noise emitted from an aircraft on approach to landing. Significant improvements have been made to the aeroengine which now position airframe noise, and landing gear noise in particular, as the threshold below which no further noise reduction can be made without addressing these now important noise sources. This current research is a numerical investigation on the use of woven wire mesh screens as fluid flow control mediums, and for landing gear noise control.

The introductory part of this thesis presents the motivation behind this research. Whilst improvements in processor speeds and the introduction of new and needed computational approaches such as the Lattice-Boltzman Method have allowed fairings and perforated plates, which serve as low noise landing gear technologies to be fully resolved and examined numerically, a full scale solution for a wire mesh screen with its very small length scales is still a significant computational challenge. Therefore, there is a need for an alternative, faster, yet sufficiently accurate method of simulating such screens numerically for aerodynamic noise studies. An alternative method is hereby proposed, and is implemented using the Volume-Averaged Method within a porous zone of interest in the numerical fluid domain, in which are added the characteristics

of realistic woven wire mesh screens. To date in the literature, wire mesh screens have not been studied using the Volume Averaged Method and where the VAM has been used for coarser studies, such as for perforated plates, only the impact of a pressure drop was implemented. In this thesis important additional consequences of the inclusion of a wire mesh screen, with its very fine and complex gap geometries, are also added to the VAM, such as turbulence suppression, so that the model might be enhanced and more accurately capture the true physics of the fluid/screen interactions.

Chapter 2 presents a literature review of aerodynamic noise generation, landing gear noise sources, noise reduction techniques applied to date, principles of computational aeroacoustics, computational modeling of perforated surfaces and wire mesh screens, and semi-empirical noise prediction models of aircraft airframe. Contributions of the thesis are also highlighted, particularly the potential benefits and applications.

So that a better understanding of turbulence fluid flow properties might be obtained around and downstream of a wire screen mesh, Chapter 3 examines, in 3-D, a fully resolved wire mesh screen and is compared to classic benchmark results published by NACA. This allows the parameters such as Flow Loss Coefficients and Turbulence Decay to be studied as a function of porosity and distance downstream. Results compare well with each other and with the near field empirical correlation of turbulence decay of Roach [1].

Chapter 4 presents a resolved 2-D realistic representation of the 3-D wire screen mesh from chapter 3 in order to examine the flow field at further downstream distances. These results compare well with both the 3-D numerical model and the NACA study.

With this detailed understanding of the effect wire mesh screens may have on the fluid mechanics of flows downstream, Chapter 5 employs the Volume Averaged Method at full scale for a wire mesh screen as a low noise technology applied to a H-Strut test case. The VAM is enhanced with the inclusion of the turbulence suppression term and is compared to the experimental flow field and acoustic results of the EU TIMPAN (Technologies to Improve Airframe

Noise) project. For this large scale study, results from this modelled method, as opposed to a resolved approach, are good, much faster and are demonstrated to be greatly improved with the addition of the turbulence effects which hitherto had been neglected.

Chapter 6 extends the evaluation of the VAM method to a comparison with half scale main landing gear EU project results: ALLEGRA. The comparison is rudimentary but demonstrate the potential for future work.

Acknowledgments

I would like to whole heartedly thank my supervisor, Prof. Gareth J. Bennett for the trust he bestowed on me by accepting me as his research student, for giving me the opportunity to study in a prestigious university like Trinity College Dublin, for making my transition into life in Dublin as smooth as I could have ever imagined, for his guidance through the course of my research study, for helping me imbibe a strong research and presentation culture, and for his vast knowledge in fluid mechanics and aeroacoustics which made it easier for me to carryout my research. Indeed it has been three years of joy, excitement and great privilege to study and perform academic related laboratories under he's supervision. Thank you so much dear supervisor.

I also like to acknowledge staffs of the department of mechanical engineering. Professor Henry Rice for his availability in answering my research related questions each time I asked. Dr. John Kennedy for helping out with questions and providing critiques for research papers and presentations, Professor Craig Meskell for giving me the opportunity to tutor in fluid mechanics modules, Dr. Tim Persoons, Dr. Ciaran Simms, and all other academic staffs I worked with/for. I absolutely enjoyed my time working for you all. A big thank you to the departmental administrative staffs like Judith Lee, Nicole Byrne, etc., whom all helped in keeping me up to date with the very frequent emails and informations. Thank you for all the communications and jokes we shared together.

Special thanks also goes out to my office colleagues, whom I shared the fluids laboratory office together for the past three years. Many have indeed come and gone, but you all left a lasting impression on me. We shared fun

times, quiet times, noisy times, research related times, pub times, party times, recreational times and most importantly humorous times together. Memories of our times together will always be cherished in my heart, and I'm glad I've made friends like you all.

Thank you to everyone I met within Trinity College Dublin. Indeed, I will keep a cherished memory of everyone of you within the deepest corners of my heart, and I hope you all keep good memories of me. Thank you all for making Dublin a home away from home for me.

To my late father, Ogbueshi Ikechukwu, I wish you could see the man I'm turning out to be, and I really wish I'm making you proud by completing this doctoral research study. You believed in me and spurred me to dream about getting a doctorate degree someday. I can only imagine how happy you would have been right now. Cheers to your joy.

Special thanks goes to my uncle, Prof Samuel Onyegegbu and my loving aunt, Prof Mrs Nkadi Onyegegbu. They both never stopped encouraging me all through the years, and they were always a source of motivation for me.

Most importantly, to my loving and understanding sweetheart, Chidinma Adanna, thanks for the support and encouragement through this research journey, for believing in me, for the various considerations and sacrifices you made on our behalf, and for being the mother of our little princess, Chiamaka Nathania.

I like to specially acknowledge Airbus Toulouse, for helping out with data utilized during the course of this research, special thanks goes to Nicola Molin for his assistance with this.

The research carried out within this thesis and leading to the results presented has received funding from Trinity College Dublin postgraduate studentship, and the European Unions Seventh Framework Program (FP7/2007-2013) for the Clean Sky Joint Technology Initiative under grant agreements number [308225] (ALLEGRA) and number [620188] (ARTIC). I also like to acknowledge the Irish Center for High End Computing (ICHEC) for enabling access to supercomputers within which most of the numerical simulations were

carried out.

Contents

List of Figures

List of Tables

Nomenclature

Abbreviations

ALLEGRA	Advanced Low Noise Landing (Main and Nose) Gear For Regional Aircraft
BANC	Benchmark for Airframe Noise Computations
CAA	Computational Aeroacoustics
CFD	Computational Fluid Dynamics
CFL	Courant Friedrichs Lewy Number
DES	Detached Eddy Simulations
DLR	German Aerospace Center
DNS	Direct Numerical Simulations
DNW	German-Dutch Wind Tunnels
$FW-H$	Ffowcs Williams and Hawkings
GCI	Grid convergence index
IDDES	Improved Delayed Detached Eddy Simulations
IDES	Improved Detached Eddy Simulations
LAGOON	LAnding Gear NOise database for CAA validatiON
LBM	Lattice Boltzmann Method

LES	Large Eddy Simulations
LG	Landing Gear
$LGMAP$	Landing Gear Model and Acoustic Prediction
MLG	Main Landing Gear
$NACA$	National Advisory Committee for Aeronautics
NLG	Nose Landing Gear
NLR	Dutch National Aerospace Laboratory
$OASPL$	Overall Sound Pressure Levels
$OPENAIR$	OPtimisation for low Environmental Noise impact AIRcraft
$PBCM$	Permeable Boundary Condition Method
$QTD2$	Quiet Technology Demonstrator 2
$RAIN$	Reduction of Airframe and Installation Noise
$RANS$	Reynolds Averaged Simulations
$SILENCER$	Significantly Lower Community Exposure to Aircraft Noise
SPL	Sound Pressure Levels
$TIMPAN$	Technology to IMProve Airframe Noise
$URANS$	Unsteady Reynolds Averaged Simulations
VAM	Volume Averaged Method

Other Nomenclatures

$MLG-1$	MLG configuration (No Treatment)
$MLG-2$	MLG configuration (Mesh Treatment)

$S1-A$	Screen S1 With Computational Grid A
$S1-B$	Screen S1 With Computational Grid B
$S2-A$	Screen S2 With Computational Grid A
$S2-B$	Screen S2 With Computational Grid B
$S3-A$	Screen S3 With Computational Grid A
$S3-B$	Screen S3 With Computational Grid B

Symbols

$\|v\|$	velocity magnitude
α	Ratio of flow angle of incidence with respect to normal to screen surface for upstream flow to angle of incidence for downstream flow
β	Open Area Ratio (Porosity)
β	porosity of mesh screen
Δp	Static Pressure Drop
ΔP_e	Pressure drop effects
ΔV_i	Volume of i^{th} cell
ΔV_N	Total Volume of grid cells
δ_{ij}	Dirac delta function
ϵ_{21}	$\phi_2 - \phi_1$
ϵ_{32}	$\phi_3 - \phi_2$
η	acoustic efficiency
μ	Dynamic Viscosity

ν	Fliud kinematic viscosity
ν	kinematic viscosity
$\Omega_1, \Omega_2, \Omega_3$	MLG Computational Domain Features
$\overline{u}$	mean velocity
ϕ	Variable of flow field
ϕ_{ext}	Extrapolated asymptotic value of variable
ρ	Density
ρ	Fluid Density
ρ_0	Atmospheric Density
σ	perforated screen open area ratio
ε	Turbulent dissipation rate
ζ_c	Lagrangian coordinate
ζ_l	perforated screen pressure loss coefficient
ζ_{wir}, K	pressure drop coefficient
A	Aperture size of wire screen
C	Streamwise pitch distance (mm)
C_c	contraction coefficient
D	Wire Screen Diameter (mm)
D, C	prescribed matrices
D_s	directivity coefficient
d_s	strut diameter

D_w	MLG wheel diameter
d_{or}	perforate orifice diameter
e_{ext}	Error between asymptotic value and find grid value
f	Wire screen volumetric porosity
$F_d(S_d)$	small components non-dimensional spectral shape function
$F_s(S_s)$	strut non-dimensional spectral shape function
f_u	Axial Turbulence Reduction Factor
f_v	Lateral Turbulence Reduction Factor
G	Wire screen geometric function
h	Computational grid size
$I(x)$	Sound Intensity
K	Flow Loss Coefficient
k	Turbulent kinetic energy
K_θ	correlation constant
K_θ	inclination angle
K_{error}	Loss coefficient prediction error when compared to experiment
K_{mesh}	Wire constant
K_{Re}	Wire Reynolds number factor
l_s	strut length
M	Mach Number
m	3D Wire Screen number of strands per unit length

m	Inclined screen pressure drop coefficient
N	Total number of cells
N_e	Screen self noise effect
P	Acoustic Power
P	Longitudinal pitch distance (mm)
p	Order of method
p	Pressure
P_s	mean square far-field pressure
P_{ij}	stress tensor
r	Grid refinement factor
r_{21}	h_2/h_1
r_{32}	h_3/h_2
Re_d	Reynolds number based on wire diameter
Re_f	Reynolds number based on wire volumetric porosity
Re_m	Reynolds number based on screen number of strands per unit length
Re_s	Reynolds number based on screen aperture velocity
S	solid boundary surface
S_i	i-th source term
Str_{or}	Strouhal number based on orifice
T	turbulence intensity
T_e	Turbulence alteration effect

T_{ij}	Lighthill Stress Tensor
U	Mean Free Stream Velocity
u'	Axial Fluctuating Velocity component
u'_{rms}	Root Mean Square (RMS) of velocity fluctuations
u'_{rms}	rms velocity perturbation in axial direction
u_i, u_j	Velocity
U_∞	Free Stream Velocity (m/s)
u_{or}	velocity in a mesh open section
U_s	Velocity Through Screen Aperture (m/s)
v'	Lateral Fluctuating Velocity component
v'_{rms}	rms velocity perturbation in axial direction
V_e	Velocity modification effect
x_i, x_j, x_k	cartesian coordinate in x-axis
y_i, y_j, y_k	cartesian coordinate in y-axis
Z_1, Z_2	Correlation constants
z_i, z_j, z_k	cartesian coordinate in z-axis
$Re_{d_{or}}$	Reynolds Number based on orifice diameter

Chapter 1

Introduction

1.1 Context and Research Motivation

Attempts to reduce aerodynamically induced noise emitted due to the non-streamlined parts of an aircraft has presented a challenge to the world at large. With the increase in population, an expectation exists that a high rise in the number commercial flights and airports runways is inevitable. Therefore it necessitates the introduction of policy's that aims to target reductions of noise emissions from aircraft's. At the landing configuration of an aircraft, elevated noise emissions are obtained. Obvious consequences as a result of these emissions include; sleep disturbance, decreased school and work performances, hearing impairment, hypertension, ischemic heart disease, annoyance [22], and in some rare conditions, noise induced hearing loss (NIHL)[23], which sometimes is sufficient enough to impair hearing over the course of a lifetime[24]. Studies of the relation between worry and annoyance from air traffic carried out by Frits et al.[2] in five municipalities showed the levels of population living in close proximity to airport routes that were annoyed and the population highly worried due to the elevated noise levels as shown in Figure1.1

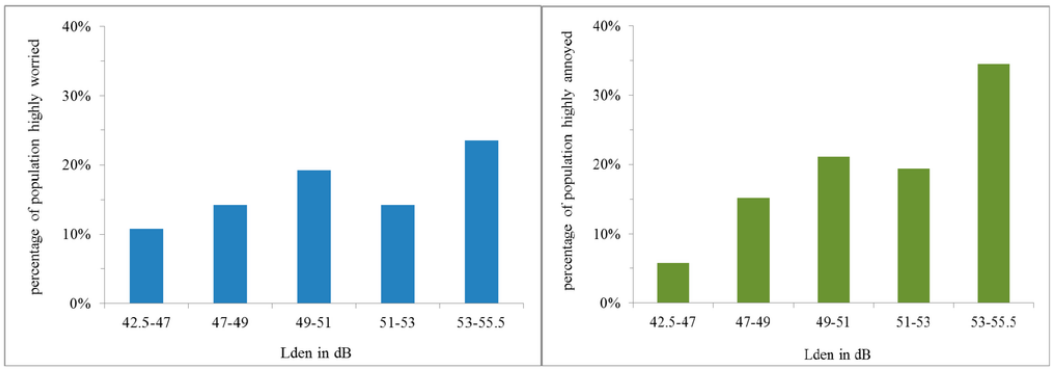

Figure 1.1: Population highly annoyed about aircraft noise and population worried about living close to aircraft routes; In Percentages [2]

Currently, due to the significant reduction of jet engine noise over the past decades, with improvement in high bypass engine ratio's, the major source of aircraft noise on approach has shifted from the engine noise to the the airframe noise, as it now contributes a major percentage to the overall noise emitted during landing configuration [25], when engines are throttled back, with high-

lift devices and landing gears deployed [25]. Aircraft noise can be classified into two categories: The engine noise and the airframe noise. Figure 1.2 shows the major noise sources within the aircraft. Figure 1.3 shows the noise levels of different aircraft's during take off, while Figure 1.4 shows dominant noise sources from both long and short range aircrafts at the approach configuration. The landing gear noise emission, leading edge devices noise emissions, trailing edge devices noise emissions, spoilers, rudders, flap side edges, gear-wake/flap interaction etc.[5], all make up the airframe noise as depicted in Figure 1.4.

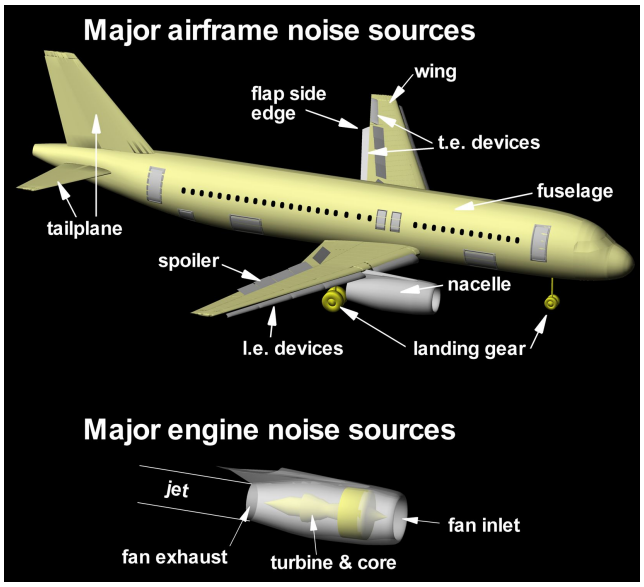

Figure 1.2: Major airframe and engine noise sources[3]

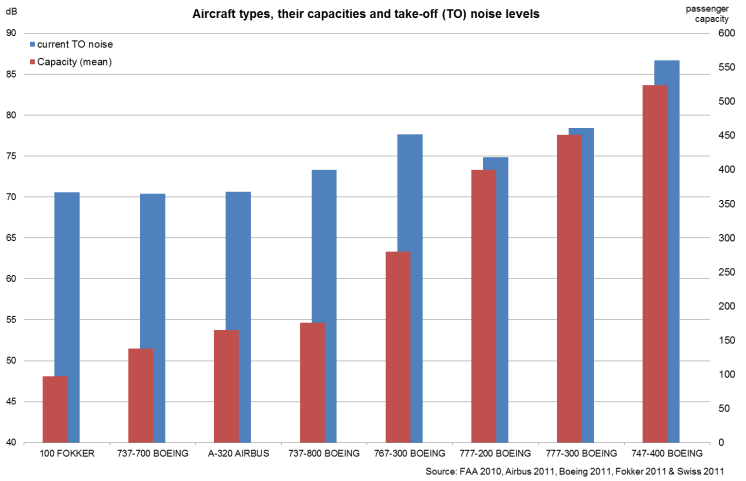

Figure 1.3: Take-off Noise levels of different aircrafts[4]

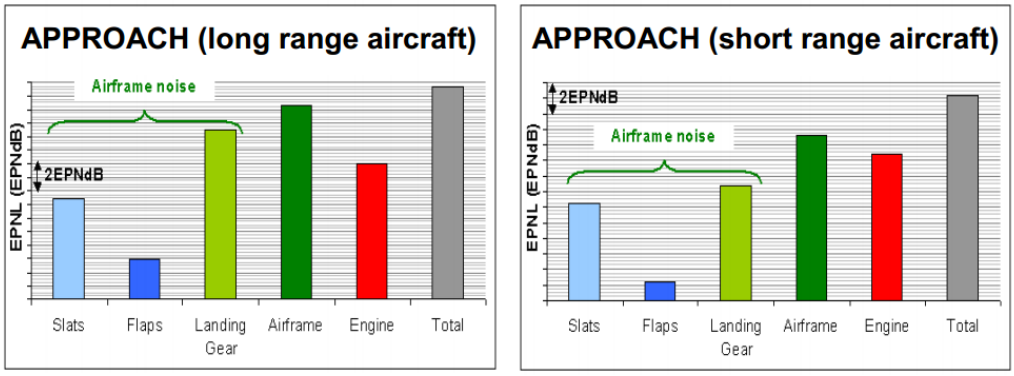

Figure 1.4: Relative approach noise source weight for short and long range Airbus aircraft(Source: airbus)[5]

The noise emitted from landing gears of aircraft's possess a larger percentage of the overall noise emitted during its aerodynamic operation[25], thereby making this section of the aircraft a primary concern for engineers and aeroacoustic researchers. Therefore a high level of attention is now focused on the reduction of noise levels within the landing gear, for both main and nose landing gear, by either active or passive noise reduction means. Noise sources within the landing gear section are majorly generated due to large scale aerodynamic interaction between turbulent airstream and its complex components. The detailed components within a landing gear contains unfavorable aerodynamic features as shown in Figure 1.5, and mid to high speed airflow impingement on the cavity sections of landing gears generally results in the scale turbulent flow phenomenon that constitutes very potent sound generating mechanism. Therefore, research into low noise techniques applied as add-on treatments for reducing these noise effects without re-designing the aircraft with acoustics as one of the added parameter for model consideration had been the subject of many coordinated test projects, and this has yielded some level of success over the years[26].

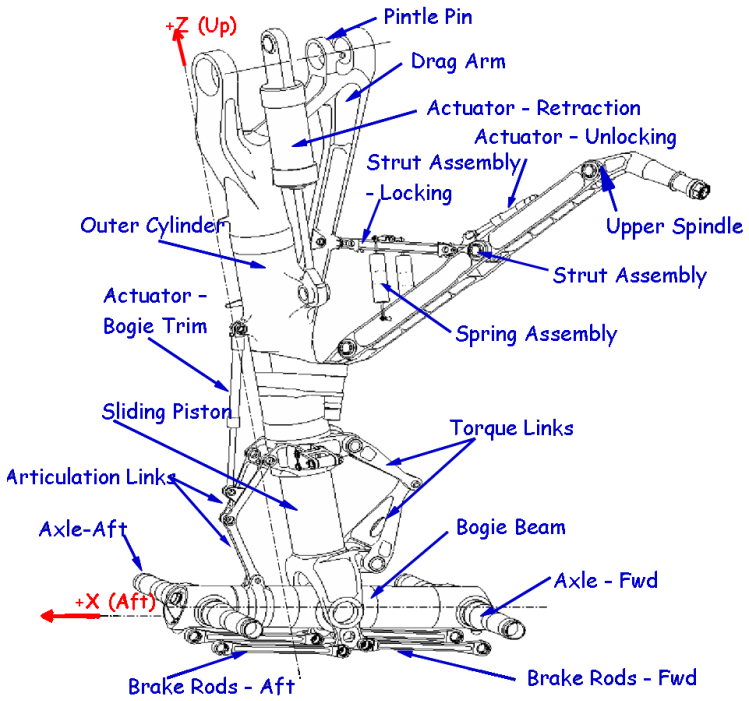

Figure 1.5: Description of landing gear components with wheels omitted[6]

Shielding some parts or all parts of the landing gear components by using closed fairings and thereby preventing the full interaction of airflow with the various protrusions and cavities were considered and carried out by Dobrzynski et al.[25, 27]. It was however observed that high speed flow deflection onto other components and fairing self-noise were major disadvantages of thesfairing type and this inhibited its further successful application. Bleeding air through these fairings by perforating them further resulted in better redistribution of the airflow and yielded better acoustic performance particularly within low and mid frequency ranges. Added advantages of perforating these fairings compared to solid fairings include weight, brake cooling and better visibility around the landing gear bogie for maintenance. Results of flight tests using these perforated fairings indicate that its application reduces the landing gear noise more effectively compared to solid fairings, within the low and mid frequency range as shown by Piet et al.[28] and Smith et al.[21]. Li et al.[7] carried out detailed experimental study of perforated undertray applications for landing gears, and performed wind tunnel tests on a 1/4 scale model A340 landing gear, where undertray treatments of solid undertray fairings,

perforated undertray fairings+brushes, slotted undertay fairings, and slotted undertray fairings+cloth where introduced individually and noise reduction studies of each application were studied, as shown in Figure 1.7.Two phased microphone arrays were mounted on the ceiling and sidewall of their tunnel test section respectively. The installed undertray designs reduced the low-frequency noise of the landing gear as was expected. The slotted undertray covered with cloth was the most effective of all undertray designs, since it not only gave a reasonable reduction at low frequencies, but also achieved significant reduction in the mid and high-frequency range. The perforated undertray represented the next most effective undertray design, however, it was observed that its perforations needed to be further developed and optimized in order to achieve better reductions in low-frequency noise and suppress its high-frequency self-noise which offsets the benefits of its mid frequency noise reductions. Also, edge brushes added to cover the brakes of the landing gear were shown to reduce some high-frequency noise, although this solution might adversely affect brake cooling of the overall landing gear system.

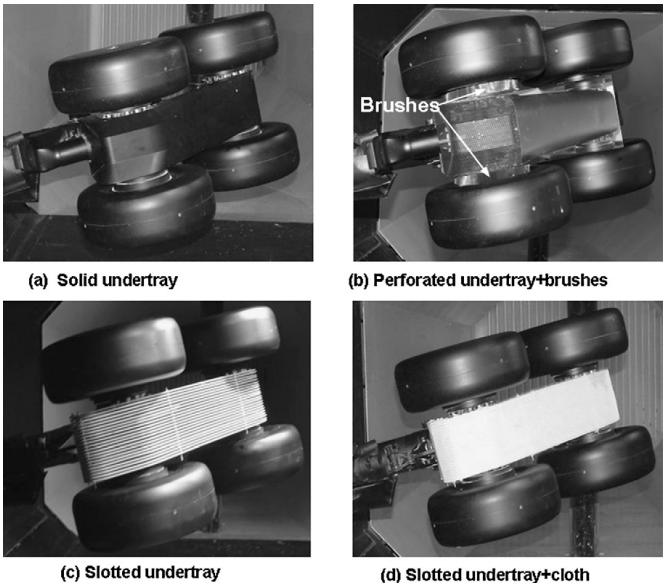

Figure 1.6: Undertray fairings installed on a 1/4 scale model A340 landing gear.[7]

Meshes have also been applied as screens on landing gears for noise reduction studies, and documented experimental results show they produced more

rewarding and promising results compared to solid or perforated fairings in the reduction of aerodynamically generated noise of landing gears, as evident in results of Smith et al.[21] and Oerlemans et al.[19]. Smith et al.[21] further investigated mesh screens on a scale model main landing gear for a long range aircraft installed in the QinetiQ NTF test facility. The gear for this aircraft is nominally the same as for an A340 aircraft. The results were achieved using a polar microphone array, and these showed significant noise reduction while using meshes. They transposed their noise data from the wind tunnel test to flight conditions in order to estimate the potential overall approach noise reduction for an existing twin long-range aircraft. The application of mesh undertray provided more than 3 EPNdB noise reduction of the main landing gear noise in approach, which gave a total aircraft noise reduction of 0.8 EPNdB

Figure 1.7: Mesh undertray and mesh leg door filler fairing and torque link fairing on a 1/4 scale model two wheel landing gear.[7]

Attempts to numerically simulate the application of perforated fairings and mesh screens for landing gear noise reduction effects and studies has been a challenge for CFD/CAA experts and engineers till date, due to the very fine grid resolution implications required for these perforates or meshes and the expensive computational cost needed to arrive at accurate and acceptable results. Mitsuhiro et al.[29] performed detailed CFD/CAA numerical simulations and noise reduction studies on perforated fairings applied on a two wheel main landing gear using a Very Large Eddy Simulation (VLES) coupled with the Ffowcs Williams-Hawkings (FW-H) acoustic analogy for noise propagation prediction to far-field receivers. This was carried out using Powerflow software,

which uses the Lattice Boltzmann Method (LBM). Their results showed good agreement with experimental data up to 1kHz. The results captured to a large extent the noise reduction effect of the fairing but it was done at a rather high computational cost. Therefore, new methods need to be developed for quicker prediction of the numerical effects of mesh screens when applied to landing gears for low noise treatments.

In summary, the key issues relating to landing gear noise related problems are as follows:

1. Landing gears consist of structures and components that are not aerodynamically optimized, hence the intricate flow separations and deflections within the landing gear aids noise generated within.

2. Wake effects from landing gears further interacts with other downstream airframe components, therefore creating secondary noise sources in the process.

3. For some aircrafts, the landing gear noise contributes approximately 30% to the overall noise emission within the approach and take-off configuration [30].

4. Noise signatures from landing gear geometries are broadband in nature and covers frequencies within the range of 90Hz to 4KHz approximately [30].

5. Communities within close proximity to airports and flight paths suffer high annoyance levels associated with the noise frequency range of aircrafts.

6. Components having non-aerodynamic shapes generates high level tonal noise as a direct noise source, which is extremely detrimental to human hearing.

1.2 Scope and Research Objectives

This investigation is an academic research exercise with industry based applications aimed at studying, understanding and improving the application of woven wire mesh screens when applied to landing gears for aerodynamic noise reduction. The objectives of the research carried out within this thesis are as follows:

1. To numerically study woven wire mesh screens as fluid flow control and noise reduction treatment applications when applied to aircraft landing gears.

2. For woven wire screens in isolation, this thesis aims to identify a suitable RANS model and domain boundary condition that accounts for the flow speed reduction achieved in realistic applications of woven wire mesh screens for fluid flow control purposes.

3. Identification of regions downstream of a woven wire screen where a flow speed reduction is achieved, and presenting a quantifiable correlation of this flow speed reduction to the woven screens solidity.

4. For two dimensional geometry related applications involving wire screens, this thesis aims to present a simplified 2D geometry of staggered cylinders that replicates the downstream effect of a 3D screen within high screen porosities, where planar views of 3D screens can be simplified as 2D cylinders in a staggered arrangement.

5. To develop a novel computational approach for modeling woven wire mesh screens within a computational domain as a virtual or porous zone. This approach should account for the pressure drop and turbulence alteration effect of a physical realistic wire screen.

6. This proposed approach is achieved by introducing pressure drop as a function of flow loss resistance and characteristic turbulence alteration

effect within an adapted porous zone of interest, which accounts for the effect of a physical realistic wire screen.

7. The porous zone method here is initially validated against experimental tests from the European project TIMPAN.

8. Wind tunnel acoustic results from the ALLEGRA project, where woven wire mesh screens were utilized as a low noise treatment for a model MLG is also utilized within this thesis as a more advanced validation of the proposed modeling approach of woven wire screens within a computational domain.

1.3 Thesis Outline

The content outline of this thesis is arranged as follows;

Chapter 1 presents the introduction to the studies carried out within this thesis, where the context and research motivation were highlighted. The scope and research objectives were also elaborated upon, with the thesis outline mentioned.

Chapter 2 provides a literature review study, where aerodynamic noise generation theories, landing gear acoustic noise sources, low noise treatments applied to landing gears and various noise prediction methods (semi-empirical and CFD-based) are highlighted. Various coordinated landing gear noise programs are also presented, with the view of providing state of the art information on landing gear noise reduction techniques and progress made in recent years in the subject of landing gear aeroacoustic noise reduction. The physics of fluid flow through wire mesh screens is also highlighted, followed by various possible techniques for wire screen computational analysis. The contribution of this Thesis to science based knowledge is presented in the concluding section of Chapter 2.

In Chapter 3, Numerical simulations of flow through three dimensional woven wire screens is performed, with flow loss coefficients, flow speeds and turbulence quantities the major parameters highlighted.

Chapter 4 takes a look at the numerical simulation of flow through two dimensional screens, where the aim was to find a 2D simplified screen geometrical feature that could replicate results for a 3D geometry within acceptable error margins.

The process of numerical modeling of woven wire mesh screens is presented in Chapter 5. Within this chapter, an alternative modeling approach is proposed and utilized for aeroacoustics computational simulations involving woven wire screens particularly when utilized as a tool for aerodynamic noise reduction. This proposed method is tested on a single simplified H-strut unit. For validation, acoustic results from TIMPAN project is utilized.

Chapter 6 applied the wire screen noise modeling approach proposed in Chapter 5 to a more realistic and advanced aerodynamic noise reduction study of a nose landing gear and a main landing gear model. Acoustic test results of ALLEGRA project coordinated by Trinity College is utilized for the validation of acoustic numerical results presented within this Chapter.

Chapter 7 concludes this Thesis by highlighting the outcomes of all studies carried out within this research, and also provides possible areas of improvement for future work related to the subject area of woven wire mesh screens applied for aerodynamic noise reduction.

Chapter 2

Literature review

2.1 Aerodynamic Noise Generation

The three most commonly cited acoustic analogies which have developed to help model aerodynamic noise generation are presented here. The Lighthill's theory for unbounded flows is first discussed, followed by the Curle's Analogy for wall bounded flows, and finally the Ffowcs Williams-Hawkings (FW-H) theory of aerodynamic sound generation by turbulence in arbitrary motion.

2.1.1 Lighthill's Theory for Unbounded Flows

A theory for aerodynamic noise generation for unbounded flows was first developed by Lighthill[31], where the sound radiated from a fluctuating fluid flow was estimated. This theory was initiated based on the equations of motion of a gas, for the purpose of estimating sound radiated from a fluid flow, which as a result of instability would definitely contain regular fluctuations or turbulence. The fluid area which is taken to be the noise generation area is decoupled from a uniform medium at rest, representative of the wave propagation area. It is argued that sound is a very small component of the whole motion and therefore the properties of the flow in the source region can be determined by neglecting the production and propagation of sound. The exact equations of motion are compared with the equations of sound propagation in a medium at rest. The equations of motion for an arbitrary continuous medium under zero external force in tensor notation are given by

$$\frac{\partial \rho}{\partial t} + \frac{\partial (\rho u_i)}{\partial x_i} = 0 \tag{2.1}$$

$$\frac{\partial (\rho u_i)}{\partial t} + \frac{\partial (\rho u_i u_j + P_{ij})}{\partial x_j} = 0 \tag{2.2}$$

x_i is the Cartesian coordinate, u_i represents the flow velocity, ρ is the fluid density and P_{ij} is the stress tensor which for a Stokesian fluid equals

$$P_{ij} = p\delta_{ij} + \mu[-\frac{\partial u_i}{\partial x_j} - \frac{\partial u_j}{\partial x_i} + (2/3)(\frac{\partial u_i}{\partial x_i})\delta_{ij}] \tag{2.3}$$

Where p is the pressure and is related to other thermodynamic variables as for a gas at rest, δ_{ij} is the Dirac delta function, which is 1 for i = j, 0 for i $\neq j$ and μ is the dynamic viscosity. Atmospheric air may be taken as a Stokesian fluid for practical purposes. The propagation of sound in a uniform medium which is at rest, without sources of matter or external forces, is governed by the equations

$$\frac{\partial \rho}{\partial t} + \frac{\partial (\rho u_i)}{\partial x_i} = 0 \tag{2.4}$$

$$\frac{\partial (\rho u_i)}{\partial t} + a_0^2 \frac{\partial \rho}{\partial x_i} = 0 \tag{2.5}$$

$$\frac{\partial^2 \rho}{\partial t^2} - a_0^2 \nabla^2 \rho = 0 \tag{2.6}$$

Equation 2.4 is the exact continuity equation, Equation 2.5 is the approximate momentum equation while Equation 2.6 is the wave equation and can be deduced by taking the time derivative of Equation 2.4 and subtracting the spatial derivative of Equation 2.5.

The equations of propagation of sound in a uniform medium at rest due to externally applied fluctuating stresses is gotten by transforming Equation 2.1 and 2.2 into a wave equation using an approach similar as was done for Equation 2.4 and 2.5. This yields

$$\frac{\partial \rho}{\partial t} + \frac{\partial (\rho u_i)}{\partial x_i} = 0 \tag{2.7}$$

$$\frac{\partial (\rho u_i)}{\partial t} + {a_0}^2 \frac{\partial \rho}{\partial x_i} = -\frac{\partial T_{ij}}{\partial x_j} \tag{2.8}$$

$$\frac{\partial^2 \rho}{\partial t^2} - a_0^2 \nabla^2 \rho = \frac{\partial^2 T_{ij}}{\partial x_i \partial x_j} \tag{2.9}$$

Where T_{ij} is the instantaneous applied stress at any point, also called the Lighthill stress tensor

$$T_{ij} = \rho u_i u_j + P_{ij} - a_0^2 \rho \delta_{ij} \tag{2.10}$$

At low Mach number, provided that any difference in temperature between the flow and the outside air is due simply to kinetic heating or cooling (heating by fluid friction or cooling by rapid acceleration), then T_{ij} is approximately $\rho_0 u_i u_j$, with a proportional error of the order of the square of the Mach number M. The resulting approximate form is

$$T_{ij} \simeq \rho_0 u_i u_j \tag{2.11}$$

Where the suffix zero signifies atmospheric values. Outside the flow region of interest, the Lighthill stress tensor will however approach zero, therefore, the velocity u_i will correspond to very small acoustic perturbations, and its quadratic appearance in Equation 2.10 will make this term negligible. Viscous stresses in P_{ij} and heat transfer are both very small negligible effects, because gradients are small without the presence of a solid body. Therefore Equation 2.9 will become the same as Equation 2.6 outside the airflow. The sound produced by T_{ij} corresponds to a quadrupole field. Therefore, using Green's functions, the acoustic density perturbation at position x due to a quadrupole at position y with strength T_{ij} is written as

$$\rho - \rho_0 = \frac{1}{4\pi a_0^2} \frac{\partial^2}{\partial x_i \partial x_j} \iiint_V T_{ij} \left(y, t - \frac{|x-y|}{a_0} \right) \frac{d^3 y}{|x-y|} \tag{2.12}$$

At points far enough from the flow to be in the radiation field of each quadrupole, that is, at a large distance compared with $\frac{1}{2\pi}$ times a typical wavelength, the differentiation in Equation 2.12 may be applied to T_{ij} only, giving

$$\rho - \rho_0 \simeq \frac{1}{4\pi a_0^2} \iiint_V \frac{(x_i - y_i)(x_j - y_j)}{|x-y|^3} \frac{1}{a_0^2} \frac{\partial^2}{\partial t^2} T_{ij} \left(y, t - \frac{|x-y|}{a_0} \right) d^3 y \tag{2.13}$$

Where Equation 2.13 for the sound radiation field must give an exact result for the total energy radiated and its directional distribution, since only

terms falling away more rapidly than the inverse first power of the distance are excluded. However, at distances large compared with the dimensions of the flow one may approximate $x_i - y_i$ by x_i in Equation 2.13, provided the origin is taken within the flow, without neglecting any terms of order x^{-1}. This gives a simplified equation of the form

$$\rho - \rho_0 \simeq \frac{1}{4\pi a_0^2} \frac{x_i x_j}{x^3} \iiint_V \frac{1}{a_0^2} \frac{\partial^2}{\partial t^2} T_{ij} \left(y, t - \frac{|x-y|}{a_0} \right) d^3 y \tag{2.14}$$

Time fluctuations of T_{ij} are roughly proportional to $\frac{U}{l}$, yielding an estimate through dimensional analysis for the squared density variations as

$$(\rho - \rho_0)^2 \propto (\frac{1}{a_0^2})^2 (\frac{1}{a_0^2})^2 (\frac{U}{l})^4 (\rho_0 U^2)^2 (\frac{l^3}{|x|})^2 = \rho_0^2 \left(\frac{U}{a_0} \right)^8 \left(\frac{l}{|x|} \right)^2 \tag{2.15}$$

Where U is the velocity, and l is a typical dimension. It is assumed that the momentum flux is the dominating contribution to T_{ij}. Therefore, this quadrupole sound is shown to scale with the 8^{th} power of flow speed.

The quantities which can be estimated by the human ear or measured by other phase-insensitive instruments are the intensity at any point and its frequency spectrum. The intensity of sound at a point where the density is ρ is $\frac{{a_0}^3}{\rho_0}$ times the mean-square fluctuation of ρ. Intensity is

$$I(x) = \frac{a_0^3}{\rho_0} \sigma^2 \{ \rho(x,t) \} \tag{2.16}$$

Where the Intensity signifies the rate at which energy crosses unit surface area at the point. Deriving this intensity from Equation 2.13 and Equation 2.16 gives

$$\begin{aligned} I(x) \simeq \frac{1}{16\pi^2 \rho_0 a_0^5} \iint & \frac{(x_i - y_i)(x_j - y_j)(x_k - z_k)(x_l - z_l)}{|x-y|^3 |x-z|^3} \\ & \times \frac{\partial^2}{\partial t^2} T_{ij}(y, t - \frac{|x-y|}{a_0}) \frac{\partial^2}{\partial t^2} T_{ij}(y, t - \frac{|x-y|}{a_0}) dy dz \end{aligned} \tag{2.17}$$

Through dimensional analysis the intensity roughly becomes

$$I(x) \propto \rho_0 U^8 a_0^{-5} (\frac{l}{x})^2 \tag{2.18}$$

Giving predictions that sound intensities scales near the eight power of a typical velocity U in the flow.

The total acoustic power output is obtained using simplified Equation 2.14 for radiation field and integrating its mean square over the surface of a large sphere. The total acoustic power output is

$$\begin{aligned} P = \frac{1}{60\pi\rho_0 a_0^5}[\sigma^2\{\iiint_V \frac{\partial^2}{\partial t^2} T_{ij}(y, t - \frac{|x-y|}{a_0})dy\} \\ + 2\sum_{i=1}^{3}\sum_{j=1}^{3}\sigma^2\{\iiint_V \frac{\partial^2}{\partial t^2} T_{ij}(y, t - \frac{|x-y|}{a_0})dy\}] \end{aligned} \tag{2.19}$$

Where the second term in Equation 2.19, each of the nine quadrupole fields $T_{ij}(i = 1 \rightarrow 3, j = 1 \rightarrow 3)$ contribute independently to the power output. Again, by dimensional analysis, this yields

$$P \propto \rho_0 U^8 a_0^{-5} l^2 \tag{2.20}$$

Which emphasises the argument that the sound intensities and acoustic power both increase as the eight power of a typical flow velocity.

2.1.2 Curle's Theory for Solid Bounded Flows

Lighthill's theory of aerodynamic noise generation for unbounded flows was modified by Curle [32], where the presence of solid boundaries was taken into account, of which Lighthill's equation did not account for. It was modified through the concept that Lighthill's quadrupole sound will be reflected and diffracted by the existing solid boundaries, and this quadrupole sound will not be distributed over the whole space, but only within the region exterior to the solid boundaries. Also, a resultant dipole field at the solid boundaries which are the limits of lighthill's quadrupole distribution was introduced as a result. These effects are exactly equivalent to a distribution of dipoles, where each dipole represents the force with which unit area of soild boundary acts upon the fliud. Implementing this concept into Lighthill's theory and solving the basic fluid flow equations and wave equations, leads to

$$\rho - \rho_0 = A_2 \frac{\partial^2}{\partial x_i \partial x_j} \iiint_V T_{ij} \left(y, t - \frac{|x-y|}{a_0} \right) \frac{d^3 y}{|x-y|} - A_2 \frac{\partial}{\partial x_i} \iint_S P_i \left(y, t - \frac{|x-y|}{a_0} \right) \frac{dS(y)}{|x-y|} \tag{2.21}$$

$$P_i = -l_j p_{ij} \tag{2.22}$$

$$A_2 = \frac{1}{4\pi {a_0}^2} \tag{2.23}$$

The surface integral, representing the modification to Lighthill's theory is exactly equivalent to the sound generated in a medium at rest by a distribution of dipoles of strength P_i per unit area. P_i is exactly the the force per unit area exerted on the fluid by the solid boundaries in the x_i direction. S denotes the surface of the solid boundary and l_j is the unit outward normal, pointing towards the fluid on S. Therefore, one can look at the sound field as the sum of that generated by a volume distribution of quadrupoles and by a surface distribution of dipoles. A similar dimensional analysis performed on Equation 2.21 of the density fluctuations due to the dipole term gives

$$(\rho - \rho_0)^2 \propto= \rho_0^2 \left(\frac{U}{a_0} \right)^6 \left(\frac{l}{|x|} \right)^2 \tag{2.24}$$

Which indicates that for a low Mach number flow, dipole radiation will dominate the sound emanating from the quadrupole source. Equation 2.21 was derived with the assumption that the normal fluid velocity on the integration surface S is zero, but if mass is added at the surface S, this causes the normal component of the fluid velocity to be non zero. Adjusting the term representing the dipole distribution, a new monopole term representing the unsteady mass addition will arise. The resulting equations becomes

$$\rho - \rho_0 = A_2 \frac{\partial^2}{\partial x_i \partial x_j} \iiint_V [T_{ij}] \frac{d^3 y}{|x-y|} + A_2 \frac{\partial}{\partial x_i} \iint_S n_j [P_{ij} + \rho u_i (u_j - V_j)] \frac{dS(y)}{|x-y|} + A_2 \frac{\partial}{\partial t} \iint_S n_j [\rho_0 V_j + \rho (u_j - V_j)] \frac{dS(y)}{|x-y|} \tag{2.25}$$

$$A_2 = \frac{1}{4\pi a_0^2} \tag{2.26}$$

The quantities in the brackets [ ] are evaluated at a retarded time of $t - \frac{|x-y|}{a_0}$, where if there is no unsteady mass addition into the system ($n_j u_j = 0$), equation 2.25 simplifies back to equation 2.21 Acoustic intensity generated by the dipoles is of the order

$$I_D(x) \propto \rho_0 U^6 a_0^{-3} f(x-y) \tag{2.27}$$

From Equation 2.18 and 2.27, it follows that

$$\frac{I_Q}{I_D} \propto \left(\frac{U}{a_0}\right)^2 f(x-y) \tag{2.28}$$

Which shows that at sufficiently low Mach numbers, the contribution to the sound field from the dipoles should be greater than that for the quadrupoles. However, exactly how small the Mach number must be for this will depend heavily on the particular fluid flow application in question. The total acoustic power output will roughly be

$$P \propto \rho_0 U^6 a_0^{-3} l^2 \tag{2.29}$$

where acoustic efficiency roughly becomes

$$\eta \propto \left(\frac{U}{a_0}\right)^3 \tag{2.30}$$

which compares with the acoustic efficiency $\eta \propto M^5$ found by Lighthill for the quadrupole field. The Modifications so far are often referred to as the Lighthill-Curle theory.

2.1.3 Ffowcs Williams and Hawkings Theory

Aerodynamic applications concerning noise generation and propagation would typically involve the movement of an aircraft, car, etc, through a fluid medium, and as such the need to account for such surfaces in motion. The Lighthill-Curle theory was extended by Ffowcs Williams and Hawkings [33], to account

for effects of arbitrary convective motion of the source, as the forward motion of the source was found to influence its radiation pattern with respect to a particular observer. Typically, an observer will perceive an increase in density perturbations when a moving source is approaching and a decrease when the source is moving away. Therefore, to account for this concepts, the equation becomes.

$$\rho - \rho_0 = A_3 \frac{\partial^2}{\partial x_i \partial x_j} \iiint_V B_3[T_{ij}] \frac{d\zeta_c}{|x-y|} + A_3 \frac{\partial}{\partial x_i} \iint_S n_j B_3[P_{ij} + \rho u_i(u_j - V_j)] \frac{dS(\zeta_c)}{|x-y|} + A_3 \frac{\partial}{\partial t} \iint_S n_j B_3[\rho_0 V_j + \rho(u_j - V_j)] \frac{dS(\zeta_c)}{|x-y|} \tag{2.31}$$

$$A_3 = \frac{1}{4\pi a_0^2} \tag{2.32}$$

$$B_3 = \frac{1}{(1 - M\cos\theta)} \tag{2.33}$$

$$\zeta_c = y - Ut \tag{2.34}$$

Where ζ_c is the Lagrangian coordinate, θ the inclination angle, M the Mach number in approach direction and U is velocity of the source.

2.2 Landing Gear Acoustics

Aircraft flyover noise measurements have been carried out in order to fully comprehend, identify and characterize the major noise sources of aircraft airframes [34, 35, 36, 37], of which landing gear is found to be a major contributor. Within the complex landing gear structure, resonance caused by airflow over cavities, turbulence interactions, vortex shedding and its coherency, boundary layer or wake interaction with downstream devices all act as potential contributors towards the general noise generation mechanism.

2.2.1 Noise Sources

Due to natural vortex shedding, larger components are expected to be responsible for lower frequencies and small-scale details for high frequency noise. Regular vortex shedding is often distorted by interaction effects due to the complexity of the gear. High resolution calculation of a simplified gear was performed by Lockard et al.[38], where the relevance of different noise sources was addressed using a DES-FW-H coupled approach. It was observed that the gear boxes and wheels were major contributors dominant over the total frequency range. Interaction between wheels as a possible source has received attention in [39]. A translating mid-wheel vortex is identified which has the potential to produce significant ground-directed noise, as it distorts upon collision with one wheel and then the other. However, validation of the energy addition principle to account for the number of wheels by Guo et al.[40] suggests that to omit tire wake-tire interaction is justified. Chow et al.[14] showed that landing gear struts exhibit a low frequency spectral peak governed by the overall component diameter and a high frequency spectrum generated by small attached dressings, joints etc. Tests with and without these small scale components indicate that they can be responsible for up to 10 dB of the high frequency noise, as shown by Jaegr et al.[41] , thereby pointing out their importance. Explanation for the high relative importance of high frequency noise on landing gear are shown by Dobrzynski et al.[27]. It was further hypothesized that high local flow velocities around small-scale components caused by blockage would relatively enhance high frequency sources to low frequency sources for a given freestream velocity.

2.2.2 Noise Directivity

Dobrzynski et al [25] showed that the polar radiation in a vertical plane containing the velocity vector for landing gear noise is almost omnidirectional at low Strouhal-numbers, showing increasingly pronounced level maxima in the rear and forward arc with increasing Strouhal number. However, this can

be seen to disproof the theory that landing gear noise is dominated by large scale vortex shedding, which is a dipole-type source, for which the maximum noise should appear perpendicular to the flow direction, i.e, overhead position. The relevant disturbance scales for intermediate Strouhal numbers is several millimeter, which corresponds to the dimensions of various dressings attached to the basic gear. It was observed that oblique local velocities may be responsible for the dressing noise generation, and could be an explanation for the mentioned trend of directivity. Another possible explanation is the suspected dominance of noise from wake interaction with downstream gear components[25]. William et al. [8] carried out further tests on noise spectra and directivity for a scale-model landing gear as shown in figure 2.1 and 2.2, for a baseline case, and with turboggan fairing, both with and without the bay door, where they found the results for the baseline configuration appear to reveal two general regions of major noise emission from the landing gear the truck assembly and the oleo/strut brace assembly. Such a finding was consistent with previous documented aeroacoustic studies on similar models. The oleo/strut noise appeared most dominant in the non-door, sideline view, where this noise region was less well defined for the door sideline view perhaps due to the strut orientation and partial obscuration by the door.

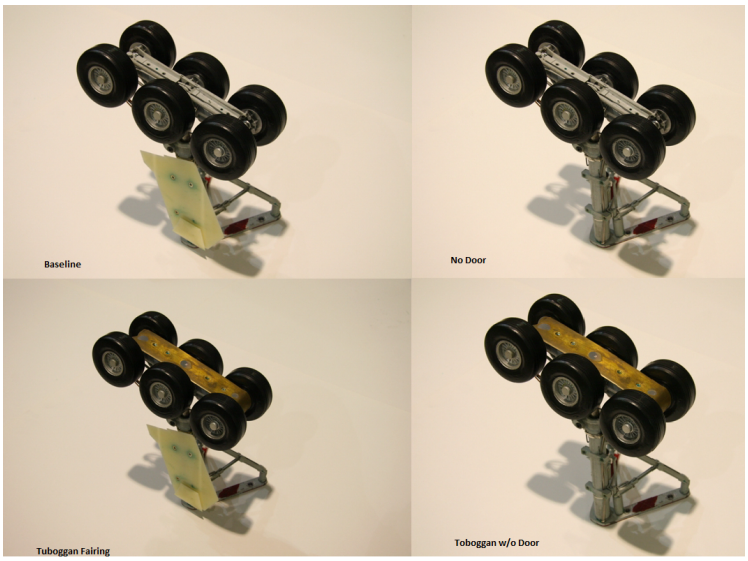

Figure 2.1: Boeing 777 main landing gear tested configurations.[8]

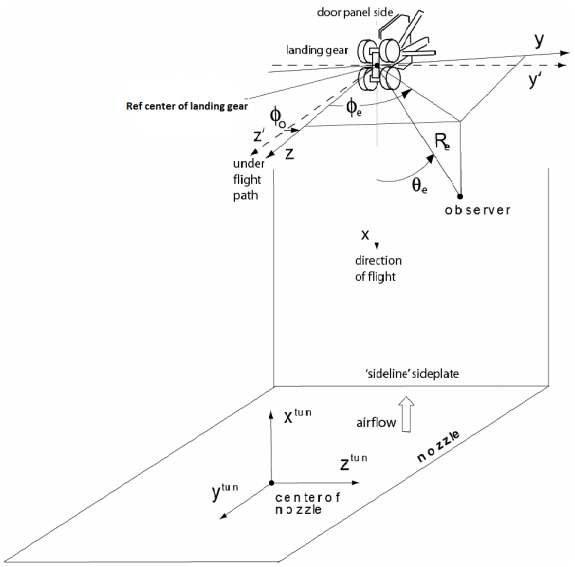

Figure 2.2: QFF landing gear polar coordinates with respect to the QFF nozzle coordinate system.[8]

2.2.3 Low Noise Treatments

Potentials exist for noise reduction of landing gears by means of flow control within the immediate vicinity of its components. Various low noise treatments have been proposed for landing gear applications, with the aim of reducing the aeroacoustic source strength, radiation strength and radiation efficiency. Such low noise treatments include; Solid Fairing Screens, Perforated Fairing Screens, Woven Wire Mesh Screens, Wheel Hub Caps, Hole Covering, Air Curtains, e.t.c. Some of these treatments have only been tested at model scale tests stages, with some having advanced further towards full scale fly over tests. However, the Technology Readiness Level (TRL) of most of these low noise treatments are still in contention. Discussions on these low noise treatments are as follows;

2.2.3.1 Solid Fairing Screens

Aerodynamic noise scales with flow speeds to within 6th-8th power, hence the idea of reducing flow speeds at intricate landing gear sections was thought to potentially reduce aerodynamic noise emitting from such sections. Initial tests of fairing implementation on landing gears started with solid surfaces as

fairings [25, 27]. However, due to high speed flow deflections onto downstream high lift devices, modification from solid to perforated fairings was seen as a better noise reduction technique, and various flight fly over, and wind tunnel tests have been conducted with results confirming its superiority compared to solid fairings.

2.2.3.2 Perforated Fairing Screens

Aircraft fairings represent a noise-reducing mechanism, that is mostly not designed to improve drag [42]. A non-practical fairing covering a total landing gear showed a 10dB noise reduction potential [27]. Several tests employing more practical fairings [25, 27] demonstrated noise reduction of about 3dB. Practical fairings includes the undertray fairing which shields the wheel axles and undertray assembly, wheel caps which covers the rim and leg door filler which covers the gap between leg door and drag arm. Boorsma et al. [9] performed experiments on bluff body noise control using perforated fairings as shown in Figure 2.3 and 2.4. Turbulence statistics showed that for the solid model, the two shear layers interacted and roll up to result in high amplitude transverse velocity fluctuations which peaks on the centerline of the wake. These statistics suggest the existence of large scale vortex shedding associated with the solid fairing. Bleeding air through the perforations prevents the communication between both shear layers. It acts as a splitter plate and therefore this shedding does not take place. As a consequence, the transverse velocity fluctuations are of significantly lower amplitude and the maxima occur close to the shear layers instead of the centerline.The spectral content of the wake is characterized by a broadband spectrum, dominated by the breakdown of turbulence through the energy cascade. Comparing shielding of the circular cylinder and H beam indicates that the noise signatures for the solid fairing shielding the cylinder or the H beam were identical. Hence the noise in each case is dominated by the large scale vortex shedding from the shell, independent of the shielded object. Application of perforations yields further noise decrease which is most effective at the lower frequencies.

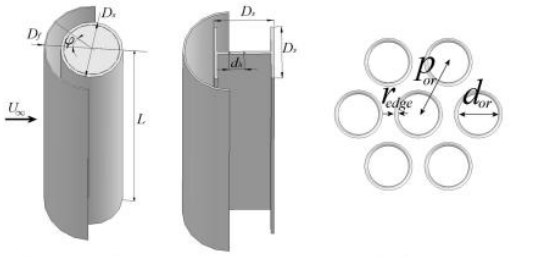

a) Shrouded cylinder b) Shrouded H-beam c) Perforation arrangement

Dimensions		
Shell (outer) diameter	D_f	152 mm
Strut diameter	D_s	100 mm
Shell length	L	514 mm
Cylinder center to shell center	–	0 mm
H-beam center to shell center	d_h	25 mm
Polar angle from shell leading edge	φ	
Orifice diameter	d_{or}	
Orifice pitch	p_{or}	
Orifice edge radius	r_{edge}	

d) Specification of dimensions

Figure 2.3: Illustration of basic model and dimensions[9]

a) View of different fairings

Shell	σ (%)	d_{or} (mm)	p_{or} (mm)	Location of perforations (φ)
solid	0	-	-	-
perf33	33	3	5	$\pm 90°$
perf42	42	3.2	4.7	$\pm 45°$
perf55	55	7	9	$\pm 90°$

b) Specification of different fairings

Figure 2.4: Summary of different fairing configurations tested[9]

A study of the influence of porosity on measured acoustics showed that the increase in porosity increases the velocity of the bled air past the cylinder. However, the resultant acoustics were not altered by this increase. The cylinder does not exhibit sharp edged or small-scale details that could be responsible for noise creation by high velocity impingement. For the H beam, the increase in bled air does modify the related acoustics, because the H beam itself is a noisy structure, therefore washing it with higher velocities increases total noise. As soon as the noise source associated with the shedding from the shell is broken down, the H beam becomes the primary noise creation mechanism. This illustrates the limitations to the perforated fairing concept. The initial purpose of the fairings is to prevent high-speed flow past the landing gear components. Therefore care needs to be taken when applying high porosities to perforated fairings.Therefore, after a certain amount of air is bled through, bleeding more air through the shell becomes less effective for reducing large

scale velocity fluctuations. After enough air is bled to break down the vortex shedding, the unsteady flow field consists of the flapping of the wake in a lateral direction. This flapping is not significantly altered by increasing the porosity further. At higher frequencies, scaling of the noise with local shearing flow velocity past the perforations is observed. To characterize the frequency content of the noise, the Strouhal numbers based on orifice diameter d_{or} and local velocity can be calculated using

$$Str_{or} = \frac{f d_{or}}{u} \tag{2.35}$$

Quantitatively, Boorsma et al. [9] observed that a fairing exhibiting 42% porosity reduces the maximum flow velocity by 18% resulting in a reduction of unwanted high-speed flow deflection by the fairing. A rough estimate of the bled mass flux has been given. Application of the perforations results in a breakdown of the vortex shedding noise at $Str_{Df} = 0.2$, illustrated by a vanishing spectral peak in the wind-tunnel measurements. The perforations are shown to create noise at higher frequencies centered around $Str_{Df} = 0.33$. The shearing flow past the perforations, tangential to the outer shell surface, is responsible for the high-frequency noise. Both intensity and spectral content are dictated by the local velocity past the perforations and the orifice diameter. This opens up the possibility for tailoring this noise phenomenon above the upper limit of the audible range.

Boorsma et al.[10] further studied the noise reduction capabilities of perforated fairings on a scaled model landing gear, as shown in Figure 2.5, with the narrow band spectra results shown in Figure 2.6

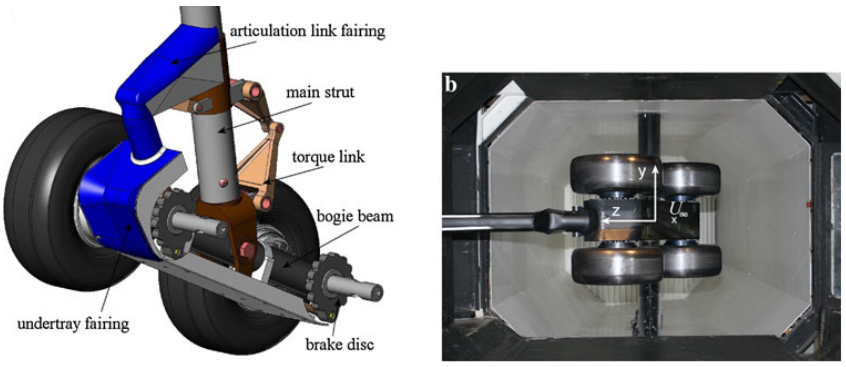

Figure 2.5: Gear components with two wheels omitted and model suspended in tunnel [10]

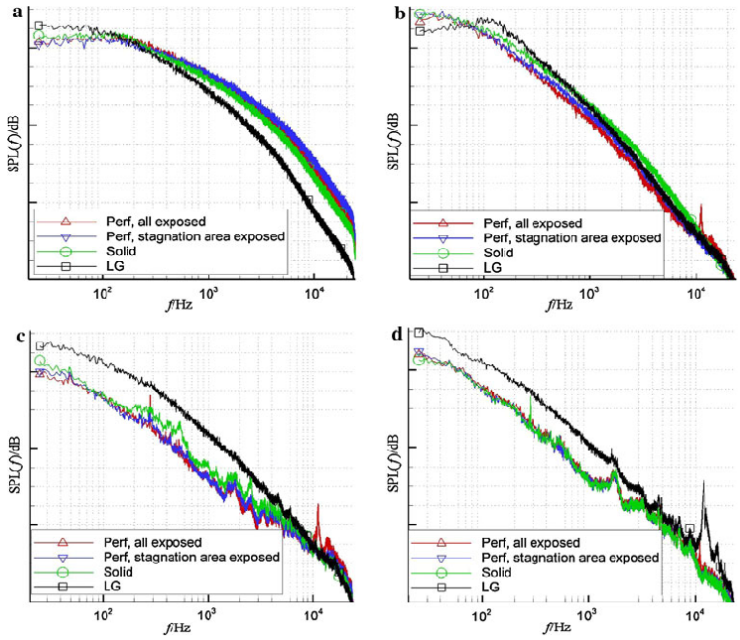

Figure 2.6: Narrow band spectra of surface microphones on the gear. Location **a**:Main leg upper. Location **b**:Main Leg lower. Location **c**: Bogie-articulation link Junction. Location **d**: Rear bogie cap [10]

On-surface microphones and two phased microphone arrays were used to measure the ground and side view noise signatures. Results for the perforated fairings showed similar trends as the results obtained by Boorsma et al.[9]. The application of solid fairings showed to reduce noise in the mid and high frequency domain compared to the plain landing gear configuration by up to 4.5 dB. However a noise increase is observed in the low frequency domain. The application of perforations reduces the low frequency noise introduced by the

solid fairings to values below the plain landing gear configuration. Also, the increase in noise at high frequencies caused by the perforate self noise occurred at Strouhal number of $St = 0.33$ based on orifice diameter of perforate and local flow velocity as expected.

Results of Li et al.[43] during the test for four different types of fairings: solid, perforated, perforated with edge brushes, slotted with cloth on the four wheel MLG configuration, already showed that the slotted under-tray covered with cloth was the most effective replacement to the standard solid under-tray since this not only gave a reasonable reduction at low frequencies, but also achieved a significant reduction in the mid and high-frequency range. The perforated under-tray represented the next most effective replacement, but the perforations needed to be developed and optimized in order to achieve better reductions in low-frequency noise and suppress the high-frequency self-noise which offsets the benefits.

2.2.3.3 Woven Wire Mesh Screens

More recently, meshes have been applied as landing gears low noise treatments, as it was observed to have potentials for improvements on the perforated fairings. It is based on similar noise and flow principles as perforated fairings. Meshes have been tested on generic bluff bodies, where a single and combined H strut was used to represent a simplified landing gear strut[11], carried out in the framework of the European research project TIMPAN (Technologies to Improve Airframe Noise). Various mesh porosities and shapes were tested and these meshes showed to yield drastic broadband noise reduction. Figure 2.9 shows the test section and the various mesh shapes tested, where noise reduction occurred for all tested meshes and angles of attack.

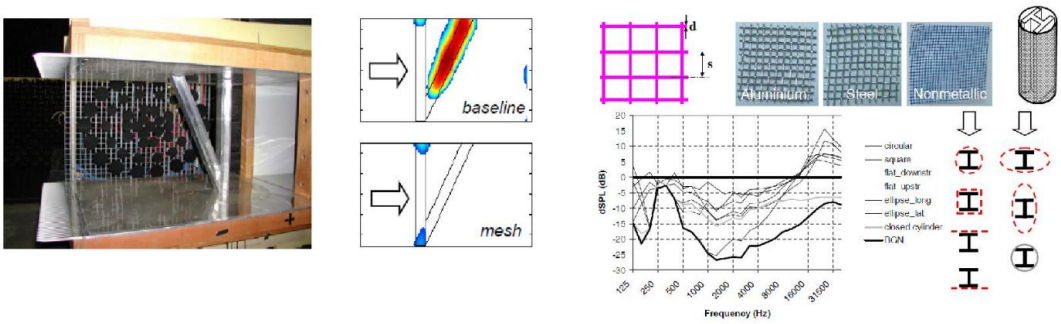

Figure 2.7: Noise reduction test using mesh[11]

Cylindrical meshes, wrapped around the struts, provided substantial noise reduction (5-10 dB) for low and intermediate frequencies. This noise reduction occurred for all tested mesh porosities, and seemed to increase slightly with decreasing porosity. The noise reduction could be increased significantly by modifying the mesh shape, where the lateral elliptical mesh shape gave best results. The noise reductions occurred for both flow speeds tested (50 m/s and 70 m/s), all tested angles of attack, and for all tested models, i.e., for the self-noise from the single strut and for the interaction noise from the combined bodies. However, at high frequencies (above about 10 kHz), the meshes caused an increase in noise due to vortex shedding from the mesh wires, which scaled with strouhal number. A-weighted OASPL which ranged between 4 dB and 21 dB for the different struts and angles of attack were recorded. Therefore, similarly to perforated fairings, several mechanisms may be responsible for the drastic noise reduction caused by the meshes. The possible reasons for this effect are.

1. Meshes reduce the local flow speed at the strut, which leads to a noise reduction because the aerodynamic noise from the strut scales with the 6th power of the flow speed.

2. Meshes may break up the incoming flow in small vortices, thereby affecting the spanwise coherent vortex shedding from the strut.

3. Meshes may move the vortex shedding away from the solid strut surface, thus reducing the acoustic radiation efficiency.

However, it was concluded that dedicated flow measurements were required to better understand the aerodynamic noise reducing mechanisms of meshes.

Smith et al.[21] also investigated mesh screens on a scale model main landing gear. The results showed significant noise reduction when using meshes as treatments. They transposed their noise data from the wind tunnel test to flight conditions in order to estimate the potential overall approach noise reduction for an existing twin long-range aircraft. The application of mesh undertray provided more than 3 EPNdB noise reduction of the main landing gear noise in approach, which gave a total aircraft noise reduction of 0.8 EPNdB

2.2.3.4 Wheel Hub Caps

Wheel hub caps are often used for the covering of wheel hubs, which causing noise as a result of flow interactions with wheels during approach conditions. An example of hub cap (part 34) is shown in Figure 2.8

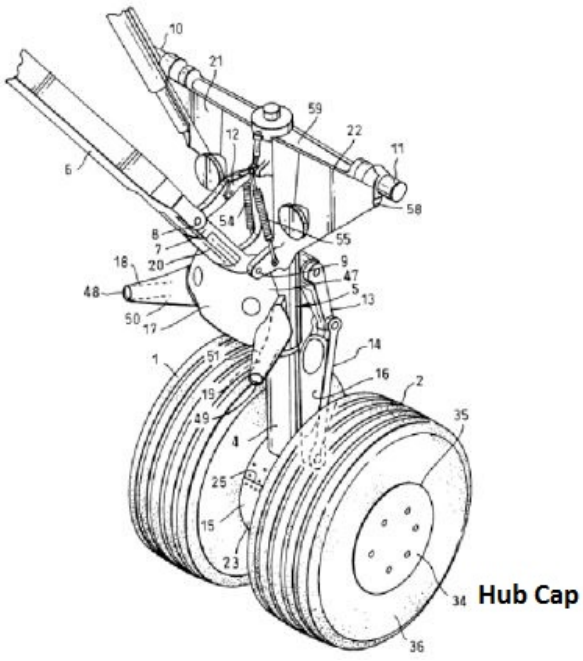

Figure 2.8: Wheel hub cap[12]

2.2.3.5 Hole Covering

Flow over small hole's can be characterized by distinctive tones (Figure [11]). This holes can be avoided easily by simple coverings. Dobrzynski et al.[5]

noted that pin-hole covers are not popularly in use due to water condensation problems.

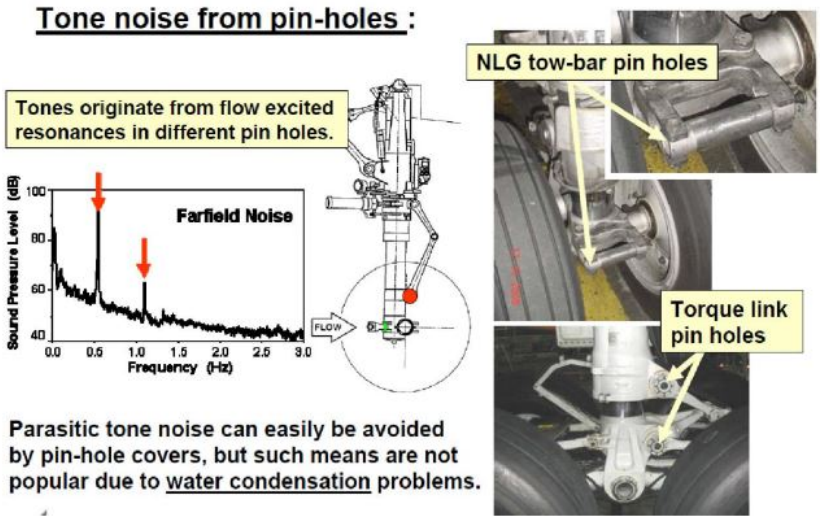

Figure 2.9: Tone noise gener[11]

2.2.3.6 Air Curtains

The concept of an air curtain introduced an application of upstream blowing air in order to deflect the flow around a landing gear component, thus reducing the local flow speeds and therefore the aerodynamic noise. Air curtain was proposed in the year 2004 [13]. Figure 2.10 shows examples of air curtains.

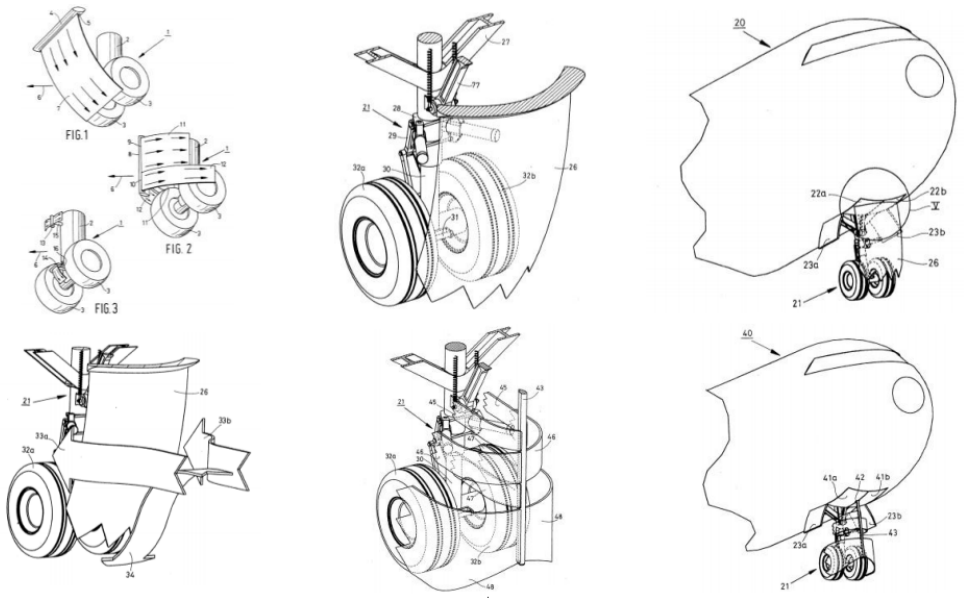

Figure 2.10: Examples of air curtain for landing gear noise reduction[13]

The air curtain jet self noise has been characterized by studies as subject of a certain classic lip noise [44, 45, 46]

Further detailed studies of air curtain applications as low noise treatments for landing gear components, and it's applications as a single or dual jet configuration can be found in [47, 48, 49, 50, 51, 52, 53]

2.2.4 Semi-Empirical Landing Gear Noise Prediction Models

Prediction of landing gear noise represents a significant challenge due to the small-scale features, complicated flow field, and potentially significant installation effects [54]. Therefore, in order to accurately predict the noise from a landing gear, all the small scale influences must also be predicted accurately.

2.2.4.1 Fink Model

Fink [55] developed one of the earliest semi empirical prediction method for a full aircraft assembly, during the late 1970s. This prediction method was based on flight tests of full-scale aircraft and noise sources for the landing gear was correlated as a function of a few gross landing gear properties such as wheel diameter and oleo strut length. Due to lack of measurements and analysis of

flow fields at that time, this prediction method does not attempt to include the small-scale details or installation effects as separable predictions. This made the Fink method unable to predict noise change due to a noise reduction concept, such as installation effects due to perforated fairings and mesh screens implementation, or gear alignment, as the gross landing gear features would remain the same.

2.2.4.2 Smith and Chow model

Another prediction scheme, the ISVR/Airbus noise model [56], uses a component based algorithm to compute the noise from the individual components of the landing gear; then the noise from each component is summed together to achieve the total noise source. Installation effects are included by direct modification of the directivity function, without knowledge of their actual physical mechanisms. This prediction method of noise from landing gear is based on fundamental scaling laws, and the landing gear noise was mainly from struts, wheels, dressings and Tyre-wake interaction. Dimensionally, expression for the mean square far-field pressure due to a strut was given by:

$$P_s = \sqrt{(\rho c^2)^2 D_s \frac{M^6}{4\pi R^2} l_s d_s [F_s(S_s) + F_d(S_d)]} \tag{2.36}$$

where l_s and d_s are the length and the diameter of the component, R is the observer radius, M is the Mach number. $F_s(S_s)$ is a non-dimensional spectral shape function associated with the component; $F_d(S_d)$ is the spectral shape function associated with small components attached to the strut, i.e. dressings. To obtain the far-field pressure, directivity must be considered, which is equivalent to multipling by the coefficient, D_s. Similar to the Guo method, this prediction method has been compared to a number of wind tunnel experiments and flight tests with moderate success, as shown for the noise prediction compared with flight test data from the A321 with main landing gear deployed and the A340 with full landing gear deployed. Figure 2.11 shows the comparison between model predictions and experimental data, where the dash-dot and the solid lines stand for the prediction and the measurement in

Figure 2.11a.

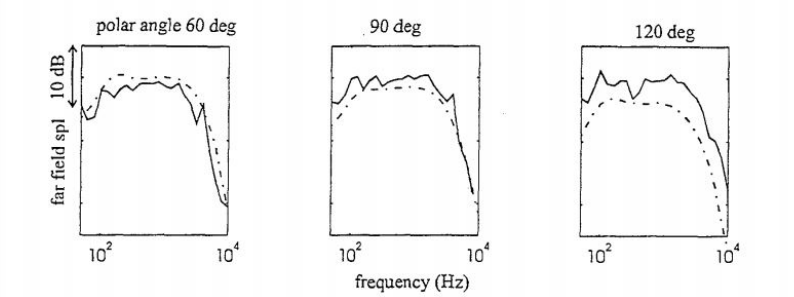

(a) Prediction of A321 main landing gear flyover data at 3 polar angles including convective amplification and atmospheric attenuation[57]

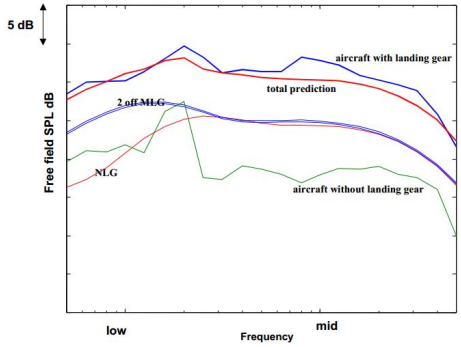

(b) Comparison with A340 flyover data[56]

Figure 2.11: Comparison of the model with experimental data

However, also similar to the Fink and Guo methods, the ISVR/Airbus noise model does not include interactions or installation effects as separable predictions, making prediction of the effect of noise reduction techniques very challenging.

2.2.4.3 Guo Model

A later prediction scheme, was developed by Guo [58], which decomposes the landing gear noise into three spectral components: the low, mid, and high spectral range. The low frequency spectral component represents the noise generated by large-scale structures such as wheels. The mid and high frequency spectral components correspond to the main struts and the small-scale details such as hydraulic lines respectively. The spectral shape, amplitude, and directivity of each component were derived separately, and each contains

factors to allow modeling of the details of each spectral component in an attempt to include more physics. The Guo method requires significantly more detailed inputs to define the landing gear assembly than the Fink method, hence, providing a higher fidelity prediction capability. These inputs include all the basic flow and geometric parameters used in the Fink method: i.e., number of wheels; wheel diameter; main strut length; but also the wheel width, axle diameters, bogie length and width, as well as details on all other struts, shock struts, vertical bars, axles, torque bars, junction rods and door details. In addition and importantly, unlike the Fink method, the Guo method was developed in terms of a narrow-band spectrum, which is converted to one-third-octave as the last step. Each frequency range has a simple directivity pattern and a list of complexity factors, which are calibrated to wind tunnel experiments. Recently, this method has been coupled with an external flow solution to include the effect of local flow conditions in the vicinity of the landing gear due to circulation around the wing [57]. Although this method does reproduce some wind tunnel and fly-over measurements reasonably well, it does not provide the prediction of each landing gear component noise source as a separable prediction. Furthermore, it does not include many other effects such as reflection, scattering, or local flow due to the landing gear geometry. Since it is unable to include the installation effects and local flow conditions in the vicinity of the landing gear, it is unable to predict the influence of noise reduction concepts on installed landing gear noise. The Fink and Guo methods have been compared to measurements of noise from the 6.3%-scale Boeing 777 main gear model performed in the NASA Quiet Flow Facility (QFF) with moderate success [58].

2.2.4.4 LGMAP

A fourth prediction method was developed at The Pennsylvania State University, called the Landing Gear Model and Acoustic Prediction (LGMAP) [59, 60]. LGMAP is a component based semi-empirical prediction scheme using an object oriented approach to acoustic prediction. The landing gear ge-

ometry is modeled as, in some cases, thousands of acoustic sources, each with their own flow input and acoustic output. The small geometric details of the landing gear are included in the noise prediction by directly including them in the landing gear representation. Including these small features has been shown to capture the noise level increase caused by an increase in landing gear geometry fidelity. Recently, aerodynamic and aeroacoustic interactions, such as scattering by the landing gear geometry, reflections by the wing, and local flow caused by the circulation of the wing, have been added to the scheme. However, the LGMAP prediction method or previous prediction methods have not been able to couple a configuration-change based flow field prediction to the their models that can predict the flow field change caused by a configuration change such as the introduction of a perforated screen fairing or wire mesh screen.

2.2.5 Landing Gear Noise Coordinated Programs

2.2.5.1 RAIN

Within the framework of RAIN (Reduction of Airframe and Installation Noise) (1998-2002), sub projects carried out experimental tests as well as numerical analysis on an A340 2-wheel nose, 4 and 6-wheel main landing gears [14, 21, 25, 61, 62, 63]. Experimental tests were carried out at DNW wind tunnel facility, and flight fly over tests were also conducted. RAIN was also tasked with identifying the most dominant noise sources within the aircraft airframe at fly over conditions and rank them accordingly, thus quantifying their contribution to overall airframe noise. Directivity and OASPL level results of A340 airframe noise sources achieved during this program are as shown in Figure 2.12

Within the program, It was concluded that the landing gears were the main contributing noise source within the aircraft airframe during approach [64], as tonal noise due to open cavities and broadband noise were largely dominant. Tests showed that the landing gear noise mainly radiated into the forward and rearward arc, and that noise generated at different aircraft components followed different velocity scaling laws, as a velocity scaling of U^6

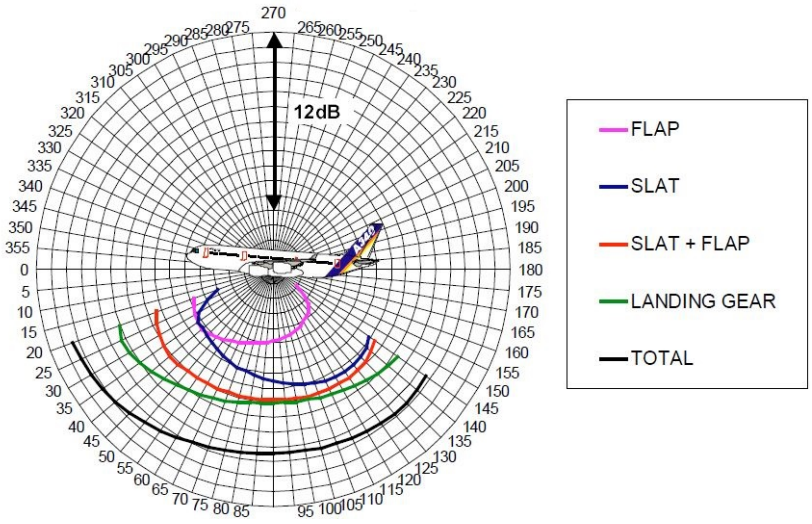

Figure 2.12: A340 Aerodynamic Noise Sources Directivity and OASPL Levels [14]

was observed for the landing gears and slats, U^8 existed for the flaps, while $U^{5.5}$ existed for the combined high lift devices [14, 65]. RAIN identified the lower part of landing gears as the dominant noise sources, which includes the brake system. RAIN further concluded that the precise location of the sources was sensitive to flow direction and thus subsequently to the bogie angle, where for all wheel configuration test cases an additional 2 dB(A) noise reduction was observed when the bogie angle was aligned to the flow direction. From the test campaign, they observed that the number of wheels, i.e 2, 4 or 6 was not sufficiently a key parameter affecting acoustic results, particularity at high frequencies, while a certain correlation exists between the landing gear size and it's resulting noise output. Noise levels from the 2 wheel gears were lower to the 4 wheel gear, and noise levels from the 4 wheel gear also lower to the 6-wheel main landing gear. Within the RAIN program, low noise treatment devices were also tested for applicability within landing gears. Perforated fairing screens was utilized in wrapping sections of landing gears, with fairings utilized for the upper leg, bogie, axle, towing bar, steering system, brake system and wheels. With a combined use of such fairings on various components, an overall noise reduction of 3 dB(A) A-weighted was achieved for the nose

landing gear, while an overall reduction of 2.5 dB(A) A-weighted was achieved for the main landing gears. It was also observed that for the nose landing gear, the fairings providing more efficient noise reduction were associated with the fairings on the towing bar, steering systems and axle, with the wheels and upper leg fairing providing further noise reduction, while for the 4 and 6 wheel main landing gears, the brake fairings were the most reliable fairings for noise reduction.

2.2.5.2 SILENCER

SILENCER (Significantly Lower Community Exposure to Aircraft Noise) (2001-2006) program was tasked with the reduction of landing gear noise by investigating low noise technologies. Within this program, wind tunnel tests carried out in DNW for novel landing gear designs and large scale tests which also utilized CFD optimized fairings. Flight fly over tests [28, 66] were also conducted for A340 similar to RAIN program. The novel landing gear design incorporated a ramp-type spoiler for shielding the upper part of the landing gear. This novel design together with applied brake fairings, bogie fairings and bogie alignment with flow direction resulted in a landing gear noise reduction of 3 dB compared to the RAIN program [26]. During the tests, source localization system that consisted of 196 phased microphone array were utilized [65, 67, 68, 69] It was also discovered that without fairings as add-ons, potential noise reduction could be achieved solely by modifying the bogie angle in relation to the flow direction. As an example, a 5 dB increase in noise levels was attained with bogie angle toe up of 35 deg for a 4-wheel A340 configuration [70, 71, 72]. However, when the bogie is aligned with the flow direction, the most dominant noise source appeared to be the frontal axle area. A logical explanation as to why the bogie alignment with flow resulted in reduced noise levels is that this configuration gives rise to a resulting flow deflection providing shield for the bogie beam components which subsequently reduces noise levels within this components [61]. Within this program, a 1.8 EPNdB noise reduction was transposed to 0.4 EPNdB for aircrafts incorporating nose and main

landing gear fairings. A rather strong recommendation of this program was that breakthrough technologies would most likely aid progress towards 'European Vision 2020' goal of 10 dB noise reduction, compared to modifications of already existing conventional aircrafts possessing wing installed engines and large landing gears [70].

2.2.5.3 QTD 2

QTD 2 (Quiet Technology Demonstrator 2) (2005-2006) was an aircraft test program that looked into the effectiveness of a number of low noise technologies applied to reduce aircraft noise in general, i.e, jet noise, high-lift devices noise, airframe noise, etc [73, 74]. Within it's framework, QTD 2 incorporated wind tunnel tests as well as flight tests. Full-scale flight tests of a B777-300ER aircraft was carried out, where a toboggan shaped solid fairing screen was designed and implemented on the main landing gear [15] as shown in Figure 2.13.

(a) Designed Toboggan Fairing **(b)** Installed Toboggan Fairing

Figure 2.13: QTD 2 Toboggan Fairing Test for B777-300ER [15]

Acoustic results had previously shown the main landing gear as a major noise contributor compared to the nose landing gear for the B777-300ER aircraft, therefore testing within the QTD 2 program focused on the main landing gear [75]. Selection process for the toboggan fairing was achieved by carrying out multiple model-scaled wind tunnel tests utilizing full-scale feasibility studies, where the fairing design was made to incorporate issues like brake cooling, gear kinematics, ground operations and most importantly, noise reduction.

Stress and flutter analysis were also performed during the toboggan fairing design. Significant noise reduction of 1 dB to 4 dB within broadband frequency range were achieved on a 26%-scale high-fidelity landing gear when toboggan fairings of different widths were utilized. Also, significant noise reduction was observed when the baseline landing gear bogie is aligned to the fluid flow direction compared to a baseline toe up configuration. Figure 2.14 shows a baseline landing gear toe-up configuration and a baseline aligned configuration.

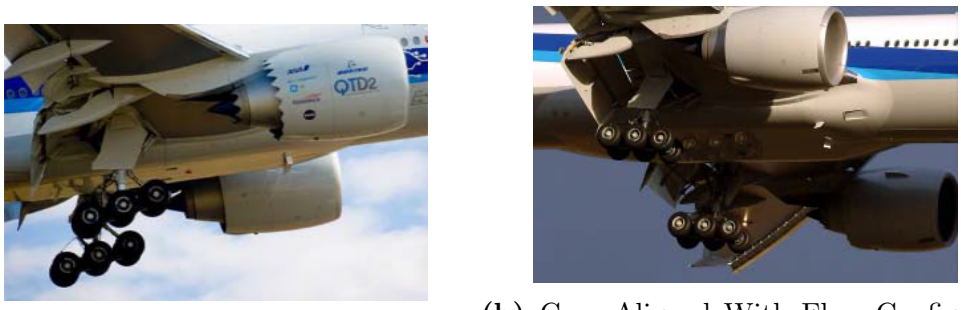

(a) Gear Toe-Up Configuration

(b) Gear Aligned With Flow Configuration

Figure 2.14: QTD 2 B777-300ER Gear Truck Orientation Tested [15]

Phased array results as shown in Figure 2.15 from noise tests carried out for these baseline configurations (Without Toboggan Fairing Installed) resulted in a noise decrease of up to 2.5 dB for the landing gear bogie aligned with flow direction configuration compared to the toe up configuration.

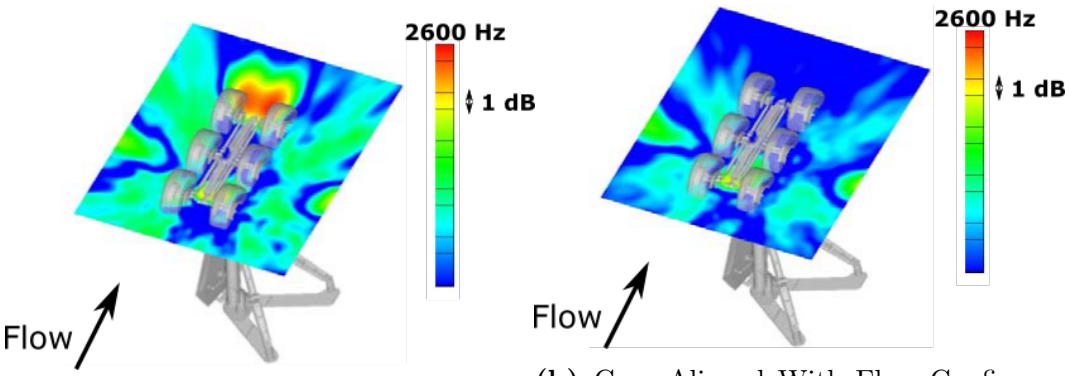

(a) Gear Toe-Up Configuration

(b) Gear Aligned With Flow Configuration

Figure 2.15: QTD 2 Phased Array Result for B777-300ER Baseline Gear [15]

Therefore, a strong recommendation from this test program regarding re-

duction of landing gear noise was a further development and optimization of such fairings (by perforating) and other fairing-like materials that could possibly result in more noise reduction, as well as utilizing a landing gear bogie configuration that is aligned with the fluid flow direction in context.

2.2.5.4 TIMPAN

Previous test programs which carried out installation of solid fairing screens showed that high speed flow deflection from such solid fairings unto downstream high lift devices resulted in increased noise levels within the downstream high lift devices [15, 76, 77]. Therefore, more focus on perforated fairing screens and woven wire mesh screens were proposed as this would result in less amount of deflected flow, yet still providing reduced flow speeds within the fairing wake region and subsequent less interaction noise levels of downstream components [71, 78, 79]. Within the framework of TIMPAN (Technology to IMProve Airframe Noise) (2006-2009), attempts were made to propose low noise gear designs through flow control means and various optimizations, both locally and globally. The idea of improved gear designs also factored in the constraint of not incorporating negative weight penalties within the landing gears. TIMPAN project incorporated low noise treatment devices such as perforated fairing screen designs, woven wire mesh screens, and air curtains [11, 80, 81]. Wind tunnel tests of 1/4 scaled model configurations of 4 wheel landing gears were carried out and results compared to the SILENCER flight test results. TIMPAN concluded that the most efficient tested configuration were configurations incorporating combined use of a narrow wheel spacing, perforated fairings, a negative angle between flow and bogie, a modified side stay design and brake fairings. The use of these combinations resulted in a noise reduction of 8 dB(A) A-weighted relative to the the SILENCER gear configuration. Similar to the RAIN project, the bogie part of the 4 wheel gear showed to be the most dominant noise source. Therefore, noise reduction techniques would need to focus more on the bogie part of landing gears. Noise from the bogie area was found to be directional, while noise from the landing gear upper parts

were more omnidirectional. Noise results were transposed to flight conditions and noise reduction at approach configuration for long range aircraft achieved more than 7 EPdNdB for the main landing gear noise reduction, resulting in an overall aircraft noise reduction of 1.5 EPNdB when high-lift device noise and engine noise are unchanged.

2.2.5.5 OPENAIR

OPENAIR (OPtimisation for low Environmental Noise impact AIRcraft) (2009-2014) program incorporated a more multi disciplinary methodology in it's framework and focused on validation of new technologies on TRL5. Amongst the programs wide scope, airframe noise was also investigated as a sub project, with particular attention on landing gear noise signatures. Both modeled scale and full scale tests were carried out in wind tunnels and numerical simulations were also investigated for low noise configurations. Deceleration plates were utilized downstream landing gears with the aim of reducing upstream flow speeds and resulting noise emissions without added negative flow displacement effects. In addition to the low noise treatments employed within the TIMPAN program, the landing gear was fitted with front leg rectangular torque links, solid covers for drag stay and leg cavity, and electric dressing [82].
Therefore, RAIN, SILENCER, TIMPAN and OPENAIR programs resulted in potential landing gear noise reductions when fairings are incorporated, and also recommended bogie aligned to flow direction [41, 83, 84]

2.2.5.6 ALLEGRA

The ALLEGRA (Advanced Low Noise Landing Gear for Regional Aircraft) (2013-2014) project was tasked with the responsibilities of testing various low noise treatments for regional aircrafts. Within the framework of ALLEGRA, wheel hub caps were installed on both sides of nose landing gear wheel models. ALLEGRA wind tunnel experiments were conducted in the Pininfarina aeroacoustic open jet semi-cylindrical wind tunnel facility in Turin, Italy[85]. Results from ALLEGRA showed that 1.5 dB noise reduction in the range of

300 Hz and 1000 Hz can be achieved for a full scale nose landing gear configuration with the application of wheel hub caps [16, 86]. Woven wire mesh treatments of a main landing gear model as shown in Figure 2.16 was also carried out within the ALLEGRA test campaign. Acoustic noise reductions of up to 5dB centered at 4000 Hz 1/3 octave band were achieved with the implementation of the woven wire mesh screen as a low noise treatment for the MLG within this project [20].

Figure 2.16: ALLEGRA Wire mesh screen installed on an MLG [16]

ALLEGRA also tested a ramp type door spoiler as one of a it's selected low noise treatment as this was considered as a low noise treatment possessing very high likelihood of success. This test was performed in combination with and also without other low noise treatments within a wind tunnel for a full scale nose landing gear model [86, 87]. The ramp type door spoiler showed to reduce noise in the frequency range of 100 Hz and 900 Hz, where significant noise reductions of 10 dB were obtained. Therefore, this ramp type spoiler showed great potential, however, it was also shown to introduce a new noise source possessing a much lower noise level, and this noise was understood to be associated to the shear layer separation from the trailing edge of the ramp

door spoiler itself.

The ALLEGRA project coordinated test campaign also utilized a bay absorber liner treatment in order to treat the MLG wheel bay cavity noise. For this purpose, a commercial 50 mm thick Basotect Melamine Resin Foam with absorption of 90% at 2kHz was utilized. From the project reports, the liner was not found to attenuate the main noise sources which were at a lower frequency than that which the foam was most effective at. Further studies within the test campaign [88] showed that significant low frequency noise can be radiated from the wheel bay due to shear layer excited resonance.

2.2.5.7 LAGOON

The LAGOON program (LAnding Gear NOise database for CAA validatiON) (Since 2006) is a coordinated program that assesses CFD-CAA techniques based on experimental results from a generic landing gear geometrical configuration [89, 90]. This program is duly supported by Airbus, and was lunched in 2006. The ambitious aims of this program includes building a large database that is highly accurate for the CFD analysis and CAA acoustic code analysis on a generic landing gear model. Since the launch of the LAGOON program, various researchers have performed CFD-CAA unsteady analysis on the LAGOON geometry, with different levels of success [91, 92]. One of the key areas of this campaign also include the identification of the most suitable computational grid structure, and accurate CFD simulation that is coupled to acoustic codes [93, 94, 95].

2.2.5.8 WP4.1

As part of the WP4.1 (Airbus/TSB Integrated Wing) (Since 2009) program, porous fairings were applied as flow and noise reduction medium to conventional landing gears, where investigations into the noise reduction potentials of such porous materials without attempting to re-design landing gears with noise as a design constraint were carried out for advanced landing gears [21]. Noise reduction achieved using porous fairings showed to vary with polar an-

gles of microphone array. Summary of reductions obtained utilizing different treatments are as presented in Table 2.1

Summary of Noise Reductions			
Description	50 deg	90 deg	130 deg
Solid Fairings	-3.6 dBA	-2.9 dBA	-0.4 dBA
All porous Fairings	-4.3 dBA	-4.3 dBA	-0.9 dBA
All porous Material Wraps	-2.6 dBA	-2.3 dBA	+0.2 dBA

Table 2.1: WP4.1 Summary of Overall Changes for Treatment Types Tested [21]

Generally, it was observed that perforated fairing screens resulted in much significant noise reduction when compared to solid fairing screens, while porous material wraps could potentially be more effective if configured to cover more areas. Noise results were transposed to flight conditions and the low noise gear configuration resulted in more than 3 EPNdB noise reduction from main landing gear during approach phase, resulting in a total aircraft noise reduction of 0.8 EPNdB.

2.3 CAA

Computational Aero-Acoustics (CAA) can be grouped into two major categories. These are

- Direct CAA Approach
- CFD-Acoustic Analogy Coupling Approach

These two categories will be briefly introduced.

2.3.1 Direct CAA Approach

The direct CAA approach, which consists of solving the full compressible equations for the unsteady flow field and the acoustic field simultaneously, is rarely used to analyze cases of engineering interest because of its very high computing power requirements and the need for non-dispersive and non-dissipative schemes to propagate the acoustic waves. If effectively used however, it can

account for effects of the fluid flow on sound, acoustic reflections, scattering, and can propagate sound through shells, giving a solution of very high accuracy. Direct numerical simulations (DNS) of this kind require no assumptions whatsoever, and can produce highly accurate solutions, as all time dependent variable fields and its interactions are accurately solved.

2.3.2 CFD-Acoustic Analogy Coupling

This approach, which is also called a hybrid method, decouples the fluid dynamics processes acting as noise source generation, from the transport and propagation of the acoustics to a far field domain, making the assumption that noise generated does not influence the dynamics of the flow. Several methods exist both for the sound generation and for the sound propagation to far field locations. For the sound flow generation process, the time-dependency must be accounted for given that aeroacoustics phenomena are intrinsically unsteady. It may be accounted for implicitly, by reconstructing the source data from RANS results which may further require some empirical calibration, as shown by Bechara et al. [96]. Once the noise sources are known, the sound propagation can be computed via transport equations or acoustic analogies, e.g FW-H analogy. The amplitudes of acoustic waves are much smaller than the mean flow. As a result, the numerical scheme must have a high resolution and extremely low numerical noise in order to produce acceptable results, because acoustic levels are as low as discretization errors. Computational aeroacoustics schemes must also have minimal numerical dispersion and dissipation in order to propagate effectively to far field receivers. Since the length scale of acoustic source are usually very different from the acoustic wavelength, great care must be taken during modeling. It must be pointed out here that these hybrid methods are not as accurate as direct methods, not as stringent, cannot account for effects of the fluid flow on sound, acoustic reflections, scattering, giving a solution that is very limited in accuracy, but which comes at a very low computational cost. Hybrid CFD-Acoustic analogy methods include;

2.3.2.1 LES Based Acoustic Coupling

Large Eddy Simulation has been the most widely used scale resolving model over the last decades. It is based on the concept of resolving only the large scales of turbulence and to model the small scales. The classical motivation for LES is that the large scales are problem-dependent and difficult to model, whereas the smaller scales become more and more universal and isotropic, therefore can be modeled more easily. LES is based on filtering the Navier-Stokes equations over a finite spatial region and aimed at only resolving the portions of turbulence larger than the filter width. Turbulence structures smaller than the filter are then modeled, typically by a simple Eddy Viscosity model [97]. The filtering operation is defined as

$$\bar{\Phi} = \int_{-\infty}^{\infty} \Phi(\vec{x'}) G(\vec{x} - \vec{x'}) d\vec{x} \tag{2.37}$$

where G is the spatial filter. Therefore, filtering the Navier-Stokes equations results in the following form, where the density fluctuations have been neglected.

$$\frac{\partial \rho \bar{U}_i}{\partial t} + \frac{\partial \rho \bar{U}_i \bar{U}_j}{\partial x_j} = \frac{\partial P}{\partial x_i} + \frac{\partial}{\partial x_j} \left(\bar{\tau}_{ij} + {\tau_{ij}}^{LES} \right) \tag{2.38}$$

where

$${\tau_{ij}}^{LES} = \rho \bar{U}_i \bar{U}_j - \rho \overline{U_i U_j} = \mu_t \left(\frac{\partial \bar{U}_i}{\partial x_j} + \frac{\partial \bar{U}_j}{\partial x_i} \right) \tag{2.39}$$

The important practical implication from this modeling approach is that the modeled momentum equations for RANS and LES are identical if an eddy-viscosity model is used in both cases. In other words, the modeled Navier-Stokes equations have no knowledge of their derivation. The only information they obtain from the turbulence model is the size of the eddy viscosity. Depending on that, the equations will operate in RANS or LES mode (or in some intermediate mode). The formal identity of the filtered Navier-Stokes and the RANS equations is the basis of hybrid RANS-LES turbulence models, which can obviously be introduced into the same set of momentum equations. Only

the model (and the numerics) have to be switched. Classical LES models are of the form of the Smagorinsky model, where

$$\mu_t = \rho(C_s \triangle)^2 S \tag{2.40}$$

$\triangle$ is a measure of the grid spacing of the numerical mesh, S is the strain rate scalar and C_s is a constant. A more appropriate goal for LES is not to model the impact of the unresolved scales onto the resolved ones, but to model the dissipation of the smallest resolved scales [97]. For free shear flows, it is typically much easier to resolve the largest turbulence scales, as they are of the order of the shear layer thickness. However, in wall boundary layers the turbulence length scale near the wall becomes very small relative to the boundary layer thickness, increasingly so at higher Re numbers. This poses severe limitations for Large Eddy Simulation (LES) as the computational effort required is still far from the computing power available to industry. For this reason, hybrid models are under development where large eddies are resolved only away from walls and the wall boundary layers are covered by a RANS model. Examples of such global hybrid models are Detached Eddy Simulation. A further step is to apply a RANS model only in the innermost part of the wall boundary layer and then to switch to a LES model for the main part of the boundary layer. Such models are termed Wall-Modelled LES (WMLES). Finally, for large domains, it is frequently necessary to cover only a small portion with a resolving model, while the majority of the flow can be computed in RANS mode. In such situations, zonal or embedded LES methods are attractive as they allow the user to specify ahead of time the region where LES is required. Such methods are typically not new models in the strict sense, but allow the combination of existing models/technologies in a flexible way in different portions of the flowfield. Important elements of zonal models are interface conditions, which convert turbulence from RANS mode to resolved mode at pre-defined locations. In most cases, this is achieved by introducing synthetic turbulence based on the length and time scales from the RANS

model.

In RANS models, a time averaging of Reynolds equations are performed to get the equations in steady form, whereas, in LES, a filter operation is performed; volume average the equations. The filtered variables are functions of space and time, the basic idea in LES is to resolve large eddy grid scales (GS) and to model the small sub-grid scales (SGS). In LES only small-scaled turbulence are modeled and no equation for the turbulent length scale is required, since the turbulent length scale can be taken as the filter width. Large Eddy Simulations (LES) are capable of computing the generation of sound and its propagation within the near-field of a landing gear. LES is a widely used scale resolving simulation approach amongst computational aeroacoustics researchers. To propagate the sound to far-field receivers, Ffowcs Williams-Hawkings (FW-H) acoustic analogy is used [98]. Imamura et al.[99], carried out aeroacoustics simulations of a simple two-wheel landing gear assembly using LES solver with structured mesh,and far-field noise results acquired by the use of FW-H.

2.3.2.2 DES Based Acoustic Coupling

Detached Eddy Simulation (DES) is a hybrid combination of LES and unsteady RANS Models. The objective of a DES is to treat the near wall boundary layer with RANS and capture the outer detached eddies with LES. DES was originally developed for wings at very high angles of attack, and the RANS model that was originally used was the Spalart and Allmaras one-equation model. Detached Eddy Simulations (DES) are capable of computing the generation of sound and its propagation within the near-field of a landing gear. DES is one of the most widely used scale resolving simulation approach, as it can be coupled with Ffowcs Williams-Hawkings (FW-H) acoustic analogy for far field noise predictions. Advancement in the field of computational aeroacoustics has led to large number of noise generation and propagation studies of simple streamlined bodies and more complex bluff bodies [100].

Spalart et al [101] introduced Detached Eddy Simulation (DES) with the

intention of eliminating the main limitations of LES models. They proposed a hybrid formulation that switches between RANS and LES based on the grid resolution provided. By this formulation, the wall boundary layers are entirely covered by the RANS model and the free shear flows away from walls are typically computed in LES mode. The formulation is mathematically simple and can be built on any RANS turbulence model. The technique of modeling, which simply switches from a RAN to LES based on the grid resolutions has attained significant attention in the turbulence community. Within this hybrid approach, the switch between RANS and LES is based on a criterion as simple as

$$C_{DES}\triangle_{max} > L_t \rightarrow RANS; \triangle_{max} = max\left(\triangle_x, \triangle_y, \triangle_z\right) \tag{2.41}$$

$$C_{DES}\triangle_{max} \leq L_t \rightarrow LES; \tag{2.42}$$

where $\triangle_{max}$ is the maximum edge length of the local computational cell. The formulation for the k-equation of the $k-\omega$ model.

$$\frac{\partial(\rho k)}{\partial t} + \frac{\partial(\rho \bar{U_j} k)}{\partial x_j} = P_k - \rho \frac{k^{\frac{3}{2}}}{min\left(L_t, C_{DES}\triangle_{max}\right)} + \frac{\partial}{\partial x_j}\left(\left(\mu + \frac{\mu_t}{\sigma_k}\right)\frac{\partial k}{\partial x_j}\right) \tag{2.43}$$

$$L_t = \frac{k^{\frac{3}{2}}}{\varepsilon} = \frac{k^{\frac{1}{2}}}{\beta^* \omega} \tag{2.44}$$

As the grid is refined below the limit $\triangle_{max} \leq L_t$ the DES-limiter is activated and switches the model from RANS to LES mode. The intention of the model is to run in RANS mode for attached flow regions, and to switch to LES mode in detached regions away from walls. This suggests that the original DES formulation, as well as its later versions, requires a grid and time step resolution to be of LES quality once they switch to the grid spacing as the defining length scale.

The DES limiter can be activated by grid refinement inside attached boundary layers. This is undesirable as it affects the RANS model by reducing the

eddy viscosity which, in turn, can lead to Grid-Induced Separation [97], where the boundary layers can separate at arbitrary locations depending on the grid spacing. In order to avoid this limitation, the DES concept has been extended to Delayed-DES (DDES), thereby shielding the boundary layer from the DES limiter. The DDES extension was also applied to the DES-SA formulation resulting in the DDES-SA model, as well as to the SST model giving the DDES-SST model. For two-equation models, the dissipation term in the k-equation is thereby re-formulated as

$$E_{DES} = \rho \frac{k^{\frac{3}{2}}}{min\left(L_t, C_{DES}\triangle\right)} = \rho \frac{k^{\frac{3}{2}}}{L_t min\left(L_t, C_{DES}\frac{\triangle}{L_t}\right)} = \rho \frac{k^{\frac{3}{2}}}{L_t} max\left(1; \frac{L_t}{C_{DES}\triangle}\right) \tag{2.45}$$

$$E_{DDES} = \rho \frac{k^{\frac{3}{2}}}{L_t} max\left(1; \frac{L_t}{C_{DES}\triangle}(1 - F_{DDES})\right) \tag{2.46}$$

The function F_{DDES} is designed in such a way as to give $F_{DDES} = 1$ inside the wall boundary layer and $F_{DDES} = 0$ away from the wall.

Detached-Eddy Simulation (DES) was first performed for flows over a landing gear by Hedges et al. [102], at Reynolds number $Re = 6 \times 10^5$. Currently, the dominant method for aeroacoustic related simulations is the combination of a DES based approach and the Ffowcs Williams-Hawkings analogy. Souliez et al. [103] performed simulations on a four-wheel main landing gear bogie model, coupled with the FWH integral equation for far-field propagation. They used both solid and permeable surfaces to compute the far-field sound and obtained similar results for both, reinforcing the dimensional argument first advanced by Curle [32], that dipoles dominate over quadrupoles at low Mach numbers. Fortin et al.[104] used DES with a commercial solver to predict the flow field, and used FW-H for the far-field noise. Jeremy et al. [105] also investigated a realistic nose landing gear configuration, including peripheral features that were expected to alter the flow field and hence contribute to the far-field sound. These features included the bay cavity, the doors and a part of the fuselage. the use of a compressible Improved Delayed-Detached Eddy Simulation (ID-DES)

coupled with FW-H analogy was implemented. Xue et al.[106] investigated noise reduction by changing torque links positions with the effects of relative positions of pillar and torque arm on noise studied both numerically using DES coupled with FW-H and experimentally in a wind tunnel. Langtry et al.[107] investigated the far-field noise produced by a rudimentary landing gear, where they made use of the Spalart Allmaras (SA) near wall turbulence model-DES hybrid, coupled with the FW-H. The unsteady time dependent flows were advanced using an implicit second-order dual time algorithm. Simulation results compared with experimental measurements.Numerical investigations aimed at modeling noise generation and propagation from landing gears have been carried out by various researchers. Hedges et al.[102] performed DES over a simplified landing gear. Dahan et al.[105] performed a compressible IDDES-FWH analysis for a simplified re-modelled landing gear geometry attached to the fuselage with open bay. Souliez et al.[103] performed similar analyisis for an unstructured grid scenerio, while Imamura et al.[99] conducted a large eddy simulation (LES) analysis for a simple two-wheel landing gear assembly using structured grids. Fortin et al. [104] performed a DES and predicted far field noise using FWH. All these results showed promising signs for further needed analysis in the field of landing gear noise predictions using hybrid computational aeroacoustic approach. Quentin et al[83] presented a review of numerical studies carried out using LBM, where optimization of low-noise solutions were also achieved. All CFD results captured to a large extent the noise reduction effects of the fairings applied but were achieved at substantial high computational costs.

2.3.2.3 LBM Based Acoustic Coupling

The Lattice Boltzmann Method (LBM) of CFD-Acoustic analogy coupling has gained recent success and popularity amongst researchers. Traditional CFD equations mainly focus on continuity equations and the Navier Stokes equations, where the principal aim is on the discretization of derivatives which requires first and second order derivatives. Many possible discretizations of

these equations exists and finding the appropriate discrete operators becomes the subject of a detailed CFD code and methodology, where most of the possible discretization serve to only conserve mass and momentum up to the actual order of discretization [108]. An alternative approach to the traditional CFD equations and methodology was invented within late 1980s, using the lattice gas methods [108, 109, 110, 111, 112, 113, 114, 115, 116, 117, 118, 119, 120, 121]. This lattice gas method allowed the movement of particles on a discrete lattice, where local collisions conserved mass and momentum. The Boltzmann transport equation is given by Equation 2.47

$$\frac{\partial f}{\partial t} + \overrightarrow{u}.\nabla f = \Omega \tag{2.47}$$

Where $f(\overrightarrow{x}, t)$ represents the particle distribution function, $\overrightarrow{u}$ represents the particle velocity, while Ω represents the collision operator. More recently, the Lattice Boltzmann technique highlights huge potentials in terms of computational costs compared to DNS and ease of dealing with complexities of a full aircraft geometry. [122, 123]. Therefore, over the years, the lattice Boltzmann method has shown to be a successful method for a wide array of applications involving fluid flows and a large number of studies have been reported with great success on the use of the LBM technique for turbulent flows and the LBM/FW-H coupled technique for noise prediction [124, 125, 126, 127, 128, 129, 130, 131, 132, 133, 134, 135, 136, 137, 138, 139, 140, 141]. Detailed application of the LBM/FW-H coupled technique for aeroacoustic noise prediction from aircraft airframe and more particularly, landing gears (nose and main) have been reported with high level of agreement when validated against co-ordinated fly-over test campaigns and wind tunnel tests [142, 143, 144, 145, 146, 147, 148, 149, 150]. Mitsuhiro et al.[29] performed very detailed LBM/FW-H based numerical simulations and noise reduction studies on perforated fairings applied on a two wheel main landing gear using a Very Large Eddy Simulation (VLES) coupled with the Ffowcs Williams-Hawkings (FW-H) acoustic analogy for noise propagation prediction to far-field receivers.

This was carried out using Powerflow software (EXA Corp), which is based on the Lattice Boltzmann Method (LBM) of fluid analysis. Results showed good agreement with experimental data up to 1kHz.

2.3.2.4 Unsteady-RANS Based Acoustic Coupling

The RANS equations can also apply to flows having time-varying mean flow, even though these equations are time-averaged'. This class of RANS are the Unsteady Reynolds-averaged Navier-Stokes (URANS). Statistically unsteady (or non-stationary) flows can equally be treated with this approach. Hedges et al. [102], compared Unsteady Reynolds-Averaged Navier-Stokes (URANS) simulations on a mesh of 2.5×10^6 cells at a modest Reynolds number $Re = 6 \times 10^5$, with a DES. A highly simplified 31%-scale of a Boeing 757 four-wheel main landing gear was considered. The numerical result was validated with experimental results of Lazos et al. [39], carried out in the Basic Aerodynamics Research Tunnel (BART) at NASA Langley Research Center. Pressure fluctuations over the landing gear surface, lift, drag, instantaneous contours of velocity, vorticity, turbulent kinetic energy and Reynolds stresses were all analyzed. Overall, a good qualitative agreement with experimental data was obtained. They observed that the URANS simulation typically under predicted the magnitude of forces and the level of unsteadiness. Therefore, the URANS coupled with an acoustic analogy will have limited applications based on the poor accuracy of its results.

2.3.2.5 RANS Based Acoustic Coupling

This method of acoustic analysis is achieved by coupling the Reynolds-averaged Navier-Stokes (RANS) equations with an analytic acoustic solver. An ensemble version of CFD governing equations (conservation of mass, momentum, and energy) is solved, which introduces new apparent stresses known as Reynolds stresses. This adds a second order tensor of unknowns for which various models can provide different levels of closure. The formulation of Reynolds-Averaged Navier Stokes (RANS) Modeling Equations considered time-averaging only.

Reynolds Averaged Navier Stokes Models can be divided in to two groups, namely the Boussinesq hypothesis models, and the Reynolds stress models. The Boussinesq hypothesis models are models based on the Boussinesq Assumption. These models are also called eddy viscosity models. In the Boussinesq assumption, an eddy viscosity is introduced to model the unknown Reynolds stresses. This method involves using an algebraic equation for the Reynolds stresses which include determining the turbulent viscosity, and depending on the level of sophistication of the model, solving transport equations for determining the turbulent kinetic energy and dissipation. The models available in this approach are often referred to by the number of transport equations associated with the method. For example, the Algebraic Models (Mixing Length model) is a "Zero Equation" model because no transport equations are solved. One equation models are so called because one transport equation is solved, i.e, k. The 'Two Equation Models' are so called because two transport equations (one for k and one for ϵ or ω) are solved. RANS based acoustic methods are however not usually relied upon for aeroacoustic results due to the steady flow based assumption imposed by the RANS solutions.

2.4 Physics of Flow Through Screens

Flow through perforated screen surfaces and woven wire mesh screens remain an important subject area in fluid mechanics because these screen surfaces are often utilized as fluid flow control mediums, for production or reduction of turbulence and for creation or elimination of large-scale velocity or pressure uniformities. Also utilized in the field of hydraulics, perforated plates and wire screens are generally used for flow control. Most investigations deal with perforated plates and wire screens placed perpendicular ($\approx 90°$) to incoming upstream flow across an entire cross section. The physics of fluid flow through a perforated screen surface or woven wire mesh screen can be viewed from its pressure drop effect, modification of velocity distribution, turbulence alterations effect, and self-noise characteristics, which are the most important

effects to put into consideration when discussing such screens. These effects are summarized in subsequent subsections, with the influence of screen open area ratio (porosity) on the aerodynamics performance of such screens discussed.

2.4.1 Pressure Drop Effect

Analyzing flow through a perforate screen section or woven wire screen section as shown in Figure 2.17 We distinguish three sections within the flow domain.

- Cross section of fluid region far upstream (approximately free-stream) of screen, potentially unaffected by presence of screen.
- Cross section of fluid region at which jets issuing from holes of screen are fully contracted but still essentially undiffused.
- Cross section of fluid region downstream of screen where fluid potentially returns to near free stream conditions.

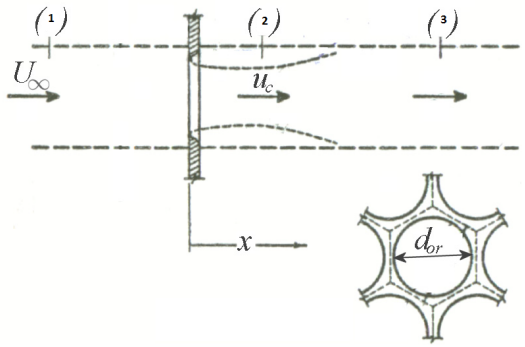

Figure 2.17: Cross section of fluid region describing flow through screen hole[17]

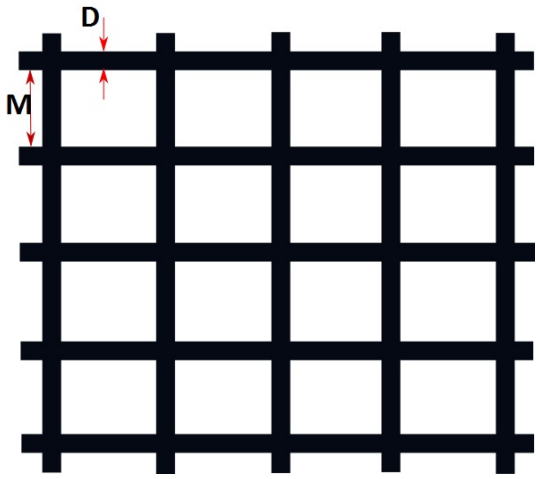

Figure 2.18: 2D schematic representation of a woven wire mesh screen

For perforated screens, open area ratio (porosity) is calculated for the cylindrical aperture arrangement as [6]

$$\sigma = \frac{1}{6}\sqrt{3}\pi(\frac{d_{or}}{p_{or}})^2 \tag{2.48}$$

In this context, porosity refers to the open area ratio of the perforated material, where σ= porosity, d_{or}= diameter of cylindrical perforate, and p_{or}= centre to centre pitch of cylindrical perforates.

Pressure loss coefficient correlation for flow past a perforate as given by Baines [17] is;

$$\zeta_l = \frac{2\Delta p}{\rho U_\infty^2} = \left(\frac{1}{C_c\sigma} - 1\right)^2 \tag{2.49}$$

where C_c= contraction coefficient with values between $\frac{2}{3}$ and 1. ζ_l= perforated screen pressure loss coefficient, and σ=perforated screen open area ratio.

It was further argued that this equation be modified for high values of σ. This was confirmed by experiments showing physical values of ζ_l to depart from equation 2.49 at σ >0.7 for thin plate screens. Pressure drop over a wide variety of perforated plates is documented by Idelchik [18], which combines the results of many previous investigations on this subject. The parameters taken into account are Reynolds and Mach numbers, perforate shape, plate

thickness, hole diameter and porosity. The Reynolds number of the perforate is defined as;

$$Re_{dor} = \frac{u_{or} d_{or}}{\nu} \tag{2.50}$$

where u_{or}= Velocity in the orifice, d_{or}= Orifice diameter.

Idelchik [18] further showed that within the turbulent fluid flow regime of $Re_{dor} \geq 1 \times 10^4$, Equation 2.49 above of Baines [17] is valid for application when using perforated screens.

However, for metal woven wire mesh screens as shown in Figure 2.18, different correlation models are documented for pressure drop calculations. Woven wire screen open area ratio (Porosity) is calculated making use of Equation 2.51. Where β = open area ratio (Porosity).

$$\beta = \frac{M^2}{(M + D)^2} \tag{2.51}$$

Equation 2.52 shows a dimensionless relationship between flow loss coefficient K of wire screens, static pressure drop and dynamic pressure through the wire screen. Static pressure drop measurements of wire screens are commonly acquired for wire screens utilized for flow control within wind tunnels [151, 152, 153, 154].

$$K = \frac{2\Delta p}{\rho U_\infty^2} \tag{2.52}$$

Empirical correlations of flow loss coefficient through single layer screens have been well documented, where such correlations based on wire diameter and open area ratio generally take the form of;

$$K = G(\beta)\left(\frac{Z_1}{Re_D} + Z_2\right) \tag{2.53}$$

In such form, G is only a function of β, while Z_1 and Z_2 are correlated constants [155]. However, choice of the G function depends also on the Reynolds number form being used, due to the fact that two different velocities can be utilized. Either the free-stream approach velocity U_∞ or a velocity related to

the woven wire screen porosity $U_s = \frac{U_\infty}{\beta}$. Reynolds number in this case can also be based on dimensions such as the wire diameter (D), minimum passage width ($\frac{1}{m} - D$) or any variant of an hydraulic mean diameter.

Wakeland [156] utilized a variant of G function for correlations on experimental data and arrived at the correlation of Equation 2.54

$$K = \frac{2\Delta p}{\rho U_\infty^2} = \frac{1-\beta}{\beta^2}\left(\frac{17.0}{Re_D} + 0.55\right) \tag{2.54}$$

This correlation worked well for $Re_D = 2$, but underestimated K for $2 \leq Re_D \leq 200$. However, for intermediate Reynolds number in the range $2 \leq Re_d \leq 400$, a Wieghardt-styled Wakeland correlation of Equation 2.55 showed to produce much better results.

$$K = 4.6\left(\frac{1-\beta}{\beta^2}\right) Re_d^{-1/3} \qquad 2 \leq Re_D \leq 400 \tag{2.55}$$

Wieghardt[157] utilized a Reynolds number based on screen aperture velocity instead, and arrived at a correlation valid for screen Reynolds number in the range $60 < Re_s < 600$ as shown by Equation 2.56. As it is thought that the maximum flow speeds attainable within the screen aperture mesh width should be more related to the screen porosity.

$$K = 5.5\left(\frac{1-\beta}{\beta^2}\right) Re_s^{-1/3} \qquad 60 < Re_s < 600 \tag{2.56}$$

Idelchik [18] documented an empirical correlated relationship for flow loss coefficient of wire screens. This correlation was found to be Reynolds number independent for $Re_D \geq 400$, as shown by Equation 5.1.

$$K = K_{mesh}K_{Re}(1-\beta) + \left(\frac{1-\beta}{\beta}\right)^2 \qquad Re_D \geq 400 \tag{2.57}$$

Where wire constant $K_{mesh} = 1$ for new screens and wire Reynolds number factor $K_{Re} = 1$ for $Re_D \geq 400$.

Roach [1] documented flow loss correlations for arrays of square meshes possessing round wires or rods (SMR) and arrays of square meshes possessing square bars (SMS). Square mesh arrays of round wires (SMR) was found to fit Equation 2.58 and 2.59 within the Reynolds number range shown.

$$K = \frac{14}{Re_D}\left(\frac{1-\beta^2}{\beta^2}\right) \qquad Re_D < 10 \tag{2.58}$$

$$K = \left(0.52 + \frac{66}{Re_D^{4/3}}\right)\left(\frac{1-\beta^2}{\beta^2}\right) \qquad 40 < Re_D < 10^5 \tag{2.59}$$

Square mesh arrays of square bars (SMS) was found to correlate to Equation 2.60.

$$K = 0.98\left(\frac{1-\beta^2}{\beta^2}\right)^{1.09} \qquad 10^2 < Re_D < 10^5 \tag{2.60}$$

2.4.2 Velocity Modification Effect

Modification of velocity distribution by perforated plates is treated by Baines [17]. Non uniformities in flow distribution are evened out more by passage through a perforated plate. A theory is developed to predict this modification, which agrees well with experiments for high open area ratios$>$ 0.5. Screens with lower values of open area ratio were found to yield unstable flow downstream. By varying the upstream velocity distribution approaching the plate, it was found that the velocity distribution downstream of the plate is almost invariant to the upstream profile for these values of open area ratio. In this case downstream means sufficiently far away from the region affected by the individual jets. It is also argued that screens at an angle to the flow will tend to deflect the flow towards the normal of the plate, simply because the flow resistance is a minimum when the flow is at right angles to the plane of the screen. Therefore a curved perforated plate is expected to deflect the flow towards the centre of the curve.

2.4.3 Turbulence Alteration Effect

Flow through screens in isolation can be represented by a number of jets that form independently and then gradually spread and coalesce with neighboring jets. The energy of the mean flow is converted into turbulent energy by eddies produced in the zone of intense shear surrounding each jet. The eddies begin to decay immediately, changing their energy into heat by viscous dissipation. Further downstream the jets are fully mixed and turbulence will become isotropic. The length necessary for decay depends on the jet geometry and therefore scales with d_{or}. Turbulence is often described by means of the turbulence intensity T which can be defined as the ratio of the Root Mean Square (RMS) of the velocity fluctuations over the mean velocity

$$T = \frac{u'_{rms}}{\overline{u}} \tag{2.61}$$

Checkel [158] performed hot wire measurements along a hole centre line aft of various plates with $\sigma = 0.4$ spanning the tunnel. Varying hole diameter and tunnel speed, the Reynolds number range covered $1.0\times10^3 \leq Re_{dor} \leq 1.3\times10^4$. Turbulence intensity T was shown to reach a maximum of 50% at $\frac{x}{d_{or}} = 2.5$ for all combinations, illustrating dependence of production and decay on hole diameter. Since hole diameter varies between 2.5 and 20 mm for a constant plate thickness (t = 5 mm), influence of hole aspect ratio becomes noticeable. Apparently, a high aspect ratio produces smaller scale turbulence resulting in lower turbulence energy levels in the downstream flows. Castro [159] researched on a perforated plate of finite width spanning a wind tunnel in the Reynolds number range between 2.5×10^4 and 9.0×10^4 (based on plate width). Hot wire measurements in the wake of the plates with a porosity between 0 and 64.5% showed that the effect of bled flow is to move the area of reversed flow further downstream. Above a porosity of approximately 40%, the reversed flow area disappears. For zero porosity ($\sigma = 0$), the two unstable shear layers interact in the near wake and roll up to form a vortex street. The bled flow prevents this interaction in the usual way and delays the vortex formation.

This is accompanied by an increase in base pressure. At a porosity of 20% the vortex street suddenly ceases to exist. This is indicated by a sudden drop in plate drag and a sudden downstream movement of the point of maximum turbulence intensity along the plate centerline. The velocity spectrum measured sideways of the wake shows a distinct peak at a Strouhal number of 0.14 (based on plate width) for a solid plate. Above $\sigma = 0.2$ a distinct spectral peak is still visible, although the frequency suddenly drops. This periodicity is believed to be due to the flapping of the unstable turbulent wake instead of vortex shedding. Above a porosity of 40% it is no longer possible to pinpoint a dominant frequency. Mehta [160] performed a detailed experimental investigation on the effects of different types of screens on turbulent flow, in particular the turbulent boundary layers. He tested both wire and plastic screen geometries, which due to their different weaving properties and elastic moduli were supposed to act differently in application. The effect of all screens on the turbulence structures were found to be similar, which was that the existing turbulence is almost completely obliterated and a new boundary layer is formed, with increased activity in the inner part of the outer layer. The recovery of the boundary layer turbulence structure is also almost complete at about $x = 40\delta_0$, where δ_0= the undisturbed boundary layer thickness at screen position. Therefore, the perturbation of a turbulent boundary layer by a screen, acted to reorganize the thickness of the turbulent boundary layer, making it less susceptible to separation. Beyond the boundary layers, metal screens were found to produce more non-uniformities than the plastic screens, and it was correlated with the uniformity of weave. It was also observed that streamline or stream inclination played an important role in determining the details of the emerging flow field. For screens inclined to the fluid flow, variation of pressure drop coefficient with screen inclination was found to be related by

$$K_\theta = K \cos^m \theta \tag{2.62}$$

With $m \sim 1.0$ for screens with $\beta \sim 0.6$, and $m \sim 1.4$ for screens of lower β ($\sim$ 0.3). K_θ = Inclined screen pressure drop coefficient, m= correlation constant, θ=angle of inclination of screen to flow.

The above mentioned investigations can aid in creating a good idea of the flow structures and factors involved when using wire mesh screens for aerodynamic applications.

Woven wire screens possess turbulence alteration characteristics which are known to depend on the flow loss coefficient of such screens [161, 162, 163, 164, 165]. Within the immediate downstream near field wake region of screens, turbulence exits in an anisotropic form with intensities much higher than upstream intensities, and at about more than 20 woven wire widths downstream of screen the turbulence returns to an isotropic form [162]. Batchelor et.al [166, 167] reported on the decay of isotropic turbulence within the initial decay period and the final decay period, thus resulting in the knowledge that a decay region exists further downstream far-field, where anisotropic intensities begin to reduce rapidly and turbulence returns to a near isotropic state. The decay of isotropic homogeneous turbulence downstream a grid or screen is known to follow an exponential decay law[168, 169, 170, 171, 172].

The damping factor introduced by a screen within a flow field is usually expressed as the ratio of turbulence intensity produced at a location after the fluid stream passes through the screen to the turbulence intensity at the same point but with the screen absent.

$$f_u = \frac{(u'_{rms})_{screen-present}}{(u'_{rms})_{screen-absent}} \ , \quad f_v = \frac{(v'_{rms})_{screen-present}}{(v'_{rms})_{screen-absent}} \tag{2.63}$$

Where f_u is the axial turbulence reduction factor, f_v the lateral turbulence reduction factor, u'_{rms} the rms velocity perturbation in axial direction, and v'_{rms} the rms velocity perturbation in lateral direction. The axial and lateral damping factors can be distinguished for screens and are expected to be markedly different within the anisotropic turbulent region of the downstream near-field wake region of screen, but as the turbulence returns to an isotropic

state further downstream, axial and lateral turbulence reduction factors almost become indistinguishable. Relations for turbulence reduction factors of woven screens have been formulated and are usually in good agreement with documented experiments. Prandtl[173] proposed Equation 2.64;

$$f_u = \frac{1}{1+K} \tag{2.64}$$

Collar[174] proposed Equation 2.65,

$$f_u = \frac{2-K}{2+K} \tag{2.65}$$

Taylor and Bachelor model [175] is shown in Equation 2.66,

$$f_u = \frac{1+\alpha-\alpha K}{1++\alpha+K}\ , \quad f_v = \alpha \tag{2.66}$$

Where α is the ratio of flow angle of incidence with respect to normal to screen surface for upstream flow to angle of incidence for downstream flow. Dryden and Schubauer[161] proposed Equation 2.67 for axial component of turbulence reduction factor.

$$f_u = \frac{1}{\sqrt{1+K}} \tag{2.67}$$

Schubauer [176] performed experiments utilizing woven wire screens and found that the Dryden and Schubauer theory had a better agreement for both axial and lateral turbulence reduction when compared with the Taylor and Bachelor theory.

Kistler et.al[177] carried out experiments for measurements of grid turbulence for flows with large Reynolds numbers ranging from 1.2×10^5 to 2.4×10^6, and results showed that turbulent energy decay fitted decay laws as expected, and spectral shapes at small wave numbers were independent of Reynolds number, hence, no new phenomenon were introduced for large Reynolds number flows through grids, and as such, experiments of low Reynolds number flows were adequate enough to describe the main features of turbulence flow phenomenon through woven wire grids.

2.4.4 Screen Self-Noise Characteristics

Research carried out by [19, 178] showed a negative effect of woven wire screens on the overall noise emission particularly at high frequency range, when such screens are utilized as flow control mediums on a simplified landing gear H-strut unit. These high frequency noise effect showed to be more predominant at frequencies greater than 12500kHz, and also showed to scale with woven wire screen diameter in a Strouhal number scaling manner.

2.5 Computational Simulations of Screens

CFD based methods which can be used for the computation of fluid flow through porous surfaces, perforated screens and woven wire screens can be classified in the following categories.

- Direct Numerical Simulation (DNS) Method
- Scale Resolving/Turbulence modeling Method
- Permeable Boundary Condition Method
- Macroscopic flow model, which uses a volume-averaged equation within a porous zone within a numerical domain.

2.5.1 Direct Numerical Simulation (DNS) Method

The DNS method of computing flow through a porous surface, perforated screens or woven wire screens requires no assumptions and accurately resolves the interaction between the flow and porous surface. A much more accurate and detailed flow field variables are obtained when the DNS is used, thereby revealing more fundamental physics, which could possibly aid in the validation of other approximate models. However, due to the high computational cost and time demands of carrying out a full DNS, this method does not present a realistic approach for most research applications. Hahn et al. [179] carried out a DNS of turbulent channel flow with permeable walls, with the objectives of

suggesting a proper boundary condition at the interface between a permeable block and turbulent channel flow and to investigate the characteristics of turbulent channel flow with permeable walls. The boundary condition suggested was an extended version of that applied to laminar channel flow of a previous research, and describes the behavior of slip velocities in the streamwise and spanwise directions at the interface between the permeable block and turbulent channel flow. The DNS method can be applied when the porous, perforated or wire screen is studied in isolation and also when it is applied within a bluff body for analysis.

2.5.2 Scale Resolving/Turbulence Modeling Method

Scale resolving methods applicable for simulations of flow through porous surfaces, perforated screens and woven wire screens include the Large Eddy Simulation (LES) and it's variants. The Lattice Boltzmann method (LBM) can also be employed for such simulations [99, 180]. The LES and LBM computational approach can be applied when the porous, perforated or wire screen is studied in isolation and also when it is applied within a bluff body for analysis. The use of RANS based turbulence models can also be applied to study the flow simulations, only when such porous, perforated or wire screens are studied in isolation from a bluff body [181].

2.5.3 Permeable Boundary Condition Method (PBCM)

The method of permeable boundary condition, uses an artificial boundary condition mimicking the effect of porous surface. Jimenez et al. [182] used this method to simulate the turbulent shear flow over active and passive porous surfaces, with the assumption that the normal velocity at the permeable boundary is proportional to the local pressure fluctuation. Tinetti et al. [183] conducted computational studies to assess the potential of passive porosity technology for reduction of wake-stator interaction noise by reducing the fluctuating forces acting on the vane surfaces. The permeable boundary method does not simulate the inner flow within the porous zone itself, and critical care must be

taken for selecting acceptable boundary conditions.

2.5.4 Volume-Averaged Method (VAM)

This is a macroscopic flow model, which uses a volume-averaged equation in the porous media zone, within which a modified Navier-Stokes equation is applied, which describes the flow through the porous zone. In this modified equation, a correction source term representing the pressure drop of the flow within the porous material is described. The Porous cell zone is modeled by the addition of a momentum source term to the standard fluid flow equations. The source term is composed of two parts, a viscous loss term, and an inertial loss term, as shown in Equation 2.68

$$S_i = -\left(\sum_{j=1}^{3} D_{ij}\mu v_j + \sum_{j=1}^{3} C_{ij}\frac{1}{2}\rho|v|v_j\right) \tag{2.68}$$

Where S_i is the source term for the i-th (x, y,or z) momentum equation, $|v|$ is the magnitude of the velocity, while D and C are prescribed matrices, which are user-defined empirical coefficients.

Liu et al.[184, 185] computed turbulent flow and noise characteristics using an LES and unsteady RANS method, respectively. Where his numerical results revealed that porous material coating prominently modified the flow characteristic of the near wake of circular cylinder and significantly mitigated the fluctuations of aerodynamic forces from two aspects of frequency and amplitude, which meant that vortex shedding from the bluff body was suppressed as a result. Schulze et al. [186] predicted the two-dimensional flow around the rigid airfoil combined with a porous leading edge and optimized the permeability of the porous material to reduce the aerodynamic noise. Bae et al. [187] simulated three dimensional flow around the porous airfoil and investigated the effect of the porous surface on the aerodynamic noise.

The volume averaged macroscopic flow model, which uses a volume-averaged equation in the porous media zone, and a modified Navier-Stokes equation will be used for our virtual mesh screen zone. As stated earlier, the Porous cell

zone is modeled by the addition of a momentum source term to the standard fluid flow equations. The source term is composed of two parts, a viscous loss term, and an inertial loss term, as shown in Equation 2.69

$$S_i = -\left(\sum_{j=1}^{3} D_{ij}\mu v_j + \sum_{j=1}^{3} C_{ij}\frac{1}{2}\rho|v|v_j\right) \tag{2.69}$$

Where S_i is the source term for the i-th (x, y,or z) momentum equation, $|v|$ is the magnitude of the velocity, while D and C are prescribed matrices, which are user-defined empirical coefficients.

For the source correction terms, flow resistance using the empirical formulation form Barlow [188], Equation 2.70 will be imposed.

$$\zeta_{wir} = K = \frac{2\Delta p}{\rho U_\infty^2} = K_{mesh}K_{Re}(1-\beta) + \left(\frac{1-\beta}{\beta}\right)^2 \tag{2.70}$$

2.6 Summary

Literature Review Summary of Papers	
Aerodynamic Noise Generation	Lighthill[31], Curle [32], Ffowcs Williams and Hawkings [33]
Low Noise Treatments	Solid Fairings [25, 27], Perforated Fairings [9, 10], Wire Meshes [11, 21], Wheel Hub Caps [12], Hole Coverings [5], Air Curtains [48, 50, 51]
Landing Gear Tests	Flyover Tests [67, 189, 190, 191, 192] Wind Tunnel Tests[27, 39, 70]
Landing Gear Noise Coordinated Programs	RAIN [25, 193], SILENCER [61, 70], QTD2 [73, 74, 75], TIMPAN [11, 80, 81], OPENAIR[82], ALLEGRA [16, 86, 88, 194], LAGOON [91, 92, 93, 94, 95], WP4.1 [21]
Semi Empirical Noise Prediction Models	Fink [55], Smith and Chow[56], Guo [58], LGMAP [59, 60]
Numerical Simulation Prediction Methods	URANS [38, 102], DES [99, 105] LBM [29, 143], LES [99, 195], DNS [195]

Table 2.2: Summary of Literature Review Papers

Table 2.2 presents a summarized form of important literature review papers. From the review of previous research carried out within the subject area of application of woven wire mesh screens and porous surfaces towards noise

reduction from bluff bodies and landing gears, we identify the following issues where improvements and advancement of knowledge are still required.

- Due to the nature of woven wire mesh screens which possess very tiny wire diameters and mesh widths, detailed experimental reports of local velocities in close proximity to the screens have never been reported, as PIV (Particle Image Velocimetry) or hot wire measurements of local velocities in close proximity to the screen surfaces are difficult to achieve. However, CFD can and will be used to achieve this within this thesis.

- Woven wire screens aid aerodynamic noise reduction when applied as low noise treatments by causing a reduction of flow speeds, however, a quantifiable measure of the flow speed reduction has never been reported. The study within this thesis investigates and reports on these flow speed reductions.

- The numerical implementation of physical woven wire screens as low noise treatments for aerodynamic bluff bodies (Landing gears in particular) presents a very expensive computational process, which is often unrealistic to achieve due to tiny length scales involved for such analysis. Therefore, a computational cost friendly alternative will be proposed within this thesis.

- The computational cost friendly alternative proposed within this thesis is implemented as a virtual mesh screen porous zone imposed within a numerical fluid domain, and which accounts for three major effects of a physical mesh screen (pressure drop, velocity change and Turbulence suppression).

Therefore, as previously stated in the objectives of this research, a numerical study to further understand the role of mesh screens as noise reducing agents was conducted. An alternative numerical-semi empirical method for a virtual mesh screen imposed within a numerical domain that accounts for all

expected characteristics of a physical mesh screen will be developed. These characteristics of screen include,

- Pressure drop across the virtual mesh screen zone
- Velocity modification
- Turbulence alteration
- Self noise generation of mesh screen at high frequencies.

Therefore, therein arises the need to investigate the possibility of developing new methods that enables quicker prediction of the numerical effects of low noise treatments such as wire screens when applied to landing gears for low noise treatments [196, 197, 198]. This thesis attempts to address such investigations.

2.7 Contribution of the Thesis

Research results of this thesis advances the knowledge surrounding woven wire mesh screens when utilized as applications for fluid flow control. Woven wire screens applied for aerodynamic noise control purposes are also studied, with a novel modeling approach towards a more computationally cost effective means proposed and validated. Contributions of this thesis include the following:

1. Three dimensional (3D) simulations of fluid flow through woven wire screens are carried out, and better understanding of loss coefficients and turbulence decays at downstream near-field sections reported in chapter 3.

2. For CFD analysis of woven wire mesh screens, a suitable computational domain extent is recommended, which has not been done before.

3. For the first time, quantifiable measures of flow speed reduction achieved by utilizing woven wire mesh screens as flow control mediums are reported. CFD flow loss results are validated against NACA documented experiments.

4. The nature of fluid flow regions at close proximity to woven wire screens possessing tiny screen mesh widths (apertures) and diameters are reported for the first time.

5. For the application of woven wire screens towards two dimensional (2D) flow field analysis, the identification of a simplified two dimensional (2D) screen geometry that provides a best approximation to realistic three dimensional screens are reported for the first time, as presented in chapter 4.

6. Calculating noise reduction effects of realistic woven wire mesh screens attached to landing gears or aerodynamic bluff bodies presents high computational cost demand and expertise, therefore an alternative porous zone modeling approach specifically designed for woven wire screens is developed and validated for noise reduction means. This modeling approach utilizes the Volume-Averaged Method (VAM) in implementing appropriate woven wire screen pressure drop and turbulence alteration within the porous fluid flow region of interest. This approach is reported in chapter 5.

7. Validation of the proposed modeling approach for noise studies is carried out using results of the TIMPAN project and the ALLEGRA experimental test campaign. Reported in Chapter 5 and Chapter 6.

These contributions are presented, discussed and assessed subsequently within this thesis.

Chapter 3

Numerical Simulations of 3D Woven Screens

3.1 Background and Aim

As highlighted previously, a detailed experimental campaign dedicated to the fluid flow physics as to why woven wire mesh screens aid aerodynamic noise reduction has never been carried out. This is due to the nature of woven wire mesh screens which possess very tiny wire diameters and mesh widths, implications of this is that PIV (Particle Image Velocimetry) or hot wire measurements of near-field local velocities through screens will be difficult to achieve. Some best attempts have been in reporting global pressure drops, far downstream velocity fields, and turbulence quantities [17, 156, 161, 162, 176]. Possible reasons for woven wire screens broadband noise reduction effects are thought to include;

1. Woven wire screens causes reduction of local flow speeds immediately downstream wake region of such wire screens when used to shield aerodynamic bodies, thereby subsequently yielding substantial noise reduction particularly within low frequency range since aerodynamic noise within landing gear components scales with sixth power of incident flow speeds (U_{∞}^{6}) [65, 193].

2. Woven wire screens causes a corresponding span-wise vortex shedding coherency distortion from aerodynamic components, which results from reduced aerodynamic surface pressure fluctuations, probably a consequence of flow speeds distortion and more probably as a result of small scale vortices's from the small wire diameters of such wire screens.

3. If woven wire screens are similar in operation to perforated fairings, then a subsequent shift in vortex shedding from aerodynamic bluff body components as a result of the interaction between wire screen small scale vortices's and vortex shedding from aerodynamic bodies.

Within this chapter, Computational Fluid Dynamics (CFD) simulations of flow through three dimensional (3D) woven wire screens is investigated.

Reynolds number range of $80 \leq Re_D \leq 200$ based on woven wire screen diameter are tested. NACA documented experimental campaign of Schubauer [176] are utilized for validation. The core aims of the research carried out within this chapter are;

1. Presenting a novel and computationally cost effective attempt at identifying and distinguishing between fluid flow regions upstream, downstream and within woven wire mesh screen apertures.

2. For fluid flow through woven screens, regions of velocity changes and regions of turbulent kinetic energy changes as the fluid flows through the screen are highlight.

3. Advancing studies of laminar-flow modeled numerical simulations for woven wire screens as carried out by previous researchers [181] by hereby accounting for turbulence with the aid of a suitably selected turbulence model.

4. Identifying the nature of turbulence decay within the near-field downstream wake region of selected woven wire screens.

5. Provide more understanding on the nature of flow speed reductions from woven wire screens.

6. Provide recommendations for suitable woven wire screen locations when applied for aerodynamic noise reduction treatments

7. Comparing CFD predicted flow loss coefficients with NACA experimental results documented by Schubauer [176] and also with classical correlation models of Wakeland [156], Wieghardt [157] and Roach [1] for woven wire screen loss coefficients, thereby highlighting correlations most suitable for practical and theoretical purposes when woven wire screens are utilized.

8. Comparing CFD predicted downstream turbulence decay with correlated turbulence decay model of Roach [1], so as to further understand the nature of immediate downstream turbulence decay from wire screens.

Numerical simulations are carried out for wire screens possessing open area ratios of $\beta = 49.38\%, 51.84\%$, and 67.26%, where β represents screen porosity or open area ratio.

Simulations of flow through single layer woven screens were previously carried out by Green[181]. In their research, simulations were performed utilizing a laminar flow model scenario with screen Reynolds numbers in the range of $50 \leq Re_s \leq 300$ with no turbulence quantities identified. Results were capable of reproducing experimental measurements of wind tunnel screen pressure drops to within 10%. Within this chapter, progress is made on the laminar-flow modeled numerical simulation studies for woven wire screens carried out by Green [181] by accounting for turbulence with the aid of a suitably selected turbulence model, thereby identifying the nature of turbulence quantities in existence within near-field wake region of selected woven wire screens. Laminar modeled simulations through woven wire screens carried out by Green [181] are not capable of studying the nature of low turbulence flows through wire screens which are needed for practical applications, hence a more detailed, yet computational cost effective model is needed, of which this chapter addresses.

3.2 Theoretical Background

Generally, in terms of the physics of fluid flow through a woven wire screen section, the screen section introduces a pressure drop, velocity change and alters the turbulence characteristics of the incoming flow [9, 197]. For wire screens, the flow loss coefficient determines the pressure drop which is introduced, while the velocity change is also a function of the wire screen porosity. Theoretical background of screen loss coefficient and current classical correlation models is presented within this subsection, together with downstream turbulence decay correlation model.

3.2.1 Screen Loss Coefficient Correlations

For woven wire screens, its open area ratio, also denoted as its porosity, is generally calculated with the the use of Equation 3.1. Where D is the wire diameter, M it's open aperture mesh width, and $\beta =$ open area ratio (Porosity).

$$\beta = \frac{M^2}{(M+D)^2} \tag{3.1}$$

The most suitable screen loss coefficient considered within this chapter are the following;

1. Idelchik [18] model as shown in Equation 3.2.

$$K = K_{mesh}K_{Re}(1-\beta) + \left(\frac{1-\beta}{\beta}\right)^2 \qquad Re_D \geq 400 \tag{3.2}$$

   Where wire constant $K_{mesh} = 1$ for new screens and wire Reynolds number factor $K_{Re} = 1$ for $Re_D \geq 400$.

2. Wakeland [156] model shown in Equation 3.3.

$$K = 4.6\left(\frac{1-\beta}{\beta^2}\right) Re_D^{-1/3} \qquad 2 \leq Re_D \leq 400 \tag{3.3}$$

3. Wieghardt[157] as shown by Equation 3.4.

$$K = 5.5\left(\frac{1-\beta}{\beta^2}\right) Re_s^{-1/3} \qquad 60 < Re_s < 600 \tag{3.4}$$

4. Roach [1] model for flow loss correlations of square meshes possessing round wires or rods (SMR), as shown in Figure 3.5

$$K = \frac{14}{Re_D}\left(\frac{1-\beta^2}{\beta^2}\right) \qquad Re_D < 10 \tag{3.5}$$

3.2.2 Screen Turbulence Decay

Mesh wire screens possess turbulence suppression characteristics which are known to depend on the flow loss coefficient of such screens [163, 164, 165]. Within the immediate downstream near field wake region of screens, fluid turbulence is known to exist in an anisotropic form, possessing turbulence intensities much higher than upstream intensities, with this intensity decaying as fluid progresses downstream. Batchelor [166, 167] reported on the isotropic turbulence decay within the initial decay period and the final decay period, thus resulting in the knowledge that a decay region exists further downstream where anisotropic intensities begin to reduce rapidly and turbulence returns to a near-isotropic state.

The decay of isotropic homogeneous turbulence downstream a grid or wire screen is known to follow exponential decay laws [168, 169, 170, 171, 172]. This decay of fluid turbulence downstream of woven wire screens follows decay laws to the power of $-5/7$ as shown in Equation 3.6, and various researchers have shown this to be valid for woven wire metal screens of varying thickness and porosity. For flow regions where viscous effects are significant, the streamwise component of turbulence intensity downstream of a screen grid is represented by Equation 3.6

$$Tu = C\left(\frac{X}{D}\right)^{-\frac{5}{7}} \tag{3.6}$$

Roach [1] showed that for arrays of square mesh possessing cylindrical rods (SMR), the constant "C" becomes independent of Reynolds number within the range $10^2 \leq Re_D \leq 10^4$, and the downstream streamwise turbulence intensity can be correlated by Equation 3.7.

$$Tu = 0.8\left(\frac{X}{D}\right)^{-\frac{5}{7}} \tag{3.7}$$

Oshinowo [163] documented a correlated turbulence decay from metal screens as shown in Equation 3.8.

$$Tu = 7.0\left(\frac{t}{M}\right)^{0.82}\left(\frac{X}{D}\right) \tag{3.8}$$

Documented experiments of Groth [162] shows that at more than 20 mesh widths downstream of a wire screen the turbulence appears to return back to an isotropic form. Wire screen damping factors introduced by a screen within a flow field has also been highly discussed by researchers [161, 173, 174, 175, 199].

3.3 Numerical Set-up

For numerical investigations conducted within this chapter, three dimensional (3D) simulations are carried out by utilizing a suitably selected turbulence model. Within this section, the geometric features of woven wire screens tested, the fluid flow domain sizes utilized, numerical grids generated, boundary conditions implemented, numerical grid independence studies carried out and turbulence model selection processes are presented.

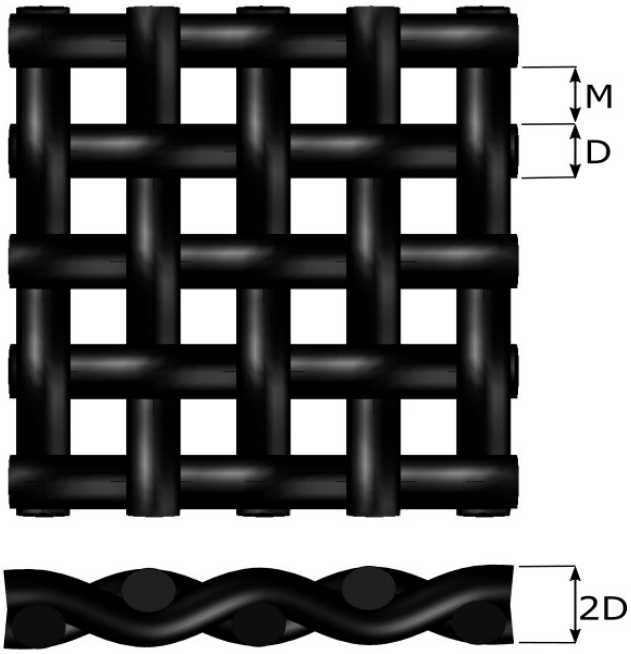

Figure 3.1: Three Dimensional Square Weave Wire Screen Geometry

3.3.1 Woven Wire Screen Features

Schematic of a modeled 3D screen sample utilized for simulations carried out in the course of this research is as presented in Figure 3.1, showing a 4x4 woven

wire mesh screen. Woven wire screen geometries were modeled by sweeping circular faces of required wire diameter along sinusoidal paths until the required wire screen geometry is created. Care is taken to always maintain accurate wire dimensions at all times. In order to minimize computational costs, simulations were carried out on a 4x4 mesh aperture width geometry section as shown. In order to generate quality numerical grids, a gap size of less than 5% of wire diameter 'D' was always introduced at screen wire strands intersection, as without this gap size, intersections of wire strands often result in poor grid cell skewness and very low quality within this intersection region, which subsequently produces poor CFD code convergence and results. Previous studies carried out by Green [181] had shown that such small gaps at intersections had very negligible effect on overall CFD results, and the flow speeds through such gaps were very negligible compared to flow speeds through screen aperture width 'M'.

	Wire Screen Samples		
Screen	**S1**	**S2**	**S3**
D (mm)	0.14	0.18	0.19
M (mm)	0.33	0.46	0.87
Porosity $\beta(\%)$	49.38	51.84	67.26
Solidity $(1-\beta)(\%)$	50.62	48.16	32.74
$(Re_D)_1$	90	85	80
$(Re_D)_2$	106	102	120
$(Re_D)_3$	114	116	154
$(Re_D)_4$	126	133	170

Table 3.1: Features of Wire Screen Samples

Table 3.1 presents the geometric features of wire screen samples experimentally tested by Schubauer[176] and hereby numerically simulated in the course of this research. Three woven wire screen types are selected for this study, S1, S2, and S3, all possessing diameters (D), mesh aperture width (M), porosity (β) and solidity as shown in Table 3.1. The range of Reynolds number tested for each screen is also shown in Table 3.1

3.3.2 Grid generation and Boundary conditions

Numerical assessment is carried out on two different types of grids possessing similar boundary conditions. Computational Grid A has domain sizes as shown in Figure 3.2 where domain sides appear to be flush with side edges of woven wire screens, as the woven screen edges are tightly fitted within a flow channel domain.

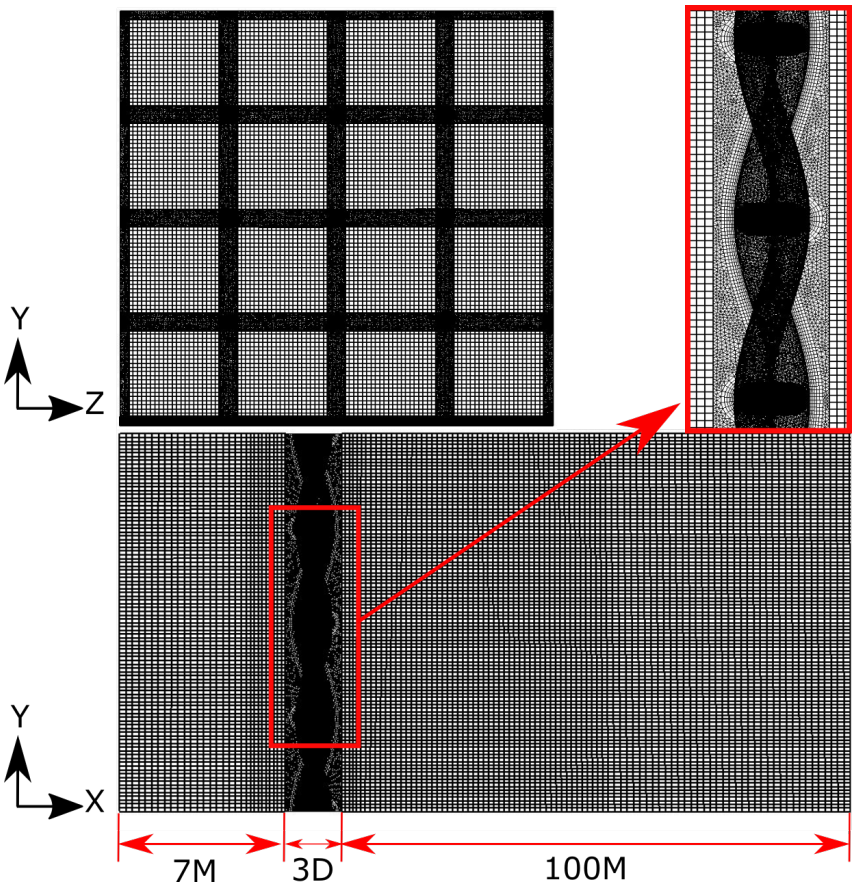

Figure 3.2: Computational Grid A

Grid A possess similar boundary conditions to the laminar flow modeled numerical simulations carried out by Green [181]. Boundary conditions at domain sides are slip wall conditions (zero shear stress, zero flow-through), a velocity inlet condition is selected at domain inlet, and pressure outlet condition at domain exit. The computational grid is made up of a hybrid combination of hexagonal and tetrahedral cells. Hexagonal cells are within upstream fluid volume, tetrahedral cells within the woven wire fluid volume, and hexagonal

cells at downstream fluid volume section.

Computational Grid B is as shown in Figure 3.3, and possess similar boundary conditions to Grid A (slip wall at domain sides, velocity inlet conditions at domain inlet and pressure outlet at domain exit), however, the side walls of domain in Grid B is made to extend far beyond a region where it does not affect fluid flow through the woven screens.

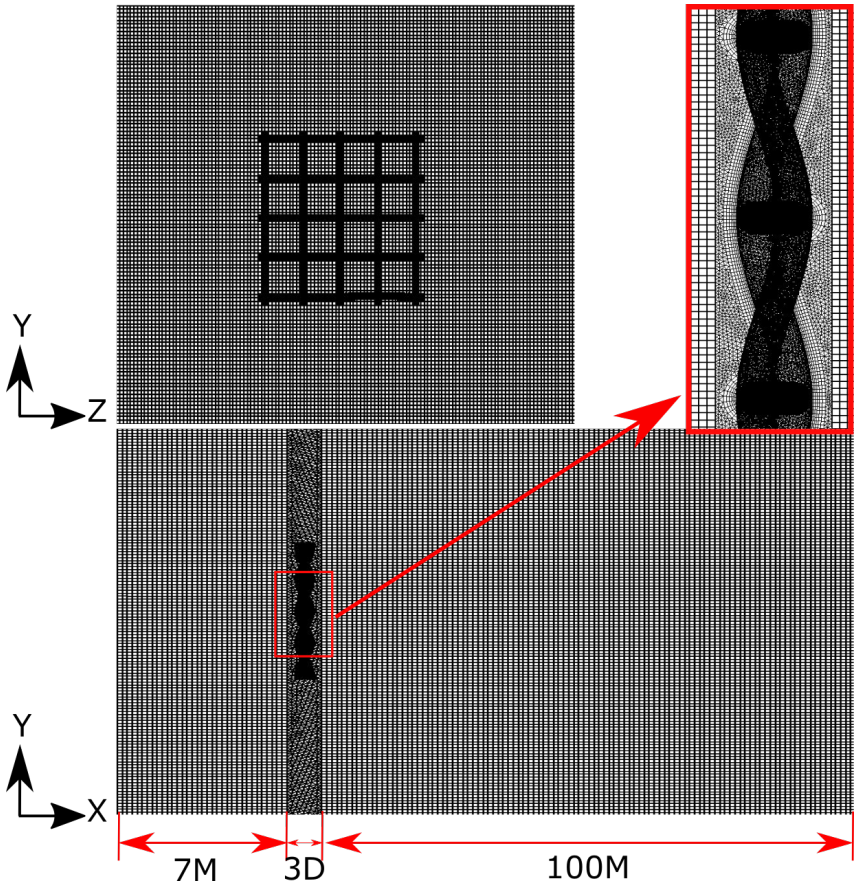

Figure 3.3: Computational Grid B

Values of average y plus (y+) of less than one was maintained at the wire screen walls at all times, as this enabled better CFD results when compared to experiments. The numerical grid fluid domain extended downstream beyond the wire screen by a minimum size of $100M$, and upstream extended by a minimum of $7M$ as shown in Figure 4.5. For the remainder of this paper, we will refer to screens and numerical grids in the following nomenclature shown in Table 3.2.

S1-A	Screen S1 with computational Grid A
S1-B	Screen S1 with computational Grid B
S2-A	Screen S2 with computational Grid A
S2-B	Screen S2 with computational Grid B
S3-A	Screen S3 with computational Grid A
S3-B	Screen S3 with computational Grid B

Table 3.2: 3D Screen-Grid Nomenclatures

3.3.3 Discretization Error Estimation

Discretization errors of the numerical results were carried out using the GCI (Grid Convergence Index) method, which is based on the Richardson Extrapolation (RE) method. This method has shown to be a reliable method for discretization errors for a wide array of CFD simulation cases [200, 201, 202], and is one of the highly recommended methods for grid discretization error studies. The documented process of GCI application is summarized as follows [203];

A representative grid size is defined, and for a three dimensional case is given by Equation 3.9

$$h = [\frac{1}{N}\sum_{i=1}^{N}(\Delta V_i)]^{\frac{1}{3}} \tag{3.9}$$

Three different sets of grids (h_1, h_2 and h_3) in decreasing order of fineness are recommended for selection and utilization, for which simulations are run and variables (ϕ_1, ϕ_2 and ϕ_3) deemed important to the overall aim of the research study under investigation are used for the discretization error analysis. Where h_1 is the finest grid, and the condition $h_2/h_1 > 1.3$ and $h_3/h_2 > 1.3$ must be satisfied at all times. For this study, the variables utilized are the pressure drop and maximum velocity at screen aperture exit. The order of the method is calculated using Equation 3.10

$$p = \frac{1}{\ln(r_{21})}|\ln|\frac{\epsilon_{32}}{\epsilon_{21}}| + q(p)| \tag{3.10}$$

$$q(p) = \ln\left(\frac{r_{21}^{p} - s}{r_{32}^{p} - s}\right) \tag{3.11}$$

$$s = 1.sign(\frac{\epsilon_{32}}{\epsilon_{21}}) \tag{3.12}$$

Where Equations 3.10, 3.11 and 3.12 are solved using a fixed point iteration approach, with the initial guess equal to the first term.

The Grid Convergence Index (GCI) is then calculated by making use of Equation 3.13

$$GCI_{fine}^{21} = \frac{1.25e_{a}^{21}}{r_{21}^{p} - 1} \tag{3.13}$$

$$e_{a}^{21} = |\frac{\phi_1 - \phi_2}{\phi_1}| \tag{3.14}$$

With the extrapolated asymptotic value given by Equation 3.15 and extrapolated relative error between asymptotic value and fine grid value given by Equation 3.16.

$$\phi_{ext}^{21} = (\frac{r_{21}^{p}\phi_1 - \phi_2}{r_{21}^{p} - 1}) \tag{3.15}$$

$$e_{ext}^{21} = |\frac{\phi_{ext}^{12} - \phi_1}{\phi_{ext}^{12}}| \tag{3.16}$$

3.3.4 Turbulence Model Study

In order to validate numerical results with experimental values, a turbulence model study was performed to identify the most suitable turbulence model that best replicates experimental values. Results of turbulence model studies for pressure drop across screen S3 is as presented in Figure 3.4, where studies for steady CFD simulations were carried out utilizing a laminar flow model, standard $k-\epsilon$, Re-Normalization Group (RNG) $k-\epsilon$, realizable $k-\epsilon$, standard $k-\omega$, Shear Stress Transport (SST) $k-\omega$, Transition $k-kl-\omega$, and Transition SST turbulence models.

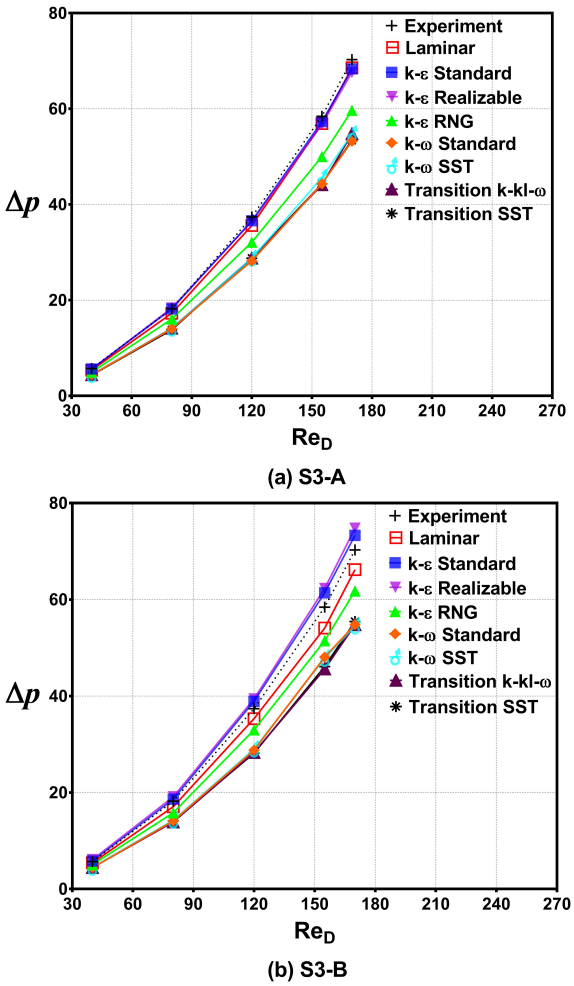

Figure 3.4: Turbulence Model Study for Screen S3 (Δp [Pa] vs Re_D)

For validation, these numerical results of pressure drop across screen S3 (ΔP) were compared against documented NACA experiments carried out by Schubauer [176]. Second order numerical discretization schemes were utilized for all turbulence models presented, and a convergence criteria of 1×10^{-6} was maintained for scaled residuals of all field variables, where in some rare cases a criteria of 1×10^{-5} was deemed sufficient. From the turbulence model study, for S3-A, the $k - \epsilon$ two equation turbulence model which models the flow by solving modeled transport equations of kinetic energy and a dissipation rate, provides a much better representation to experimental results when compared to other turbulence model tested. The laminar flow model also provides good results as the Reynolds numbers under consideration are still very much mod-

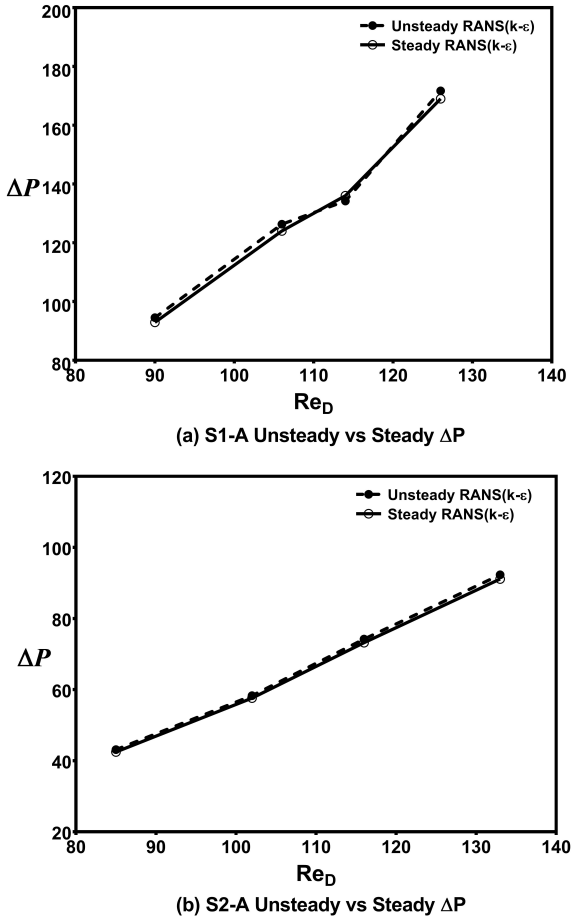

Figure 3.5: Unsteady vs Steady ΔP Results for S1-A and S2-A (ΔP vs Re_D)

est. Variants of the $k-\epsilon$ model, i.e, the realizable model, and Re-Normalization Group (RNG) model also produce nearly adequate results as shown. The $k-\omega$ turbulence model which models the flow by solving transport equations of kinetic energy and a specific dissipation rate appears to predict the pressure drop across 3D wire screens poorly compared to the $k-\epsilon$ model variants. Similarly, variants of the $k-\omega$ model, and also transition models provided poor pressure drop comparisons for fluid flow across woven wire screens within the Reynolds number tested. For S3-B, a similar scenario to S3-A can be observed from the plots, as $k-\epsilon$ and its variants produced better comparisons to experiment when compared to the $k-\omega$ turbulence model, its variants and the transition models. Therefore, from this study observations are drawn and possible conclusions that for obtaining pressure drop of flow through woven

wire screens, solving turbulent transport equations by modeling the dissipation term ϵ is preferable and provides better results compared to experiments than solving transport equations modeling the specific dissipation term ω, or utilizing transition models. The $k-\epsilon$ turbulence model is therefore selected as the suitable model needed to carryout all subsequent simulations presented. The SIMPLE pressure-velocity coupling scheme is used, with least squares cell based gradient method, and standard pressure equation calculations. Second order discretization schemes for momentum, turbulent kinetic energy and turbulent dissipation rate were utilized. Relaxation factors for pressure was 0.3, for momentum equations was 0.7, and was set as 0.8 for the turbulent kinetic energy and the turbulent dissipation rate.

3.3.5 Unsteady vs Steady Simulations

Taking fluid flow around a single wire strand-cylinder as an indicator, there arises an expectation that flow through woven wire screens should exhibit unsteadiness, and therefore experience alternate shedding, particularly as regimes of interest fall within the two regime wake where vortex street is laminar and clearly alternating $40 \leq \ Re_D \leq 150$, or within the transition range to turbulence $150 \leq \ Re_D \leq 300$ [204]. Therefore, for screen S1-A and S2-A, unsteady simulations were carried out and compared with steady averaged RANS results as shown in Figure 3.5. For pressure drop across screens, difference between mean unsteady and average steady values were within a range of 2%. Therefore in order to save computational costs, all further simulations are carried out utilizing the steady RANS based approach, with the $k-\epsilon$ turbulence model suitably selected.

3.4 Screen S1 Results

Computational results obtained for S1-A and S1-B Utilizing the standard $k-\epsilon$ turbulence model is presented within this section. A grid independence study, results of screen flow loss coefficients, flow speed fields, turbulent kinetic

	S1-A		**S1-B**	
	$\phi = \Delta P$	$\phi = U$	$\phi = \Delta P$	$\phi = U$
N_1, N_2, N_3 (10^6)	4, 1.5, 0.6	4, 1.5, 0.6	5, 2, 0.8	5, 2, 0.8
r_{21}	1.39	1.39	1.36	1.36
r_{32}	1.37	1.37	1.36	1.36
ϕ_1	169.1	25.3	172.5	17.16
ϕ_2	163.0	24.0	164.1	16.7
ϕ_3	151.1	21.4	160.4	15.8
p	2.3	2.4	2.5	2.2
ϕ_{ext}^{21}	174.4	26.4	179.1	17.64
e_a^{21}	3.6%	5.1%	4.8%	2.6%
e_{ext}^{21}	3.0%	4.1%	3.7%	2.7%
GCI_{fine}^{21}	3.9%	5.3%	4.7%	3.5%

Table 3.3: Discretization Error Calculations at $Re_D = 126$ for S1-A and S1-B

energies and turbulence intensities are presented. For flow field variables scaled convergence residuals plot of screens S1-A and S1-B, refer to Appendix A.

3.4.1 Screen S1 Grid Independence Study

In order to show that computational fluid flow results were independent of the computational grid utilized, a grid independence study together with a GCI based discretization error analysis was carried out on S1-A and S1-B utilizing the steady standard $k - \epsilon$ turbulence model. Discretization errors are carried out for pressure drop across screen and maximum velocity at screen aperture. Using the Richardson Extrapolation base GCI discretization method, the order of the method, extrapolated asymptotic values, relative error between utilized fine grid value and asymptotic value, and the GCI are all presented in Table 3.3, while Figure 3.6 shows results of grid independence analysis at $Re_D = 126$. For S1-A, $\Delta V_N = 1.246345 \times 10^{-7}$, while S1-B had $\Delta V_N = 1.8446 \times 10^{-6}$.

For S1-A, a computational fine grid size of 4×10^6 was selected as the relative error between asymptotic values and this fine grid values was within 3.0% difference for pressure drop and 4.1% for flow speeds. For S1-B, a fine grid size of 5×10^6 was selected as relative error between asymptotic value were within 3.7% difference for pressure drop and 2.7% for flow speeds. GCI

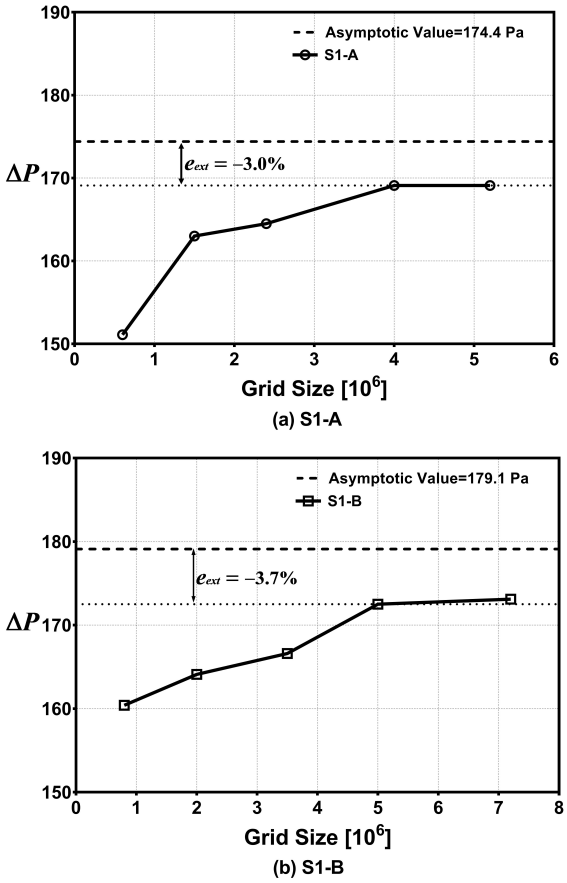

Figure 3.6: Grid independence study for S1-A and S1-B at $Re_D = 126$

values for S1-A was 3.9% for pressure drop, and 5.3% for flow speeds, while GCI values for S1-B were 4.7% for pressure drops and 3.5% for flow speeds.

3.4.2 S1 Flow Loss Coefficients

CFD predicted flow loss coefficients of screen S1-A and S1-B compared to experiments is as shown in Figure 3.7, where comparisons with some existing correlation models are also carried out as shown. Within the Reynolds number range tested, S1-A produced results that differed from experimental values by -2.6% for the best case and -4.3% for the worst case. S1-B produced results that differed to experimental values by 1% for the best case and +6% for the worst case.

From Figure 3.7 an observation is made that S1-A consistently under-predicted flow loss coefficient values, while S1-B consistently over predicted

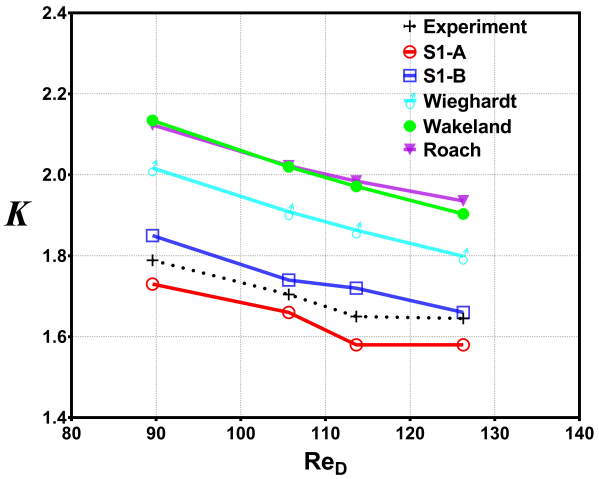

Figure 3.7: Flow Loss Coefficients for S1-A and S1-B at $Re_D = 126$

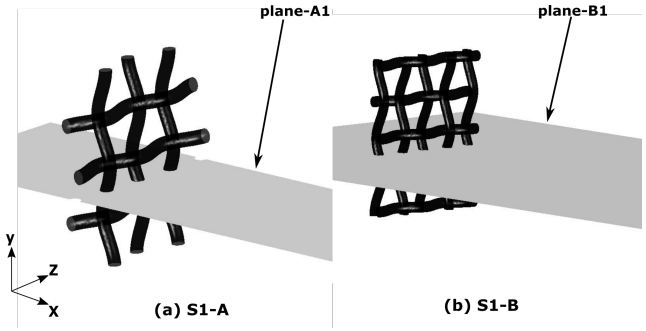

Figure 3.8: Screen S1 cut plane: plane-A1 and plane-B1

results compared to experimental values. This is consistent with the trend from the grid independent study of S1-A and S1-B carried out. Comparing S1-A and S1-B against prediction performance of correlation models, an observation is made that S1-A and S1-B produced better comparisons to experiments when compared to these screen flow loss correlation models. The Wieghardt's [157] model produced better predictions compared to the Wakeland[156] and Roach [1] models.

3.4.3 S1 Flow Speeds

For presentation of flow speeds through screens S1-A and S1-B along the fluid flow direction, cut plane in the X-Z direction as shown in Figure 3.8 is utilized.

Cut plane-A1 and plane-B1 along the X-Z direction are located on the Y coordinates at the center of selected apertures for screen S1-A and S1-B as

shown. Flow speeds along these planes at different Reynolds number tested are presented in Figure 3.9

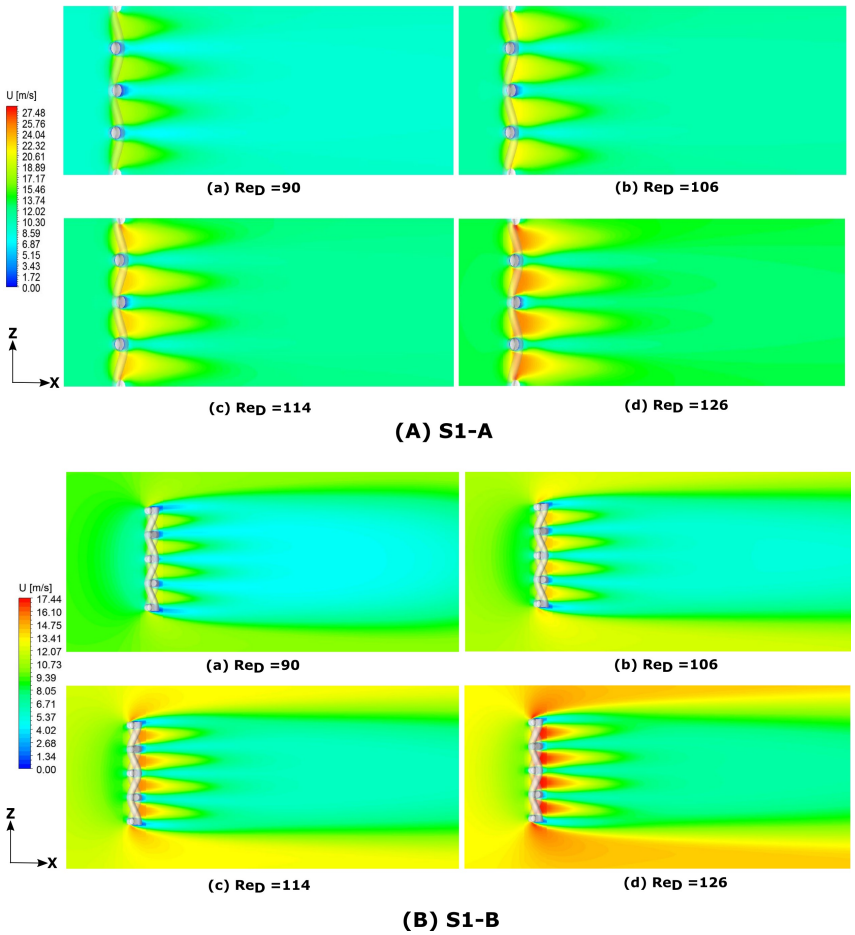

Figure 3.9: Flow speeds for S1-A(plane-A1) and S1-B(plane-B1)

Results of Normalized velocity by locating line probes through aperture center of screens S1-A and S1-B are presented in Figure 3.10.

Grid domain extents of 7M upstream and 100M downstream are utilized within the plots. For S1-A, incoming upstream flow speeds are relatively unchanged until the fluid flow proceeds into the screen aperture mesh width, where a sudden spike in flow speeds is observed as fluid flows within the wire screen aperture. Maximum flow speeds of up to $1.9U_\infty$ are observed within the screen aperture. At exit from the screen, flow speeds start to drop sharply until about a downstream distance of $X/M = 10$, where flow speeds drop slightly below incoming levels to within $0.02U_\infty$, and this reduced speed levels continues till roughly about $X/M = 60$, where flow speeds again reach inlet values.

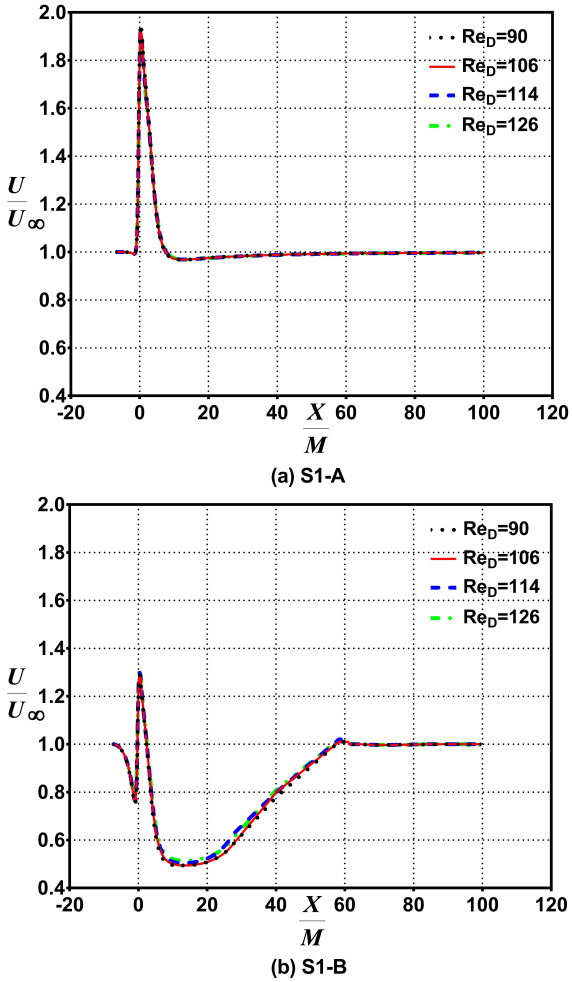

Figure 3.10: Normalized speed vs normalized distance for S1-A and S1-B

For S1-B, a slightly different fluid flow transport mechanism is observed. At upstream section, fluid flow clearly progresses from a region where the fluid is unaffected by the presence of the screen, until about $X/M = -2$ where the presence of the wire screen becomes evident to the fluid and a maximum drop in flow speeds by about $0.2U_\infty$ is observed just before entrance into the screen. Within screen apertures, maximum flow speeds up to $1.3U_\infty$ is observed, after which flow speeds decrease as fluid exits the aperture. This decrease in fluid flow speed continues and at roughly about $X/M = 5$, flow speeds go below inlet free-stream speeds, and continue decreasing till it gets to a maximum flow decrease of roughly $0.5U_\infty$ at about $X/M = 15$. The region of reduced flow speeds exists up to about $X/M = 60$, after which a return to free-stream

speed levels is observed.

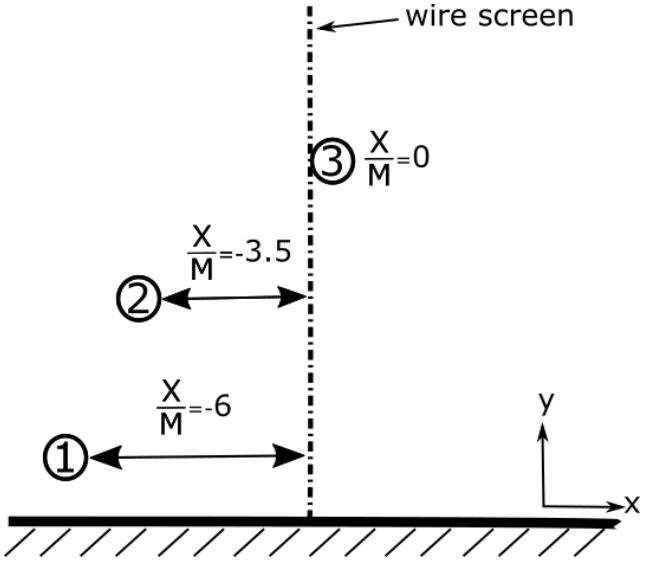

Figure 3.11: Locations 1, 2 and 3 for S1-A and S1-B

For the fluid flow through screens, identification of three locations in the Y-Z planes at X locations as shown in Figure 3.11 is carried out. These locations will be used to analyze all of screens S1-A, S1-B, S2-A, S2-B, S3-A and S3-B presented within this Chapter.

Location 1 is the location upstream of screen where fluid flow just begins to feel the effect of screen presence i.e, where screen effect on fluid flow is initialized. Location 2 is the location upstream of screen where a strong effect of screen presence is felt by the progressive fluid flow prior to it's full entrance into the mesh screen aperture, while Location 3 is the location at which flow speeds attain their maximum values at the screen aperture exit.

Figure 3.12 shows U_x velocity contour plots at location 1 for S1-A and S1-B at the Reynolds numbers tested, while Figure 3.13 presents for locations 2 and 3. For clarity, the wire screens are introduced within the contour field plots as transparent screens.

Fluid flow moving from inlet conditions immediately begins with a flow region upstream of wire mesh screen where the fluid flow remains unaffected by presence of the downstream wire screen until it gets to location 1 where the screen effect on the fluid flow is initiated. The screen presence begins to

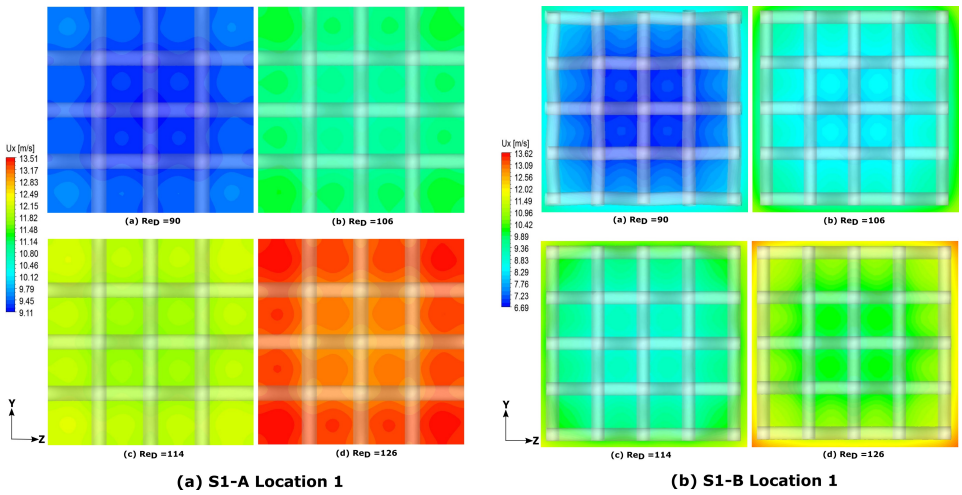

Figure 3.12: U_x contour plots at location 1 for S1-A and S1-B

affect the nature of fluid flow, as fluid flow contours gradually take the shape or form of screen aperture constrictions. For locations 1, lower flow speeds are observed close to the center core of screens, where the wire screen strands would be located if the screen was projected further upstream. Average flow speeds at the planes of interest still remain within inlet velocity average values, and no increase in mean velocities are observed within this region. Flow contour changes continue until location 2 is attained, Figure 3.13, where the effect of the screen is now more predominant than for location 1 case. Flow contours within this region tend to take circular shapes as they get closer and closer to the screen. For S1-B, an initial drop in flow speeds is observed just before entering into the screen aperture as highlighted in Figure 3.10 and clearly seen in the plots of Figure 3.9, which increases abruptly on entrance into the aperture section. This drop in flow speeds was however not observed for S1-A case. As the fluid flow progresses into screen, a location approximately within the screen aperture exit exists where flow speeds attain maximum values as shown by location 3 contour plots for both S1-A and S1-B in Figure 3.13. S1-A and S1-B contour plots for U_y at locations 1, 2 and 3 are presented in Appendix B.

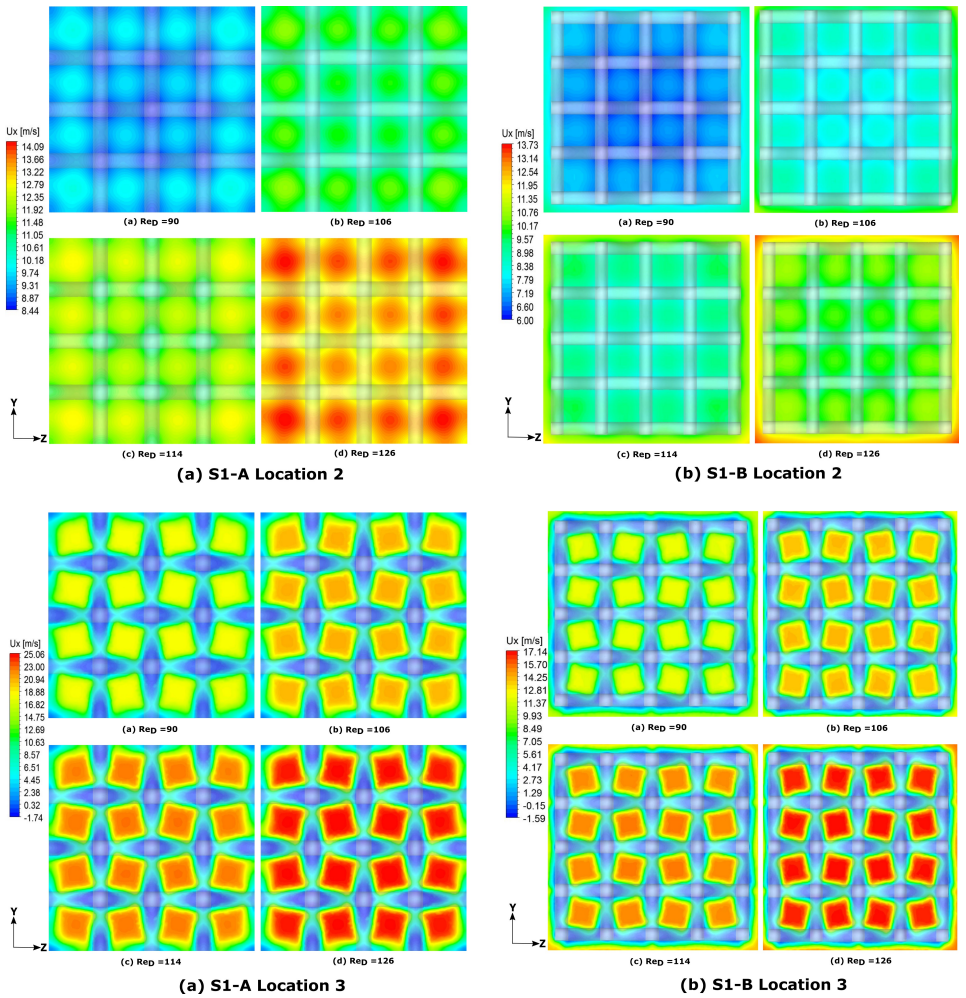

Figure 3.13: U_x contour plots at locations 2 and 3 for S1-A and S1-B

3.4.4 S1 Turbulent Kinetic Energy

The $k-\epsilon$ turbulence model is a two-class equation model solving transport equations of turbulent kinetic energy and turbulent dissipation rates. Turbulent kinetic energy results achieved when utilizing the $k-\epsilon$ model were contrastingly different from turbulent kinetic energy results when using other turbulence model tested. At velocity inlet boundary conditions, turbulent intensity ratio of 0.9% was set, this value was selected from the turbulent intensity ratio at screen inlet utilized within the experimental campaign as recorded by Schubauer [176] for the Reynolds number range of interest. Turbulent kinetic energy (TKE) can be quantified in relation to local velocity fluctuations by Equation 3.17;

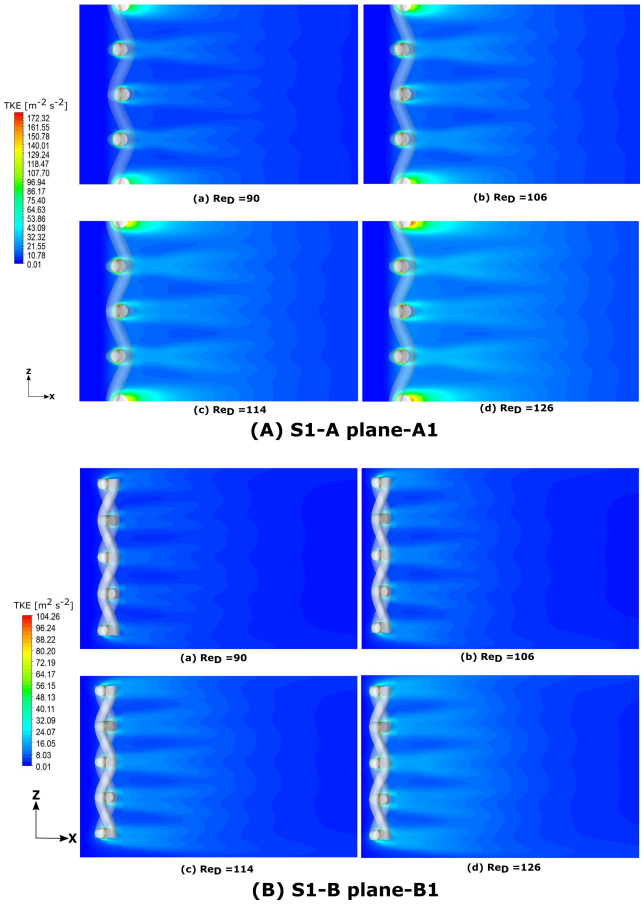

Figure 3.14: Turbulent kinetic energy: S1-A plane-A1 and S1-B plane-B1

$$TKE = \frac{1}{2}(u'^2 + v'^2 + w'^2) \tag{3.17}$$

$$TKE = \frac{3}{2}(u')^2 \qquad (u' = v' = w') \tag{3.18}$$

For isotropic turbulence flow scenario, $u' = v' = w'$, therefore Equation 3.17 simplifies into Equation 3.18. Therefore from CFD point of view, i.e, when $Re_D = 126$ at velocity inlet boundary condition and a turbulence intensity ratio of 0.9% is introduced, the turbulent kinetic energy is approximated as $1.31414 \times 10^{-2} m^2 s^{-2}$.

Turbulent kinetic energy contour plots for flow plane-A1 and plane-B1 is presented Figure 3.14, where maximum kinetic energy values are observable on the edges of the wire strands. A clearer look at these maximum kinetic energy

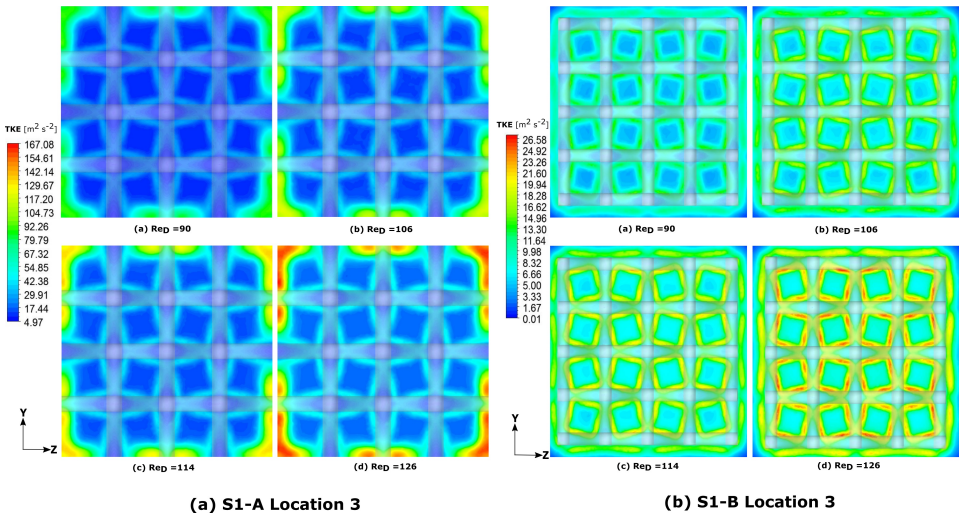

Figure 3.15: Turbulent kinetic energy at location 3: S1-A and S1-B

values can be seen by looking at kinetic energy values at location 3, where the maximum velocities also exist. Screen S1-A and S1-B kinetic energy values at location 3 is presented in Figure 3.15, while kinetic energy values at locations 1 and 2 are presented in Appendix B.

A plot of kinetic energy values through the aperture center position is as shown in Figure 3.16, where results of the turbulent kinetic energy of fluid flow through wire screen S1-A and S1-B aperture center is shown. From the plots of Figure 3.16, kinetic energy values of fluid flow upstream screens were comparable up to regions very-near field of screen aperture entrance. The first major difference in turbulence kinetic energy results were found within the screen apertures, as shown by Figure 3.16. A first observation between plotted results for turbulent kinetic energy shows that peak kinetic energy values at screen exit of S1-A approximately doubles the values of S1-B. Also, the peak turbulence intensities of flow through S1-A occurred within the screen aperture while peaks from S1-B occurred further downstream at an approximate distance of $X/M = 7$.

3.4.5 S1 Turbulence Intensities Decay

Results of downstream turbulence intensities u'/U_∞ (Normalized by free stream flow speed) for S1-A and S1-B is as shown in Figure 3.17, where u' denotes

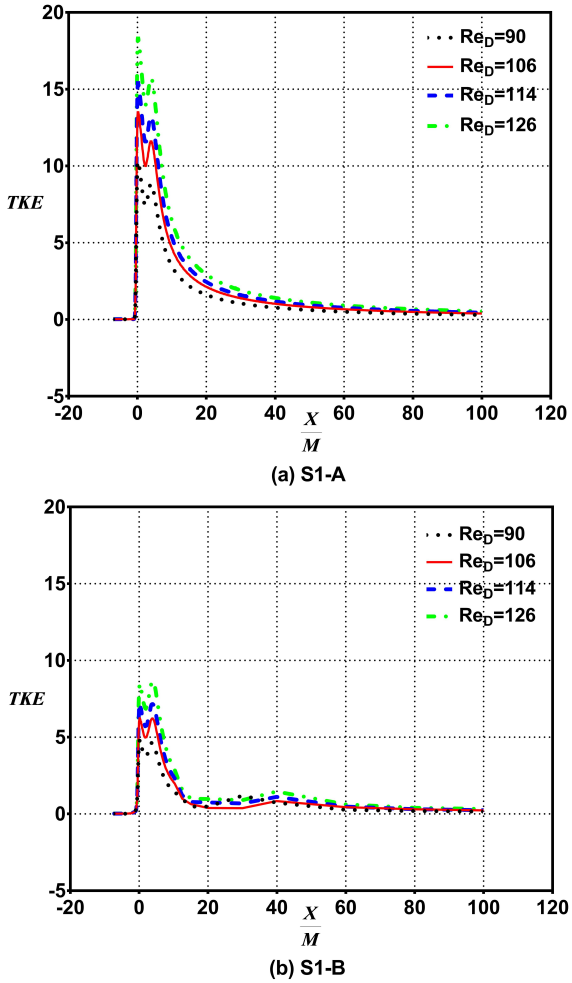

Figure 3.16: Turbulent kinetic energy through screen aperture for S1-A and S1-B

the stream-wise component of fluctuation velocity, and U_∞ is the mean free stream velocity. As stated previously, inlet turbulence intensities were chosen so as to match reported experimental inlet intensities.

From plots of Figure 3.17, an immediate observation is made, as peak turbulence intensities of S1-A occurred within the screen aperture, compared to S1-B where peaks occurred downstream, at approximate distance of $X/M = 7$. S1-B compares better to the decay relationship of Roach [1] when compared to S1-A.

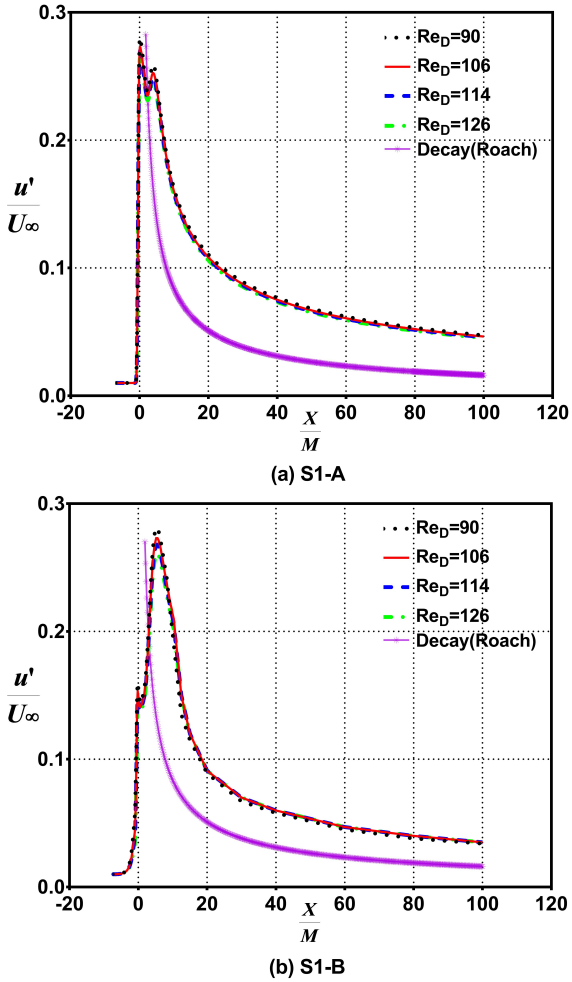

Figure 3.17: Turbulence intensity decay for S1-A and S1-B

3.4.6 S1 Wall Y+

The range of average Y+ values across was monitored, as the acceptable range of average values was kept below one and in some rare cases, below two across the screen models. For emphasis, Figure 3.18 presents Y+ values across the S1-A and S1-B screen models.

Surface pressures and wall shear stress on screen models S1-A and S1-A are further presented in Appendix B.

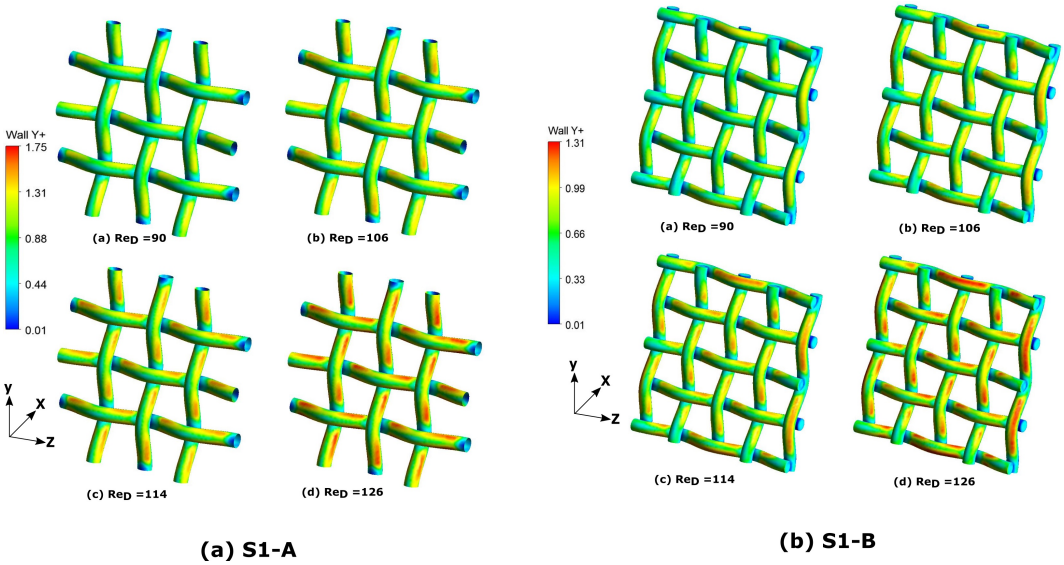

Figure 3.18: Wall Y+ values for S1-A and S1-B

	S2-A		**S2-B**	
	$\phi = \Delta P$	$\phi = U$	$\phi = \Delta P$	$\phi = U$
N_1, N_2, N_3 (10^6)	4.5, 1.8, 0.7	4.5, 1.8, 0.7	5.6, 2.4, 1.0	5.6, 2.4, 1.0
r_{21}	1.36	1.36	1.33	1.33
r_{32}	1.37	1.37	1.34	1.34
ϕ_1	73.2	17.34	77.4	12.39
ϕ_2	68.8	16.34	74.3	11.8
ϕ_3	57.4	13.80	67.2	10.4
p	2.6	2.8	2.5	2.7
ϕ_{ext}^{21}	76.2	18.04	80.02	12.85
e_a^{21}	6%%	5.6%	4.0%	4.7%
e_{ext}^{21}	3.8%	3.7%	3.2%	3.6%
GCI_{fine}^{21}	4.9%	5.0%	4.2%	4.6%

Table 3.4: Discretization Error Calculations at $Re_D = 116$ for S2-A and S2-B

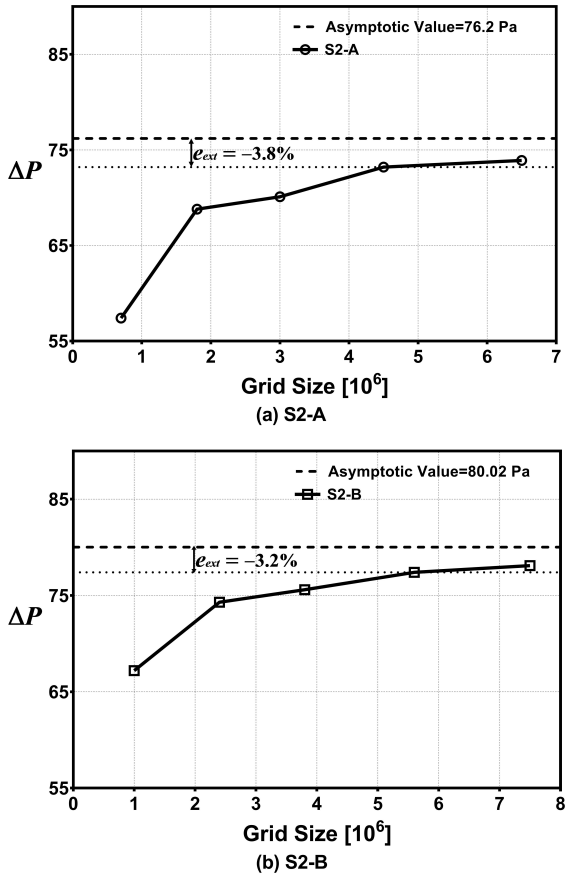

Figure 3.19: Grid independence study for S2-A and S2-B at $Re_D = 116$

3.5 Screen S2 Results

Computational results obtained for S2-A and S-B utilizing the standard $k-\epsilon$ turbulence model is presented within this section. Similarly to S1 screen cases, grid independence study, results of screen flow loss coefficients, averaged flow speeds, turbulent kinetic energies and turbulence intensities are presented here for S2 screen cases. For flow field variables scaled convergence residuals plot of screens S2-A and S2-B, refer to Appendix A.

3.5.1 Screen S2 Grid Independence Study

Grid independence study using the GCI discretization method was carried out on S2-A and S2-B utilizing the steady standard $k-\epsilon$ turbulence model. Results of this study carried out at $Re_D = 116$ is presented in Table 3.4 and Figure 3.19. S2-A had a $\Delta V_N = 3.29943\times10^{-7}$, while S2-B had $\Delta V_N = 3.66999\times10^{-6}$. For S2-A a fine grid of 4.5×10^6 was deemed sufficient, as the RE extrapolated errors between asymptotic values and this grid values were 3.8% for pressure drop and 3.7% for flow speeds, while GCI values for pressure drop and flow speeds were 4.9% are 5% respectively. Analysis of S2-B showed that a grid size of 5.6×10^6 was sufficient enough for use as it produced extrapolated errors between asymptotic values of 3.2% for pressure drop and 3.6% for flow speeds. GCI for S2-B were within acceptable ranges of 4.2% for pressure drop and 4.6% for flow speeds.

3.5.2 S2 Flow Loss Coefficients

CFD predicted flow loss coefficients of screen S2-A and S2-B compared to experiments is as shown in Figure 3.20, where comparisons with existing correlation models are presented. Within the range of Reynolds number range tested, S2-A produced results that differed from experimental values by -4% for the best case and -6.3% for the worst case. S2-B produced results that differed to experimental values by 5% for the best case and +7% for the worst case.

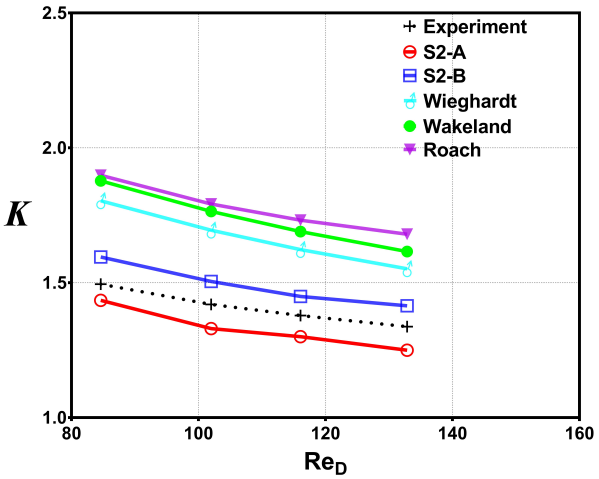

Figure 3.20: Flow Loss Coefficients for S2-A and S2-B at $Re_D = 116$

S2-A consistently under-predicted loss coefficients, while S2-B over-predicted results. Similar to S1-A and S1-B, the correlation models performed poorly when compared to S2-A and S2-B, with the Wieghardt model closer to experiments than the Wakeland and Roach models.

3.5.2.1 S2 Flow Speeds

Flow speeds through screens S2-A and S2-B in the fluid flow direction are shown for a cut plane in the X-Z direction as shown in Figure 3.21 is utilized.

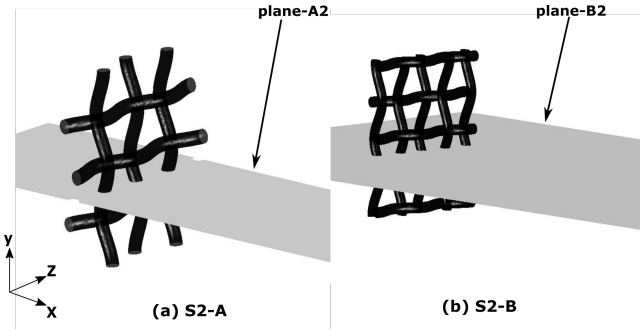

Figure 3.21: Screen S2 cut plane: plane-A2 and plane-B2

Where plane-A2 and plane-B2 in the X-Z direction are located Y coordinates value at the center of selected apertures for screen S2-A and S2-B. Flow speeds along these planes at different Reynolds number tested are presented in Figure 3.22.

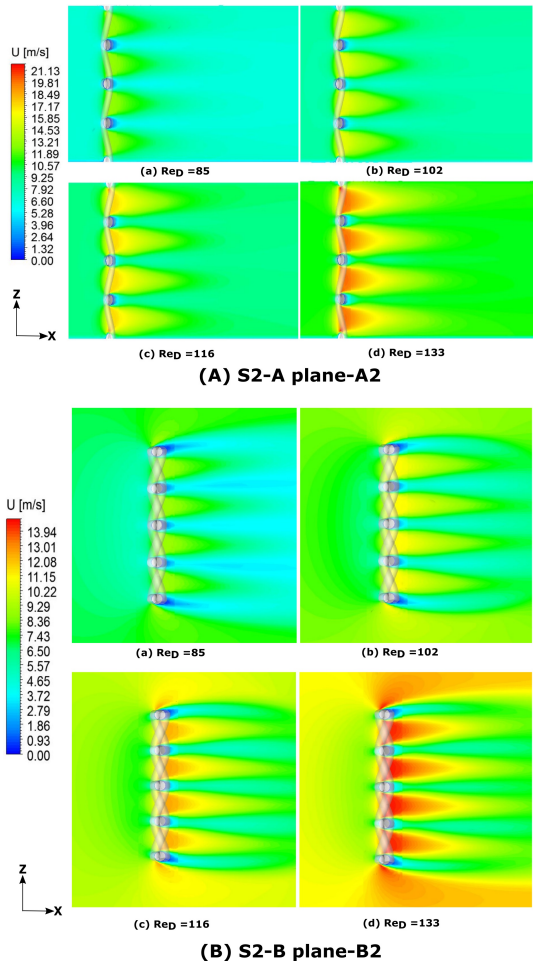

Figure 3.22: Flow speeds for S2-A(plane-A2) and S2-B(plane-B2)

XZ contour plots for S2-A and S2-B at location 3 is as shown in Figure 3.23. Contour plots for U_x at locations 1 and 2, along with U_y plots at locations 1, 2 and 3 are further presented in Appendix C.

Results of Normalized velocity through aperture of screens S2-A and S2-B are presented in Figure 3.24.

For S2-A, a similar fluid flow scenario to S1-A is observed, with maximum speeds of $1.85U_\infty$ attained. Flow speeds drop until a very slight reduced flow speed initializes from $X/M = 10$, which can be seen to increase gradually up till roughly $X/M = 60$. S2-B also shows similar trends to S1-B, with regions where incoming upstream flow becomes affected by presence of screen, then a drop in flow speeds just before the increment as fluid enters the aperture. Maximum flow speeds within the screen aperture increases up to $1.3U_\infty$, and a

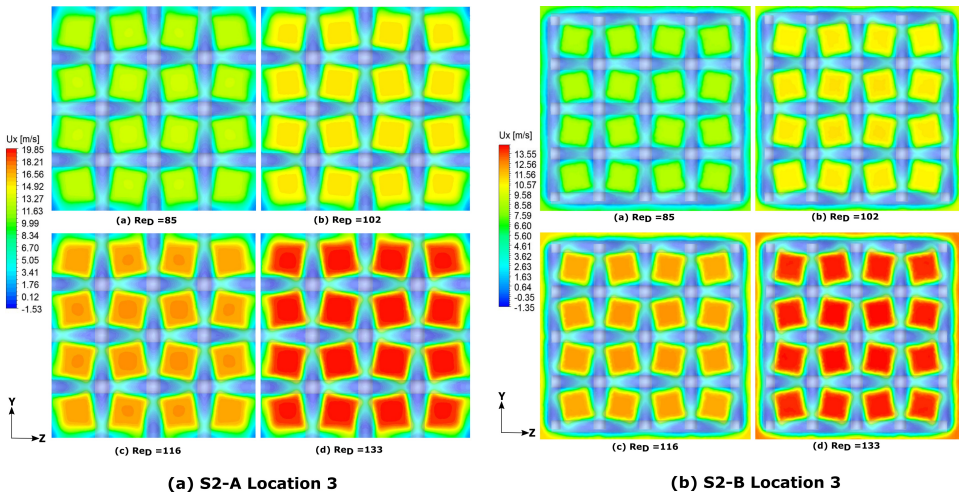

Figure 3.23: U_x contour plots at location 3 for S2-A and S2-B

downstream decrease is observed, with reductions up to approximately $0.5U_\infty$ that occurs within $7 < X/M < 60$.

Similar to S1-A and S1-B, identification of the three locations shown in Figure 3.11 is also carried out. Location 1 remains the location upstream of screen S2-A and S2-B where fluid flow just begins to feel the effect of screen presence i.e, where screen effect on fluid flow is initialized. Location 2 is the location upstream of screen where a strong effect of screen presence is felt by the progressive fluid flow prior to it's full entrance into the mesh screen aperture, while Location 3 is the location at which flow speeds attain their maximum values at the screen aperture exit.

3.5.3 S2 Turbulent Kinetic Energy

Probe plots through screen aperture center is as shown in Figure 3.25, where results of turbulent kinetic energy of fluid flow through wire screen S2-A and S2-B is presented. Similar to S1, the first major difference in turbulence kinetic energy results were found within the screen apertures, as shown by Figure 3.25. An observation is made, as the peak kinetic energy values at screen exit for S2-A approximately doubles the values of S1-B. Similar trends were observed between S1-A and S2-B. These high kinetic energy values can be associated with the grid domain sides, as the domain sides aided the increase in local fluid

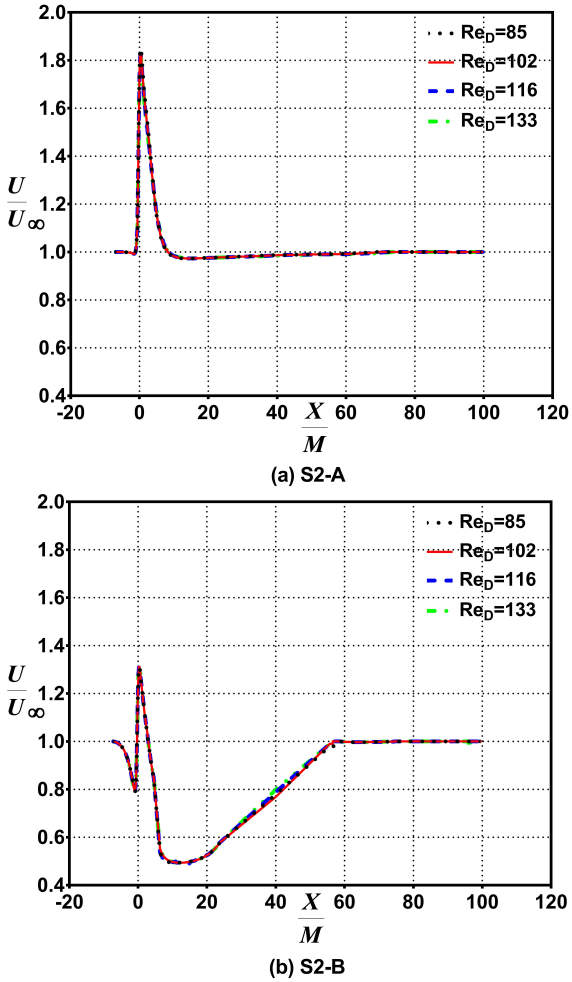

Figure 3.24: Normalized speed vs normalized distance for S2-A and S2-B

kinetic energies. Maximum peak kinetic energy values at screen aperture exit show to increase with increasing Reynolds number, as larger Reynolds number flows possessed higher kinetic energy values. Peak turbulence intensities of flow through S2-A occurred within the screen aperture exit while peaks from S2-B occurred downstream, at approximate distance of $X/M = 7$.

Turbulent kinetic energies at plane-A2 and plane-B2 are as shown in Figure 3.26. For a much clearer observation of the effect of domain conditions on screen S2-A, contour plots for kinetic energy in the YZ direction at location 3 is also presented in Figure 3.27. YZ kinetic energy values at locations 1 and 2 are further presented in Appendix C.

For S2-A, maximum flow kinetic energy values are located very close to the

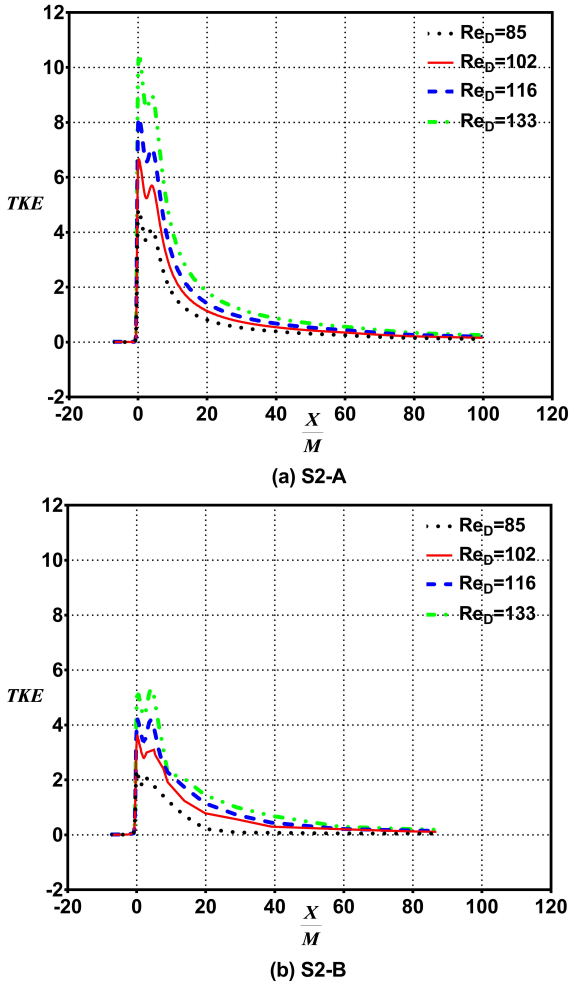

Figure 3.25: Turbulent kinetic energy through screen aperture for S2-A and S2-B

slip wall boundary condition sides, and this affected local kinetic energies of flows passing within the screens as maximum kinetic energy values increased from inlet values abruptly. The implication of this is that local averaged fluid velocities and fluctuations within this location are much higher than local fluctuations within the fluid screen flow. However, for S2-B, maximum kinetic energy values are limited to within screen aperture flow and close to screen edges. Therefore, turbulent kinetic energies of fluid flow within screen apertures are much smaller for S2-B compared to S2-A. Further implications of this observation is the fact that maximum local flow speeds within screen apertures for S1-A and S2-A might be affected as a result of interference from sides of the

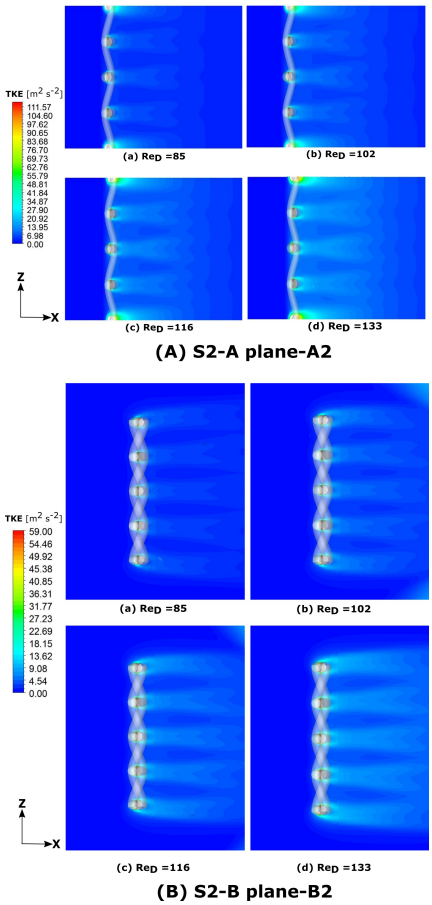

Figure 3.26: Turbulent kinetic energy: S2-A plane-A2 and S2-B plane-B2

domain acting as a boundary condition, thereby presenting superfluous local peak flow speeds at aperture exit.

3.5.4 S2 Turbulence Intensities Decay

Results of downstream turbulence intensities u'/U_∞ (Normalized by free stream flow speed) for S2-A and S2-B is as shown in Figure 3.28, where u' denotes the streamwise component of fluctuation velocity, and U_∞ is the mean free stream velocity.

Inlet turbulence intensities were chosen to match reported experimental inlet intensities. From plots of Figure 3.28 an observation is made, as the peak turbulence intensities of S2-A occurred within the screen aperture compared S2-B where peaks occurred downstream, at approximate distances of $X/M = 7$. This trend is similar to trends observed in S1-A and S1-B. Therefore, this

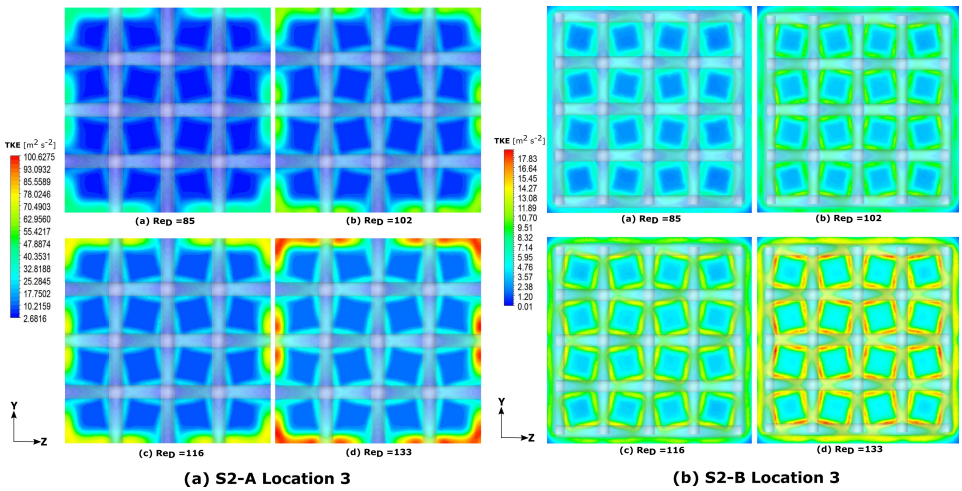

Figure 3.27: Turbulent kinetic energy at location 3: S2-A and S2-B

further illustrates the interference of side domains in S1-A and S2-A on the nature of fluid flow through the wire screens. We also observe that turbulence intensities increases immediately after exit from wire screens and locations of peak intensities are different from locations where peak flow speeds occurred for screens S2-B which is similar to screen S1-B. The decay of turbulence intensities were compared to the Roach [1] model, and S2-B showed to provide much comparison with this model when compared to S2-A. This again is similar to screen S1-A and S1-B cases, which points to the fact that fluid flow through S1-A and S2-A screens possess much higher intensities than S1-B and S2-B, due to interference from side domain.

Other CFD obtained variables and values, e.g; Wall Y+, surface pressures and wall shear stress values across screens S2-A and S2-B are presented in Appendix C.

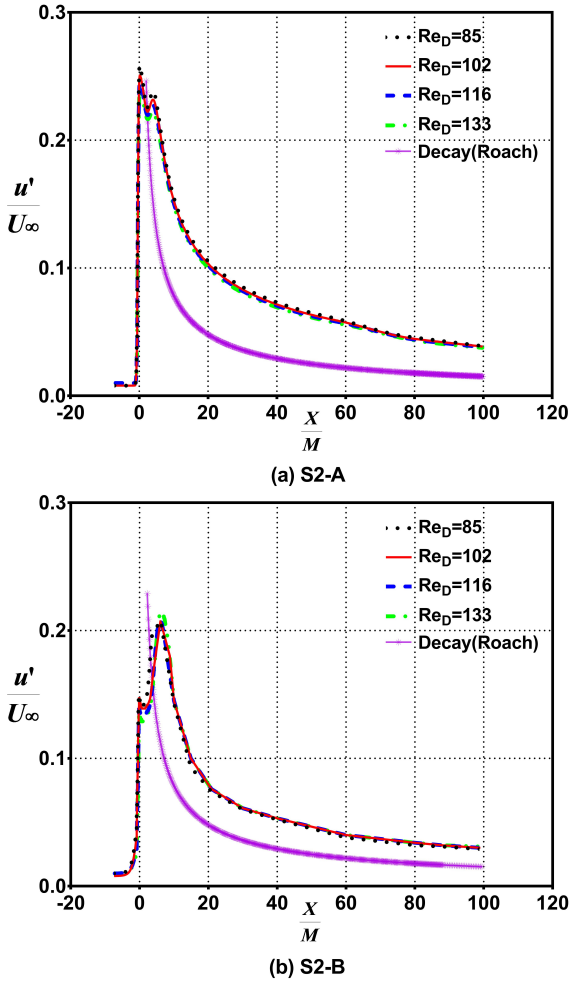

Figure 3.28: Turbulence intensity decay for S2-A and S2-B

	S3-A		**S3-B**	
	$\phi = \Delta P$	$\phi = U$	$\phi = \Delta P$	$\phi = U$
N_1, N_2, N_3 (10^6)	6.0, 2.6, 1.1	6.0, 2.6, 1.1	7.4, 3.2, 1.4	7.4, 3.2, 1.4
r_{21}	1.32	1.32	1.32	1.32
r_{32}	1.33	1.33	1.32	1.32
ϕ_1	33.5	13.7	36.5	11.16
ϕ_2	31.2	12.8	33.3	10.6
ϕ_3	25.1	10.67	23.5	9.4
p	2.9	2.9	2.9	2.6
ϕ_{ext}^{21}	34.9	14.41	37.9	11.63
e_a^{21}	6.8%	6.5%	7.7%	4.8%
e_{ext}^{21}	4.2%	4.9%	3.9%	3.9%
GCI_{fine}^{21}	5.5%	6.1%	4.9%	5.1%

Table 3.5: Discretization Error Calculations; $Re_D = 120$, S3-A, S3-B

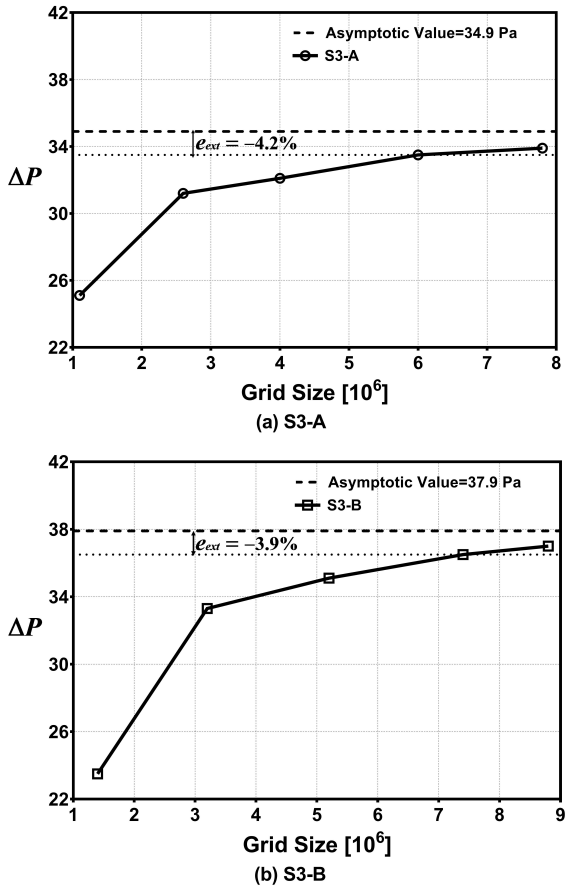

Figure 3.29: Grid independence study for S3-A and S3-B at $Re_D = 120$

3.6 Screen S3 Results

Results for S3-A and S3-B are presented within this section. For flow field variables scaled convergence residuals plot of screens S3-A and S3-B, refer to Appendix A.

3.6.1 Screen S3 Grid Independence Study

Similar to cases for screens S1 and S2, a grid independence study was carried out on S3-A and S3-B utilizing the steady standard $k-\epsilon$ turbulence model. Table 3.5 and Figure 3.29 shows summarized results of grid sensitivity and discretization error analysis for S3-A and S3-B at $Re_D = 120$. Total volume of S3-A was $\Delta V_N = 1.7205 \times 10^{-6}$ while S3-B had $\Delta V_N = 2.07198 \times 10^{-5}$.

For S3-A, computational grid size of 6.0×10^6 was selected as this grid size produced relative extrapolation error values of 4.2% for pressure drop and 4.9% for flow speeds. Grid size of 7.4×10^6 selected for S3-B produced relative extrapolation error of 3.9% for pressure drop and flow speeds.

3.6.2 S3 Flow Loss Coefficients

Figure 3.30 presents plots of flow loss coefficient for screen S3-A and S3-B compared to experimental measured values and correlation models.

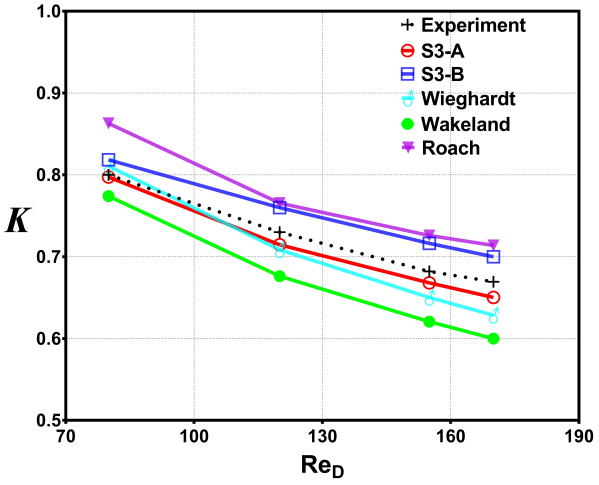

Figure 3.30: Flow Loss Coefficients for S3-A and S3-B at $Re_D = 116$

S3-A predicts loss coefficients at a best case scenario of -0.5% and worst case of -3%, while S3-B predicts by best case of 2% and worst case of 7%. The Wieghardt model predicts much better results compared to other models for screen S3. Therefore, from observations for S3-A and S3-B, CFD predicted flow loss coefficients possess the capacity of replicating experimental results. Within the Reynolds number range tested, CFD predicted flow loss coefficients also presents much better predictions when compared to the current correlation models.

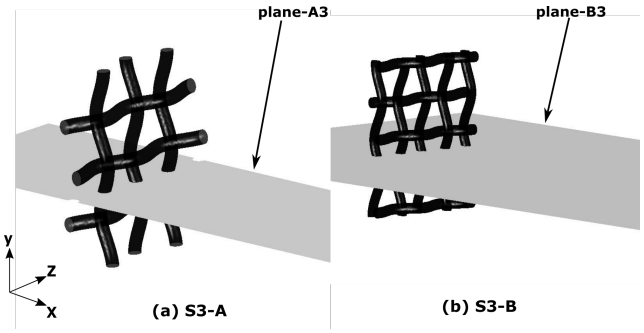

Figure 3.31: Screen S3 cut plane: plane-A3 and plane-B3

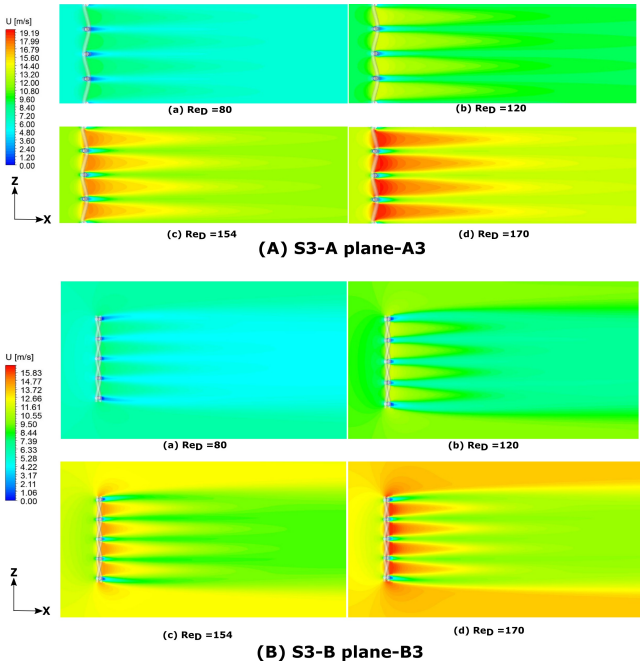

Figure 3.32: Flow speeds for S3-A(plane-A3) and S3-B(plane-B3)

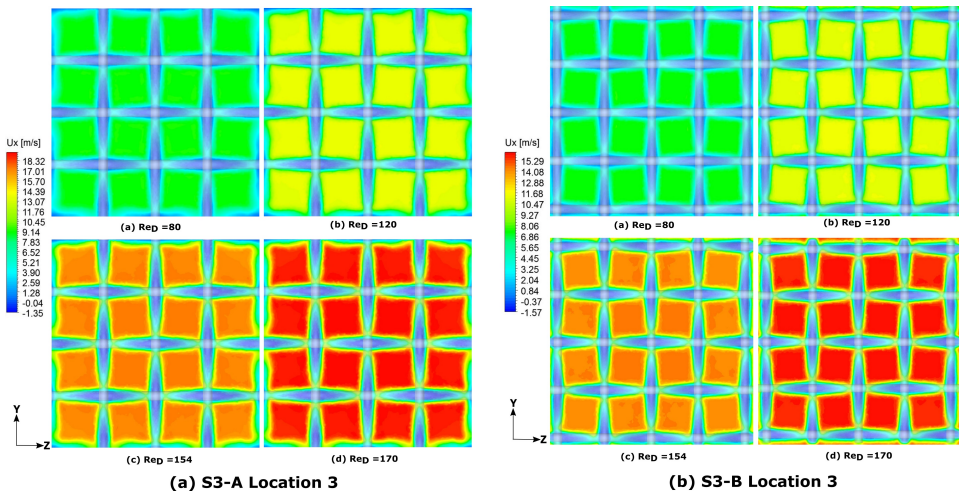

Figure 3.33: U_x contour plots at location 3 for S3-A and S3-B

3.6.3 S3 Flow Speeds

For flow speeds through screens S3-A and S3-B, planes as shown in Figure 3.31 are used to present flow speeds in the X-Z plane shown in Figure 3.32. Contour plots in the Y-Z plane for location 3 where maximum speeds exists are shown in Figure 3.33.

Contour plots for U_x at locations 1 and 2, along with U_y plots at locations 1, 2 and 3 are further presented in Appendix D.

Normalized flow speeds through aperture center of screens S3-A and S3-B are presented in Figure 3.34. Fluid flow through S3-A shows similar trends to S1-A and S2-A. However, fluid flow through S3-A attains maximum flow speeds of roughly $1.5U_\infty$, and very negligible flow speed reduction downstream. For S3-B, fluid flow through screen again experiences region where it becomes affected by presence of screen, and a decrease just before the increasing to the peak flow speeds within screen aperture exit. Maximum aperture flow speeds of about $1.2U_\infty$ is attained. Downstream flow speeds drops up to $0.25U_\infty$ at approximately $X/M = 15$, and returns to free-stream speed levels at about $X/M = 60$. It is worth highlighting at this point that the similarities in S1-A with S2-A, and S1-B and S2-B are noticed due to their relatively close porosities, even though their wire diameter and aperture mesh width are very different. For S1-A, S2-A and S3-A, maximum peak flow speeds at

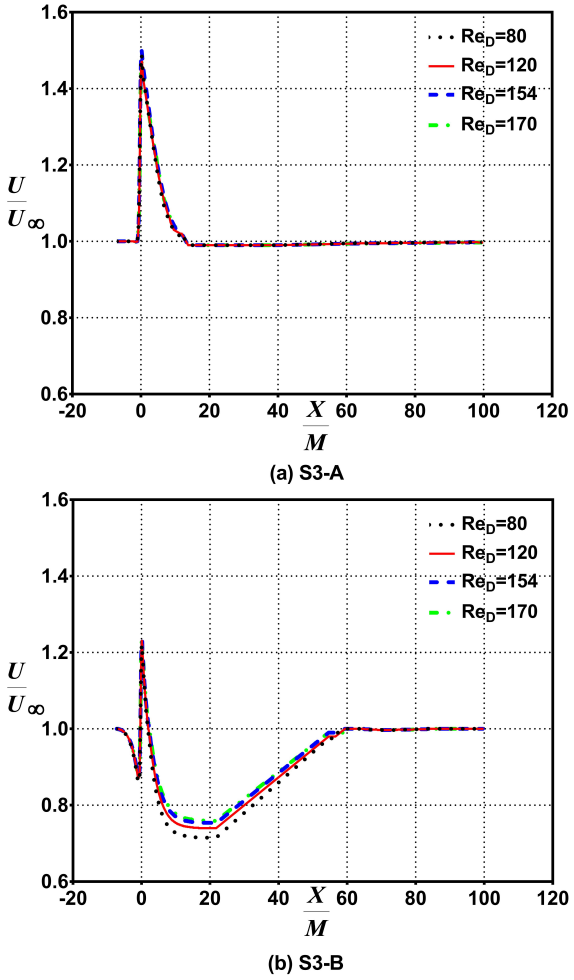

Figure 3.34: Normalized speed vs normalized distance for S3-A and S3-B

screen apertures appears to correlate with screen porosity (β) closely to within $U_{max} = U_\infty/\beta$, while downstream flow speeds reduction appears to only attain minimum reductions of $U_{min} = 0.02U_\infty$. For S1-B, S2-B, and S3-B, upstream flow experiences a region where it is affected by presence of screen, where flow speeds reduce momentarily, and peak flow speeds at screen aperture produces $U_{max} = 1.3U_\infty$, and does not correlate directly with porosity, however, downstream flow speed reductions appears to correlate with the screen solidity $(1-\beta)$ to within $U_{min} = (1-\beta)U_\infty$, and strong effects of flow speed reduction of wire screens are observed.

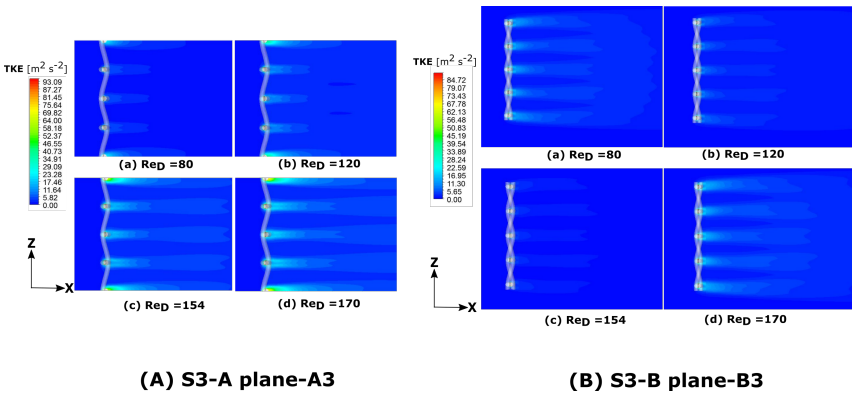

Figure 3.35: Turbulent kinetic energy: S3-A plane-A3 and S3-B plane-B3

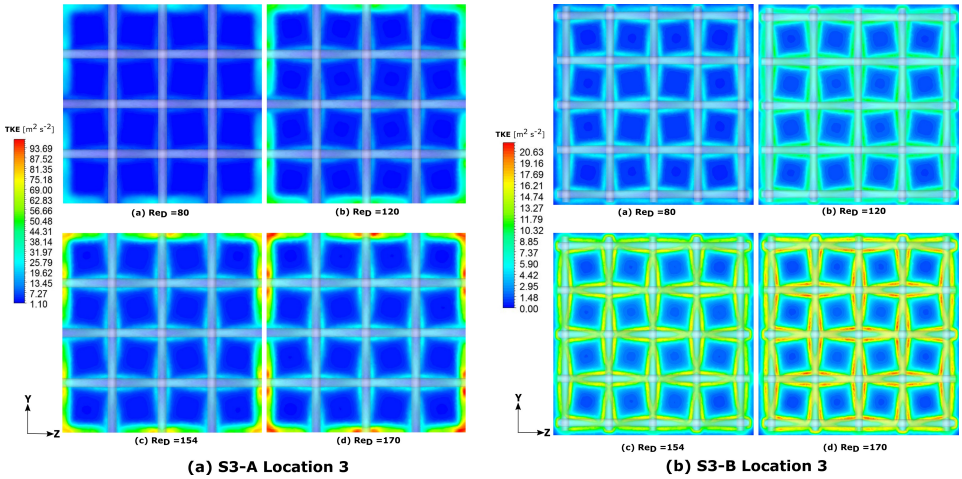

Figure 3.36: Turbulent kinetic energy at location 3: S3-A and S3-B

3.6.4 S3 Turbulent Kinetic Energy

Turbulent kinetic energy contour plots along plane-A3 and plane-B3 are as shown in Figure 3.35, while a clearer look at the maximum values at the Y-Z plane of location 3 is as presented in Figure 3.36.

To illustrate the flow phenomenon within the screen aperture, Figure 3.37 presents the turbulent kinetic energy of fluid flow through wire screens S3-A and S3-B. Similar to S1 and S2, the first major difference in turbulence kinetic energy results were found within the screen apertures. An observation is made, that peak kinetic energy values at screen exit of S2-A approximately doubles the values of S1-B. These trend was similar in S1 and S2, and these high kinetic energy values can be associated with the grid domain sides of S1-A, S2-A and S3-A, as it caused an interference and subsequent increase in local fluid kinetic

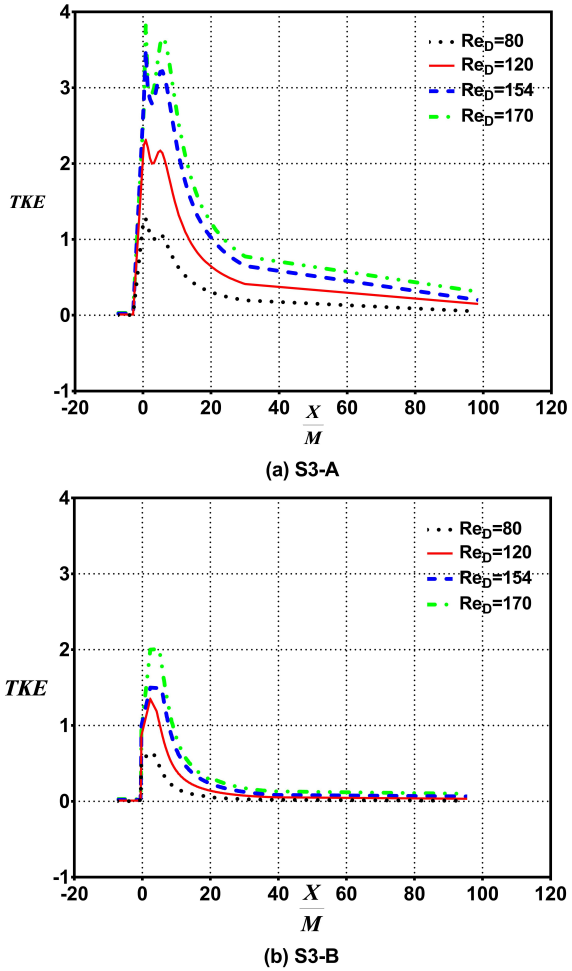

Figure 3.37: Turbulent kinetic energy through screen aperture for S3-A and S3-B

energies.

For S3-A, maximum flow kinetic energy values are located very close to the slip wall boundary condition sides, and this affected local kinetic energies of flows passing within the screens as maximum kinetic energy values increased from inlet values abruptly. The implication of this is that averaged fluid velocities and fluctuations within this location are much higher than fluctuations within the fluid screen flow. However, for S3-B, maximum kinetic energy values are limited to within screen aperture flow and close to screen edges. Therefore, turbulent kinetic energies of fluid flow within screen apertures are much smaller for S3-B compared to S3-A. Further implications of this observation

is the fact that maximum flow speeds within screen apertures for S1-A, S2-A and S3-A might be affected as a result of interference from sides of the domain acting as a boundary condition, thereby presenting superfluous local peak flow speeds at aperture exit.

3.6.5 S3 Turbulence Intensities Decay

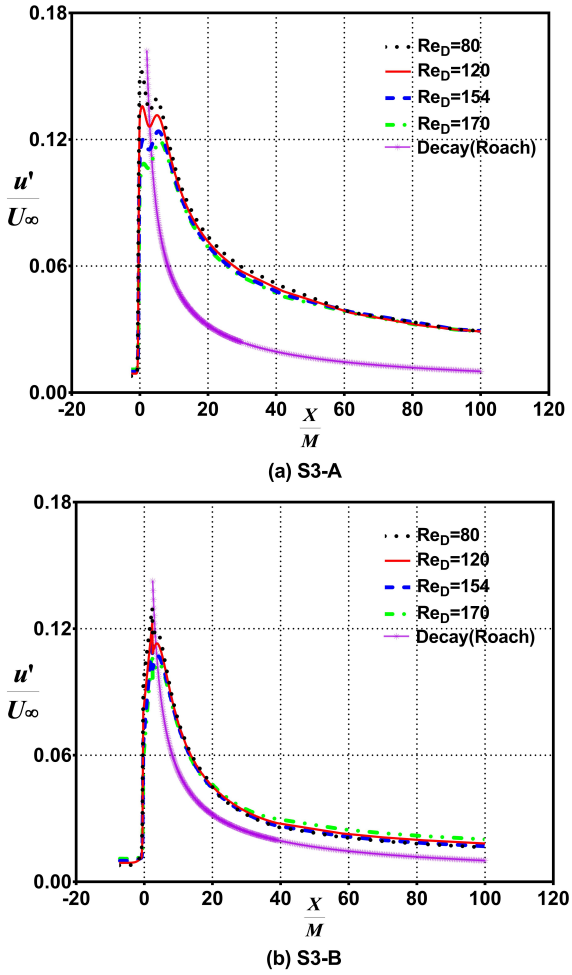

Figure 3.38: Turbulence intensity decay for S3-A and S3-B

Turbulence intensity decay through screen S3-A and S3-B is presented in Figure 3.38. Peak turbulence intensities of flow through S3-A occurred within the screen aperture while peaks from S3-B occurred downstream, at approximate distance of $X/M = 7$. Similar to cases of screen S1 and S2, the decay rate of low turbulence flow through screen S3-B compared better to Roach

model [1] than the decay through case S3-A.

3.7 Summary

From simulations carried out for the three different 3D woven wire mesh screens possessing open area ratios of $\beta = 49.38\%(S1), 51.84\%(S2)$, and $67.26\%(S3)$, modeled as presented within this chapter, the following observations and findings are summarized;

1. For obtaining pressure drop of flow through woven wire screens, solving turbulent transport equations by modeling the dissipation term ϵ replicates experimental results better than transport equations modeling the specific dissipation term ω or utilizing transition models. The $k - \epsilon$ turbulence model is suitable for this.

2. This approach therefore presents a computationally cost effective alternative to more expensive and highly accurate simulation models such as the DNS (Direct Numerical Simulations), LES (Large Eddy Simulations), LBM (Lattice Boltzmann Method) or DES (Detached Eddy Simulations) approach.

3. CFD predicted flow loss coefficients while using the $k - \epsilon$ turbulence model have the capacity to replicate experimental results within best case scenario error margins of -0.5% (Grid A), 1% (Grid B) and worst case error margins of -6.3% (Grid A) and 8% (Grid B).

4. Within the Reynolds number range tested, CFD predicted flow loss coefficients also presents much better predictions when compared to the loss coefficient correlation models of Wieghardt [157], Wakeland [156] and Roach [1].

5. With the use of a computational grid possessing much extended domain sides (S1-B, S2-B and S3-B), an estimate for flow speed reductions at

downstream regions of wire screens is presented. This flow speed reduction is shown to correlate with wire screens solidity $(1 - \beta)$ to within $U_{min} = (1 - \beta)U_{\infty}$, and occurs mainly within downstream distances of $7 < X/M < 60$ from wire screens. Therefore, for aerodynamic noise reduction applications, locating aerodynamic components within distances of $7 < X/M = 60$ downstream of wire screens is recommended.

6. Turbulent kinetic energy results shows that peak kinetic energy values at screen exit of S1-A, S2-A and S3-A approximately double the values of S1-B, S2-B and S3-B. These high kinetic energy values can be associated with the grid domain sides, as the domain sides aided the increase in fluid kinetic energy within the screen.

7. Implications of the observed rise in kinetic energies within screen exit for S1-A, S2-A and S3-A is the fact that maximum flow speeds within screen apertures for S1-A, S2-A and S3-A are affected as a result of interference from sides of the domain, thereby presenting superfluous peak flow speeds within the screen apertures.

8. Results from the turbulence decay of flow through screens tested show that S1-B, S2-B and S3-B represented the popular turbulence decay correlation model of Roach [1] much better than S1-A, S2-A, and S3-A for the range of Reynolds number tested. Again, due to the interference of the side wall boundary conditions on the fluid flow phenomenon through woven wire screens in S1-A, S2-A, and S3-A, the use of an extended sides fluid domain such as cases S1-B, S2-B and S3-B provides much better comparison to the turbulence decay correlation model utilized for downstream screen turbulence intensity decay.

9. Therefore, comparing results from the use of the two different computational grids utilized on screens S1, S2 and S3 in the course of the study within this Chapter, an observation and inference is made, that computational grid B provides a domain case that is more suitable for woven

wire screens analysis.

Chapter 4

Numerical Analysis For 2D Screens Identification

4.1 Background and Aim

Utilizing Computational Fluid Dynamics (CFD) to numerically resolve fluid flow through 3D realistic woven wire screens is problematic due to the fact that generating high quality grids of sufficient density at regions of intersections between strands of wire weaves introduces complexities within these regions [181]. Woven wire screens also possess relatively small thickness (stream-wise direction length), thereby possessing very little contact surface region for stream-wise flow, making it difficult to obtain quality grids needed to accurately capture the boundary layer within this contact region without utilizing advanced grid generation techniques [205]. Therefore, it presents a time demanding process towards achieving quality grid generation needed in order to properly capture boundary layer flows within the contact surface region and the region of wire strands intersection for realistic 3D woven wire screens. While the CFD studies carried out in chapter 3 presents an approach of analyzing wire screens, the analysis would be highly suitable for stand-alone wire screens, and would not be suitable for applications on 2D screen analysis.

Therefore, the aims of this chapter are;

1. A method for the simplification of 3D woven wire screens for 2D analysis is presented

2. Based on comparisons with pressure drop values of 3D screens, suitable geometric characteristics of a staggered array of 2D cylinder screen is identified and presented.

3. Turbulence reduction of a 2D screen will be compared to downstream turbulence reduction of a 3D screen and based on this conclusions are drawn on the suitability of 2D screens acting as simplifications to 3D woven wire screens.

For modest open area ratios of woven wire screens, an attempt is made here to represent three dimensional woven wire screens in a simplified two dimensional form as shown in Figure 4.1.

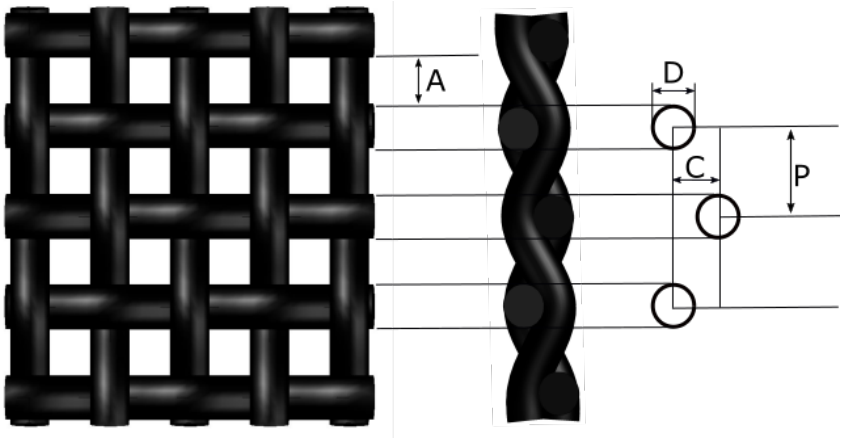

Figure 4.1: 3D to 2D Simplified Screen

where D is wire diameter, A is open aperture size, P is longitudinal pitch distance, and C is stream-wise pitch distance. Such a simplification is carried out with the assumption that 3D woven wire screens consist of 3D cylinders inter-twinned together to form a woven wire mesh screen, hence it's simplification as a 2D geometry becomes valid.

4.2 3D to 2D simplification concept

The concept that a 2D screen represents a sufficient simplification for 3D screens is presented in the course of this chapter. The flow through such a simplification can be viewed as flow through rows of 2D planar cylinders. In so doing, a quick time saving approach is developed to account for the physics of flows through woven wire screens possessing modest porosities and low Reynolds numbers. This is potentially useful for practical applications, where the effect of wire screens could be obtained by utilizing staggered screens as a simplification.

Across a typical 3D woven wire screen configuration as shown in Figure 4.2, taking a 2D planar sectional view in the X-Z plane into consideration, one can observe that the stream-wise pitch distance between each cylinder pair 'C' shifts between $0 \leq \frac{C}{D} \leq 1$ across a 3D screen aperture. On plane 1, $C/D = 0$ at the wire screen aperture center, and can be simplified by 2D representative cylinders possessing an in-line configuration. While $C/D = 1$ on plane 2 at

the wire screen aperture edge, or just at the end of an aperture, and at this point the 3D screen can be simplified in a 2D view as an array of staggered 2D cylinders. Implications of this is that the configuration will shift from an in-line row arrangement ($\frac{C}{D} = 0$) to a somewhat staggered row arrangement ($\frac{C}{D} = 1$) across a typical 3D wire screen aperture. The effect of such shifting across a wire aperture is studied in this chapter for two dimensional six cylinder row configuration.

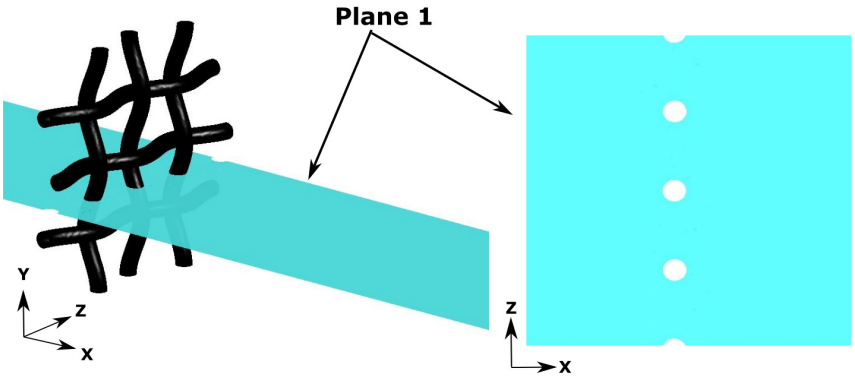

(a) Plane 1 showing when C/D= 0 at aperture center

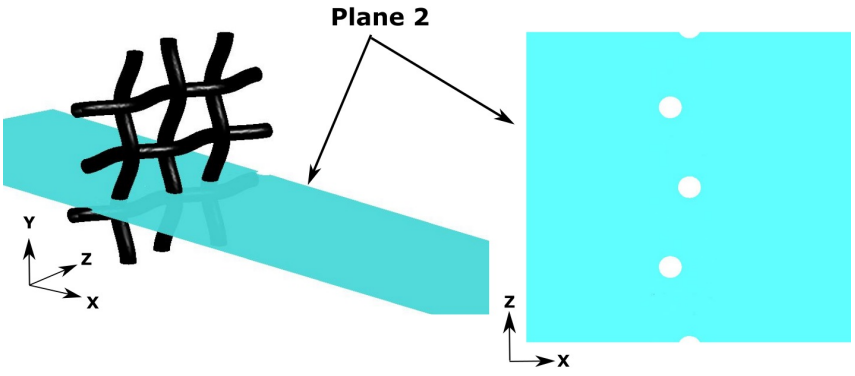

(b) Plane 2 showing when C/D= 1 at aperture edge

Figure 4.2: Planes showing 3D screens to 2D screen simplification

4.3 Theoretical Background

For flow past cylinder pairs, vortex shedding patterns largely depend on a characteristic spacing, i.e, the longitudinal pitch to diameter ratio $\frac{P}{D}$ [206, 207, 208], where the vortex shedding between cylinder pairs could predominantly exist in a 180° out of-phase pattern or an in-phase pattern depicted by Figure.

4.3.

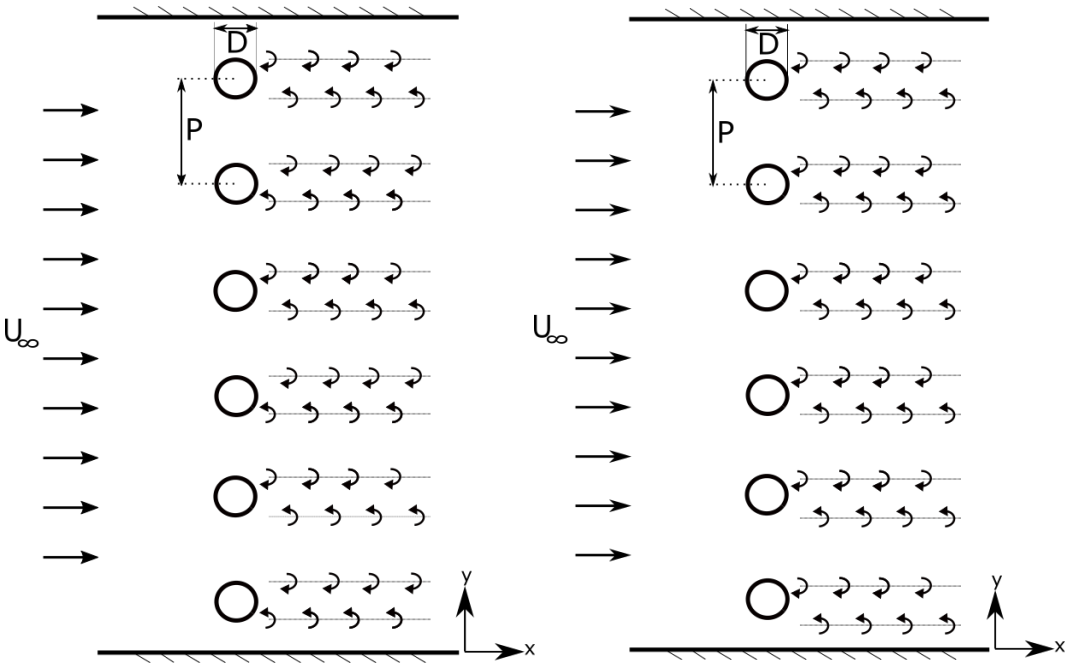

(a) Out of-Phase Pattern $2 \leq \frac{P}{D} \leq 6$ **(b)** In-Phase Pattern $\frac{P}{D} > 6$

Figure 4.3: Phase pattern of vortex shedding in the wake of cylinders

Experimental results [206] show that When $\frac{P}{D} \leq 1$ the effect of interaction between side by side cylinders becomes unnoticed and a single vortex wake pattern exists for the cylinder pair. This can be viewed as a merging of cylinder pair wakes. For $1.1 < \frac{P}{D} < 2$, a clear off-phase or in-phase pattern is not predominant, as cylinder pair close proximity still affects and distorts formation of patterned vortex shedding. However, Within this range an unsteady flip-flopping pattern occurs between two quasi-stable asymmetric states. In the range of $2 \leq \frac{P}{D} \leq 6$, the vortex shedding pattern from a pair of side by side in-line cylinder configuration becomes predominantly out of phase by approximately 180°. Within this range the interaction between a side by side pair of cylinder exists weakly, thus even though in-phase vortex shedding synchronization might be in existence the vortex shedding are predominantly 180° off-phase. While for $\frac{P}{D} > 6$, interaction between side by side cylinder pair does not exist, and in this case vortex are shed in a synchronized in-phase pattern predominantly.

As enumerated previously, the aim of this current chapter is to characterize 3D realistic woven wire screen geometries as simplified 2D screen geometries at low Reynolds numbers, thereby finding the most suitable 2D geometric characteristic that best approximates a 3D realistic geometry based on flow loss behaviors and isotropic turbulence characteristics. The most appropriate 2D screen geometry is realized by varying geometry characteristics in the range $0 \leq \frac{C}{D} \leq 1$ and CFD results validated against NACA documented experiments [176]. As highlighted previously, due to the time demand needed to achieve quality grid generation for 3D realistic woven wire screens in order to accurately capture boundary layer flows within the contact surface region and the region of wire strands intersection, an appropriate 2D screen geometry potentially aids fast turnaround CFD applications and results needed for studying the effect of flow control and noise reduction studies on various 2D aerodynamic shapes. Proof of concept studies can be performed utilizing 2D aerodynamic shapes, and the effect of studying the application of woven wire screens applied to 2D shapes becomes important for flow and noise control studies, as such, the most suitable 2D woven screen that best approximates a realistic woven screen would provide scientists and researchers with a good means of performing aerodynamic flow and noise control studies utilizing 2D woven screens.

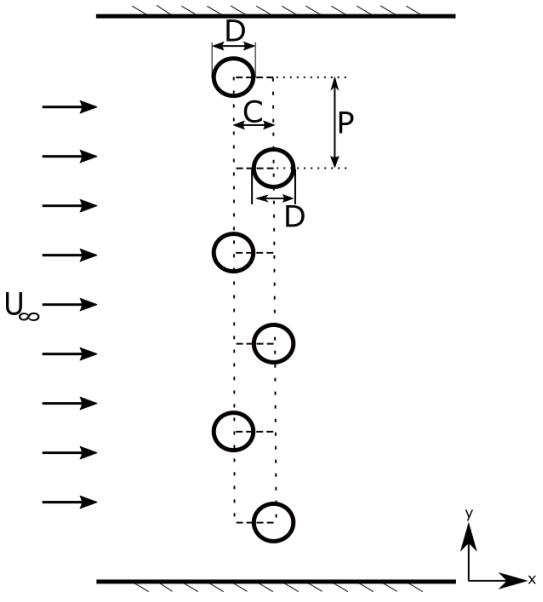

Figure 4.4: 2D Screen Configuration; $2.94 \leq \frac{P}{D} \leq 5.56$ and $0 \leq \frac{C}{D} \leq 1$

2D Screens Tested				
Sample	D (mm)	P (mm)	P/D	β (%)
1	0.43	1.27	2.94	43.56
2	0.14	0.47	3.36	49.38
3	0.18	0.64	3.57	51.84
4	0.19	1.06	5.56	67.26

Table 4.1: Geometric Characteristics of 2D Screen Samples

4.4 Numerical Set-up

In order to obtain CFD results, two dimensional unsteady simulations are carried out.

4.4.1 Geometric Characteristics

A row containing six cylinders as shown in Figure 4.4 is simulated. Geometric characteristics of the cylinders tested are as shown in Table 4.1. Simulations are carried out for each row sample for a range of $0 \leq \frac{C}{D} \leq 1$. It is pointed out here that screen samples 1,2,3 and 4 refers to experimental screen C, screen F, screen D and screen B of Schubauer[176] used for validation and comparison.

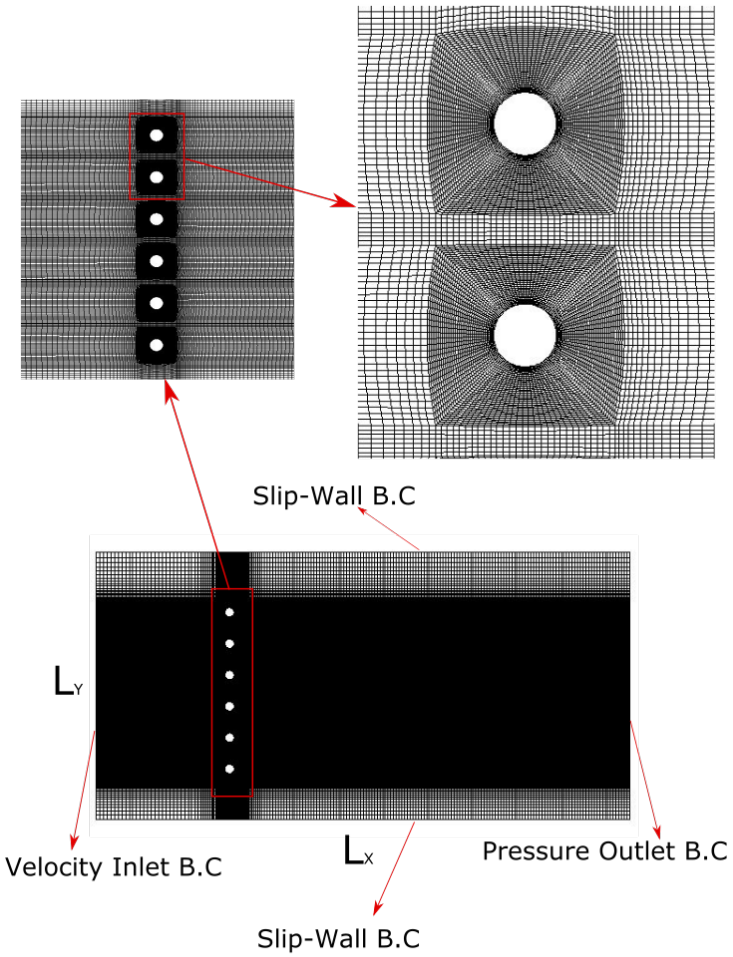

Figure 4.5: Numerical Grid showing Boundary conditions

4.4.2 Meshing and Boundary Conditions

Numerical grid generation was carried out using ICEM meshing software, and grid sample showing applied boundary conditions as shown in Figure 4.5 was utilized. Velocity inlet conditions were applied at the grid inlet, and pressure outlet conditions applied at the grid exit. Slip wall conditions (no shear stress, no flow-through) conditions were applied at the top and bottom sides, while the cylinders had no-slip wall boundary conditions. Domain sizes of $20D \leq L_y$ and $575D \leq L_x$ were utilized for all screen samples simulated.

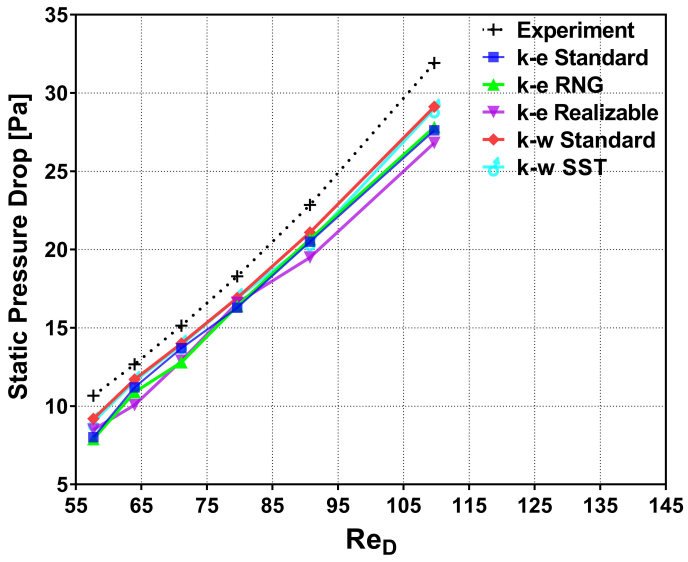

Figure 4.6: Turbulence model study

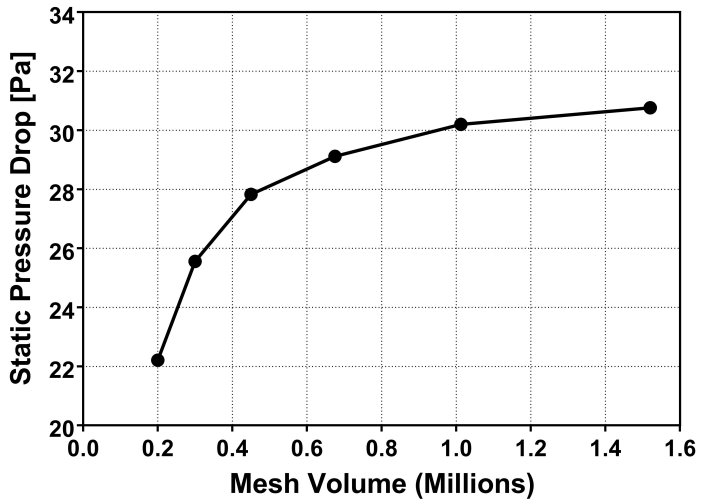

Figure 4.7: Static pressure drop against mesh volumes for screen sample 4 at $Re_D = 110$ and $\frac{C}{D} = 0$ using the standard $k - \omega$ turbulence model

4.5 Results

Results from the turbulence model selection study, grid independence study, flow loss coefficients, downstream turbulence intensities, turbulence reduction factors and obtained vortex shedding patterns are presented within this section.

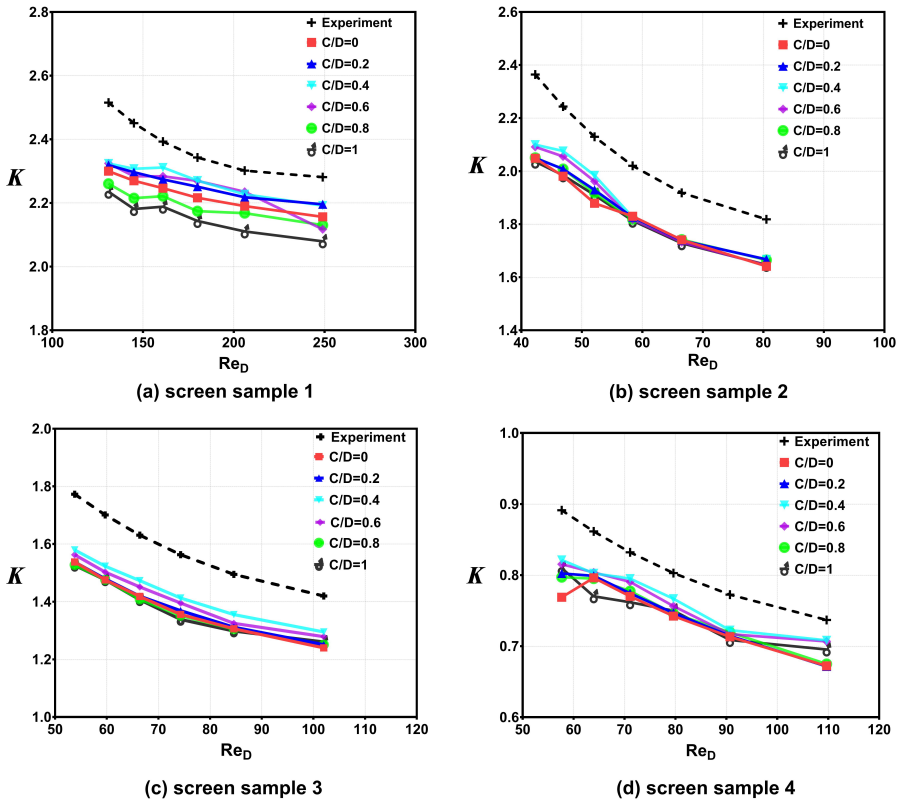

Figure 4.8: Comparison of Experiment and CFD prediction; K vs Re_D

4.5.1 Turbulence Model Selection and Grid Independence Study

In this study, the regimes of interest for fluid flow across screen samples 2, 3 and 4 are within the two regime wake where vortex street is laminar and clearly alternating $40 \leq \mathrm{Re}_D \leq 150$, while flow regime for screen sample 1 lies within the transition range to turbulence within the vortex street $150 \leq \mathrm{Re}_D \leq 300$ [204]. An appropriate turbulence model selection study was carried out for screen sample 4 utilizing a medium refined grid of 0.6 million cells. The standard $k-\omega$, Shear Stress Transport (SST) $k-\omega$, standard $k-\epsilon$, Re-

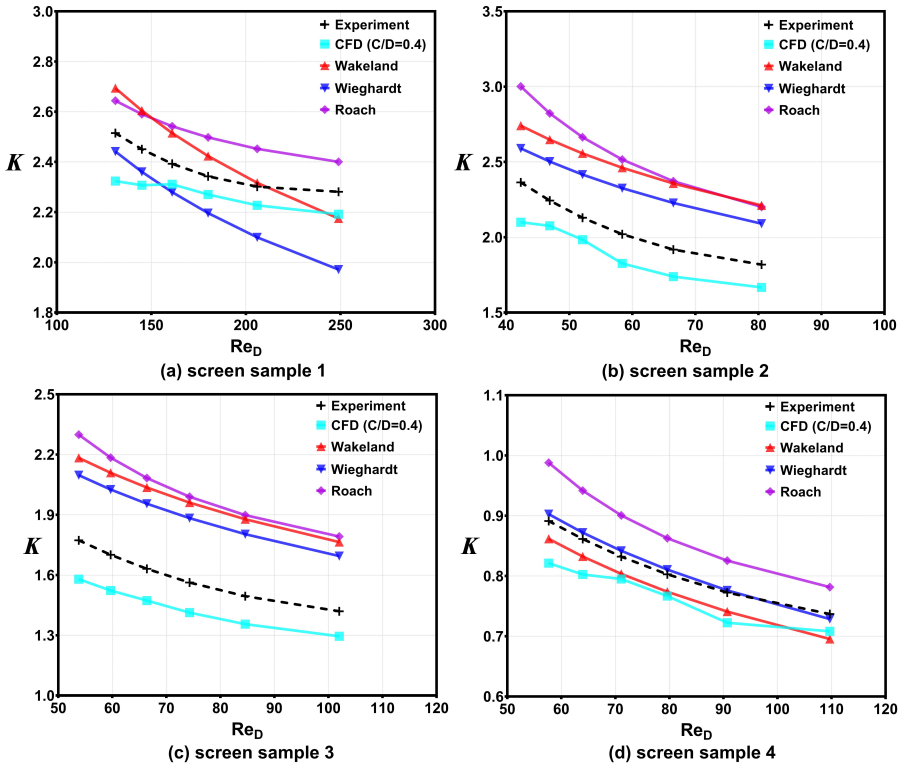

Figure 4.9: Flow loss coefficient comparison with correlations

Normalisation Group (RNG) $k-\epsilon$ and realizable $k-\epsilon$ turbulence models are utilized for test studies in order to capture the flow physics through an in-line screen configuration at three different Reynolds numbers.

Screen flow loss coefficient were calculated at three different Reynolds number, and results of such studies of static pressure drop of screens compared to experiment [176] are presented in Figure. 4.6

Turbulence studies show that the SST $k-\omega$ turbulence model provides the most reflective comparison to experiment, hence this turbulence model was utilized for all subsequent analysis with low Reynolds number corrections, and production limiter. The SIMPLE pressure-velocity coupling scheme was utilized, with least squares cell based gradient spatial discretization, second order discretization for pressure, second order upwind discretization for momentum, turbulent kinetic energy and specific dissipation rate. Pressure under-relaxation factor of 0.2 was utilized, with 0.5 for momentum, 0.6 for turbulent kinetic energy and 0.6 for specific dissipation rate under-relaxation

factors. $y+ \approx 1$ were maintained on all screen surfaces, and time-step for unsteady analysis was such as produced average CFL number of less than one for all grids, and which also resulted in having a minimum of 30 period cycles per time-step based on cylinder Strouhal number of 0.2. Turbulence intensity at inlet boundary condition was chosen as to match experimental utilized turbulence intensities, where as low as 0.02% were utilized during the low speed wind tunnel tests. Therefore, from experimental results, inlet turbulence intensities of within 0.7%, 0.8% and 1% were sufficient for CFD simulations.

Grid independence studies were carried out for screen samples 1-4 tested. Results for screen sample 4 is as shown in Figure 4.7.

Grid volumes were generated for screen samples with approximately 1million cells, as this proved sufficient enough to capture flow details of vortex streets, and static pressure drop characteristics.

4.5.2 Flow Loss Coefficient

Validation of the numerical code implemented was benchmarked against documented NACA experiments carried out by Schubauer et.al [176].

Loss coefficients of screen samples are presented as shown in Figure 4.8, where CFD predicted results are compared with experiments.

As screen geometric characteristics are altered, switching from an in-line geometry $C/D = 0$ to a off-line staggered geometry $0 < \frac{C}{D} \leq 1$, varying results are obtained for the same flow conditions. CFD results of screen sample 3 (screen D) showed much better comparisons within the range $0.4 \leq \frac{C}{D} \leq 0.6$, with agreements up to -12.2% obtained for $C/D = 0.4$ and -13.4% for $C/D = 0.6$. Screen sample 4 (screen B) results show a -8.5% agreement for $C/D = 0.4$ and result of -9.3% agreement for $C/D = 0.6$. Similar reflective results were obtained for screen samples 1 and 2 as shown in Figure 4.8. Therefore, a trend is established, were it is observed that better flow loss characteristics are obtained for the range of $0.4 \leq \frac{C}{D} \leq 0.6$. Results show this trend exists because as screen geometry changes within the range of $0 < \frac{C}{D} \leq 1$, near-field downstream wake pressure values are altered, resulting in a reduced pressure

field in this wake region, where the reduced pressure field are strongest for screen geometry within the range of $0.4 \leq \frac{C}{D} \leq 0.6$, thereby invariably causing better reduced loss coefficient values for this geometry range. Therefore, flow loss coefficient results showed better comparisons to experiments within $0.4 \leq \frac{C}{D} \leq 0.6$.

Comparison between CFD predicted flow loss coefficients and some existing semi-empirical correlations are also carried out as shown in Figure 4.9 for screen samples simulated. Screen samples with $C/D = 0.4$ has been used for comparisons as this configuration showed to represent a 3D screen better than other configurations. Loss coefficients for screen sample 1 showed that Wakeland's [156] semi-empirical correlation predicts loss resistance within the range of Reynolds number tested with error margins of $\pm 6\%$, Wieghardt's [157] correlation under predicted to within -15.6%, the Roach [1] correlation over predicts to within 6.2%, while CFD prediction for $C/D = 0.4$ under predicted to within -8.2%. Screen sample 2 results showed Wakeland's correlation over predicting by up to 18.6%, Wieghardt's correlation over predicting by up to 14%, Roach correlation over predicting by up to 21.2%, while CFD under predicted by -12.6%. For screen sample 3, Wakeland's correlation over predicted up to 20.4%, Wieghardt's correlation over predicted by 17.1%, Roach correlation over predicted by 23%, while CFD under predicted by up to -12.2%. comparisons for screen sample 4 shows under prediction using the Wakeland's correlation to within -6%, Wieghardt's correlation predicting with accuracy of $\pm 1.26\%$, Roach correlation over predicting up to 9.8%, while CFD under predicted within -8.5%. Taking these compared predictions into consideration, it becomes clear that the CFD prediction approach presents better results when compared to semi-empirical models within the range of Reynolds number tested.

4.5.3 Turbulence Intensities

Green et.al [181] performed numerical laminar flow simulations for flow through three dimensional woven fabrics, and achieved favorable comparisons of flow

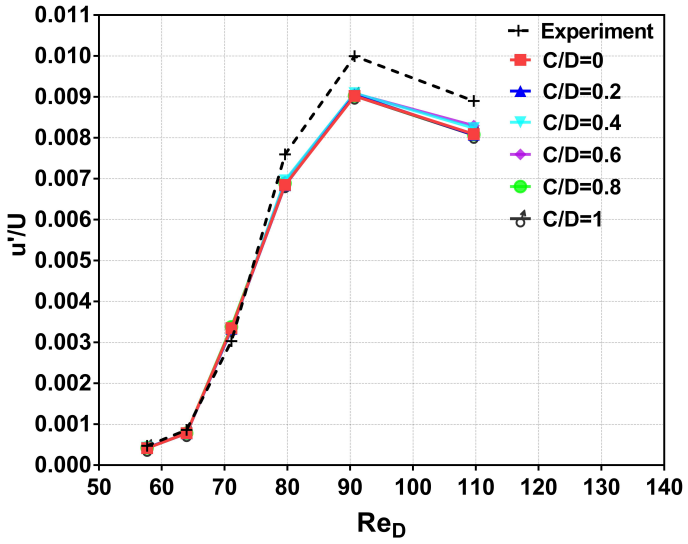

Figure 4.10: Axial turbulence intensity 556D downstream screen 4

loss coefficient with the experimental report of Schubauer et al [176], but the reported numerical work lacked turbulence characteristics comparisons due to the laminar flow model utilized.

CFD informed axial turbulence intensity prediction was carried out, and results are as presented in Figure 4.10. The comparison of experimental to CFD axial turbulence intensity prediction was carried out at 556 wire diameter downstream of screen sample 4. In the range of Reynolds number tested, axial turbulence were predicted to within ±10% difference to experimental values. Geometric configurations for C/D= 0.4 and 0.6 yielded better comparisons when compared to other configurations.

4.5.4 Turbulence Reduction Factor

Turbulence behavior far downstream of wire screens are expected to be isotropic in nature as documented experimental results have shown [1, 162], where decay of progressive turbulence could be regarded as an isotropic decay. Comparisons with semi empirical isotropic turbulence reduction correlation models is carried out and results are as shown in Figure 4.11. The Prandtl [173], Collar [174], Dryden and Schubauer [161] correlation's are utilized for comparison with CFD predicted axial component of turbulence reduction factors. As seen

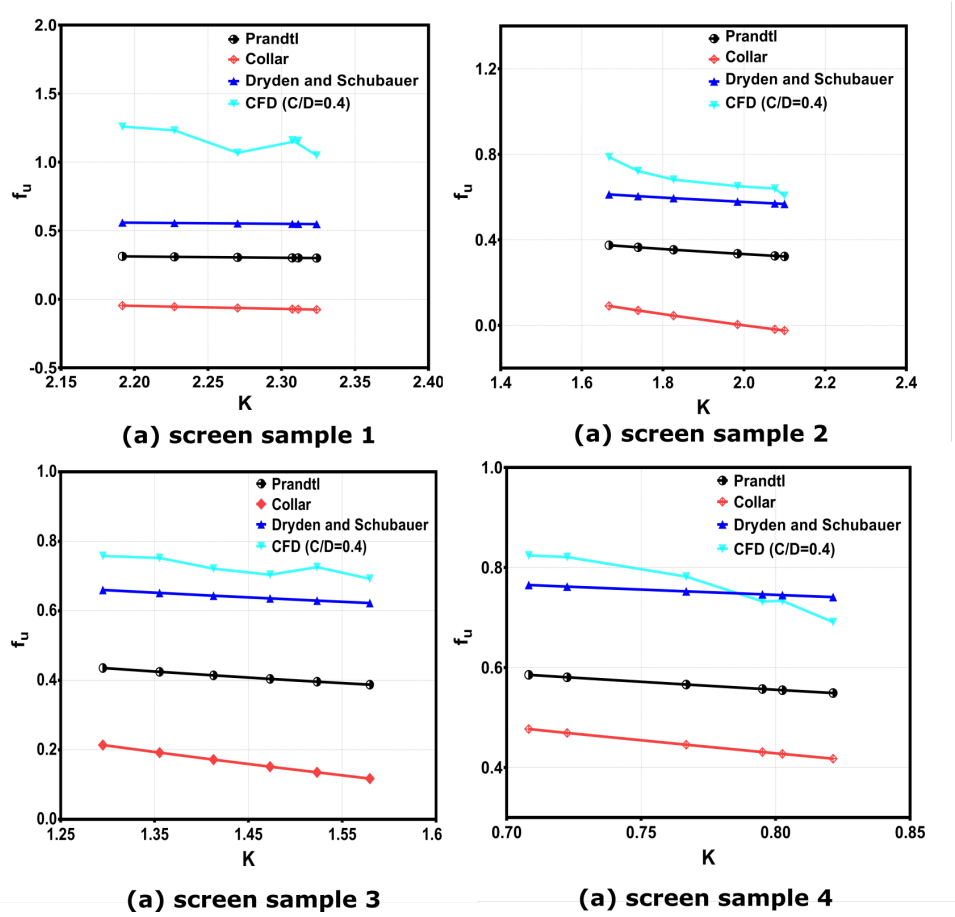

Figure 4.11: Reduction factors for axial component of turbulence

from Figure 4.11, results for screen samples 2, 3 and 4 show good agreement with expected component of turbulence reduction factors. Experimental results of NACA [176] particularly showed good agreement with axial turbulence reduction factors when the Dryden and Schubauer [161] correlation was utilized for comparison between experiments and correlation of screen samples. Hence, an observation and conclusion that the 2D screens CFD informed reduction factors compare very well to reduction factors using the Dryden and Schubauer [161] correlation.

4.5.5 Vortex Shedding Phase Patterns

Vortex shedding patterns were analyzed for all screen samples tested. The vortex shedding pattern for screen sample 4 (screen B) having $P/D = 5.56$, and $0 \leq \frac{C}{D} \leq 1$ is as shown in Figure 4.12 and Figure 4.13. As shown in

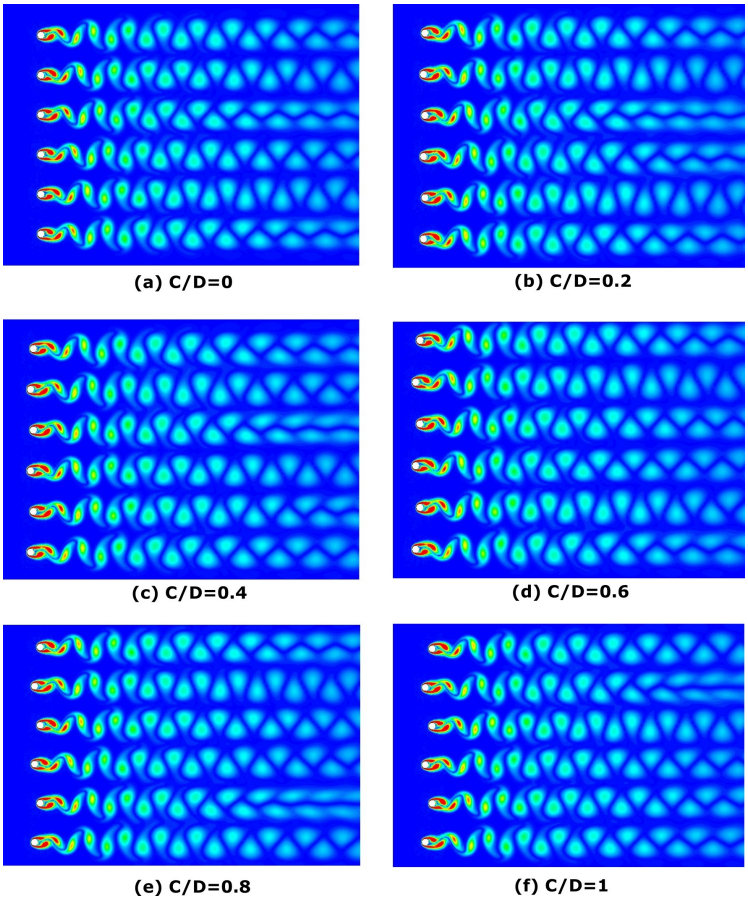

Figure 4.12: Instantaneous vorticity magnitude of wake flow past screen configuration $Re = 120$, $D = 0.1905mm$, $P/D = 5.56$ and $0 \leq \frac{C}{D} \leq 1$

the Figures, when cylinders possess an in-line configuration $\frac{C}{D} = 0$, the vortex shedding pattern from adjacent cylinders are predominantly 180 degree out of phase, which is rightly expected for this range of $P/D = 5.56$, where interaction between adjacent side by side cylinders are rather weak, and as such vortex shedding from each cylinder are not affected by the existence of vortex shedding from adjacent cylinders. Experimental [208, 209] and numerical [210] documented results have shown similar vortex shedding trends for this range of P/D. However, as the configuration changes, i.e $0.4 \leq \frac{C}{D} \leq 1$, there exists a slight shift in the vortex shedding pattern from adjacent cylinders, with the vortex shedding pattern alternating between an in-phase pattern and off-phase pattern for some configurations. For $\frac{C}{D} = 0.2$, the cylinders vortex shedding pattern remain predominantly 180° out of phase, as shown in Figure 4.12 (b). When $0.4 \leq \frac{C}{D}$, an in-line pair of vortex shedding pattern exists within the flow

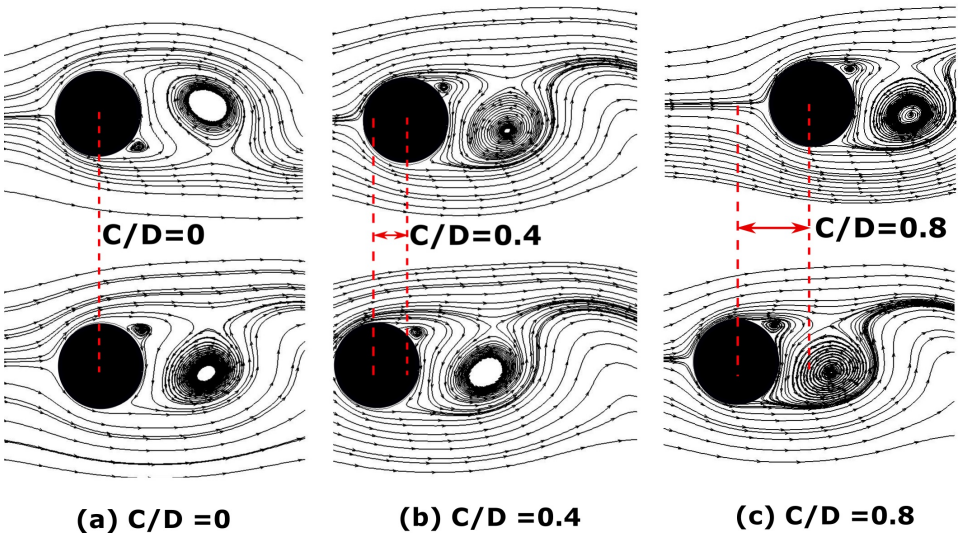

Figure 4.13: Unsteady streamlines of wake flow past screen 4; $Re = 110$, $D = 0.1905mm$, $P/D = 5.56$ and $0 \leq \frac{C}{D} \leq 1$

pattern as shown in Figure 4.12 (c)-(f), also illustrated in Figure 4.13. As the screen geometry changes within $0.4 \leq \frac{C}{D} \leq 1$, the slight vortex shedding pattern alteration from a well patterned off-phase to a somewhat in-phase pattern equally aids reduction of pressures within the cylinder near-field wake region. This pattern effect is evident within $0.4 \leq \frac{C}{D} \leq 1$. Figure 4.14 shows the out of phase vortex shedding patters well expected, while Figure 4.15 presents the equivalent time-averaged (mean) vortices's.

Therefore, for a typical 3D configuration of wire mesh screen, having $0 \leq \frac{C}{D} \leq 1$ across the wire screen, one might expect the vortex shedding pattern to deviate slightly from patterns expected from a regular 3D cylinder configuration. This could possibly be connected to the documented [176] NACA technical report, where it was found that the critical Reynolds number for which eddy begins to shed from cylindrical wire mesh screens deviated from those expected for a single cylinder geometry.

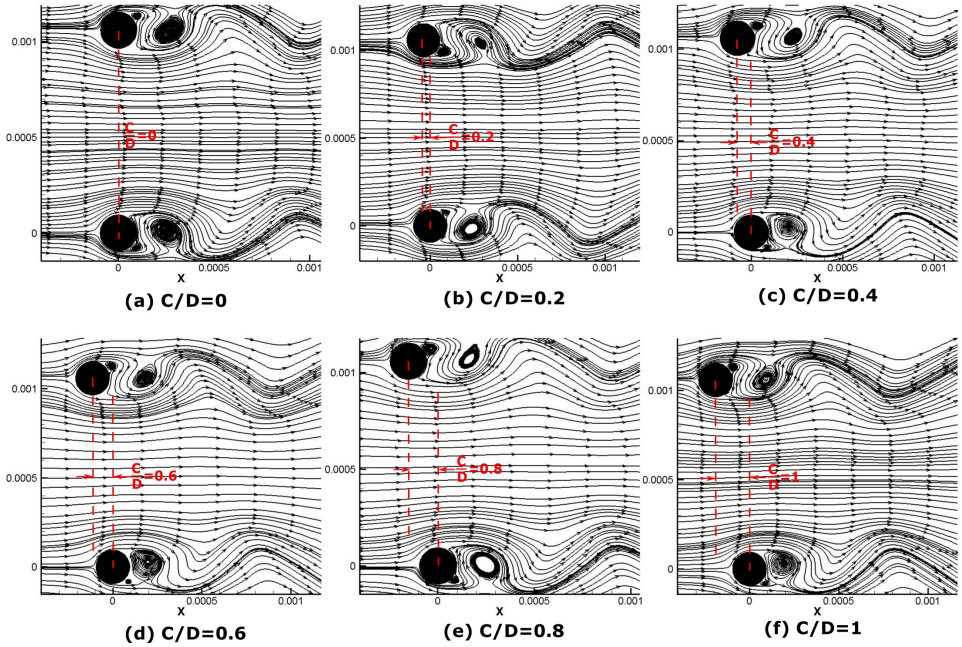

Figure 4.14: Unsteady streamlines of wake flow past screen 4; $Re = 110$, $D = 0.1905mm$, $P/D = 5.56$ and $0 \leq \frac{C}{D} \leq 1$

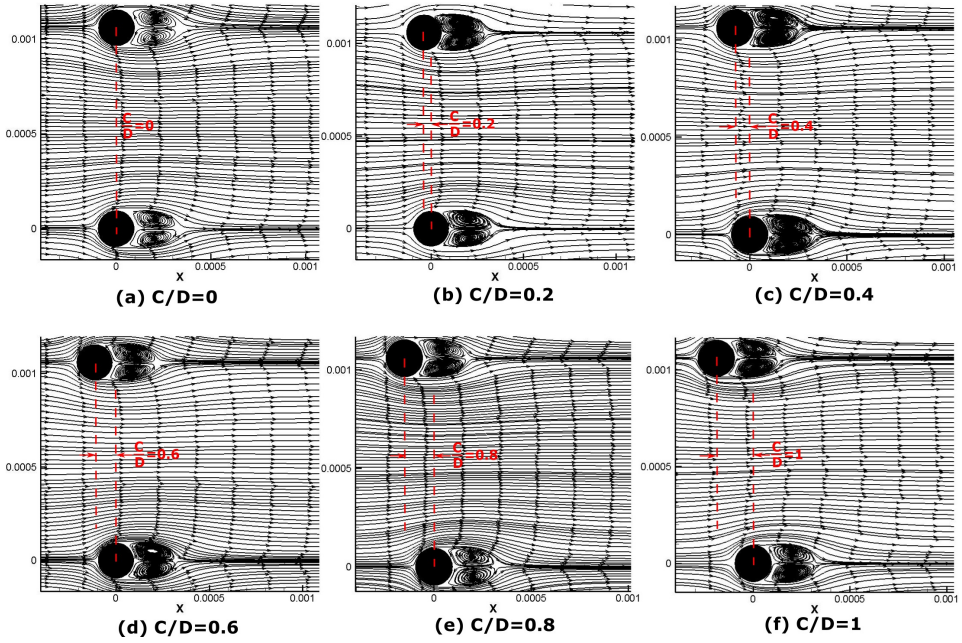

Figure 4.15: Time-Averaged streamlines of wake flow past screen 4; $Re = 110$, $D = 0.1905mm$, $P/D = 5.56$ and $0 \leq \frac{C}{D} \leq 1$

4.6 Summary

In this chapter, studies were carried out in order characterize 3D wire screens using simplified 2D screen geometry configuration approach. The following presents highlighted summary of this research;

1. 2D screen configurations in the range of $0 \leq \frac{C}{D} \leq 1$ were simulated and studied with experimental flow loss characteristics and isotropic turbulence behavior utilized as benchmark for validating numerical studies.

2. For modest open area ratio's, 2D geometry of staggered cylinders can represent realistic 3D woven screens within a range of C/D ratios.

3. CFD predicted flow loss coefficients from 2D geometry characteristics yields better agreement to experiments when compared to some existing semi-empirical correlations.

4. The nature of isotropic turbulence downstream of a screen was also well predicted, and comparisons of CFD predicted turbulence reduction factors to a selected semi-empirical correlation model showed good agreement.

5. 2D screen geometries possessing $0.4 \leq \frac{C}{D} \leq 0.6$ showed better representation to 3D experimental results, therefore, for 2D simplified analysis of a woven wire screen, better flow characteristics can be obtained when the range $0.4 \leq \frac{C}{D} \leq 0.6$ is utilized, compared to an in-line simplified cylinder configuration.

6. For staggered arrangement of 2D cylindrical screens, as screen geometries shift within $0.4 \leq \frac{C}{D} \leq 1$, a slight vortex shedding pattern alteration from a well patterned out of-phase to a somewhat in-phase pattern is introduced.

Generally, 2D screen geometries possessing $0.4 \leq \frac{C}{D} \leq 0.6$ have shown to possess much better representation to experimental results. This geometry

range is hereby recommended for use in applications and analysis involving 2D shapes where flow and noise control studies are of significance.

Chapter 5

Modeling 3D Woven Wire Mesh Screens for Noise Control

5.1 Background and Aim

Noise reduction capabilities of woven wire mesh screens are further investigated within this chapter, with the aim of potential application towards low noise treatments of aircraft landing gears.

In chapter 3, simulations of stand-alone woven wire screens were carried out, where a suitable turbulence model and domain boundary condition consideration needed to reflect a realistic screen configuration was proposed. However, the numerical simulations of woven wire screens as add-ons for low noise treatments of complex geometries like an aircraft landing gear, presents a challenging computational exercise due to the following reasons;

1. Length scales within the landing gear geometry fluid dynamics are very different to the length scales for flow through the woven wire mesh screens. The woven wire screens in context would sometimes possess characteristic wire diameters of less than 0.2mm, which in most cases is over 600 times smaller than the characteristic length associated with strut diameters of landing gears.

2. Due to these large differences in length scales, generating CFD computational grids of sufficient quality needed to capture realistic fluid dynamics features of the flow through wire screens upstream or wrapped around landing gear geometries becomes very challenging, and in some cases, impossible.

3. For landing gears noise studies and far-field propagation, the computational flow domain requires an unsteady flow field analysis, which is time consuming, and the added smaller length scales of the woven wire screens would result in a much more expensive computational task.

Therefore, in view of these reasons, an alternative low computational cost and CFD computational grid friendly approach that replicates the effect of woven wire screens as add-on low noise treatments for realistic and complex geometries like landing gears is needed.

This chapter aims to provide an alternative modeling approach for the implementation of woven wire screens within a computational flow domain.

This numerical modeling of woven wire mesh screens is implemented by making use of porous zones that are modeled within the flow domain in such a manner that these porous zones would account for the pressure drop effects ΔP_e and turbulence alteration effects T_e of woven wire mesh screens. The pressure drop effect ΔP_e is introduced by making use of a Volume Averaged Method (VAM) within the CFD solver, which introduces sink terms into the Navier-Stokes Equations. Semi-empirical flow loss properties of wire screens are utilized within the sink, and tests are further conducted in a closed test section wind tunnel facility in a bid to generate model fit curves of flow resistance as a function of porosity for wire screens, and to compare its flow loss properties to the semi-empirical derived values. Turbulence alteration characteristics T_e are introduced by further injecting turbulence suppression sinks within the porous zone. A landing gear strut section, represented as a simple H strut unit is used to test this numerical approach methodology and is therefore simulated for turbulence induced noise generation and propagation using the Improved Delayed-Detached Eddy Simulation (ID-DES) which is coupled to the Ffowcs Williams-Hawkings (FWH) acoustic analogy for far-field noise propagation. Results of this simulation methodology are validated using documented experimental results performed in the framework of the European project TIMPAN (Technologies to IMProve Airframe Noise), carried out in NLR (National Aerospace Laboratory) anechoic wind tunnel, where woven wire screens intended for landing gear noise reduction applications were tested.

The macroscopic flow model, which uses a Volume-Averaged Method (VAM) equation within a porous media zone [186, 187] presents a relatively less expensive approach which is preferable for fast turn around analysis. Therefore, the approach adopted within this paper will be based on the macroscopic Volume Averaged method (VAM) applied for the specific nature of woven wire screens.

From the physics of flows through perforated screens or woven wire screen

sections, the major effects of screens on the fluid flow is the introduction of a pressure drop effect ΔP_e, turbulence alteration effect T_e and the screens self noise effect N_e when noise propagation studies are needed [9, 80]. The pressure drop effect ΔP_e and turbulence alteration effect T_e will be the main focus of the research presented within this chapter.

5.2 Theoretical Background

The pressure drop effects and turbulence alteration utilized within the porous zone mimicking a woven wire screen is presented within this section.

5.2.1 Pressure Drop Effect (ΔP_e)

The pressure drop effect introduced by the presence of a woven wire screen will be estimated using the Idelchik's semi-empirical model [18] shown in Equation 5.1.

$$K = K_{mesh} K_{Re}(1-\beta) + \left(\frac{1-\beta}{\beta}\right)^2 \quad , \quad Re_D \geq 400 \tag{5.1}$$

Where woven wire constant $K_{mesh} = 1$ for new screens and wire Reynolds number factor $K_{Re} = 1$ as recommended. This relationship is reported to be independent of Reynolds number within $Re_D \geq 400$.

The non-dimensional relationship between screen flow loss coefficient of wire screens, static pressure drop and dynamic pressure through screens presented in Equation 5.2 will be used for pressure drop to flow loss calculations.

$$K = \frac{\Delta P}{0.5 \rho U_\infty^2} \tag{5.2}$$

Where K is the flow loss coefficient, ΔP the static pressure drop through screen, ρ the fluid density, and U_∞ the free stream velocity.

5.2.2 Turbulence Alteration effect (T_e)

Mesh screens possess turbulence alteration effects in the form of turbulence suppression effects which are also known to depend on the flow loss coefficient of

such screens [161, 162, 163, 164, 165]. At the immediate downstream near field wake region of screens, turbulence exits in an anisotropic form with intensities much higher than upstream intensities. Batchelor et.al [166, 167] reported on the decay of isotropic turbulence in the initial decay period and the final decay period, thus resulting in the knowledge that a decay region exists further downstream far-field, where anisotropic intensities begin to reduce rapidly and turbulence returns to a near isotropic state.

The Dryden and Schubauer[161] Equation 5.3 for axial component of turbulence reduction factor will be used for the modeling approach proposed within this chapter.

$$f_u = \frac{1}{\sqrt{1+K}} \tag{5.3}$$

Experimental results of NACA [176] particularly showed good agreement with axial turbulence reduction factors when the Dryden and Schubauer [161] correlation was utilized for comparison between experiments and correlation of screen samples. Therefore, for the purpose of numerical modeling for turbulence alteration effects, the Dryden and Schubauer [161] correlation will be imposed as a sink term for turbulence intensities at the virtual zone of interest.

5.3 Modeling Approach

Attempts to numerically simulate or resolve the application of wire screens for landing gear noise reduction effects presents a highly expensive task for CFD/CAA experts and engineers till date, due to the very fine grid resolution implication and computational costs required to actually resolve or simulate the physical wire screen within a CFD flow domain at such large scale and at close proximity to the landing gear.

Therefore, within this research framework, focus is directed on implementing an alternative approach, where numerically modeling the effect of wire screens is proposed and adopted by introducing a virtual porous zone within the CFD flow domain as shown in Figure 5.1, where pressure drop characteristics ΔP_e, velocity modification effect V_e, turbulence alteration effect T_e and

self noise effect N_e of such wire screens can be subsequently imposed. This porous zone can be selected so as to possess similar geometric characteristics, such as length and thickness of a a physical wire screen.

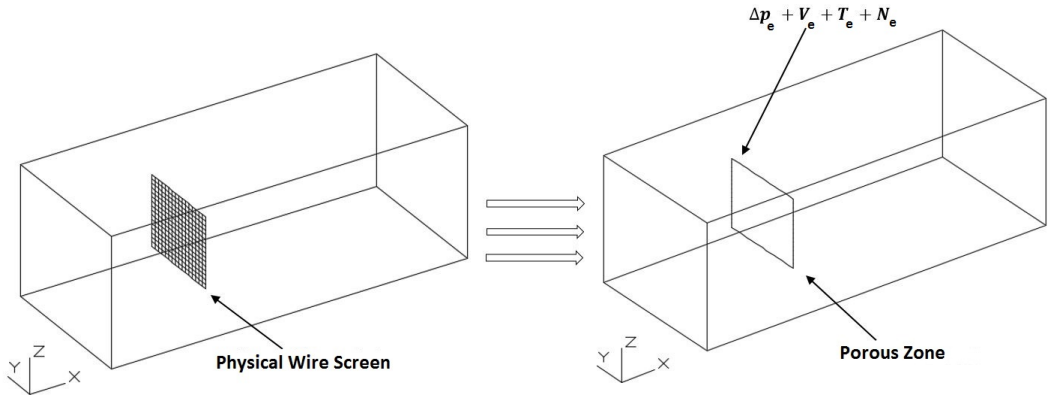

Figure 5.1: Simulating a Physical Wire Screen vs Modeling a Virtual Wire Screen as a Porous Zone

These characteristics, such as pressure drop ΔP_e, velocity modification V_e, turbulence alteration T_e and self noise N_e will be introduced within the virtual wire screen porous zone one after the other within the CFD domain, and the effects of this introduction studied and discussed.

To account for these characteristics, the pressure drop characteristics ΔP_e is introduced by using a Volume Averaged Method within the CFD solver, which introduces sinks into the Navier-Stokes Equations. Empirical flow loss properties of wire screens are utilized within the sink, and experiments are further conducted in a closed test section wind tunnel facility in a bid to generate model fit curves of flow loss resistance as a function of porosity for wire screens, and to compare its flow loss properties to empirical derived values, where the effectiveness and suitability of each approach are discussed. For the empirical flow loss properties, Idelchik's relation [18] is used to model the flow loss resistance within the porous wire screen zone. Velocity modification V_e and turbulence alteration effects T_e will be introduced by further injecting turbulence characteristics.

Figure 5.2 shows a 2D representative of a square weave wire screen, where the open area ratio (Porosity) is calculated making use Equation 5.4. Where

D is wire diameter, and M is the length of open aperture (Mesh Width), and β = Open Area Ratio (Porosity).

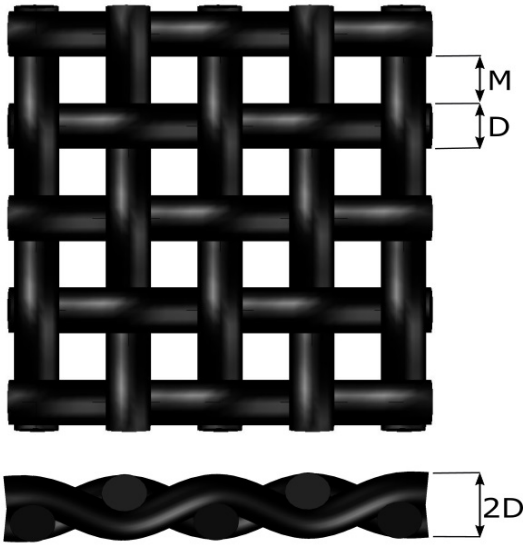

Figure 5.2: Representative Square Weave Wire Screen

$$\beta = \frac{M^2}{(M+D)^2} \tag{5.4}$$

Of the four characteristics mentioned, the pressure drop effect ΔP_e can be evidently applied, however, the velocity modification V_e characteristics appears to be embedded to a large extent within the turbulence alteration characteristics T_e. Hence, for the purpose of this research study, focus and priority is placed on modeling the pressure drop characteristics ΔP_e and the turbulence alteration characteristics T_e.

5.4 Loss Coefficient Test

Tests were conducted in a closed test section wind tunnel facility in order to generate model fit curves of flow loss resistance K as a function of porosity β for wire screens, and in so doing, compare the acquired flow loss properties to the Idelchik [18] semi-empirical derived values.

5.4.1 Loss Coefficient Test Facility

Schematic representation of the wind tunnel facility utilized for the flow loss coefficient tests is as shown in Figure 5.3, which comprises of a closed rectangular test section of 125mm × 12.5mm × 34mm long polycarbonate transparent material, possessing a thickness of 12mm. Within the test section, holes were drilled, to enable the insertion of two pressure taps having 3mm outer diameter, which were used for pressure drop measurements across the wire screens. The pressure taps were made from brass tubing, and both possessed 3mm and 2.5mm outer and inner diameters. These taps were drilled and carefully dressed. Holes of similar dimensions were drilled for the insertion of hot wire probes for fluid flow velocity measurements, and temperature probes for fluid flow temperature monitoring, as shown in Figure 5.4. Hot wire anemometer (HWA), which utilizes the principle of forced convection giving rise to a change of electrical resistance of hot filaments, are used to determine the relative flow velocity within the experimental test section. Voltage readings during calibration and testing were recorded from the hot wire probe through a 4m VNC cable connected to a Dantec Dynamics Streamline Frame 90N10.

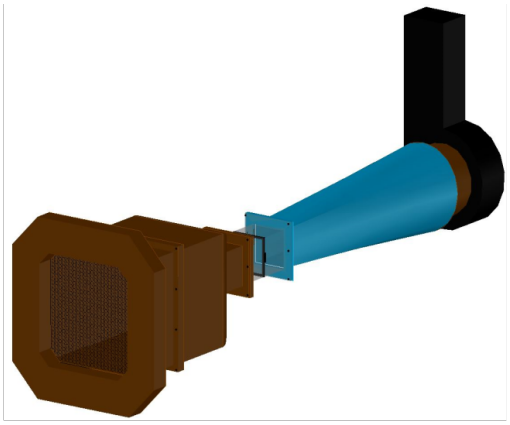

(a) Wind Tunnel Schematic

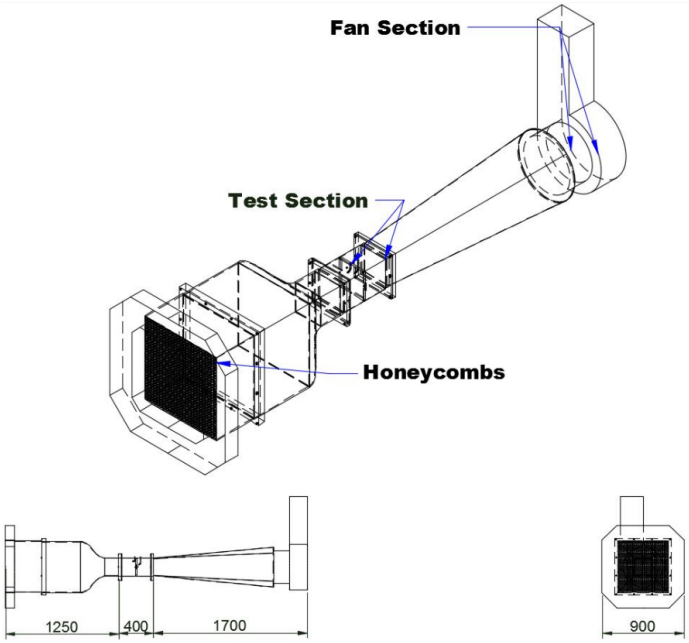

(b) Transparent Tunnel View

Figure 5.3: Wind Tunnel Schematic (Dimensions in mm)

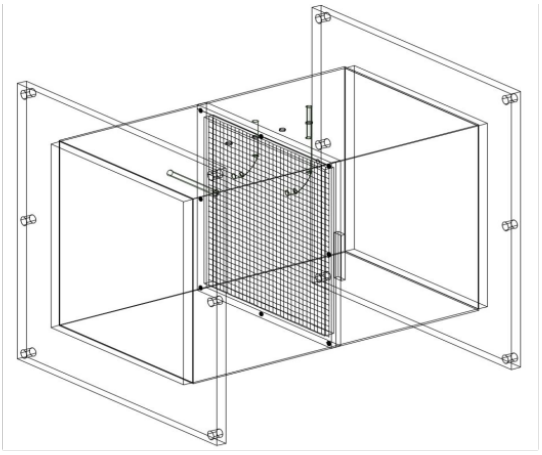

(a) Test Section (3D View)

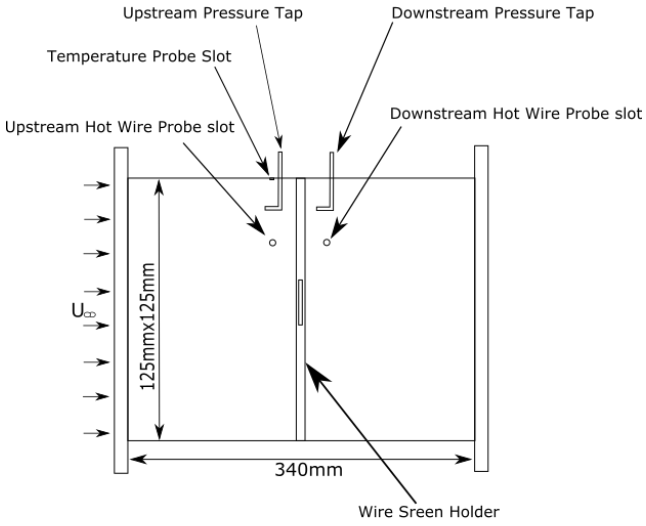

(b) Test Section (2D view)

Figure 5.4: Wind Tunnel Test Section View

5.4.2 Loss Coefficient Test Procedure

The major aim of the loss coefficient test conducted herein was to extract flow loss measurements for wire screens, and in so doing, compare the results with empirically predicted results, particularly when these results are further imposed within a virtual wire screen zone of a computational fluid dynamics (CFD) domain. This would enable a better insight as to the performance of wire screens when modeled as per the approach proposed above. In terms of flow resistance, the first effect of a wire screen will be to impose a differential pressure drop proportional to the square of the flow velocity, also refracting the impinging incident flow toward the local normal to the screen [160]. Therefore,

in order to measure accurate static pressure drops, pressure taps were located along the length of the test section, at upstream and downstream locations. The boundary layer effect of the test section walls were found to be about 18% of its height, hence all measurements were taken within the potential core of the tunnel test section. Pressure drop measurements were recorded via rubber tubing connection from the pressure taps to a digital micro-manometer (Finness Controls Limited, FC0510), which measures average pressure differential across a time period. Tubes from upstream and downstream pressure taps were fed into the positive and negative terminals of this device, and the pressure differential across the wire screen for varying wind tunnel fan flow speeds were recorded. The wire screen samples are mounted at the desired test location by means of a wire screen holder frame which rigidly holds the screen in place, as shown in Figure 5.4. For the purpose of this analysis, effect of the holding frame on the open area ratio of the wire screens were neglected.

Dantec Dynamics miniature hot wire probes were utilized (55P15 configuration) during this test campaign. The hot wire probes were carefully calibrated before usage within the wind tunnel test section. Readings were fed through the National Instruments data acquisition device, PXI 1002 and processed using the Streamware software. A LabView program was used to control the fan flow speed, by controlling it's voltage output, which had a range of 0-9 Volts, and was also used for data collection. Data were recorded for a sample size of 500,000 and a sampling rate of 100 kHz. Hot wire probe readings, as well as pressure drop readings were recorded at positions 40 mm, 50 mm, 60 mm, 70 mm and 80 mm from test section walls in order to avoid boundary layer effects on measurements.

The physical characteristics of wire screen samples tested are shown in Table 5.1. Square weave wire screens and a twill weave screen are tested with the aim of correlations for flow loss coefficient.

Wire Screen Samples Tested					
Sample	M(mm)	D(mm)	$\beta(\%)$	Wire Count	Weave Type
1	0.178	0.14	31.3	80×80	Twill Weave
2	0.318	0.19	39.2	50×50	Square Weave
3	0.939	0.331	54.7	20×20	Square Weave
4	0.746	0.1	77.8	30×30	Square Weave

Table 5.1: Physical Characteristics of Wire Screen Samples Tested

5.5 Loss Coefficient Results

To obtain results for flow loss coefficients (K) of wire samples, a linear regression fitting of data points was achieved by correlating pressure drop (ΔP) measurements with dynamic pressure measurements ($0.5\rho U_\infty^2$). The data regression lines and computed loss coefficients for all tested wire screen samples are shown in Figure 5.5. The correlated values of loss coefficients K, and the fitted data R^2 are clearly shown within the Figure 5.5.

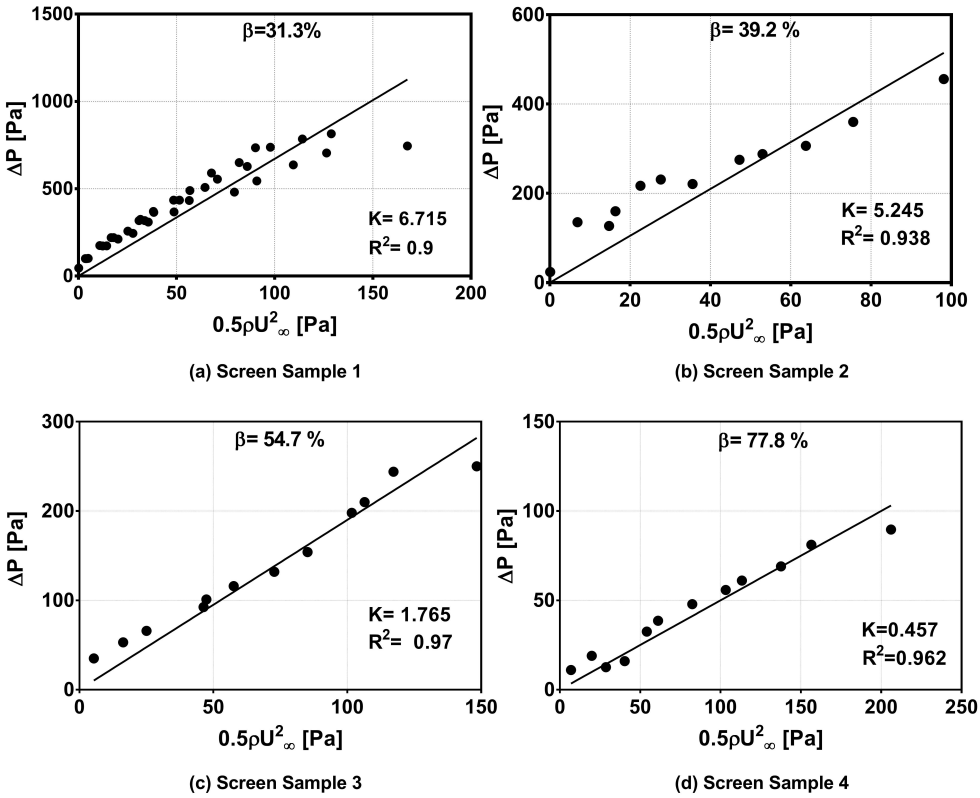

Figure 5.5: Measured Loss Coefficient for Wire Screen Samples Tested

A comparison between the measured loss coefficient values and predicted values obtained when using the Idelchik [18] semi-empirical model for wire screens is carried out and presented in Figure 5.6. It can be observed that fairly good agreement exists between measured loss coefficients and Idelchik's relationship for the range of screens tested. The measured values roughly followed the empirical model. Previous measurements of wire samples carried out by Oerlemans [19] showed that this empirical relation was agreeable as $\beta > 0.4\%$, and less agreeable as $\beta < 0.4\%$,. A possible reason for the discrepancies within some porosity range could be the assumed values of wire screen dependent constant K_{mesh}, where a value of $K_{mesh} = 1$ had been recommended for use for new wire screens.

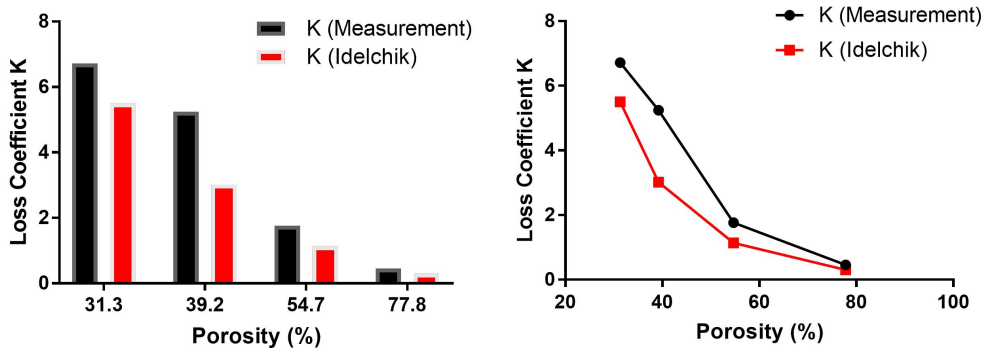

Figure 5.6: Comparison of Measured and Idelchik's prediction model[18] (K vs β)

5.6 Computational Approach

The computational methodology utilized within this study is carried out by implementing the Improved Delayed Detached Eddy Simulation (IDDES) as used by Dahan et al.[105], for a hybrid CFD-FWH coupled technique of computational aeroacoustics analysis of a full scale simplified model landing gear strut as shown in Figure 5.7. This turbulence model has shown to produce good results at modest computational cost when coupled with the Ffowcs Williams-Hawkings (FWH) acoustic analogy for external aeroacoustics noise predictions. The sound generation mechanism and near field of the landing

gear strut can be computed with this turbulence model, while far field receiver acoustic results are computed using the impermeable FWH analogy.[98]

5.6.1 Implementing The Volume Averaged Method (VAM)

The routinely applied two step modeling process for Unsteady CFD analysis is carried out here, where initialization of the unsteady flow field is carried out using a converged steady RANS flow field simulation. The $k-\omega$ shear stress tranport (SST) RANS model is implemented for this task. Care is taken to ensure the average boundary layer y^+ values are less than 1. Velocity field at inlet boundary condition is taken to be uniform, with a value of $U_\infty = 70m/s$ ($Ma \approx 0.2$). Outflow boundary condition is imposed at the outlet, while a no-slip boundary condition is imposed on the floor so as to correspond experimentally to the tunnel floor. Within the computational domain, a zone is adapted for the introduction of correction sinks[196]. The volume averaged macroscopic flow model (VAM), which uses a volume-averaged modified Navier-Stokes equation within the virtual screen porous zone is implemented. The Porous zone is modeled by the addition of a momentum correction terms to the standard Navier-Stokes fluid flow equations. The correction term is composed of two parts, a viscous loss term, and an inertial loss term, as shown in Equation 2.69.

5.6.2 Computational Domain and Grid

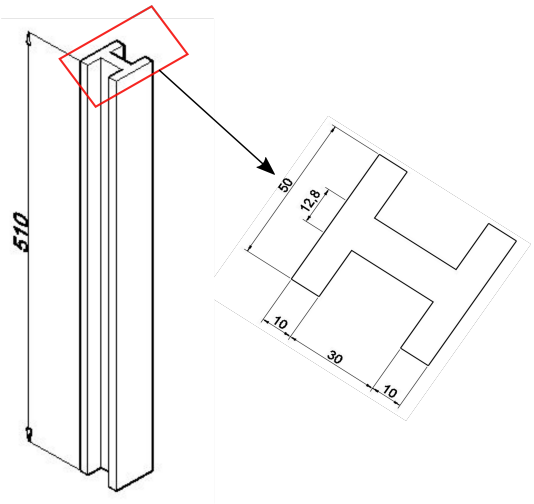

Figure 5.7: H-strut geometry representing a simplified LG strut

Figure 5.7 shows the geometric features of the simplified landing gear strut unit utilized during the test campaign of Oerlemans [80]. This configuration was adopted for numerical simulations carried out within this chapter.

Table 5.2 shows the computational grid levels utilized for this study. Two unstructured grids and a structured grid was utilized in the course of this study, where the grids were tested for suitability. An example of the structured grid C utilized is as shown in Figure 5.8.

Mesh Grid Levels						
Grid	Type	Min Cell Size	$L_x(mm)$	$L_y(mm)$	$L_z(mm)$	Cell Count
A	Unstructured	$0.05L_w$	$18L_w$	$9L_w$	$14L_w$	13.5×10^6
B	Unstructured	$0.04L_w$	$18L_w$	$9L_w$	$14L_w$	18.5×10^6
C	Structured	$0.01L_w$	$16L_w$	$8L_w$	$14L_w$	12.5×10^6

Table 5.2: Computational grid levels utilized for study

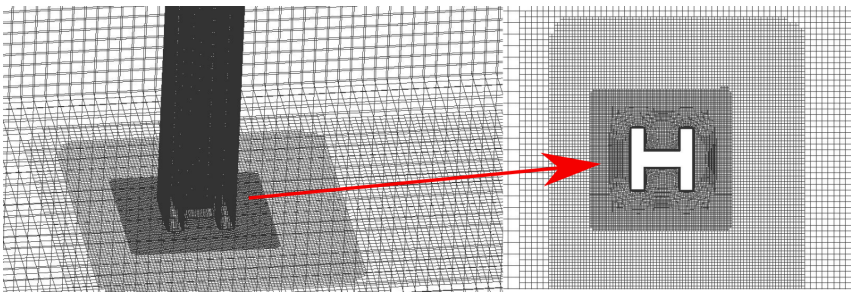

Figure 5.8: Structured grid utilized for H-strut

5.6.3 Acoustic Propagation

The Ffowcs Williams and Hawkings (FW-H) analogy is utilized for far-field noise propagation, with the re-formulated analogy by Farassat[211] as implemented within Ansys FLUENT commercial CFD code. Far-field receivers are defined at locations as shown in Figure 5.9, which is similar to the microphone array location of TIMPAN reported tests [80] used for validation of this study. Fluctuating pressure data from the strut unit is used as input to the FW-H analogy, where the integration region is taken as the impermeable surface coinciding with the strut surface.

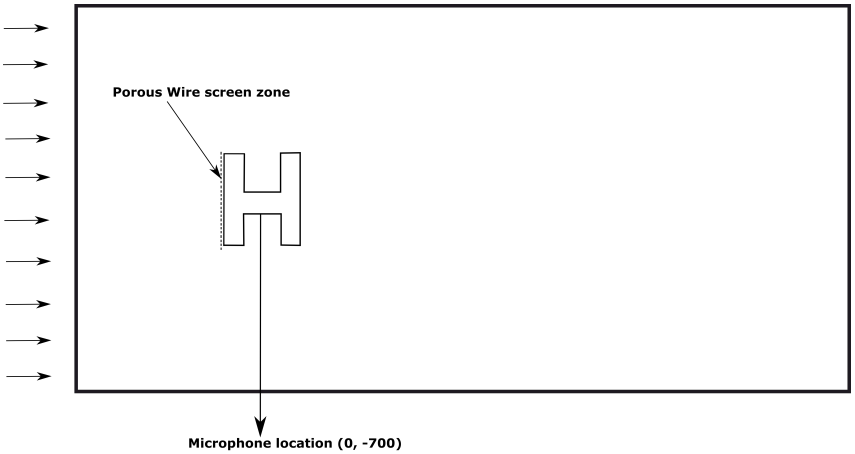

Figure 5.9: Schematic of computational domain showing microphone location

5.7 Computational Results

Computational aeroacoustic results will be presented in the following order;

1. CAA Baseline H-Strut (No Modeling Implemented)

2. CAA-VAM (K Semi-Empirical Model vs Measured K Implementation)

3. CAA-VAM (K Semi-Empirical Model Implemented)

4. CAA-VAM (K Semi-Empirical Model + Turbulence Suppression Implemented)

5.7.1 Baseline Case (No Modeling Implemented)

The Improved-Delayed Detached Eddy Simulation (IDDES) was initialized from Steady $k-\omega$ RANS turbulence model simulations, which were conducted for numerical unstructured grids A, B and structured non-conformal multi block grid C shown in Table 5.2. Comparison of solutions obtained for the three different grid densities was performed and assessment of convergence were carried out for the steady simulations based on evolution of residuals, thereby forming a basis for proceeding with grid C for acoustic propagation analysis.

5.7.1.1 FW-H Results

Acoustic results obtained are compared against documented experimental campaign of Oerlemans [19], where acoustic tests were performed in an anechoic wind tunnel for wire screens intended for landing gear noise reduction applications. Out-of-flow microphone array were utilized so as to localize and quantify noise sources on a H-strut model with geometric features previously shown in Figure 5.7.

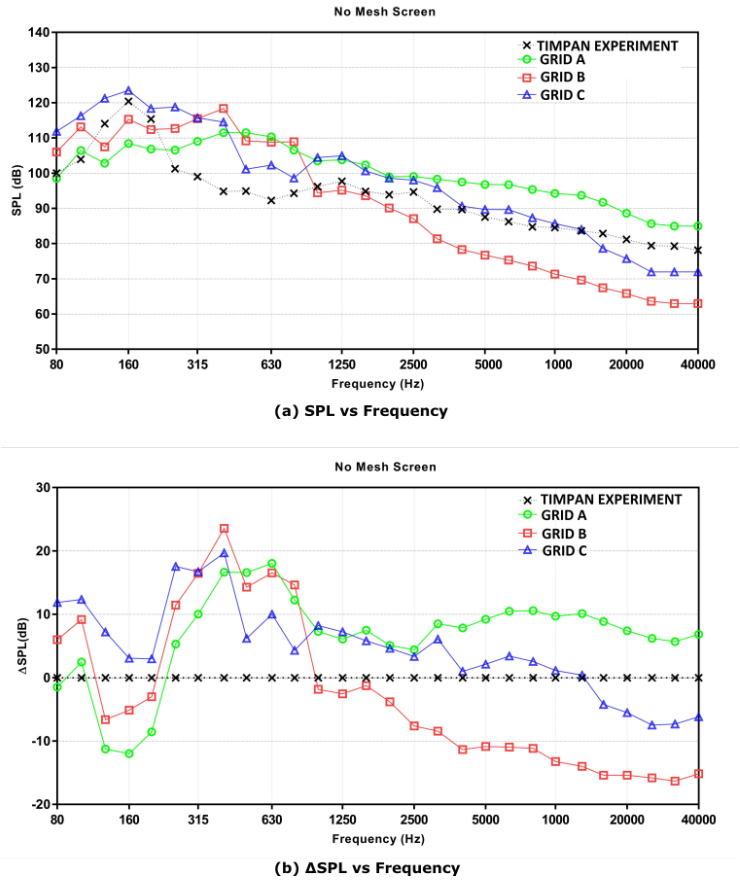

Figure 5.10: Acoustic result for Baseline Single H-Model Strut with No Wire Screen ($Re_{Lw} = 2.5 \times 10^5, \alpha = 0$)

An assessment of the capability of predicting the baseline noise from H-strut model without a porous modeling zone implemented is carried out. Propagating far-field noise from the simplified landing gear H-strut unit using FWH impermeable acoustic analogy produced results which were compared as shown in Figure 5.10. Observation of the comparison between experimental baseline H-model strut noise propagation, and numerical prediction making use of the Volume-Averaged IDDES-FWH technique for three different mesh density levels (Mesh A, Mesh B, and Mesh C), shows that within a low frequency range, good prediction of noise levels were achieved with all three mesh levels, however, a better trend of prediction was achieved with Mesh C. Although being more computationally demanding, it predicts noise levels better when compared to an unstructured grid. This trend was also observed at higher frequencies, which further emphasizes a structured grid's superiority. Comparing

1/3 Octave band results for the baseline H strut, vortex shedding peak's of 111.50 dB, 118.5 dB and 123.52 dB were predicted by Mesh A, B and C respectively, compared to experimental peak of 120.41 dB. Mesh A predicted its peak at 1/3 octave band frequency of 500 Hz, mesh B predicted it's peak at 400 Hz, while mesh C predicted its peak at 1/3 octave band frequency of 160 Hz, which compares with experimental measured vortex shedding peak at a 1/3 octave band frequency of 160 Hz.

The experimental anechoic chamber where Oerlemans [19] tests were carried out had a cut-off frequency of around 500Hz, therefore, they performed some correction effects for all noise results below 500Hz. This could possible explain the deviation and relatively poor comparison of acoustic results from Mesh grid sample A, B and C for frequencies below 500Hz. For frequency range within 500-20000Hz, mesh grid C produced comparisons within ±9 dB of experiments. Hence, subsequent simulations are carried out making use of mesh grid C.

Comparison of Experiment to Numerical Vortex Shedding Peaks		
	Vortex Shedding Peak	Frequency
NLR Experiment	120.41dB	160.0Hz
Grid A	111.50dB	500.0Hz
Grid B	118.54dB	400.0Hz
Grid C	123.52dB	160.5Hz

Table 5.3: Comparison of Experiment to Numerical Vortex Shedding Peaks

5.7.2 Comparing Experimental vs Empirical Pressure drop Implementation

A comparison of implementing Idelchik's empirical model for thin flat screens within a porous zone and loss coefficient values measured within this test campaign is carried out, and is shown in Figure 5.11. Wire screen sample 1 of porosity 31.3% is used for this analysis.

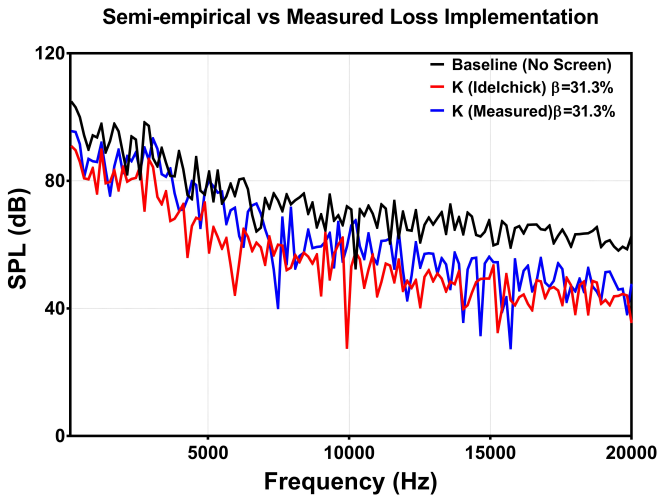

Figure 5.11: Comparing Spectra of Semi-empirical vs Measured Pressure Drop Implementation for $\beta = 31.3\%$

From the result presented, there exists a trend of similarity in predictions between implementations when using Idelchick's model for flow loss coefficient and the measured correlated flow loss coefficient. Idelchik's empirical model predicted greater noise reduction at lower frequencies compared to predictions using the measured values, yet the trend across the acoustic spectrum depicts that for the 31.3% porosity wire screen, one could use either the Idelchik's empirical model or the measured flow loss coefficient in modeling the porous zone within a numerical flow domain. Therefore, for numerical modeling, no gain whatsoever is achieved by carrying out an experimental test in order to obtain pressure loss coefficients of wire mesh screens as against making use of empirical models. Hence, subsequent pressure drop characteristics within porous zones will be implemented using the Idelchick's model for flow loss coefficient.

5.7.3 CFD-VAM (Pressure Drop) Implemented

Pressure drop is implemented by making use of sink correction terms for resistance drop as discussed previously and the empirical flow loss resistance of Idelchik [18] for which flow loss resistance becomes independent of flow Reynolds number for $Re_d \geq 400$.

5.7.3.1 FW-H Results

Acoustic results are compared against experimental results of Oerlemans [19] as shown in Figure 5.12

Comparisons carried out in Figure 5.12 is for an experimental geometric linear wire screen against a linear virtual porous wire screen as implemented within the numerical domain. For the CFD-VAM (Pressure Drop) modeling approach, a substantial drop in sound pressure levels is observed, with a strong over-prediction of noise reduction within the low to mid frequency range, and relatively no noise reduction at higher frequency. A comparison of the noise reduction achieved experimentally to the equivalent reduction achieved numerically is presented in Figure 5.13

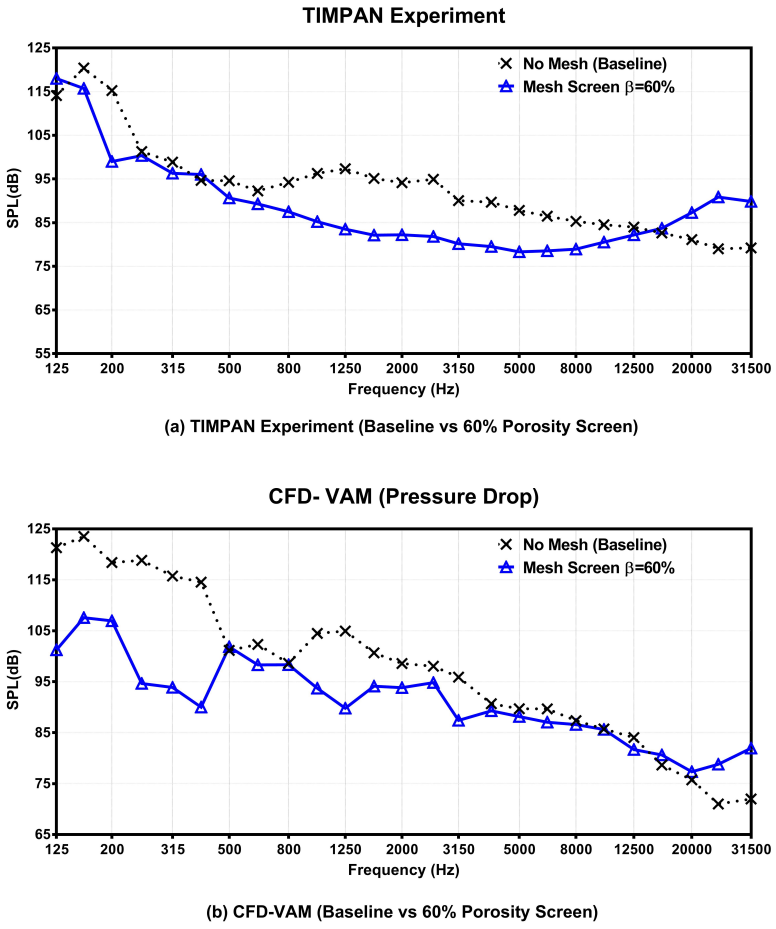

Figure 5.12: Implementing Mesh Screen: (a)Experiment [19] (b) CFD-VAM (Pressure Drop) (SPL vs 1/3 Octave Band) $(70m/s, \alpha = 0)$

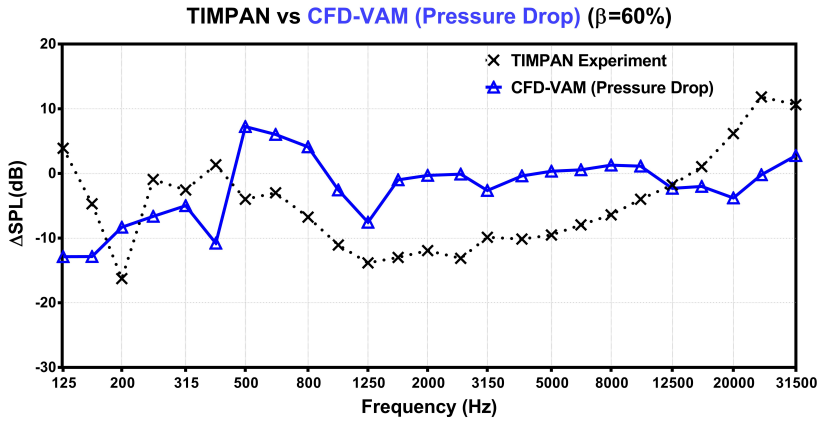

Figure 5.13: Noise reduction from experiment [19] compared with CFD-VAM (Pressure Drop) (ΔSPL vs 1/3 Octave Band) ($70m/s, \alpha = 0$)

From observations, the CFD-VAM (Pressure drop) over-predicts a reduction in noise between 125Hz and 500Hz, with best case comparisons to experiment of 3dB and under-predicts reductions between 500Hz and 12500Hz with best case comparison to experiment of 12dB, while beyond 12500Hz it does not account for the strong tonal effects of the self noise of wire screens.

5.7.4 CFD-VAM (Pressure Drop + Turbulence Alteration) Implemented

In addition to the pressure drop, a turbulence alteration effect is implemented in the form of a turbulence suppression effect as discussed earlier. This turbulence suppression effect is modeled as a sink term for the turbulent kinetic energy within the porous zone of interest. The Dryden and Schubauer [161] correlation is hereby utilized as sink terms for turbulence intensities at the virtual zone of interest. It is worth pointing out again that the experimental campaign of NACA [176] particularly showed good agreement for axial turbulence reduction factors using the Dryden and Schubauer [161] correlation for comparison between experiments and correlation of screen samples. Therefore, to numerically model for turbulence alteration or suppression effects, the Dryden and Schubauer [161] correlation is imposed as a sink term for turbulence intensities by implementing a sink effect for turbulent kinetic energy within the porous zone of interest. Therefore, two different sink terms are utilized, a

porous pressure drop sink term and a sink term for turbulence kinetic energy as a result of turbulence intensity reduction.

5.7.4.1 FW-H Results

Acoustic result obtained using this technique is as shown in Figure 5.14. An immediate observation shows that the introduction of a turbulence suppression effect together with a pressure drop effect produces a positive influence on the noise reduction capabilities of a virtual wire screen, as can be seen when Figure 5.13 is compared with Figure 5.14. Within the 1/3 Octave band as shown in Figure 5.14(b), the CFD-VAM (Pressure Drop + Turbulence suppression) noise reduction effects agreed to within a best case of 1dB of experimental results for frequencies in the range of 125Hz to 500Hz, and agreed to a best case scenario of 7dB for frequencies between 500Hz to 12500Hz. Below 500Hz, deviations of up to 10dB to experimental values are observed. This can be linked similarly with the previous cases to the cut-off frequency effect of the experimental chamber utilized for the noise tests carried out by Oerlemans [19]. Similar to the case where only pressure drop effects were implemented, an observation is made that at frequencies above 12500Hz the added noise increase which is attributed to the self noise of wire screens is not detected by the CFD-VAM approach when both pressure drop and turbulence suppression are implemented. This self noise giving rise to an increased noise at high frequencies could not be captured by the implementation of both a pressure drop effect and a turbulence suppression term.

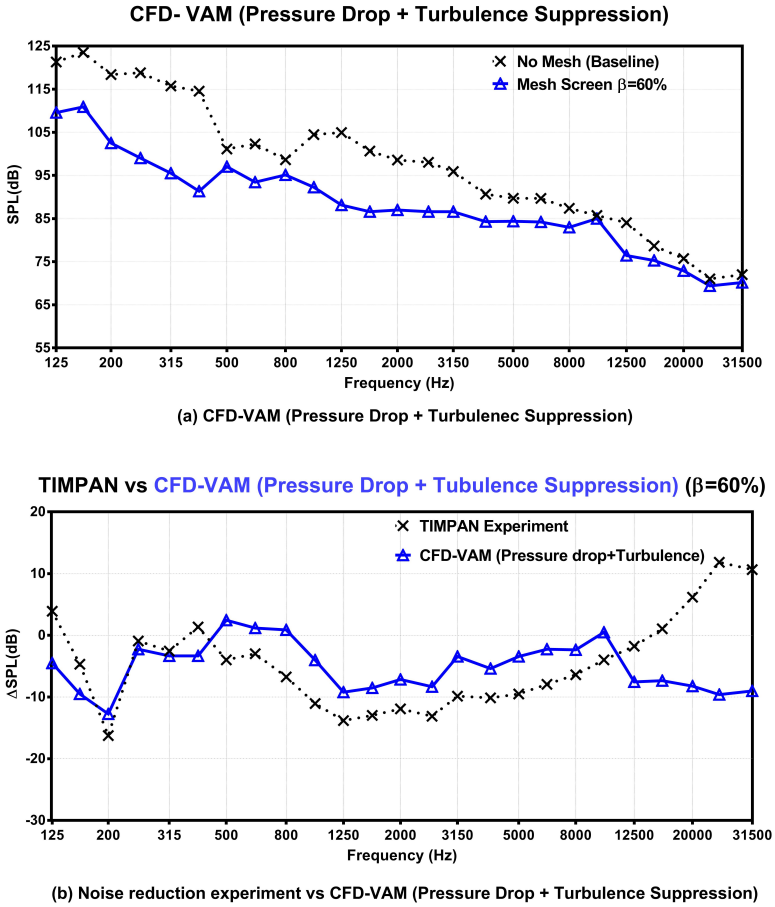

Figure 5.14: Effect of Implementing Pressure Drop and Turbulence Alteration Characteristics (Δ SPL vs 1/3 Octave Band) ($70m/s, \alpha = 0$)

5.8 Summary

Within this chapter, numerical investigations of wire screens modeling for aerodynamic noise reduction studies are carried out, where the aim was to substantially and adequately model a physical wire screen within a numerical flow domain by implementing a virtual porous zone modeling approach. The following are summary of findings from this chapter;

1. The IDDES-FWH coupling approach was utilized to model noise predictions from a simplified landing gear H-strut unit. Baseline noise predictions are compared with experimental data, where comparisons show poor predictions at frequencies below 500Hz, which is due to the exper-

imental facility cut-off frequency correction effect carried out during the test campaign results used for validation.

2. Pressure drop characteristics implementation is also carried out within the porous zone. Correlated values of flow loss coefficient were determined from flow loss tests carried out, and implemented within a numerical porous zone in comparison with the popular Idelchick's empirical model.

3. The numerical modeled porous zone should account for pressure drop effects, velocity reduction effects, and turbulence suppression effects, which when implemented as a porous adapted layer within a numerical domain promotes noise reduction when a coupled CFD-FWH approach of noise prediction from bluff bodies is used.

4. A dual numerical sink term comprising pressure drop characteristics and turbulence alteration characteristics was further implemented within the numerical domain, and acoustic results obtained showed improved comparison with experimental results.

5. Comparisons for frequencies within the range of 500Hz to 12500Hz compared favorably to experiments, however, for frequencies above 12500Hz, numerical acoustic results could not match experimental results. This is well explained due to the fact that at such high frequencies, the self noise effects of wire screens are predominant and must be taken into account for a more elaborate noise reduction modeling approach.

Chapter 6

Landing Gear Noise Reduction Modeling

6.1 Aim and Background

Landing gear noise reduction is a primary concern because it is a major contributor to the overall noise emission of aircraft airframes, as pointed out in the literature review of chapter 2.

Within the framework of the ALLEGRA project coordinated by Trinity College Dublin, wind tunnel tests were carried out in Pininfarina wind tunnel, Turin, Italy, on landing gear models. This coordinated test were carried out for main (MLG) and nose (NLG) landing gear models. Within the test campaign, various low noise treatments were tested for the landing gears noise reduction, and the application of woven wire mesh screen on the MLG was one of these low noise treatments. Acoustic noise reductions of up to 5dB centered at 4000 Hz 1/3 octave band were achieved with the implementation of the woven wire mesh screen as a low noise treatment for the MLG [20].

The aims of the research carried out and reported within this chapter are as follows;

1. To perform CFD-Acoustic analogy coupled computational studies for a bluff body geometry different from that utilized in chapter 5, in order to test the noise reduction modeling approach proposed therein.

2. Chapter 5 applied this modeling approach to a simplified landing gear strut, represented by a H-strut unit, and it is the intention of this current chapter to apply this technique to a more advanced and realistic representation of an aircraft main landing gear (MLG).

3. This chapter aims to show that implementation of the modeling approach for woven wire mesh screens proposed in chapter 5 presents a viable alternative to more expensive means of fully resolving the effect of wire screens upstream or wrapped around landing gear models within a CFD flow domain.

Within this current chapter, the effect of woven wire screens pressure drop (loss coefficient effect) and turbulence suppression effect are implemented in an

adapted porous zone within the fluid domain upstream of the landing gear geometry. For the purpose of this research, the effect of sound radiation through the modeled screen will not be investigated.

The complex nature of landing gears makes it difficult and highly computationally demanding to simulate a physical woven wire mesh screen upstream or wrapped around the complicated geometry of landing gears, hence the proposed modeling approach provides a less computational expensive means of testing the effect of woven wire screens upstream a landing gear geometry.

The pressure drop effect ΔP_e of a wire screen is modeled by using the Volume Averaged Method (VAM), with the loss coefficient relation of Idelchik [18] implemented within a re-written Navier-Stokes equation. The turbulence suppression effect T_e of wire screens is also modeled within the porous zone using the VAM approach and implementing the woven wire screen turbulence suppression relation of Dryden and Schbauer [161] as a sink term for turbulence quantities.

Figure 6.1: Pininfarina wind tunnel, showing top and side microphone arrays [20]

6.2 ALLEGRA Test Set-up

The ALLEGRA project conducted coordinated experimental acoustics tests on a MLG and NLG model installed at the Pininfarina wind tunnel. The Pininfarina wind tunnel is a aeroacoustic facility comprising of an open jet

set-up of a semi-cylindrical tunnel as shown in Figure 6.1, located in Turin, Italy. Dimensions of the test section are $8.0m \times 9.6m \times 4.2m$. Wind speeds of up to 260 km/h are achievable within the tunnel, and helps to reduce background noise level to within 68 dBA at 100 Km/h [20]. Flow speeds within the tunnel are approximately uniform, and turbulence levels are within 0.3% to 8%.

Microphone arrays installed within the tunnel facility include a top array, side array, linear far-field array and front arrays.

6.2.1 MLG Model Dimensions

Figure 6.2 presents the MLG model installed within the Pininfarina wind tunnel, while Figure 6.3 shows the MLG model dimensions.

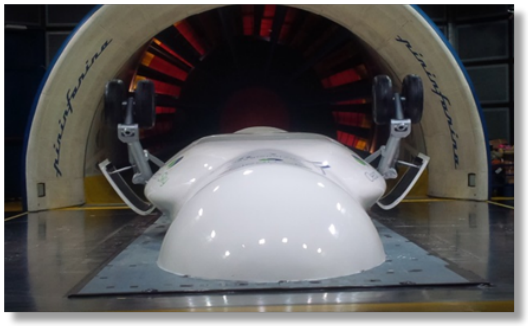

Figure 6.2: MLG Test Model Installed in Pininfarina Tunnel [20]

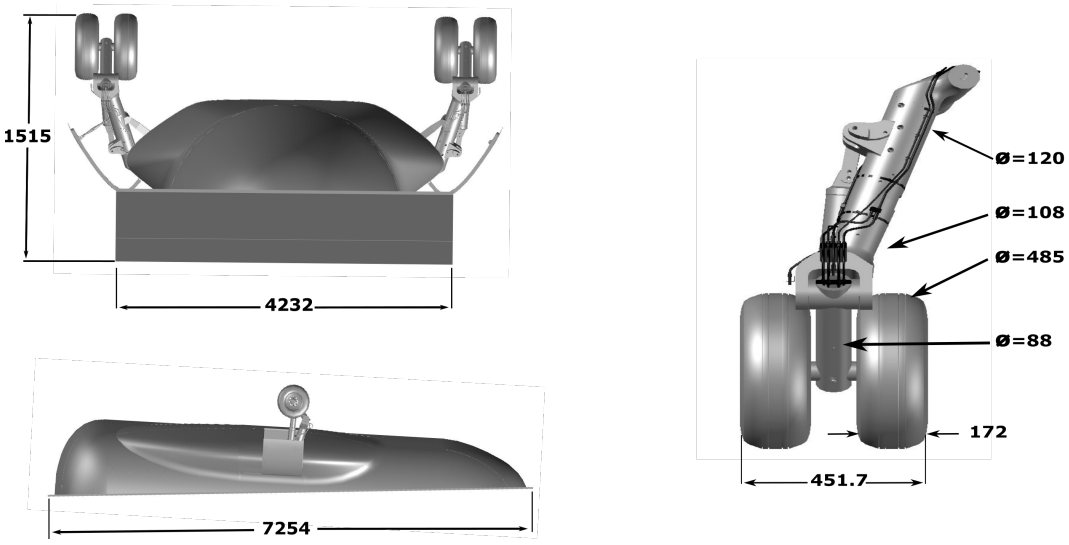

Figure 6.3: MLG Test Model Dimensions (mm)

6.3 Geometry Modification

In order to carryout successful CFD simulations, a quality grid generation and minimized numerical diffusions are dependent on the number of detailed non-streamlined intricacies of the MLG geometry that is utilized within the computational grid. Therefore, the MLG CAD geometry received from the MLG model designers had to be cleaned up and some modifications carried out in order to simplify the CFD simulation process, whilst still keeping the most important geometry details of the gear systems. Modified geometry of the MLG model utilized for the CFD-CAA analysis carried out within this study of wire screen noise modeling implementation is presented in the following subsection.

6.3.1 MLG Geometry Modification

The original and modified MLG geometry is as shown in Figure 6.4. The dressings were deemed unnecessary for the CFD analysis. All tiny holes, including bolts and nuts were closed or removed. A closer look at the remodeled wheels are presented in Figure 6.5, where the wheels section meant for brakes inclusion is completely closed.

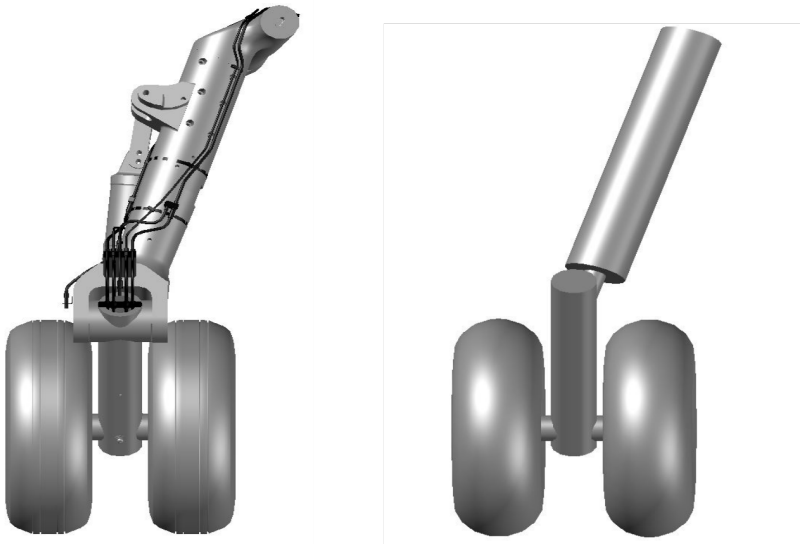

(a) Original MLG **(b) Remodeled MLG**

Figure 6.4: Remodeled MLG (front view)

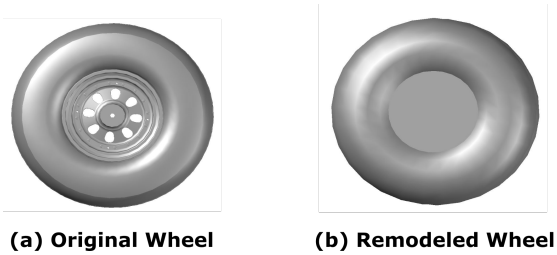

Figure 6.5: Remodeled MLG Wheels (side view)

6.4 Computational Domain

The nomenclature showed in Table 6.1 is utilized for simulation cases carried out within this chapter.

MLG-1	MLG configuration (No Treatment)
MLG-2	MLG configuration (Mesh Treatment)

Table 6.1: MLG Nomenclature Utilized

The computational domain utilized for this analysis is as shown in Figure 6.6, with domain dimensions presented in Table 6.2, where D_w represents MLG wheel diameter, L_x the x-direction domain extent, L_y the y-direction domain extent, and L_z the z-direction domain extent.

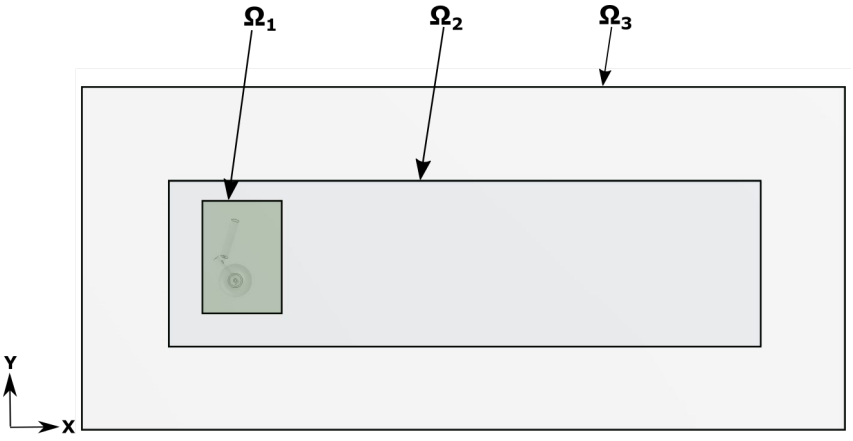

Figure 6.6: MLG Computational Domain

The unsteady IDDES used for this simulations utilizes a criteria for switching between LES and URANS solver. If the grid size within a zone of interest is lesser than $0.05D_w$, the solver switches to an LES, but for cell sizes greater

Domain	L_x	L_y	L_z	Max cell size (m)	Zone
Ω_1	$2.5D_w$	$4D_w$	$2.3D_w$	0.02	LES zone
Ω_2	$18.5D_w$	$5D_w$	$5D_w$	0.10	LES/URANS zone
Ω_3	$23D_w$	$8D_w$	$8D_w$	0.17	URANS zone

Table 6.2: MLG Domain Dimensions and Features

than this value, a URANS approach is utilized. The benefit of the IDDES also means that while an LES is solved within the LES zone of interest, the LES simulations carried out at the near wall region is delayed, and solved as a URANS instead, therefore saving computational time in the process.

For both cases of MLG-1 and MLG-2 computational analysis, unstructured grids were utilized, with a maximum cell grid count of 4.5 million cells utilized. For boundary conditions used, the inlet was a uniform inlet flow velocity with turbulence intensities of 2%. Inlet velocity of $40m/s$ was utilized to match the flow speeds used within the ALLEGRA test campaign. Pressure outlet conditions were utilized for the computational domain exit, while symmetry conditions were utilized for domain side walls, as these walls were placed sufficiently far away from the MLG geometry so as not to affect the flow results.

6.5 MLG-1 Steady Results

MLG-1 results from the steady flow simulations carried out by utilizing the $k-\omega$ turbulence model are presented within this section. Results for MLG-1 wall Y+ values, velocity field contours, surface pressures and wall shear stress values are presented.

6.5.1 MLG-1 Wall y+

The acceptable range of average y+ values across a CFD model for the Fluent code utilized within this study was a value of less than one, so as to limit excessive wall functions utilization within the RANS model, which for this particular case would subsequently have an effect on the improved delayed detached eddy simulation (IDDES) results. Therefore, in order to limit the

use of wall functions within the RANS model, average y+ values across the MLG-1 model was kept below one. Figure 6.7 presents y+ values across the MLG-1 model configuration. Maximum wall y+ on MLG-1 is 1.1.

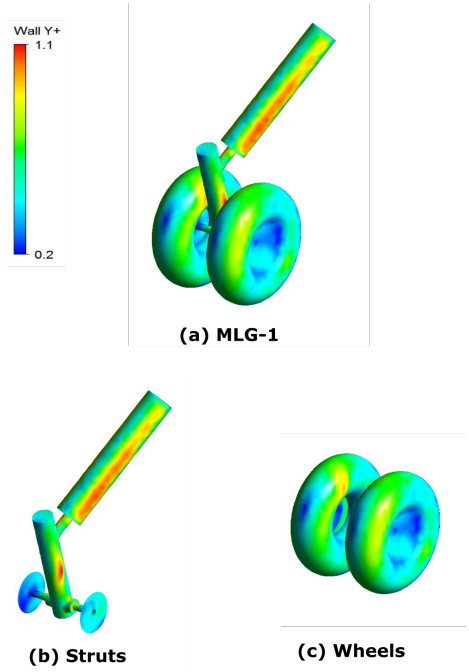

Figure 6.7: MLG-1 Wall y+

6.5.2 MLG-1 Velocity Field

For presentation of flow speeds, field contours are extracted at four different planes as identified in Table 6.3.

Plane 1	y=-0.2044 m
Plane 2	y=0 m
Plane 3	y=0.2525 m
Plane 4	y=0.8132 m

Table 6.3: Plane locations (y=0 at center of wheel)

Steady flow field contours of velocity flow past the MLG-1 configuration is as presented in Figure 6.8 and steady field Q-criterion in Figure 6.9 . Results presented here are for a uniform inlet velocity value of $U_\infty = 40m/s$. For plane 1, maximum flow speed results from flow deflection at the wheels, and this maximum values are well within the wheel geometry.

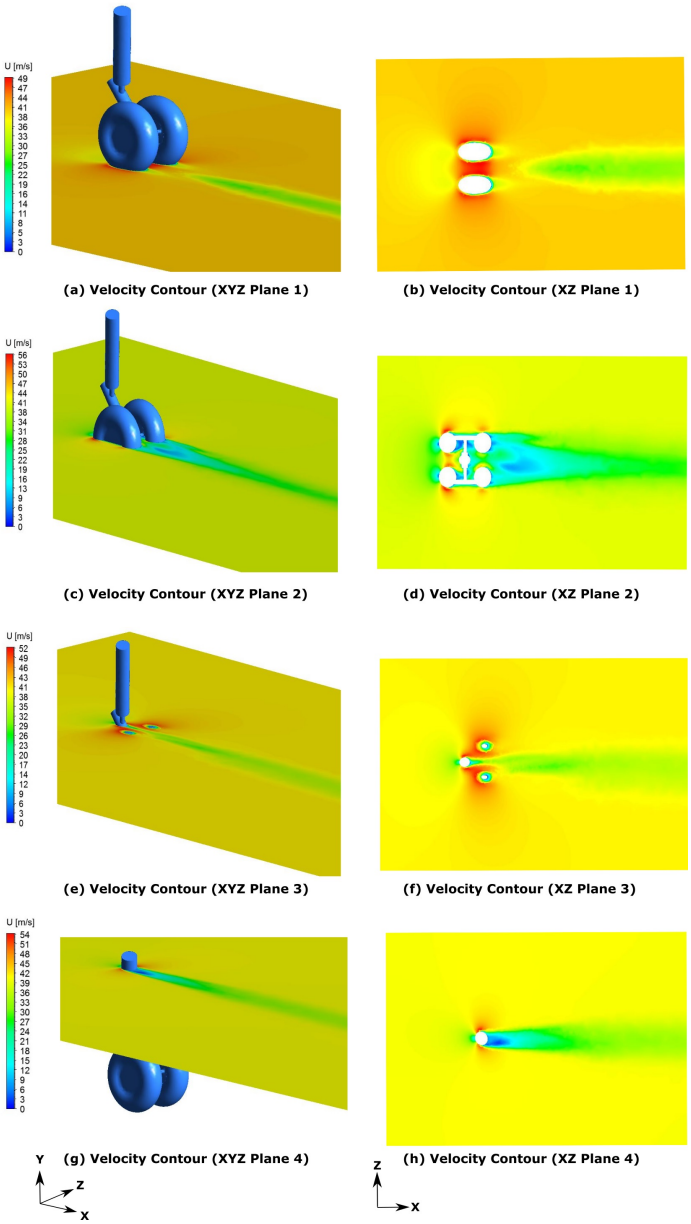

Figure 6.8: MLG-1 steady state velocity field contours, $U_\infty = 40m/s$, 0° Yaw

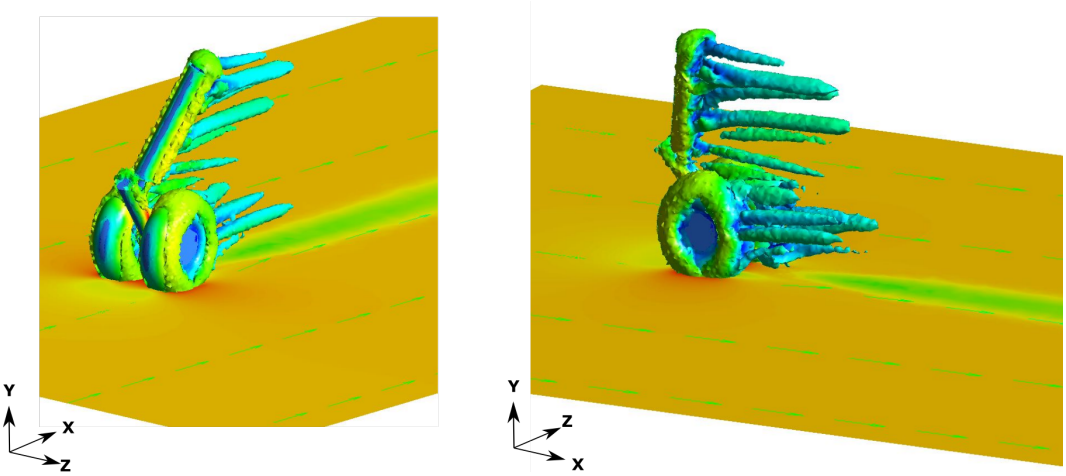

Figure 6.9: MLG-1 steady field Q-criterion colored by velocity magnitude

6.5.3 MLG-1 Surface Pressure

The nature and value of surface pressures on the MLG-1 model is as presented in Figure 6.10. Surface pressure across the entire MLG-1 as well as values across strut components and wheels are highlighted. Maximum values of surface pressures are observable on the frontal area section of the strut. Surface pressure values on frontal section of wheels are also high, with lower values at the wheel sides, and much minimum values at the aft side of the wheels.

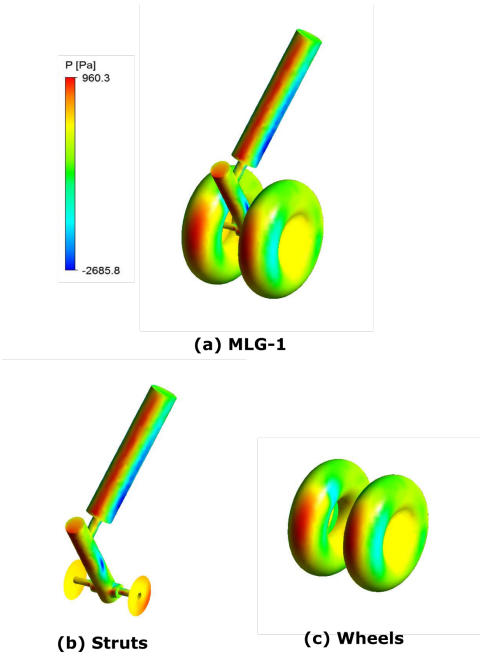

Figure 6.10: MLG-1 Surface Pressures

6.5.4 MLG-1 Wall Shear Stress

The distribution of wall surface pressures on the MLG-1 model is as presented in Figure 6.11. Unlike for the case of surface pressures, where maximum values of surface pressures existed in the frontal area sections of the struts and wheel components, the wall shear stress distribution shows a different trend. Maximum values of wall shear stress are located at the sides of the strut components. The shear stress values on the strut units are higher than values at the wheel component.

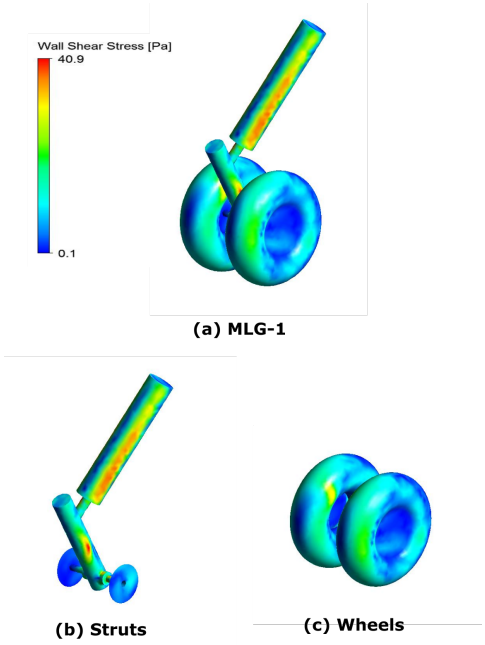

Figure 6.11: MLG-1 Wall Shear Stress Magnitude

6.6 MLG-2 Steady Results

MLG-2 results from the steady flow simulations carried out by utilizing the $k-\omega$ turbulence model when the numerical wire screen porous zone is implemented, are presented within this section. Results for MLG-2 wall Y+ values, velocity field contours, surface pressures and wall shear stress values are presented.

It is worth noting at this point that the woven wire mesh screen utilized had a porosity of 65%, as this was chosen to match wire screen porosity utilized

during the ALLEGRA test campaign. For the CFD-VAM modeling approach carried out here, the wire screen porous zone was located 10mm upstream of the MLG-2 wheels outer diameter. The wire screen porous zone stream wise thickness was 2mm, and its y and z dimensions were chosen so as to extend beyond the MLG-2 wheels and strut by $1/4D_w$.

6.6.1 Wall Y+

Wall y+ distribution across MLG-2 is as presented in Figure 6.12. A quick observation on the effect of flow speeds reduction as a result of the upstream porous layer where a virtual woven wire mesh screen was introduced is noticed, where the maximum y+ value across MLG-2 is 0.7, compared to MLG-1 where maximum y+ values of 1.1 were obtained.

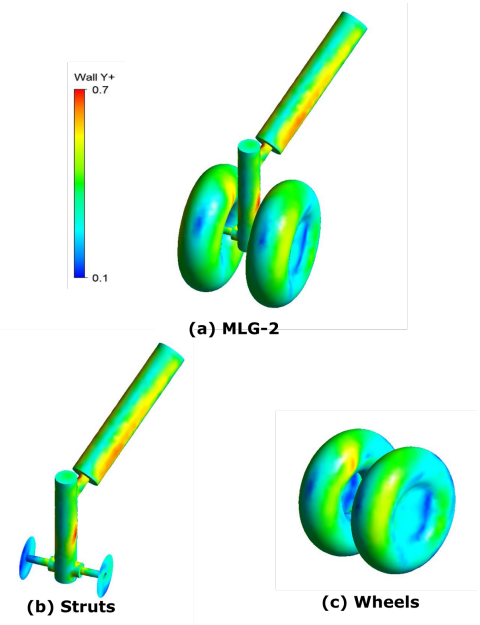

Figure 6.12: MLG-2 Wall y+

6.6.2 MLG-2 Velocity Field

Similar to the presentation of MLG-1, contours are extracted at four different planes as previously identified in Table 6.3.

Field contours of velocity flow past MLG-2 configuration is as presented in Figure 6.13 and field Q-criterion in Figure 6.14. Results presented here are for

a similar uniform inlet velocity value of $U_\infty = 40m/s$ of MLG-1.

The woven wire screen porous zone is highlighted just upstream of MLG-2, and the effect of this screen on the flow field around MLG-2 is immediately noticed when compared to MLG-1. For plane 1, the flow speeds deflection as a result of the wire screen causes a shift in the maximum flow speeds from the MLG-2 proximity to the edges of the screen, thereby resulting in reduced flow speeds impinging on MLG-2. Similar effects are observable on planes 2 to 4.

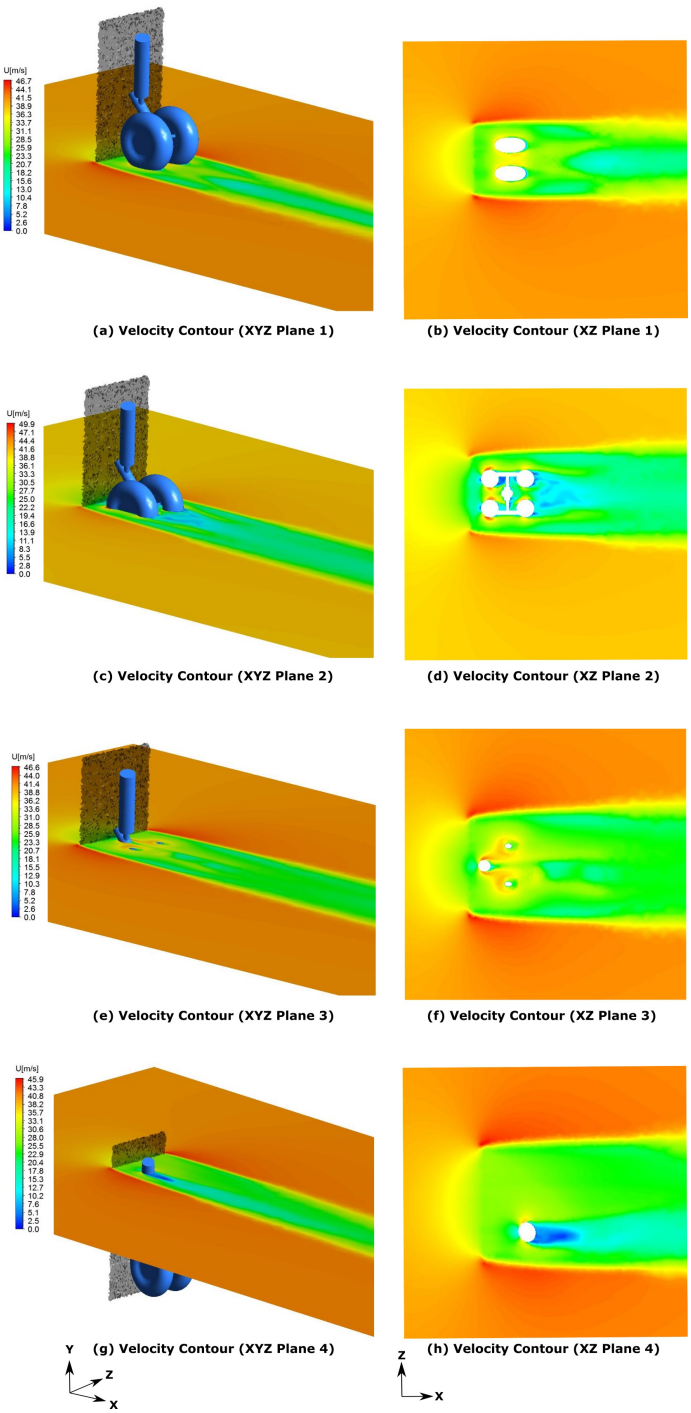

Figure 6.13: MLG-2 steady state velocity field contours. $U_\infty = 40m/s$, 0° Yaw

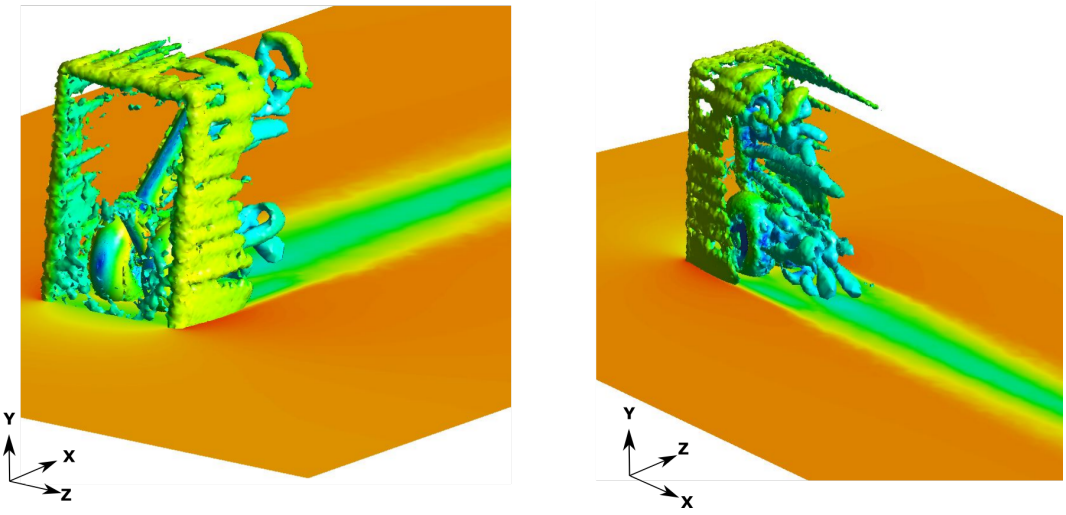

Figure 6.14: MLG-2 Q-criterion colored by velocity magnitude

6.6.3 MLG-2 Surface Pressure

Results of surface pressure across MLG-2 is presented in Figure 6.15. An observation of surface pressure reductions on MLG-2 compared to MLG-1 is made, where maximum surface forces on MLG-2 are reduced by roughly 4% compared to MLG-1.

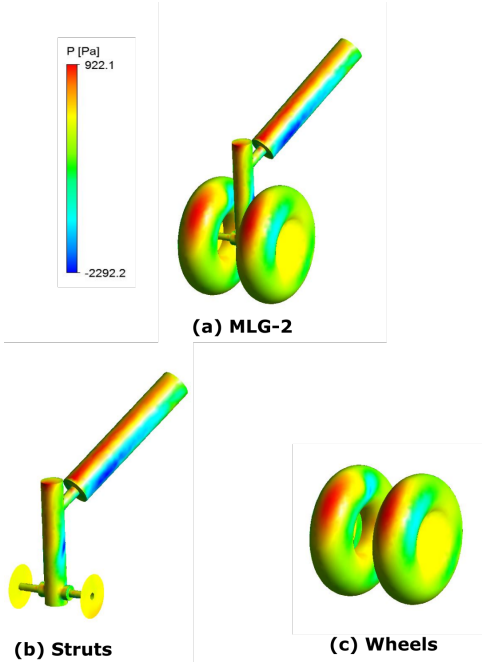

Figure 6.15: MLG-2 Surface Pressures

6.6.4 MLG-2 Wall Shear Stress

Walls shear distribution across MLG-2 is presented in Figure 6.16. Compared to MLG-1, a reduction in shear forces are observable in MLG-2, with maximum shear forces acting on MLG-2 reduced by roughly 58%.

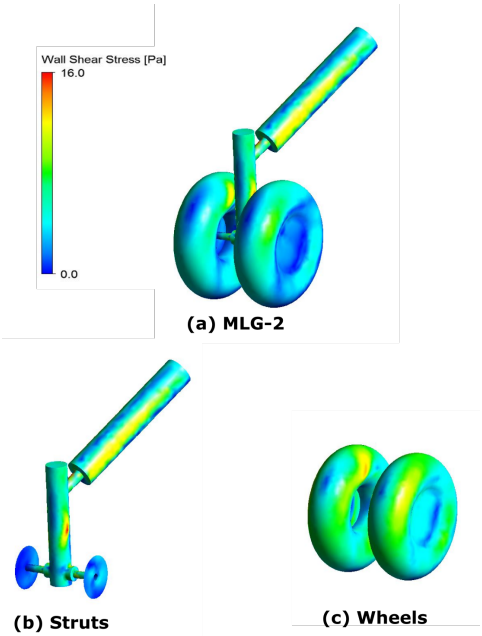

Figure 6.16: MLG-2 Wall Shear Stress Magnitude

6.7 Unsteady IDDES Result

MLG-1 and MLG2 results from the unsteady flow analysis using the IDDES approach are presented within this section. Unsteady results obtained from the IDDES CFD analysis will be analyzed by presenting unsteady plots of vortex core regions.

6.7.1 Unsteady Velocity Field

The IDDES utilized a $k-\omega$ URANS model at the MLG near-wall so as to save computational cost. A time step of 3.2×10^{-6} was sufficient enough to ensure domain average CFL number of less than one was maintained throughout the unsteady simulation process. Also, based on characteristic length of the main

strut diameter, this time step value was more than sufficient to ensure that based on Strouhal number of cylindrical strut, i.e, 0.2, the unsteady field time to complete one full cycle (Period) was covered by over 200 time steps within each period. Unsteady results of vortex core region for Q-criterion colored by U_x magnitude after 1.05 secs is as shown Figure 6.17.

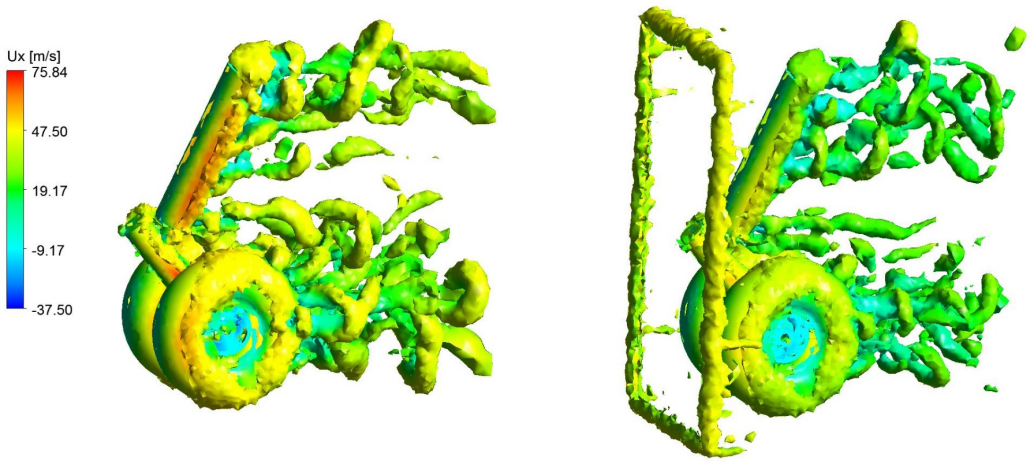

(a) MLG-1 **(b) MLG-2**

Figure 6.17: MLG-1 and MLG-2: Q-Criterion vortex core region colored by U_x

From this result the effect of wire screen implementation is noticed, as the impinging flow speeds on MLG-2 wheels are much lower than the impinging speeds on MLG-1. Also, a look at the upper and lower strut components also show flow speeds reduction of impinging flows. Therefore, as expected, the woven wire screens modeling implementation produced a flow speed reduction on the downstream MLG-2 geometry, and because aerodynamic noise scales with flow speeds to within the sixth power from landing gear components, we therefore expect noise reduction as a result of the wire screen modeled implementation.

6.7.2 Unsteady Turbulent Kinetic Energy

To present the turbulent kinetic energy changes within the MLG geometry as a result of wire screen implementation, Unsteady results of vortex core region for Q-criterion colored by turbulent kinetic energy values after 1.05

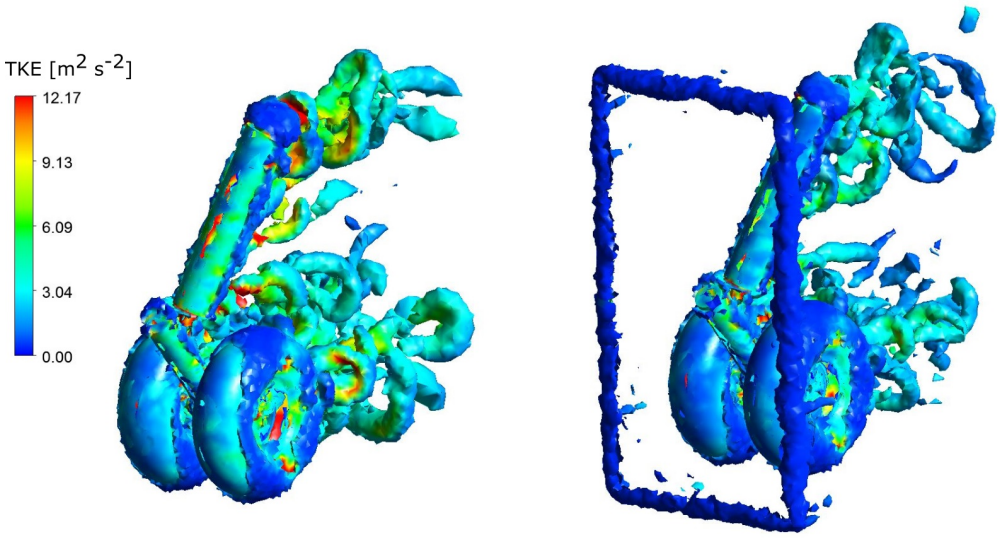

(a) MLG-1 **(b) MLG-2**

Figure 6.18: MLG-1 and MLG-2: Q-Criterion vortex core region colored by TKE

secs is presented in Figure 6.18. From the plot, we observe that the turbulent kinetic energy of flows impinging on and within the MLG-2 near-field region are substantially reduced compared to the impinging flows turbulent kinetic energy on MLG-1. This turbulent kinetic energy reduction is not only as a result of flow speeds reduction, but also as a result of the turbulence suppression sink term which was implemented at the porous zone mimicking or representing the woven wire screen.

6.8 MLG FW-H Results

Presentation of acoustic results obtained during the MLG wire screen modeling approach is carried out within this section. For all acoustic cases presented within this section, the numerical FW-H microphone receiver location corresponds to a specific microphone position within the ALLEGRA linear far-field array, viz. 90◦ at a horizontal distance of 2.92m.

6.8.1 MLG-1 FW-H Results

Coupling the FW-H acoustic analogy to the IDDES numerical results by extracting unsteady surface fluctuation pressures from the MLG-1 model produces sound pressure level plot as presented in Figure 6.19. Results of SPL are presented against 1/3 octave bands. From this plot, SPL peaks are seen to exist at 1/3 octave band values of 16 Hz, 160 Hz and 1250 Hz, with SPL values of 29.5 dB, 32.5 dB and 33.2 dB respectively.

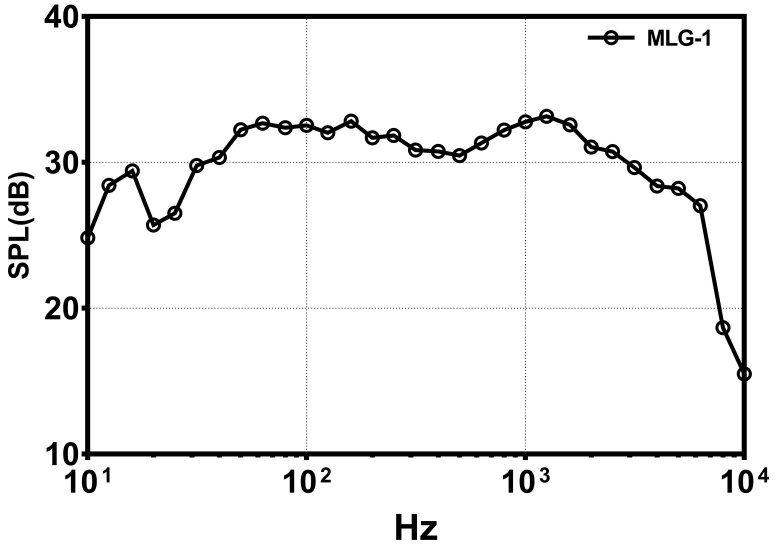

Figure 6.19: MLG-1: SPL vs 1/3 Octave Band

6.8.2 MLG-2 FW-H Results

An acoustic analogy coupling of IDDES numerical results to FW-H acoustic analogy from the MLG-2 model produces sound pressure level plot as presented in Figure 6.20. From this plot, we observe peak SPL values of 26.2 dB, 30.3 dB and 30.5dB at 1/3 octave bands of 20 Hz, 125 Hz and 1250 Hz.

6.8.3 MLG-1 vs MLG-2 SPL Comparison

A comparison of acoustic results obtained from MLG-1 and MLG-2 is presented as shown in Figure 6.21. From this plot, an observation is made that the peak values of MLG-1 were reduced by 3.8 dB, 3.1 dB and 3 dB at the 1/3 octave

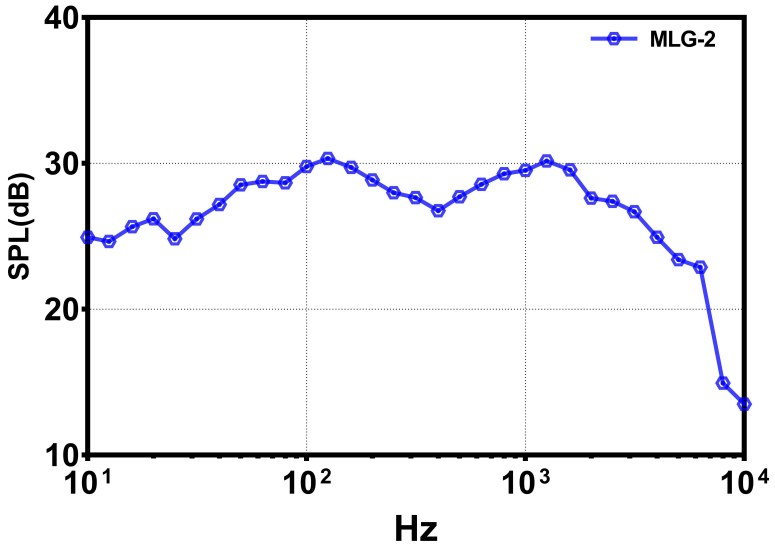

Figure 6.20: MLG-2: SPL vs 1/3 Octave Band

bands of 16 Hz, 160 Hz and 1250 Hz respectively. Therefore, the potentials of wire screens modeling application is hereby evident.

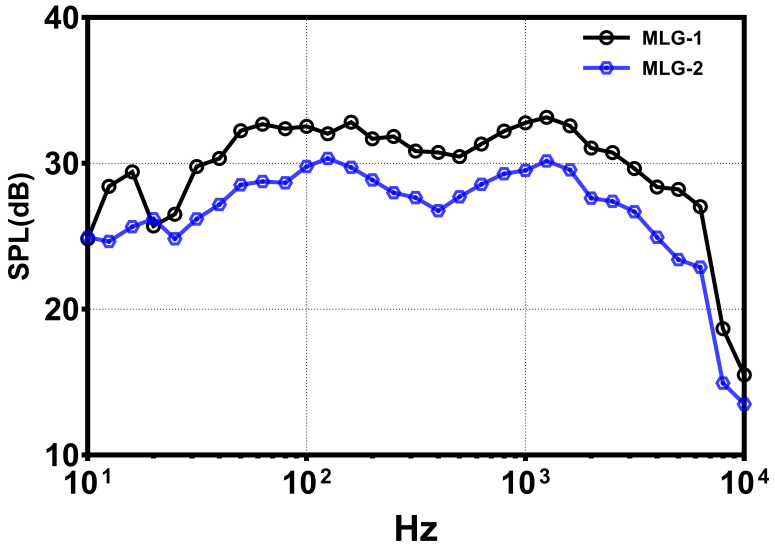

Figure 6.21: MLG-1 and MLG-2 Comparison: SPL vs 1/3 Octave Band

6.9 ALLEGRA Comparison

CFD-VAM predicted noise reduction effect obtained as a result of wire screen modeling is compared with experimental noise reduction effect as a result of

wire screen introduction as obtained within the ALLEGRA test campaign. This comparison is presented in Figure 6.22. The ALLEGRA screen effect ΔSPL results were obtained by subtracting the acoustic results obtained when the woven wire screen was introduced from the acoustic results obtained without the woven wire mesh screen. The CFD-VAM screen effect as shown in Figure 6.22 is obtained by subtracting IDDES-FW-H acoustic result of MLG-1 from MLG-2.

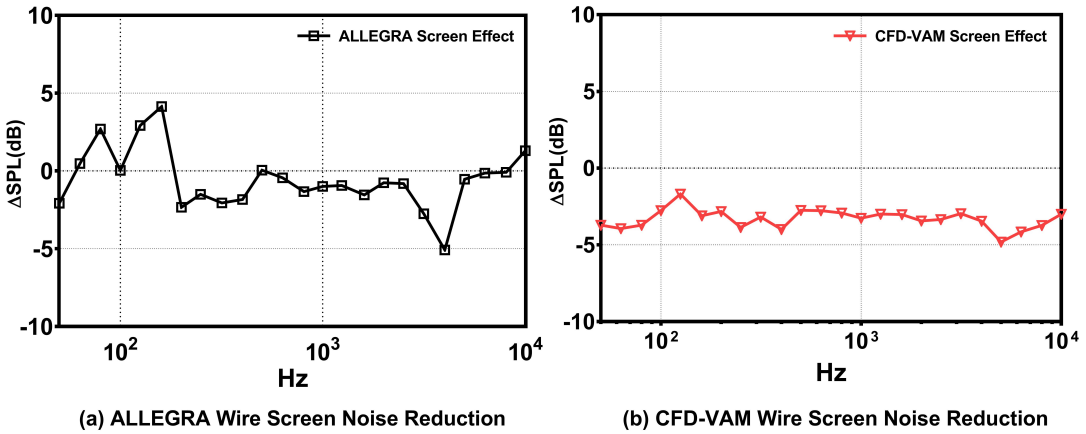

Figure 6.22: ALLEGRA vs CFD-VAM Comparison ΔSPL vs 1/3 Octave Band

From the result of Figure 6.22, an observation is made, that the experimental noise increase within the low 1/3 octave band frequency range was not detected by the numerical modeling approach. However, from 315 Hz, comparable noise reduction results were obtained. From the ALLEGRA experiments, maximum noise reduction of 5 dB occurred at 4000 Hz, while the equivalent reduction obtained utilizing the CFD-VAM modeling approach was 3.5 dB at that same frequency, but a noise reduction of 4.8 dB at 5000 Hz 1/3 octave band.

6.10 Summary

This chapter presents for the first time the implementation of the Volume Averaged Method for a wire screen mesh as a noise reduction technology for a

realistic main landing gear model. Whilst the numerical results are compared to experimental test results from an EU Collaborative Research project, it must be noted that this comparison is only rudimentary give the fundamental difference in test set-up. For instance, in the ALLEGRA project two MLGs were tested, the fuselage and belly fairing would have effected the boundary layer and also included was the landing gear bay and doors. However, the comparison serves as an important fist step towards the evaluation of wire mesh screens as a low noise technology using a simplified numerical approach.

The following are the key summary points from this findings;

1. Noise Modeling of wire screens within a computational domain by implementing the CFD-VAM approach of pressure drop and turbulence suppression effects possess great potentials as an alternative to a fully resolved model for simulating the effect of woven wire screens within a CFD flow domain as add-on low noise treatments for aerodynamic applications.

2. The steady and unsteady flow field analysis from the resulting MLG-1 and MLG-2 cases show that the effect of the wire screen porous zone modeling is in the introduction of wall surface pressure reduction, fluctuating pressure suppressions, wall shear stress reduction, turbulent kinetic energy and velocity reduction of downstream fluid flow.

3. From the comparisons of MLG-1 and MLG-2 acoustic results, an observation is noticed that the modeling of woven wire screens potentially reduces peak SPL by up to -3.8 dB.

4. When comparisons between CFD-VAM approach and experimental tests from the ALLEGRA test campaign are made, noise reductions from the ALLEGRA test when wire mesh screen was utilized resulted in a maximum ΔSPL value of -5 dB centered at 4000 Hz of 1/3 octave band, while a maximum noise reduction ΔSPL value of -4.8 dB centered at

5000 Hz of the 1/3 octave band was obtained for the CFD-VAM screen modeling approach.

5. Therefore, aerodynamic noise reductions achieved by using the CFD-VAM approach proposed within chapter 5 and utilized in this chapter shows promising signs and potentials, with room for further improvements.

Chapter 7

Conclusions and Future Work

7.1 Conclusions

Investigations carried out in the course of this thesis research focused on the numerical investigation of woven wire mesh screens as aerodynamic flow control and noise reduction mechanisms when applied to landing gears or aerodynamic bluff bodies. This research provides an advancement of scientific knowledge in the field of aeroacoustics for the application of woven screens.

The following conclusions can be drawn from the research carried out within this thesis;

- Mesh screens possess potentials when applied to landing gears for aerodynamic noise reduction. They help to achieve noise reduction levels at low and mid frequencies. Their self noise effects becomes pronounced at high frequencies, and this self noise is Strouhal dependent, based on the mesh hole diameters.

- From Chapter 3, for obtaining pressure drop of flow through three dimensional woven wire screens, solving turbulent transport equations by modeling the dissipation term ϵ replicates experimental results better than transport equations modeling the specific dissipation term ω or utilizing transition models. The $k-\epsilon$ turbulence model showed to be suitable for this purpose.

- This $k-\epsilon$ turbulence model approach provides a computationally cost effective alternative to expensive and more accurate simulations such as the LES (Large Eddy Simulations), LBM (Lattice Boltzmann Method) or DES (Detached Eddy Simulations) approach.

- CFD predicted flow loss coefficients replicate experimental results within best case scenario error margins of 1% and worst case error margins of 8% (Grid B).

- CFD predicted flow loss coefficients presents better predictions when compared to the classical loss coefficient correlation models, e.g, Wieghardt

[157], Wakeland [156] and Roach [1].

- With the use of a computational grid possessing much extended domain sides (S1-B, S2-B and S3-B), an estimate for flow speed reductions within downstream regions of wire screens is presented. This flow speed reduction shows to correlate with wire screens solidity $(1 - \beta)$ within $U_{min} = (1 - \beta)U_{\infty}$, and occurs mainly within downstream distances of $7 < X/M < 60$ from wire screen. Therefore, for aerodynamic noise reduction applications, locating aerodynamic components within distances of $7 < X/M = 60$ downstream of wire screens is recommended.

- Turbulent kinetic energy results showed that peak kinetic energy values at screen exit of S1-A, S2-A and S3-A approximately doubled the values of S1-B, S2-B and S3-B. These high kinetic energy values can be associated with the grid domain sides, as the domain sides aided the increase in fluid kinetic energy within the screen.

- Implications of the observed rise in kinetic energies within screen exit for S1-A, S2-A and S3-A is the fact that maximum flow speeds within screen apertures for S1-A, S2-A and S3-A are affected as a result of interference from sides of the domain, thereby presenting superfluous peak flow speeds within the screen apertures.

- Results from the turbulence decay of fluid flow through screens tested showed that S1-B, S2-B and S3-B represented the popular turbulence decay correlation model of Roach [1] much better than S1-A, S2-A, and S3-A for the range of Reynolds number tested. Again, due to the interference of the side wall boundary conditions on the fluid flow phenomenon through woven wire screens in S1-A, S2-A, and S3-A, the use of an extended sides fluid domain such as cases S1-B, S2-B and S3-B provides much better comparison to the turbulence decay correlation model utilized for downstream screen turbulence intensity decay.

- From Chapter 4, for two dimensional analysis of the effect of a wire

screen, a very simplified 2D approach was proposed. This approach was carried out using In-line and off-line (staggered) cylinder arrangement, where the stream-wise pitch to diameter ratio was parametrized and utilized to provide a modest simplification.

- For these open area ratios, 2D geometry of staggered cylinders can represent a simplification to 3D woven screens within a range of C/D ratios. The nature of isotropic turbulence downstream of a 2D screen was in agreement, and comparisons of CFD predicted turbulence reduction factors to existing semi-empirical correlations showed favorable good agreements.

- 2D screen geometries possessing $0.4 \leq \frac{C}{D} \leq 0.6$ showed better representation to 3D experimental results, therefore, for a 2D simplified analysis of a wire screen, better flow characteristics can be obtained when the range $0.4 \leq \frac{C}{D} \leq 0.6$ is utilized, compared to an in-line simplified cylinder configuration.

- For a staggered arrangement of 2D cylindrical screens, when screen geometries shift within $0.4 \leq \frac{C}{D} \leq 1$, a slight vortex shedding pattern alteration is evidenced, as shedding patterns go from a well patterned out of-phase manner to a somewhat in-phase pattern.

- Generally, because 2D screen geometries possessing $0.4 \leq \frac{C}{D} \leq 0.6$ showed to possess much better representation to experimental results, this geometry range is hereby recommended for use in applications and analysis involving 2D screens where flow and noise control studies are of significance.

- From Chapter 5, a less computational expensive method of modeling and therefore simulating woven wire mesh screens was presented. This alternative method accounts for the pressure drop effect and turbulence suppression effect which a physical woven wire mesh screen can be characterized with.

- An approach of utilizing the flow loss resistance of wire screens in a virtually imposed screen porous zone within a flow domain in close proximity to bluff bodies is adopted.

- The Volume averaged method (VAM) was utilized for this modeling process, where sink terms for pressure drop and turbulence quantities were introduced to account for the effect of woven wire screens.

- The flow loss resistance implemented within the screen porous zone produces moderate noise reduction results, however, better results are achieved when an added sink term for turbulence alteration effect is introduced. CFD-VAM results for frequencies within the range of 500Hz to 12500Hz compared favorably to experiments, however, for frequencies above 12500Hz, numerical acoustic results could not match experimental results. This is well explained due to the fact that at such high frequencies, the self noise effects of wire screens are more predominant and must be taken into account for a more elaborate noise reduction modeling approach.

- From Chapter 6, the proposed wire screen noise reduction modeling method of implementing sink terms for pressure drop and turbulence suppression is performed on more advanced geometry of a realistic MLG model. The ALLEGRA acoustic results were used for validation and testing of this modeling approach.

- The steady and unsteady flow field analysis from the resulting cases of MLG-1 and MLG-2 showed that the effect of wire screen porous zone modeling is in the introduction of wall surface pressure reduction, fluctuating pressure suppressions, wall shear stress reduction, turbulent kinetic energy and velocity reduction of downstream fluid flow.

- From the comparisons of MLG-1 and MLG-2 acoustic results, an observation is noticed that the modeling of woven wire screens potentially reduces peak SPL values to within -3.8 dB.

- When comparisons between the CFD-VAM approach and experimental tests from the ALLEGRA campaign are made, noise reductions from the ALLEGRA results when wire mesh screen were utilized resulted in a maximum ΔSPL value of -5 dB centered at 4000 Hz of 1/3 octave band, while a maximum noise reduction ΔSPL value of -4.8 dB centered at 5000 Hz of the 1/3 octave band was obtained for the CFD-VAM screen modeling approach.

- Therefore, aerodynamic noise reductions achieved by using the CFD-VAM approach proposed within this thesis and utilized in chapter 5 and chapter 6 shows promising signs and potentials, with room for further improvements.

Therefore, the research carried out within this thesis advances the understanding of wire mesh screen applications, and also laid a strong foundation towards solving the deficiencies of numerically modeling wire mesh screens particularly for aerodynamic applications.

7.2 Future Work

There indeed exist future areas of improvements within the subject area of wire screen modeling for aerodynamic noise reduction. The following highlights are possible areas of future work and developments;

- Further improvements to the CFD-VAM approach can be studied by studies on its application within a URANS solver. As getting it coupled to a URANS would definitely result in a much more economical process.

- A method of accounting for the self-noise effect of wire mesh screens within a numerical modeled domain is needed, so as to account for the high frequency noise effect it introduces on bluff body noise.

- A full LES-FW-H analysis should be carried out on the MLG-1 and MLG-2 by resolving the wire screen geometries, and results compared

with the IDDES-FW-H performed within this thesis, so as to get a quantifiable record of the advantages of performing the CFD-VAM approach in terms of computational costs.

- Further analysis should be performed on higher detailed MLG geometry, so as to observe if there are much gains in performing the analysis for a simplified geometry against a more detailed geometry.

1.

Bibliography

[1] P. Roach, "The generation of nearly isotropic turbulence by means of grids," *International Journal of Heat and Fluid Flow*, vol. 8, pp. 82–92, June 1987.

[2] F. van den Berg, C. Verhagen, and D. Uitenbroek, "The Relation between Self-Reported Worry and Annoyance from Air and Road Traffic," *International Journal of Environmental Research and Public Health*, vol. 12, pp. 2486–2500, feb 2015.

[3] "Activities at the institute of aerodynamics and flow technology, DLR - QICE," Nov. 2015.

[4] T.-M. Seppnen, "RECREATE Aircraft noise analysis."

[5] W. Dobrzynski, "Almost 40 years of airframe noise research: What did we achieve?," *Journal of aircraft*, vol. 47, no. 2, pp. 353–367, 2010.

[6] K. Boorsma, *Aeroacoustic Control of Landing Gear Noise using Perforated Fairings*. PhD thesis, University of Southampton, School of Engineering Sciences. Page 3, 2008.

[7] Y. Li, M. Smith, and X. Zhang, "Measurement and control of aircraft landing gear broadband noise," *Aerospace Science and Technology*, vol. 23, pp. 213–223, Dec. 2012.

[8] W. Humphreys and T. Brooks, "Noise spectra and directivity for a

scale-model landing gear," *International Journal of Aeroacoustics*, vol. 8, pp. 409–443, July 2009.

[9] K. Boorsma, X. Zhang, N. Molin, and L. C. Chow, "Bluff Body Noise Control Using Perforated Fairings," *AIAA Journal*, vol. 47, pp. 33–43, Jan. 2009.

[10] K. Boorsma, X. Zhang, and N. Molin, "Landing gear noise control using perforated fairings," *ACTA MECHANICA SINICA*, vol. 26, pp. 159–174, May 2010.

[11] O. Stefan, S. Constantin, M. Nicolas, and P. Jean-Francois, "Reduction of landing gear noise using meshes," in *16th AIAA/CEAS Aeroacoustics Conference*, (Stockholm, Sweden), 2010.

[12] L. C. Chow, D. A. Foot, and C. N. Wood, "Aircraft noise reduction apparatus," sep 2003. US Patent 6,619,587.

[13] T. Sijpkes and J. Wickerhoff, "Aeroplane provided with noise-reducing means, as well as a landing gear and blowing means," June 2004. US20040104301 A1.

[14] L. C. Chow, K. Mau, and H. Remy, "Landing Gears and High Lift Devices Airframe Noise Research," in *8th AIAA/CEAS Aeroacoustics Conference & Exhibit*, American Institute of Aeronautics and Astronautics.

[15] A. Abeysinghe, J. Whitmire, D. Nesthus, J. Moe, and G. Stuczynski, "QTD 2 (Quiet Technology Demonstrator 2) Main Landing Gear Noise Reduction Fairing Design and Analysis," American Institute of Aeronautics and Astronautics, May 2007.

[16] J. Kennedy, E. Neri, and G. J. Bennett, "The reduction of main landing gear noise," in *22nd AIAA/CEAS Aeroacoustics Conference*, p. 2900, 2016.

[17] W. D. Baines, *An Investigation of Flow Through Screens*. American Society of Mechanical Engineers, 1950.

[18] I. E. Idelik, M. Steinberg, I. E. Idelik, and I. E. Idelik, *Handbook of hydraulic resistance*. New York: begell house, 1996.

[19] S. Oerlemans, C. Sandu, N. Molin, and J.-F. Piet, "Reduction of Landing Gear Noise Using Meshes," in *16th AIAA/CEAS Aeroacoustics Conference*, American Institute of Aeronautics and Astronautics, 2011.

[20] E. Neri, *Characterisation and Reduction of Aircraft Landing Gear Noise*. PhD thesis, Trinity College Dublin, University of Dublin, Ireland, July 2017.

[21] M. Smith, L. C. Chow, and N. Molin, "Control of landing gear noise using meshes," in *16th AIAA/CEAS Aeroacoustics Conference*, 2010-3974.

[22] U. Rosenhall, K. Pedersen, and A. Svanborg, "Presbycusis and noise-induced hearing loss," *Ear and hearing*, vol. 11, no. 4, pp. 257–263, 1990.

[23] P. M. Rabinowitz, "Noise-induced hearing loss," *American Family Physician*, vol. 61, no. 9, pp. 2759–2760, 2000.

[24] K. D. Kryter, *The handbook of hearing and the effects of noise: Physiology, psychology, and public health*. Academic Press, 1994.

[25] W. Dobrzynski, L. Chow, P. Guion, and D. Shiells, "A European study on landing gear airframe noise sources," American Institute of Aeronautics and Astronautics, June 2000.

[26] W. Dobrzynski, "Almost 40 Years of Airframe Noise Research: What Did We Achieve?," *Journal of Aircraft*, vol. 47, no. 2, pp. 353–367, 2010.

[27] W. Dobrzynski and H. Buchholz, "Full-Scale Noise Testing on Airbus Landing Gears in the German-Dutch Wind Tunnel.," in *3rd AIAA/CEAS Aeroacoustics Conference, Atlanta/GA, USA, 12.-14.5.1997, Paper-No. AIAA/CEAS 97-1597*, 1997.

[28] R. D. J. Piet, "Flight Test Investigation of Add-On Treatments to Reduce Aircraft Airframe Noise," 2005.

[29] M. Murayama, Y. Yokokawa, K. Yamamoto, and T. Hirai, "Computational study of low-noise fairings around tire-axle region of a two-wheel main landing gear," *Computers & Fluids*, vol. 85, pp. 114–124, 2013.

[30] J.-F. Piet, N. Molin, and C. Sandu, "Aircraft landing gear provided with at least one noise reducing means," May 2012. US20100108805 A1.

[31] M. J. Lighthill, "On Sound Generated Aerodynamically. I. General Theory," *Proceedings of the Royal Society of London A: Mathematical, Physical and Engineering Sciences*, vol. 211, pp. 564–587, Mar. 1952.

[32] N. Curle, "The Influence of Solid Boundaries upon Aerodynamic Sound," *Proceedings of the Royal Society of London A: Mathematical, Physical and Engineering Sciences*, vol. 231, pp. 505–514, Sept. 1955.

[33] J. F. Williams and D. L. Hawkings, "Sound generation by turbulence and surfaces in arbitrary motion," *Philosophical Transactions of the Royal Society of London. Series A, Mathematical and Physical Sciences*, vol. 264, no. 1151, pp. 321–342, 1969.

[34] J. S. Gibson, "The ultimate noise barrier-far field radiated aerodynamic noise," in *Inter-Noise and NOISE-CON congress and confer-*

ence proceedings, vol. 1972, pp. 332–337, Institute of Noise Control Engineering, 1972.

[35] G. J. Healy, *Measurement and analysis of aircraft far-field aerodynamic noise*, vol. 2377. National Aeronautics and Space Administration, 1974.

[36] J. D. Revell, "On the calculation of aerodynamic noise generated by large aircraft at landing approach," *The Journal of the Acoustical Society of America*, vol. 55, no. S1, pp. S73–S73, 1974.

[37] Y. Li, X. Wang, and D. Zhang, "Control strategies for aircraft airframe noise reduction," *Chinese Journal of Aeronautics*, vol. 26, no. 2, pp. 249–260, 2013.

[38] D. Lockard, M. Khorrami, and F. Li, "High Resolution Calculation of a Simplified Landing Gear," in *10th AIAA/CEAS Aeroacoustics Conference*, American Institute of Aeronautics and Astronautics.

[39] B. S. Lazos, "Mean Flow Features Around the Inline Wheels of Four-Wheel Landing Gear," *AIAA Journal*, vol. 40, no. 2, pp. 193–198, 2002.

[40] Y. Guo, K. Yamamoto, and R. Stoker, "An Empirical Model for Landing Gear Noise Prediction," in *10th AIAA/CEAS Aeroacoustics Conference*, American Institute of Aeronautics and Astronautics.

[41] S. Jaeger, N. Burnside, P. Soderman, W. Horne, and K. James, "Microphone Array Assessment of an Isolated, 26%-scale, High-fidelity Landing Gear," in *8th AIAA/CEAS Aeroacoustics Conference & Exhibit*, American Institute of Aeronautics and Astronautics.

[42] P. Eret, J. G. Bennett, J. Kennedy, and M. Bruno, "Review of state of the art of landing gear noise reduction technologies," report, TCD, KTH, 2012.

[43] Y. Li, M. Smith, and X. Zhang, "Measurement and control of aircraft landing gear broadband noise," *Aerospace Science and Technology*, vol. 23, no. 1, pp. 213–223, 2012.

[44] J. Ffowcs Williams and C. Gordon, "Noise of highly turbulent jets at low exhaust speeds," *AIAA Journal*, vol. 3, no. 4, pp. 791–793, 1965.

[45] W. Olsen and A. Karchmer, "Lip noise generated by flow separation from nozzle surfaces (1976-3)," in *14th Aerospace Sciences Meeting*, (Washington, D.C., USA), 1976.

[46] F. Leppington, "Scattering of quadrupole sources bear the end of a rigid semi-infinite circular pipe," *Aeronautical Research Council*, vol. 1195, p. 5, 1972.

[47] K. Zhao, X.-x. Yang, P. N. Okolo, and W.-h. Zhang, "Use of a plane jet for flow-induced noise reduction of tandem rods," *Chinese Physics B*, vol. 25, no. 6, p. 064301, 2016.

[48] H. Haniu and B. Ramaprian, "Studies on two-dimensional curved nonbuoyant jets in cross flow," *Journal of Fluids Engineering*, vol. 111, no. 1, pp. 78–86, 1989.

[49] K. Zhao, P. N. Okolo, J. Kennedy, and G. J. Bennett, "A study of planar jet flow control and perforated fairings for the reduction of the flow-induced noise of tandem rods in a cross-flow," in *22nd AIAA/CEAS Aeroacoustics Conference, Lyon, France, 30 May-1 Jun., 2016*, p. 2772, 2016.

[50] Y. Kamotani and I. Greber, "Experiments on confined turbulent jets in cross flow," *NASA STI/Recon Technical Report N*, vol. 3, p. 05108, 1974.

[51] D. Yu, M. Ali, and J. H. Lee, "Multiple tandem jets in cross-flow," *Journal of hydraulic engineering*, vol. 132, no. 9, pp. 971–982, 2006.

[52] K. Zhao, X. Yang, P. N. Okolo, Z. Wu, W. Zhang, and G. J. Bennett, "A novel method for defining the leeward edge of the planar jet in crossflow," *Journal of Applied Fluid Mechanics*, vol. 10, no. 5, 2017.

[53] K. Zhao, X. Yang, P. N. Okolo, Z. Wu, and G. J. Bennett, "Use of dual planar jets for the reduction of flow-induced noise," *AIP Advances*, vol. 7, no. 2, p. 025312, 2017.

[54] Y. Guo, "A Study on Local Flow Variations for Landing Gear Noise Research," in *14th AIAA/CEAS Aeroacoustics Conference (29th AIAA Aeroacoustics Conference)*, American Institute of Aeronautics and Astronautics.

[55] M. R. Fink, "Noise Component Method for Airframe Noise," *Journal of Aircraft*, vol. 16, pp. 659–665, Oct. 1979.

[56] M. G. Smith and L. Chow, "Validation of a prediction model for aerodynamic noise from aircraft landing gear," *8th AIAA/CEAS Aeroacoustics Conference*, 2002-2581.

[57] M. Smith and L. Chow, "Prediction method for aerodynamic noise from aircraft landing gear," *AIAA paper*, vol. 2228, p. 1998, 1998.

[58] C. Burley, T. Brooks, W. Humphreys, and J. Rawls, "ANOPP Landing Gear Noise Prediction Comparisons to Model-Scale Data," in *13th AIAA/CEAS Aeroacoustics Conference (28th AIAA Aeroacoustics Conference)*, American Institute of Aeronautics and Astronautics.

[59] L. V. Lopes, *A new approach to complete aircraft landing gear noise prediction.* PhD thesis, The Pennsylvania State University, 2009.

[60] L. V. Lopes, K. S. Brentner, P. J. Morris, and D. P. Lockard, "Increased Fidelity in Prediction Methods for Landing Gear Noise," in *AIAA/CEAS Aeroacoustics Conference*, 2008.

[61] W. Dobrzynski, L. Chow, P. Guion, and D. Shiells, "Research into Landing Gear Airframe Noise Reduction," American Institute of Aeronautics and Astronautics, June 2002.

[62] R. Davy, F. Moens, and H. Remy, "Aeroacoustic Behaviour of a 1:11 Scale Airbus Model in the Open Anechoic Wind Tunnel CEPRA 19," American Institute of Aeronautics and Astronautics, June 2002.

[63] L. C. Chow and W. Dobrzynski, "Landing Gear Airframe Noise Research Study," 9th International Congress on Sound and Vibration, Orlando (USA), 2002.

[64] R. Stoker and R. Sen, "An experimental investigation of airframe noise using a model-scale Boeing 777," American Institute of Aeronautics and Astronautics, Jan. 2001.

[65] J. Piet, U. Michel, and P. Bhning, "Localization of the Acoustic Sources of the A340 with a Large Phased Microphone Array During Flight Tests," American Institute of Aeronautics and Astronautics, June 2002.

[66] J. Piet, L. Chow, F. Laporte, and H. Remy, "Flight test investigation of high-lift devices and landing gear modifications to achieve airframe noise reduction," in *ECCOMAS 2004 Conference. Jyvaeskylae, Finland*, 2004.

[67] G. Howell, A. Bradley, M. McCormick, and J. Brown, "De-Dopplerization and acoustic imaging of aircraft flyover noise measurements," *Journal of Sound and Vibration*, vol. 105, pp. 151–167, Feb. 1986.

[68] G. Elias, "Source localization with a two-dimensional focused array: Optimal signal processing for a cross-shaped array," Inter-Noise 95, Newport Beach (USA), 1995.

[69] P. Sijtsma and H. Holthusen, "Source location by phased array measurements in closed wind tunnel test sections," American Institute of Aeronautics and Astronautics, May 1999.

[70] W. M. Dobrzynski, B. Schöning, L. C. Chow, C. Wood, M. Smith, and C. Seror, "Design and testing of low noise landing gears," *International Journal of Aeroacoustics*, vol. 5, no. 3, pp. 233–262, 2006.

[71] M. Smith, B. Fenech, L. Chow, N. Molin, W. Dobrzynski, and C. Seror, "Control of Noise Sources on Aircraft Landing Gear Bogies," American Institute of Aeronautics and Astronautics, May 2006.

[72] W. Dobrzynski, B. Schning, L.-C. Chow, C. Wood, M. Smith, and C. Seror, "Design and Testing of Low Noise Landing Gears," American Institute of Aeronautics and Astronautics, May 2005.

[73] P. Ravetta, R. Burdisso, W. Ng, M. Khorrami, and R. Stoker, "Screening of Potential Noise Control Devices at Virginia Tech for QTD II Flight Test," American Institute of Aeronautics and Astronautics, May 2007.

[74] R. Elkoby, L. Brusniak, R. Stoker, M. Khorrami, A. Abeysinghe, and J. Moe, "Airframe Noise Test Results from the QTD II Flight

Test Program," American Institute of Aeronautics and Astronautics, May 2007.

[75] R. Stoker, Y. Guo, C. Streett, and N. Burnside, "Airframe Noise Source Locations of a 777 Aircraft in Flight and Comparisons with Past Model-Scale Tests," American Institute of Aeronautics and Astronautics, May 2003.

[76] P. Ravetta, R. Burdisso, and W. Ng, "Wind Tunnel Aeroacoustic Measurements of a 26%-scale 777 Main Landing Gear," American Institute of Aeronautics and Astronautics, May 2004.

[77] M. Remillieux, H. Camargo, P. Ravetta, R. Burdisso, and W. Ng, "Noise Reduction of a Model-Scale Landing Gear Measured in the Virginia Tech Aeroacoustic Wind Tunnel," American Institute of Aeronautics and Astronautics, May 2008.

[78] P. Ravetta, R. Burdisso, and W. Ng, "Noise Control of Landing Gears Using Elastic Membrane-Based Fairings," American Institute of Aeronautics and Astronautics, May 2007.

[79] K. Boorsma, X. Zhang, and N. Molin, "Perforated Fairings for Landing Gear Noise Control," American Institute of Aeronautics and Astronautics, May 2008.

[80] S. Oerlemans and A. de Bruin, "Reduction of Landing Gear Noise Using an Air Curtain," American Institute of Aeronautics and Astronautics, May 2009.

[81] W. Dobrzynski, L. C. Chow, M. Smith, A. Boillot, O. Dereure, and N. Molin, "Experimental Assessment of Low Noise Landing Gear Component Design," *International Journal of Aeroacoustics*, vol. 9, pp. 763–786, July 2010.

[82] E. Kors and D. Collins, "OPtimisation for low Environmental Noise impact AIRcraft -OPENAIR," in *Inter-Noise conference proceedings*, (Melbourne, Australia), 2014.

[83] Q. Bouvy, B. Petot, and T. Rougier, "Review of landing gear acoustic research at messier-bugatti-dowty," American Institute of Aeronautics and Astronautics, May 2016.

[84] M. Smith, L. C. Chow, and N. Molin, "The Influence of Aerodynamic Interactions between Components on Landing Gear Noise," American Institute of Aeronautics and Astronautics, May 2013.

[85] A. Cogotti, "Update on the pininfarina turbulence generation system and its effects on the car aerodynamics and aeroacoustics," tech. rep., SAE Technical Paper, 2004.

[86] E. Neri, J. Kennedy, and G. J. Bennett, "Characterization of low noise technologies applied to a full scale fuselage mounted nose landing gear," in *ASME 2015 Noise Control and Acoustics Division Conference at InterNoise 2015*, pp. V001T01A005–V001T01A005, American Society of Mechanical Engineers, 2015.

[87] E. Neri, J. Kennedy, and G. J. Bennett, "Noise characterization and noise treatment of a detailed full-scale nose landing gear," in *Greener Aviation: Achievements and Perspectives in Clean Sky and Worldwide, Brussels, Belgium, 3AFAssociation Aronautique et Astronautique de France*, October 2016.

[88] E. Neri, J. Kennedy, and G. J. Bennett, "Experimental and numerical study of the wheel bay cavity noise for full scale nose landing gear," in *23rd AIAA/CEAS Aeroacoutics Conference*, (Denver, CO, USA), 2017.

[89] E. Manoha, J. Bult, and B. Caruelle, "Lagoon : An Experimental Database for the Validation of CFD/CAA Methods for Landing

Gear Noise Prediction," American Institute of Aeronautics and Astronautics, May 2008.

[90] E. Manoha, J. Bulte, V. Ciobaca, and B. Caruelle, "LAGOON: Further Analysis of Aerodynamic Experiments and Early Aeroacoustics Results," American Institute of Aeronautics and Astronautics, May 2009.

[91] L. Sanders, E. Manoha, S. Ben Khelil, and C. Francois, "LAGOON : CFD/CAA Coupling for Landing Gear Noise and Comparison with Experimental Database," American Institute of Aeronautics and Astronautics, June 2011.

[92] L. Sanders, E. Manoha, S. Ben Khelil, and C. Francois, "LAGOON: New Mach Landing Gear Noise Computation and further analysis of the CAA process," American Institute of Aeronautics and Astronautics, June 2012.

[93] A. F. Ribeiro, D. Casalino, E. Fares, and S. E. Noelting, "CFD/-CAA Analysis of the LAGOON Landing Gear Configuration," American Institute of Aeronautics and Astronautics, May 2013.

[94] P. Azevedo and W. Wolf, "Noise Prediction of the LAGOON Landing Gear Using Acoustic Analogy and Proper Orthogonal Decomposition," American Institute of Aeronautics and Astronautics, May 2016.

[95] T. Rodarte Ricciardi, P. Azevedo, W. Wolf, and R. Speth, "Noise Prediction of the LAGOON Landing Gear Using Detached Eddy Simulation and Acoustic Analogy," American Institute of Aeronautics and Astronautics, June 2017.

[96] W. Bechara, C. Bailly, P. Lafon, and S. M. Candel, "Stochastic approach to noise modeling for free turbulent flows," *AIAA Journal*, vol. 32, no. 3, pp. 455–463, 1994.

[97] F. R. Menter, "Best practice: Scale-resolving simulations in ANSYS CFD," *ANSYS Germany GmbH*, pp. 1–70, 2012.

[98] J. F. Williams and D. L. Hawkings, "Sound generation by turbulence and surfaces in arbitrary motion," *Philosophical Transactions of the Royal Society of London A: Mathematical, Physical and Engineering Sciences*, vol. 264, pp. 321–342, 1969.

[99] T. Imamura, T. Hirai, K. Amemiya, Y. Yokokawa, S. Enomoto, and K. Yamamoto, "Aerodynamic and aeroacoustic simulations of a two-wheel landing gear," *Procedia Engineering*, vol. 6, pp. 293–302, 2010.

[100] M. Wang, J. B. Freund, and S. K. Lele, "Computational Prediction of Flow-Generated Sound," *Annual Review of Fluid Mechanics*, vol. 38, no. 1, pp. 483–512, 2006.

[101] S. Fu, W. Haase, S.-H. Peng, and D. Schwamborn, *Progress in Hybrid RANS-LES Modelling: Papers Contributed to the 4th Symposium on Hybrid RANS-LES Methods, Beijing, China, September 2011*. Springer Science & Business Media, Aug. 2012.

[102] L. S. Hedges, A. K. Travin, and P. R. Spalart, "Detached-Eddy Simulations Over a Simplified Landing Gear," *Journal of Fluids Engineering*, vol. 124, pp. 413–423, May 2002.

[103] Souliez, Long, and Sharma, "Landing gear aerodynamic noise prediction using unstructured grids," *International Journal of Aeroacoustics*, vol. 1, no. 2, pp. 115–135, 2002.

[104] F. Fortin, J. Syms, C. Clark, and S. McIlwain, "CFD investigation of noise around a landing gear," in *18th AIAA/CEAS Aeroacoustics Conference (33rd AIAA Aeroacoustics Conference)*, American Institute of Aeronautics and Astronautics.

[105] J. Dahan, C. O'Reilly, and G. Efraimsson, "Numerical Investigation of a Realistic Nose Landing Gear," American Institute of Aeronautics and Astronautics, June 2014.

[106] C. J. Xue, G. Zheng, W. Tang, and S. L. Long, "Aeroacoustic noise reduction design of a landing gear structure based on wind tunnel experiment and simulation," *Journal of Vibro-engineering*, vol. 14, no. 4, pp. 1591–1600, 2012.

[107] R. B. Langtry, J. V. Larssen, C. M. Winkler, A. J. Dorgan, and M. Mani, "Ddes and acoustic prediction of rudimentary landing gear experiment using unstructured finite volume methods," *Flow Turbulence and Combustion*, vol. 91, no. 3, pp. 717–745, 2013.

[108] Alexander Wagner, "A practical Introduction to Lattice Boltzmann Method," tech. rep., North Dakota State University, Mar. 2008.

[109] Z. Guo, B. Shi, and N. Wang, "Lattice BGK Model for Incompressible NavierStokes Equation," *Journal of Computational Physics*, vol. 165, pp. 288–306, Nov. 2000.

[110] Z. Guo and C. Shu, *Lattice Boltzmann Method and Its Applications in Engineering*, vol. 3 of *Advances in Computational Fluid Dynamics*. World Scientific, May 2013. DOI: 10.1142/8806.

[111] X. He and L.-S. Luo, "Lattice Boltzmann Model for the Incompressible NavierStokes Equation," *Journal of Statistical Physics*, vol. 88, pp. 927–944, Aug. 1997.

[112] Y. He, Q. Li, Y. Wang, and G. Tang, "Lattice Boltzmann method and its applications in engineering thermophysics," *Chinese Science Bulletin*, vol. 54, pp. 4117–4134, Nov. 2009.

[113] M. C. Sukop and D. T. Thorne, *Lattice Boltzmann Modeling*. Berlin, Heidelberg: Springer Berlin Heidelberg, 2006. DOI: 10.1007/978-3-540-27982-2.

[114] Y. H. Qian, D. D'Humires, and P. Lallemand, "Lattice BGK Models for Navier-Stokes Equation," *Europhysics Letters (EPL)*, vol. 17, pp. 479–484, Feb. 1992.

[115] S. Chen and G. D. Doolen, "Lattice Boltzmann method for fluid flows," *Annual Review of Fluid Mechanics*, vol. 30, pp. 329–364, Jan. 1998.

[116] H. Chen, "Volumetric formulation of the lattice Boltzmann method for fluid dynamics: Basic concept," *Physical Review E*, vol. 58, pp. 3955–3963, Sept. 1998.

[117] H. Chen, S. A. Orszag, I. Staroselsky, and S. Succi, "Expanded analogy between Boltzmann kinetic theory of fluids and turbulence," *Journal of Fluid Mechanics*, vol. 519, pp. 301–314, Nov. 2004.

[118] H. Chen, S. Chen, and W. H. Matthaeus, "Recovery of the Navier-Stokes equations using a lattice-gas Boltzmann method," *Physical Review A*, vol. 45, pp. R5339–R5342, Apr. 1992.

[119] H. Chen, "Extended Boltzmann Kinetic Equation for Turbulent Flows," *Science*, vol. 301, pp. 633–636, Aug. 2003.

[120] H. Chen, C. Teixeira, and K. Molvig, "Realization of Fluid Boundary Conditions via Discrete Boltzmann Dynamics," *International Journal of Modern Physics C*, vol. 09, pp. 1281–1292, Dec. 1998.

[121] P. L. Bhatnagar, E. P. Gross, and M. Krook, "A Model for Collision Processes in Gases. I. Small Amplitude Processes in Charged and Neutral One-Component Systems," *Physical Review*, vol. 94, pp. 511–525, May 1954.

[122] A. N.-Y. Daniel B Armstrong, "Numerical Simulations of Flow over a Landing Gear with Noise Reduction Devices using the Lattice-Boltzmann Method," *19th AIAA/CEAS Aeroacoustics Conference*, 2013.

[123] Ehab Fares, Damiano Casalino, and Mehdi R. Khorrami, "Evaluation of Airframe Noise Reduction Concepts via Simulations Using a Lattice Boltzmann Approach," in *21st AIAA/CEAS Aeroacoustics Conference*, AIAA Aviation, American Institute of Aeronautics and Astronautics, June 2015.

[124] H. Yu and S. S. Girimaji, "Near-field turbulent simulations of rectangular jets using lattice Boltzmann method," *Physics of Fluids*, vol. 17, p. 125106, Dec. 2005.

[125] W. C. van der Velden, F. Avallone, and D. Ragni, "Numerical analysis of noise reduction mechanisms of serrated trailing edges under zero lift condition," American Institute of Aeronautics and Astronautics, June 2017.

[126] C. M. Teixeira, "Incorporating Turbulence Models into the Lattice-Boltzmann Method," *International Journal of Modern Physics C*, vol. 09, pp. 1159–1175, Dec. 1998.

[127] C. Sun and A. Hsu, "Multi-level lattice Boltzmann model on square lattice for compressible flows," *Computers & Fluids*, vol. 33, pp. 1363–1385, Dec. 2004.

[128] H. Si and Y. Shi, "Study on lattice Boltzmann method/large eddy simulation and its application at high Reynolds number flow," *Advances in Mechanical Engineering*, vol. 7, p. 168781401557382, Mar. 2015.

[129] Y. Shi, A. R. d. Silva, and G. P. Scavone, "Lattice Boltzmann simulations of sound directivity of a cylindrical pipe with mean

flow," *Journal of Physics A: Mathematical and Theoretical*, vol. 46, p. 315501, Aug. 2013.

[130] R. Satti, Y. Li, R. Shock, and S. Noelting, "Unsteady Flow Analysis of a Multi-Element Airfoil Using Lattice Boltzmann Method," *AIAA Journal*, vol. 50, pp. 1805–1816, Sept. 2012.

[131] S. Mari, D. Ricot, and P. Sagaut, "Comparison between lattice Boltzmann method and NavierStokes high order schemes for computational aeroacoustics," *Journal of Computational Physics*, vol. 228, pp. 1056–1070, Mar. 2009.

[132] A. Mann, F. Perot, M.-S. Kim, D. Casalino, and E. Fares, "Advanced Noise Control Fan Direct Aeroacoustics Predictions Using a Lattice-Boltzmann Method," American Institute of Aeronautics and Astronautics, June 2012.

[133] C. Y. Lim, C. Shu, X. D. Niu, and Y. T. Chew, "Application of lattice Boltzmann method to simulate microchannel flows," *Physics of Fluids*, vol. 14, no. 7, p. 2299, 2002.

[134] X. M. Li, R. C. K. Leung, and R. M. C. So, "One-Step Aeroacoustics Simulation Using Lattice Boltzmann Method," *AIAA Journal*, vol. 44, pp. 78–89, Jan. 2006.

[135] P.-T. Lew, L. Mongeau, and A. Lyrintzis, "Noise prediction of a subsonic turbulent round jet using the lattice-Boltzmann method," *The Journal of the Acoustical Society of America*, vol. 128, no. 3, p. 1118, 2010.

[136] P.-T. Lew, P. Gopalakrishnan, D. Casalino, R. Shock, Y. Li, R. Zhang, H. Chen, K. Habibi, and L. G. Mongeau, "An Extended Lattice Boltzmann Methodology for High Subsonic Jet Noise Prediction," American Institute of Aeronautics and Astronautics, June 2014.

[137] J. Feaster, F. Battaglia, R. Deiterding, and J. Bayandor, "Validation of an Adaptive Meshing Implementation of the Lattice-Boltzmann Method for Insect Flight," p. V01AT12A007, ASME, July 2016.

[138] E. Fares, "Unsteady flow simulation of the Ahmed reference body using a lattice Boltzmann approach," *Computers & Fluids*, vol. 35, pp. 940–950, Sept. 2006.

[139] B. Duda and E. Fares, "Farfield Noise Prediction Using Large-Scale Lattice-Boltzmann Simulations," in *High-Performance Scientific Computing* (E. Di Napoli, M.-A. Hermanns, H. Iliev, A. Lintermann, and A. Peyser, eds.), pp. 48–57, Cham: Springer International Publishing, 2017. DOI: 10.1007/978-3-319-53862-4_5.

[140] G. Brs, F. Prot, and D. Freed, "Properties of the Lattice Boltzmann Method for Acoustics," American Institute of Aeronautics and Astronautics, May 2009.

[141] G. A. Brs, D. Freed, M. Wessels, S. Noelting, and F. Prot, "Flow and noise predictions for the tandem cylinder aeroacoustic benchmark," *Physics of Fluids*, vol. 24, p. 036101, Mar. 2012.

[142] S. Noelting, M. Wessels, and D. Freed, "Prediction of Aeroacoustic Noise from a Simplified Landing Gear Using a Lattice-Boltzmann-Scheme," American Institute of Aeronautics and Astronautics, Jan. 2008.

[143] Y. Li, R. Satti, P.-T. Lew, R. Shock, and S. Noelting, "Computational Aeroacoustic Analysis of Flow Around a Complex Nose Landing Gear Configuration," American Institute of Aeronautics and Astronautics, May 2008.

[144] A. Keating, P. Dethioux, R. Satti, S. Noelting, J. Louis, T. Van de Ven, and R. Vieito, "Computational Aeroacoustics Validation and

Analysis of a Nose Landing Gear," American Institute of Aeronautics and Astronautics, May 2009.

[145] D. Neuhart, M. Khorrami, and M. Choudhari, "Aerodynamics of a Gulfstream G550 Nose Landing Gear Model," American Institute of Aeronautics and Astronautics, May 2009.

[146] N. Zawodny, F. Liu, T. Yardibi, L. Cattafesta, M. Khorrami, D. Neuhart, and T. Van de Ven, "A Comparative Study of a 1/4-Scale Gulfstream G550 Aircraft Nose Gear Model," American Institute of Aeronautics and Astronautics, May 2009.

[147] S. Noelting and E. Fares, "The Lattice-Boltzmann Method: An Alternative to LES for Complex Aerodynamic and Aeroacoustic Simulations in the Aerospace Industry," Sept. 2015.

[148] S. Noelting, G. Brs, and P. Dethioux, "A Hybrid Lattice-Boltzmann/FH-W Method to Predict Sources and Propagation of Landing Gear Noise," American Institute of Aeronautics and Astronautics, June 2010.

[149] M. R. F. Khorrami, "Towards Full Aircraft Airframe Noise Prediction: Lattice Boltzmann Simulations," (Atlanta, GA, United States), June 2014.

[150] D. Casalino, F. Diozzi, R. Sannino, and A. Paonessa, "Aircraft noise reduction technologies: A bibliographic review," *Aerospace Science and Technology*, vol. 12, pp. 1–17, Jan. 2008.

[151] P. Bradshaw, "The effect of wind-tunnel screens on nominally two-dimensional boundary layers," *Journal of Fluid Mechanics*, vol. 22, pp. 679–687, Aug. 1965.

[152] W. T. Wu, J. F. Liu, W. J. Li, and W. H. Hsieh, "Measurement and correlation of hydraulic resistance of flow through woven metal

screens," *International Journal of Heat and Mass Transfer*, vol. 48, pp. 3008–3017, July 2005.

[153] J. C. Armour and J. N. Cannon, "Fluid flow through woven screens," *AIChE Journal*, vol. 14, pp. 415–420, May 1968.

[154] M. M. Seltsman, "Experimental and theoretical study of wide-angle diffuser flow with screens," *AIAA Journal*, vol. 33, no. 11, pp. 2092–2100, 1995.

[155] R. A. Pinker and M. V. Herbert, "Pressure loss associated with compressible flow through squaremesh wire gauzes," *ARCHIVE: Journal of Mechanical Engineering Science 1959-1982 (vols 1-23)*, vol. 9, pp. 11–23, Feb 1967.

[156] R. S. Wakeland and R. M. Keolian, "Measurements of resistance of individual square-mesh screens to oscillating flow at low and intermediate reynolds numbers," *Journal of Fluids Engineering*, vol. 125, no. 5, p. 851, 2003.

[157] K. E. G. Wieghardt, "On the resistance of screens," *Aeronautical Quarterly*, vol. 4, pp. 186–192, Aug 1953.

[158] M. D. Checkel, "Measurements of Turbulence Generated by 60 Percent Solid Perforated Plates," *Journal of Fluids Engineering*, vol. 108, pp. 55–63, Mar. 1986.

[159] I. P. Castro, "Wake characteristics of two-dimensional perforated plates normal to an air-stream," *Journal of Fluid Mechanics*, vol. 46, pp. 599–609, Apr. 1971.

[160] R. D. MEHTA, "Turbulent boundary layer perturbed by a screen," *AIAA Journal*, vol. 23, no. 9, pp. 1335–1342, 1985.

[161] Hugh L. Dryden, "The Use of Damping Screens for the Reduction

of Wind-Tunnel Turbulence," *Journal of the Aeronautical Sciences*, vol. 14, pp. 221–228, Apr. 1947.

[162] J. Groth and A. V. Johansson, "Turbulence reduction by screens," *Journal of Fluid Mechanics*, vol. 197, p. 139, Dec. 1988.

[163] L. Oshinowo and D. C. S. Kuhn, "Turbulence decay behind expanded metal screens," *The Canadian Journal of Chemical Engineering*, vol. 78, pp. 1032–1039, Dec. 2000.

[164] G. I. Taylor, "Statistical Theory of Turbulence," *Proceedings of the Royal Society A: Mathematical, Physical and Engineering Sciences*, vol. 151, pp. 421–444, Sept. 1935.

[165] P. Krogstad and P. A. Davidson, "Freely decaying, homogeneous turbulence generated by multi-scale grids," *Journal of Fluid Mechanics*, vol. 680, pp. 417–434, Aug. 2011.

[166] G. K. Batchelor and A. A. Townsend, "Decay of Isotropic Turbulence in the Initial Period," *Proceedings of the Royal Society A: Mathematical, Physical and Engineering Sciences*, vol. 193, pp. 539–558, July 1948.

[167] G. K. Batchelor and A. A. Townsend, "Decay of Turbulence in the Final Period," *Proceedings of the Royal Society A: Mathematical, Physical and Engineering Sciences*, vol. 194, pp. 527–543, Nov. 1948.

[168] W. K. George, "The decay of homogeneous isotropic turbulence," *Physics of Fluids A: Fluid Dynamics*, vol. 4, pp. 1492–1509, July 1992.

[169] W. K. George and H. Wang, "The exponential decay of homogeneous turbulence," *Physics of Fluids*, vol. 21, p. 025108, Feb. 2009.

[170] C. G. Speziale and P. S. Bernard, "The energy decay in self-preserving isotropic turbulence revisited," *Journal of Fluid Mechanics*, vol. 241, p. 645, Aug 1992.

[171] A. Thormann and C. Meneveau, "Decay of homogeneous, nearly isotropic turbulence behind active fractal grids," *Physics of Fluids*, vol. 26, p. 025112, Feb. 2014.

[172] R. Liu, D. S. Ting, and G. W. Rankin, "On the generation of turbulence with a perforated plate," *Experimental thermal and fluid science*, vol. 28, no. 4, pp. 307–316, 2004.

[173] L. Prandtl, *Attaining a steady air stream in wind tunnels*. NACA TM 726, 1933.

[174] A. R. Collar, *The effect of a gauze on the velocity distribution in a uniform duct*. London: British Aeronautical Research Council, 1939.

[175] G. I. Taylor, G. K. Batchelor, H. L. Dryden, and G. B. Schubauer, "The Effect of Wire Gauze on Small Disturbances in a Uniform Stream," *The Quarterly Journal of Mechanics and Applied Mathematics*, vol. 2, pp. 1–29, Jan. 1949.

[176] G. Schubauer, W. Spangenberg, and P. Klebanoff, "Aerodynamic characteristics of damping screens." NACA TN 2001, Jan. 1950.

[177] A. L. Kistler and T. Vrebalovich, "Grid turbulence at large Reynolds numbers," *Journal of Fluid Mechanics*, vol. 26, p. 37, Sept. 1966.

[178] O. Stefan and B. Anton de, "Reduction of landing gear noise using an air curtain," in *15th AIAA/CEAS Aeroacoustics Conference*, (Miami, Florida), 2009.

[179] S. Hahn, J. Je, and H. Choi, "Direct numerical simulation of turbulent channel flow with permeable walls," *Journal of Fluid Mechanics*, vol. 450, pp. 259–285, Jan. 2002.

[180] E. S. Boek and M. Venturoli, "Lattice-Boltzmann studies of fluid flow in porous media with realistic rock geometries," *Computers & Mathematics with Applications*, vol. 59, pp. 2305–2314, Apr. 2010.

[181] S. I. Green, Z. Wang, T. Waung, and A. Vakil, "Simulation of the flow through woven fabrics," *Computers & Fluids*, vol. 37, pp. 1148–1156, Oct. 2008.

[182] J. Jimnez, M. Uhlmann, A. Pinelli, and G. Kawahara, "Turbulent shear flow over active and passive porous surfaces," *Journal of Fluid Mechanics*, vol. 442, pp. 89–117, Sept. 2001.

[183] A. Tinetti, J. Kelly, R. Thomas, and S. Bauer, "Reduction of wake-stator interaction noise using passive porosity," in *40th AIAA Aerospace Sciences Meeting & Exhibit*, American Institute of Aeronautics and Astronautics.

[184] H. Liu, J. Wei, and Z. Qu, "The Interaction of Porous Material Coating With the Near Wake of Bluff Body," *Journal of Fluids Engineering*, vol. 136, p. 021302, Dec. 2013.

[185] H. Liu, J. Wei, and Z. Qu, "Prediction of aerodynamic noise reduction by using open-cell metal foam," *Journal of Sound and Vibration*, vol. 331, pp. 1483–1497, Mar. 2012.

[186] J. Schulze and J. Sesterhenn, "Optimal distribution of porous media to reduce trailing edge noise," *Computers & Fluids*, vol. 78, pp. 41–53, Apr. 2013.

[187] Y. Bae and Y. J. Moon, "Effect of passive porous surface on the trailing-edge noise," *Physics of Fluids (1994-present)*, vol. 23, p. 126101, Dec. 2011.

[188] A. P. Jewel B. Barlow, William H. Rae, "Wiley: Low-Speed Wind Tunnel Testing, 3rd Edition."

[189] M. Pott-Pollenske, W. Dobrzynski, H. Buchholz, S. Gurin, G. Saueressig, and U. Finke, "Airframe Noise Characteristics from Flyover Measurements and Prediction (AIAA 2006-2567)," American Institute of Aeronautics and Astronautics, May 2006.

[190] U. Michel, B. Barsikow, B. Haverich, M. Schuettpelz, U. Michel, B. Barsikow, B. Haverich, and M. Schuettpelz, "Investigation of airframe and jet noise in high-speed flight with a microphone array," in *3rd AIAA/CEAS Aeroacoustics Conference*, American Institute of Aeronautics and Astronautics.

[191] U. Michel, J. Helbig, B. Barsikow, M. Hellmig, and M. Schuettpelz, "Flyover noise measurements on landing aircraft with a microphone array," in *4th AIAA/CEAS Aeroacoustics Conference*, American Institute of Aeronautics and Astronautics.

[192] U. Michel and W. Qiao, "Directivity of landing-gear noise based on flyover measurements," American Institute of Aeronautics and Astronautics, May 1999.

[193] L. Chow, K. Mau, and H. Remy, "Landing gears and high lift devices airframe noise research," American Institute of Aeronautics and Astronautics, June 2002.

[194] E. Neri, J. Kennedy, and G. J. Bennett, "Bay cavity noise for full-scale nose landing gear: A comparison between experimental and numerical results," *Aerospace Science and Technology*, vol. 72, Jan. 2017.

[195] R. V. de Abreu, N. Jansson, and J. Hoffman, "Adaptive computation of aeroacoustic sources for a rudimentary landing gear,"

International Journal for Numerical Methods in Fluids, vol. 74, pp. 406–421, Feb. 2014.

[196] Patrick N. Okolo, Kun Zhao, John Kennedy, and Gareth J. Bennett, "Mesh Screen Application for Noise Reduction of Landing Gear Strut, (AIAA 2016-2845)," in *22nd AIAA/CEAS Aeroacoustics Conference*, (Lyon, France), American Institute of Aeronautics and Astronautics, May 2016.

[197] P. N. Okolo, K. Zhao, J. Kennedy, and G. J. Bennett, "Numerical Modeling of Wire Screens for Flow and Noise Control," in *23rd AIAA/CEAS Aeroacoustics Conference*, American Institute of Aeronautics and Astronautics, 2017.

[198] P. N. Okolo, K. Zhao, E. Neri, J. Kennedy, and G. J. Bennett, "Caa noise reduction parametric study of mesh screens applied to landing gears," in *22nd International Congress on Sound and Vibration, 12 to 16 July, Florence, Italy*, 2015.

[199] J. Scheiman, *Comparison of experimental and theoretical turbulence reduction characteristics for screens, honeycomb, and honeycomb-screen combinations.* NASA-TP-1958, L-14628, Dec. 1981.

[200] P. J. Roache, "Quantification of Uncertainty In Computational Fluid Dynamics," *Annual Review of Fluid Mechanics*, vol. 29, pp. 123–160, Jan. 1997.

[201] P. J. Roache, "Perspective: A Method for Uniform Reporting of Grid Refinement Studies," *Journal of Fluids Engineering*, vol. 116, no. 3, p. 405, 1994.

[202] L. Ea, M. Hoekstra, and P. Roache, "Verification of Calculations: An Overview of the 2nd Lisbon Workshop," American Institute of Aeronautics and Astronautics, June 2007.

[203] "Procedure for Estimation and Reporting of Uncertainty Due to Discretization in CFD Applications," *Journal of Fluids Engineering*, vol. 130, no. 7, p. 078001, 2008.

[204] H. J. Lienhard, "Synopsis of lift, drag and vortex frequency data for rigid circular cylinders.," in *Washington State University College of Engineering Research Division Bulletin 300:3*, 1966.

[205] A. Valli, J. Hyvluoma, A. Jsberg, A. Koponen, and J. Timonen, "Pressure Drop for Low Reynolds-Number Flows Through Regular and Random Screens," *Transport in Porous Media*, vol. 80, pp. 193–208, Nov. 2009.

[206] W. C. H. K, "Vortex Dynamics in the Cylinder Wake," *Annual Review of Fluid Mechanics*, vol. 28, no. 1, pp. 477–539, 1996.

[207] A. Asghar and E. J. Jumper, "Phase Synchronization of Vortex Shedding from Two Circular Cylinders Using Plasma Actuators," *AIAA Journal*, vol. 47, no. 7, pp. 1608–1616, 2009.

[208] S. Ishigai and E. Nishikawa, "Experimental Study of Structure of Gas Flow in Tube Banks with Tube Axes Normal to Flow Part II ; On the Structure of Gas Flow in Single-Column, Single-Row, and Double-Rows Tube Banks," *Bulletin of JSME*, vol. 18, no. 119, pp. 528–535, 1975.

[209] S. Ishigai, E. Nishikawa, K. Nishimura, and K. Cho, "Experimental Study on Structure of Gas Flow in Tube Banks with Tube Axes Normal to Flow : Part 1, Karman Vortex Flow from Two Tubes at Various Spacings," *Bulletin of JSME*, vol. 15, no. 86, pp. 949–956, 1972.

[210] Z. Huang, J. Olson, R. Kerekes, and S. Green, "Numerical simulation of the flow around rows of cylinders," *Computers & Fluids*, vol. 35, pp. 485–491, June 2006.

[211] F. Farassat and G. P. Succi, "A review of propeller discrete frequency noise prediction technology with emphasis on two current methods for time domain calculations," *Journal of Sound and Vibration*, Aug. 1980.

Appendix A

Convergence Residual Plots

A.1 S1-A Scaled Residual Plots

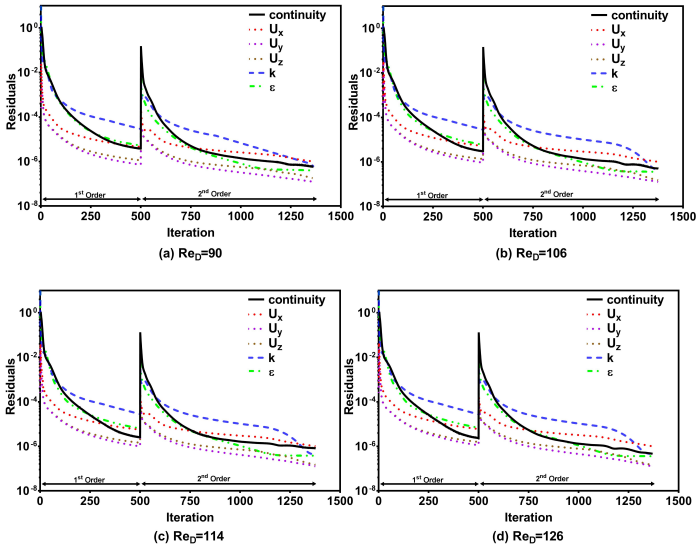

Figure A.1: S1-A Scaled Residuals Convergence

A.2 S1-B Scaled Residual Plots

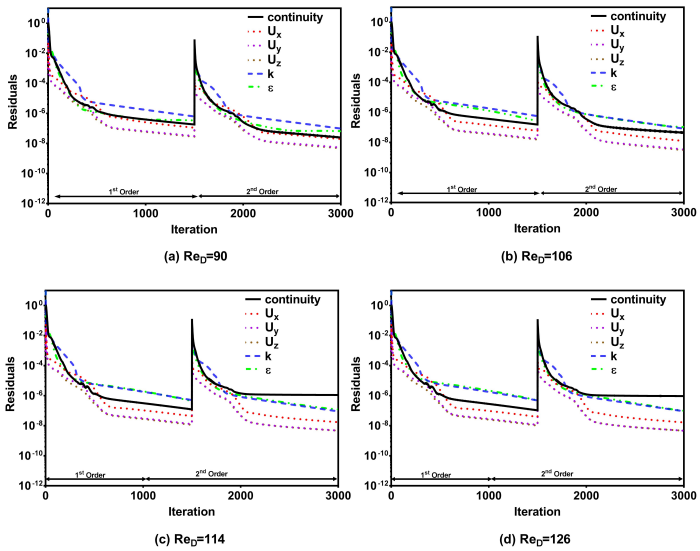

Figure A.2: S1-B Scaled Residuals Convergence

A.3 S2-A Scaled Residual Plots

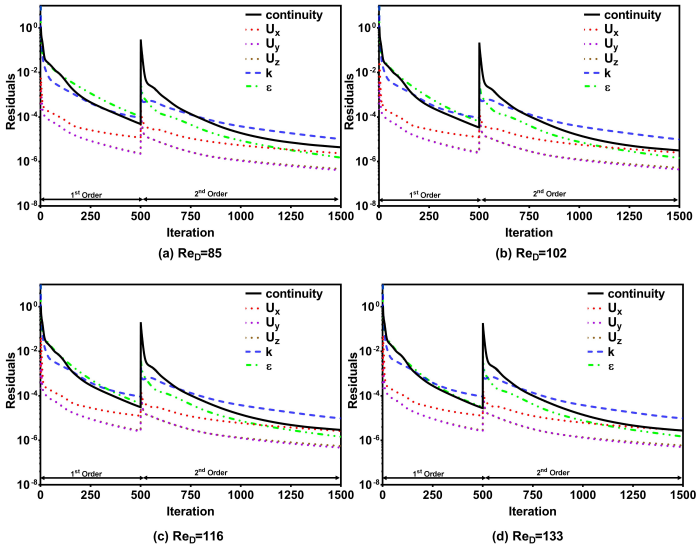

Figure A.3: S2-A Scaled Residuals Convergence

A.4 S2-B Scaled Residual Plots

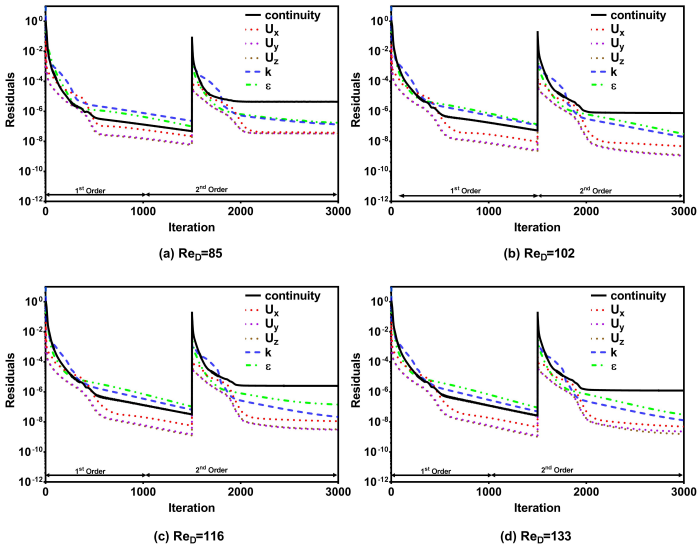

Figure A.4: S2-B Scaled Residuals Convergence

A.5 S3-A Scaled Residual Plots

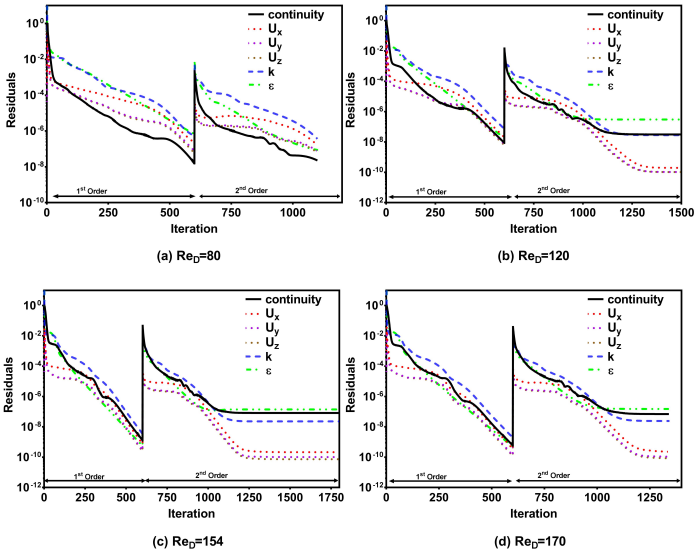

Figure A.5: S3-A Scaled Residuals Convergence

A.6 S3-B Scaled Residual Plots

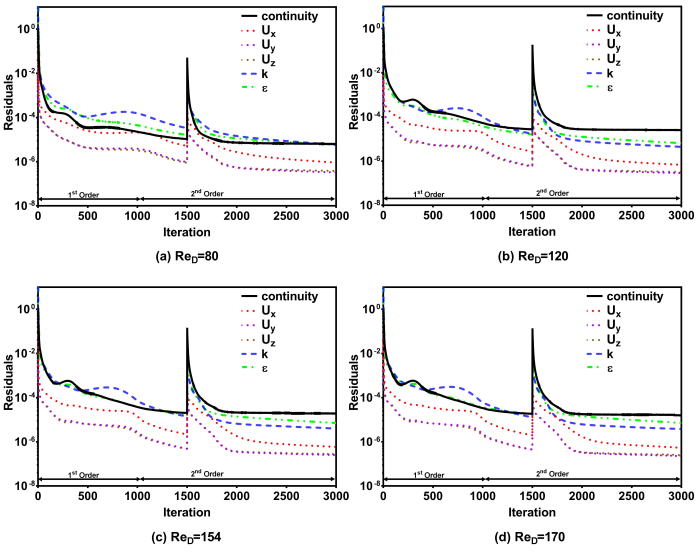

Figure A.6: S3-B Scaled Residuals Convergence

Appendix B

Screen S1 Contour Plots

B.1 S1 U_y Contours

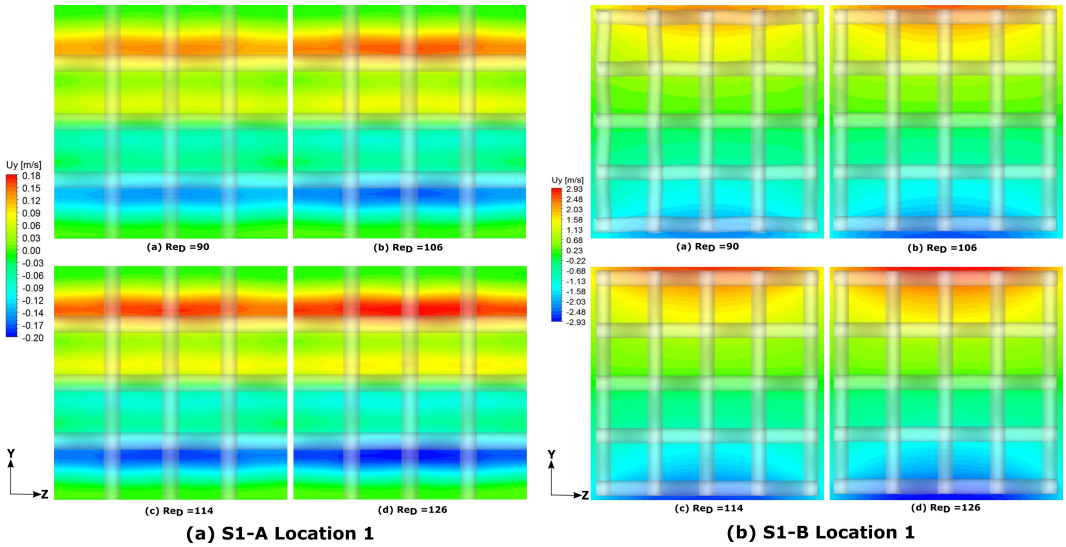

Figure B.1: U_y contour plots at location 1 for S1-A and S1-B

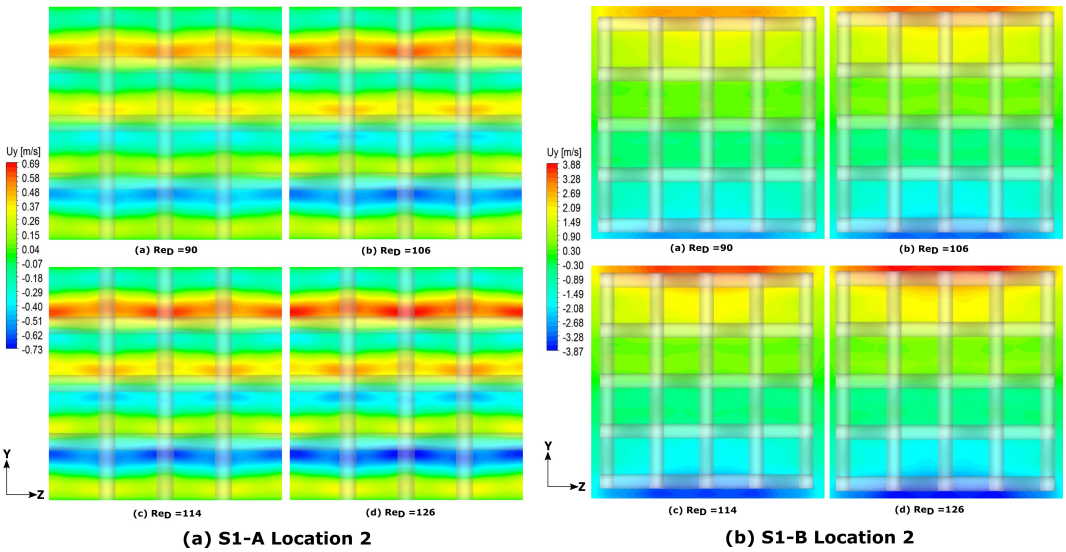

Figure B.2: U_y contour plots at location 2 for S1-A and S1-B

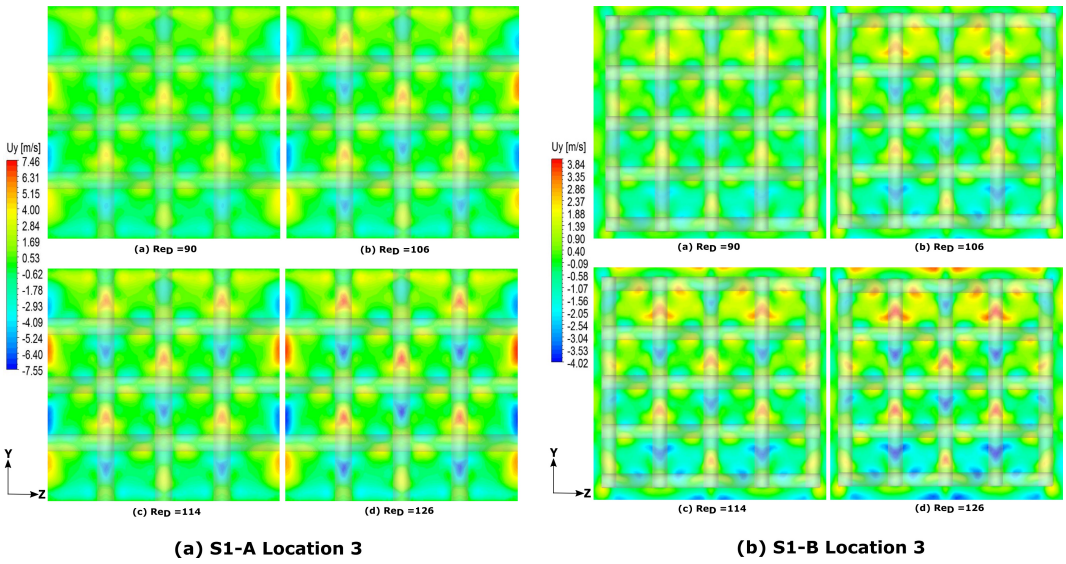

Figure B.3: U_y contour plots at location 3 for S1-A and S1-B

B.2 S1 TKE Contours

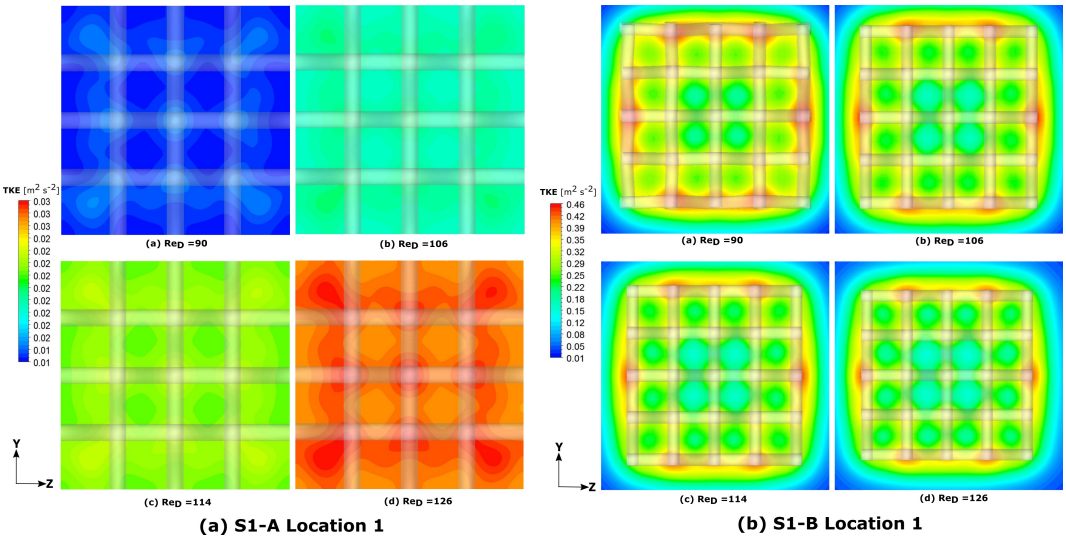

Figure B.4: TKE contour plots at location 1 for S1-A and S1-B

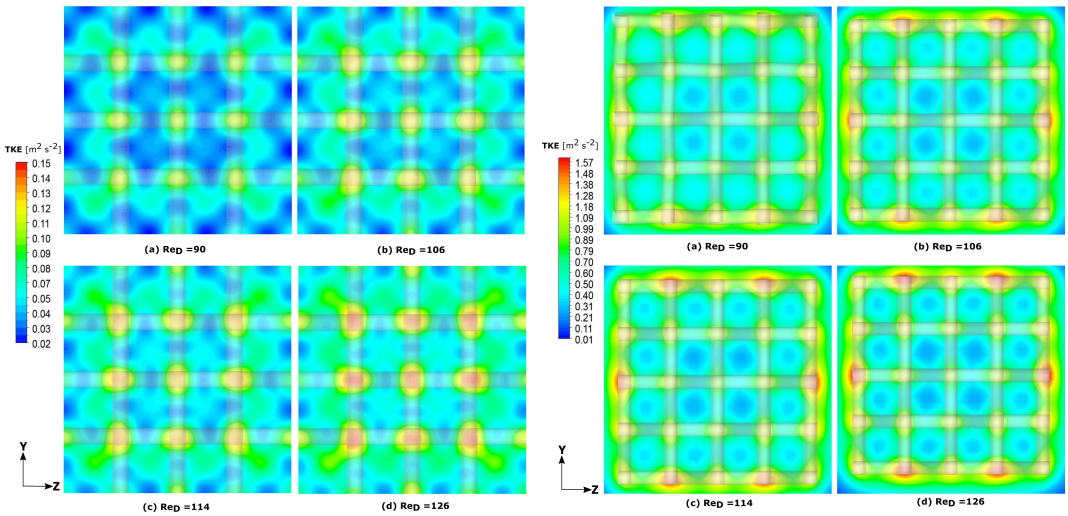

Figure B.5: TKE contour plots at location 2 for S1-A and S1-B

B.3 S1 Surface Pressures

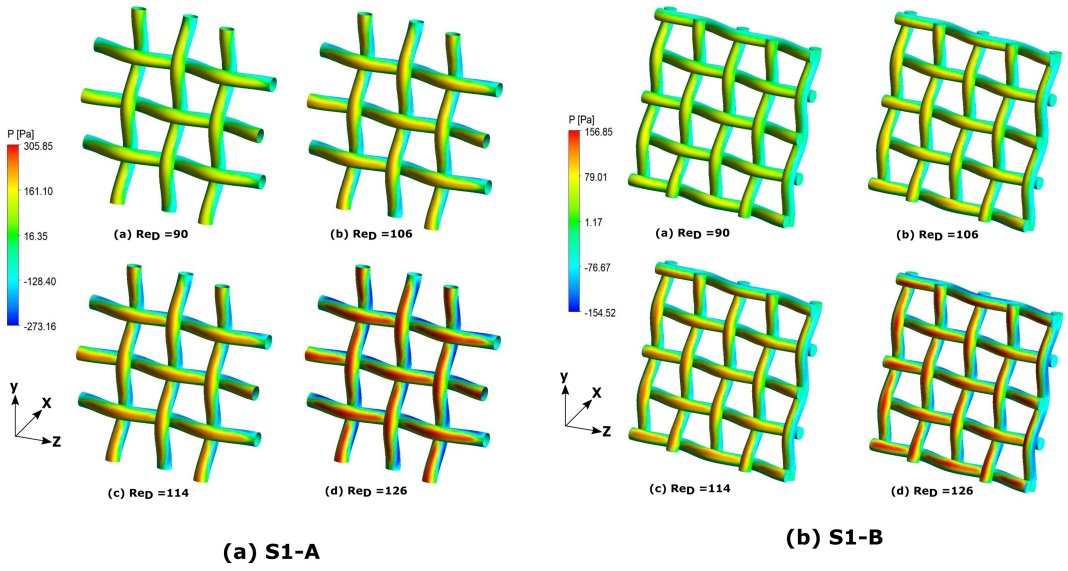

Figure B.6: Surface pressure values on S1-A and S1-B

B.4 S1 Wall Shear Stress

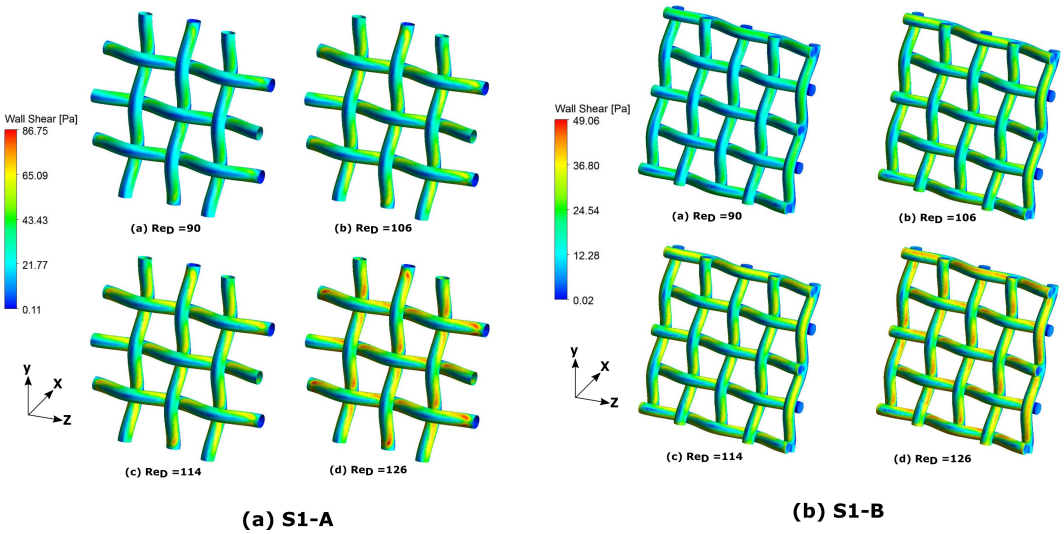

Figure B.7: Wall Shear Stress Values on S1-A and S1-B

Appendix C

Screen S2 Contour Plots

C.1 S2 U_x Contours

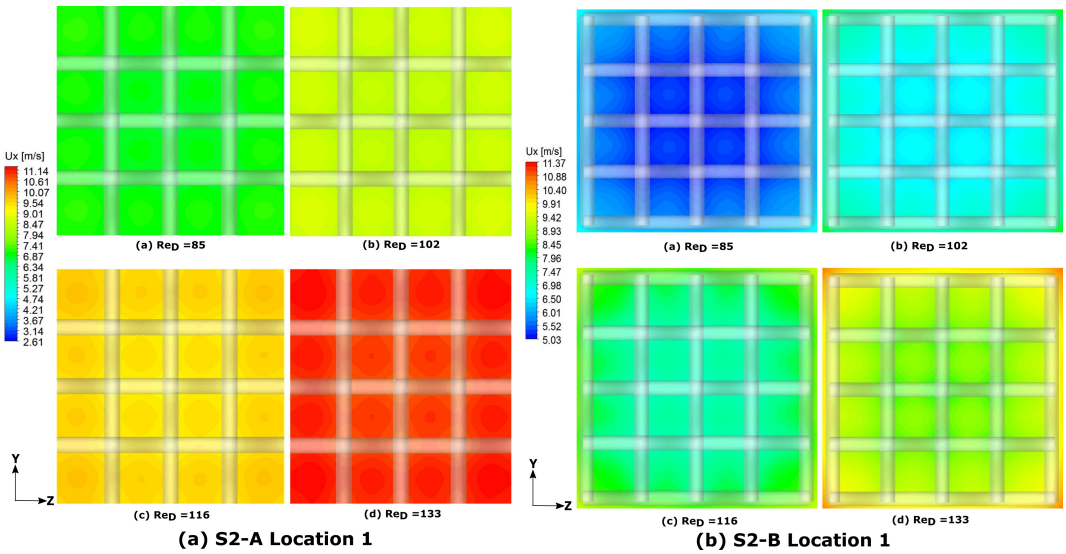

Figure C.1: U_x contour plots at location 1 for S2-A and S2-B

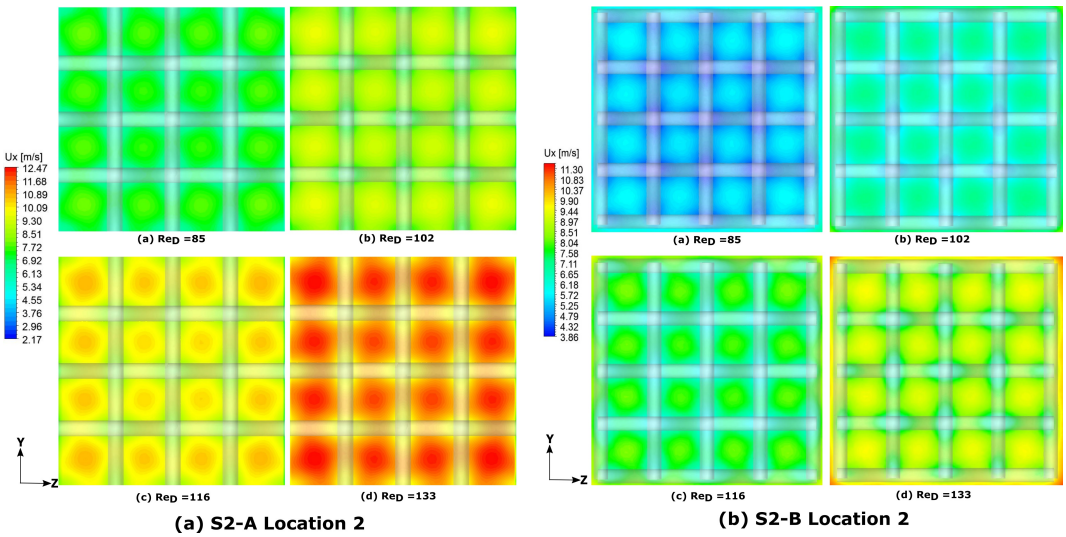

Figure C.2: U_x contour plots at location 2 for S2-A and S2-B

C.2 S2 U_y Contours

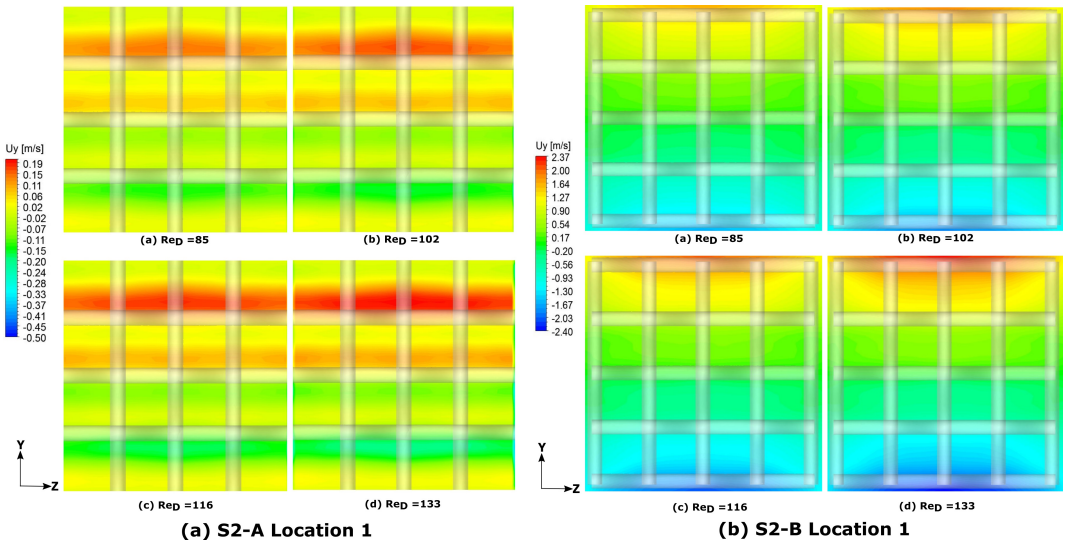

Figure C.3: U_y contour plots at location 1 for S2-A and S2-B

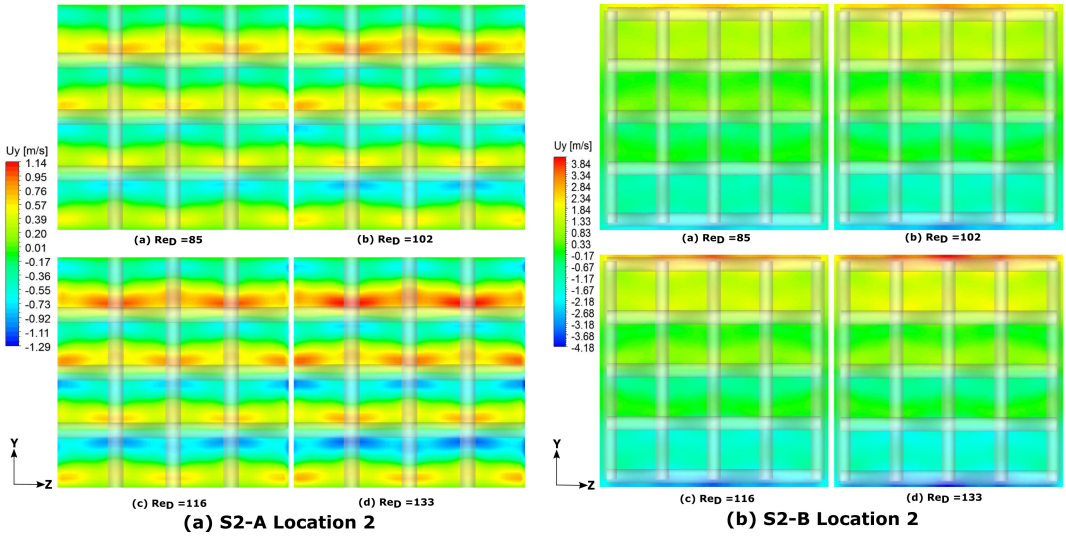

Figure C.4: U_y contour plots at location 2 for S2-A and S2-B

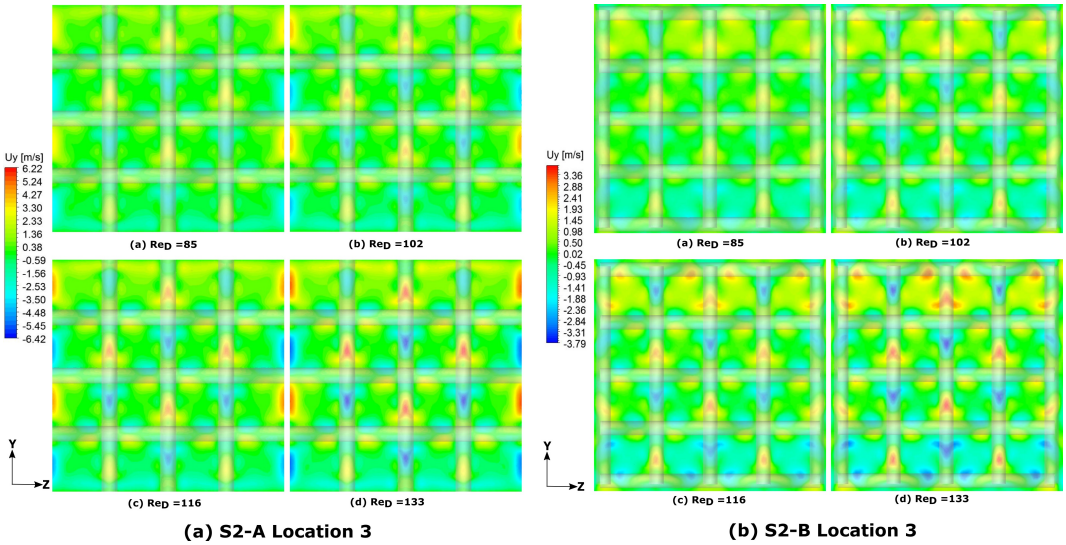

Figure C.5: U_y contour plots at location 2 for S2-A and S2-B

C.3 S2 TKE Contours

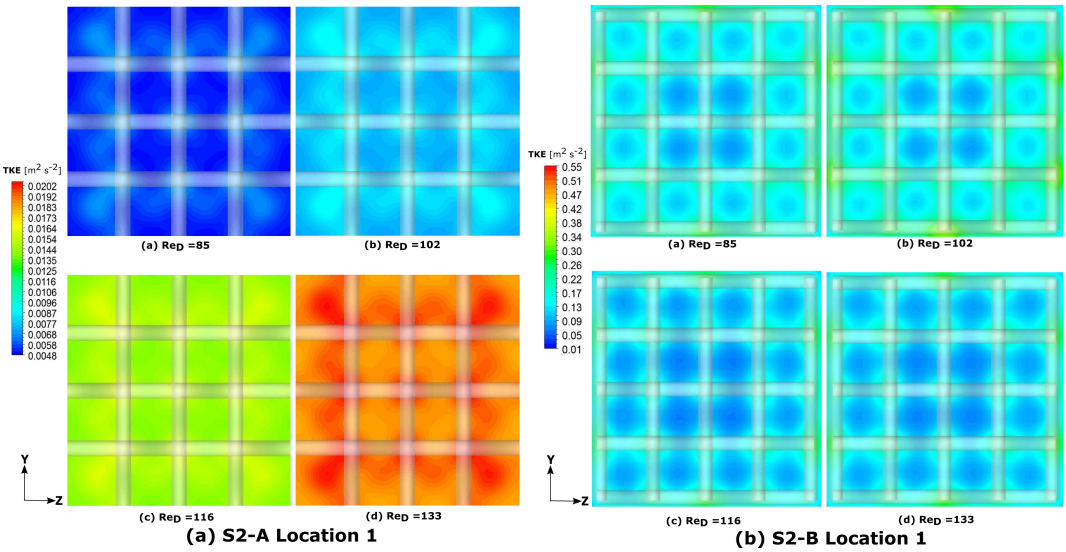

Figure C.6: TKE contour plots at location 1 for S2-A and S2-B

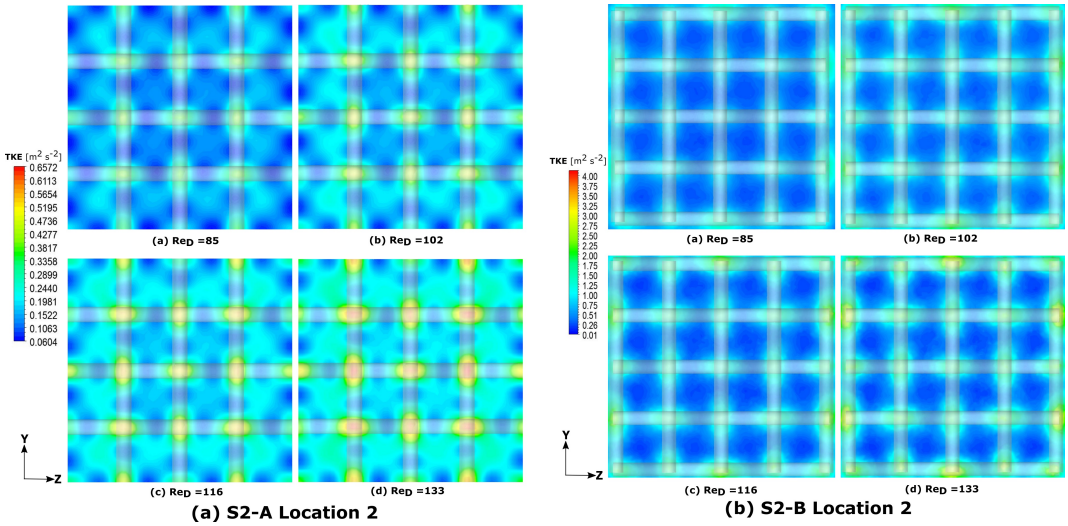

Figure C.7: TKE contour plots at location 2 for S2-A and S2-B

C.4 S2 Wall Y+

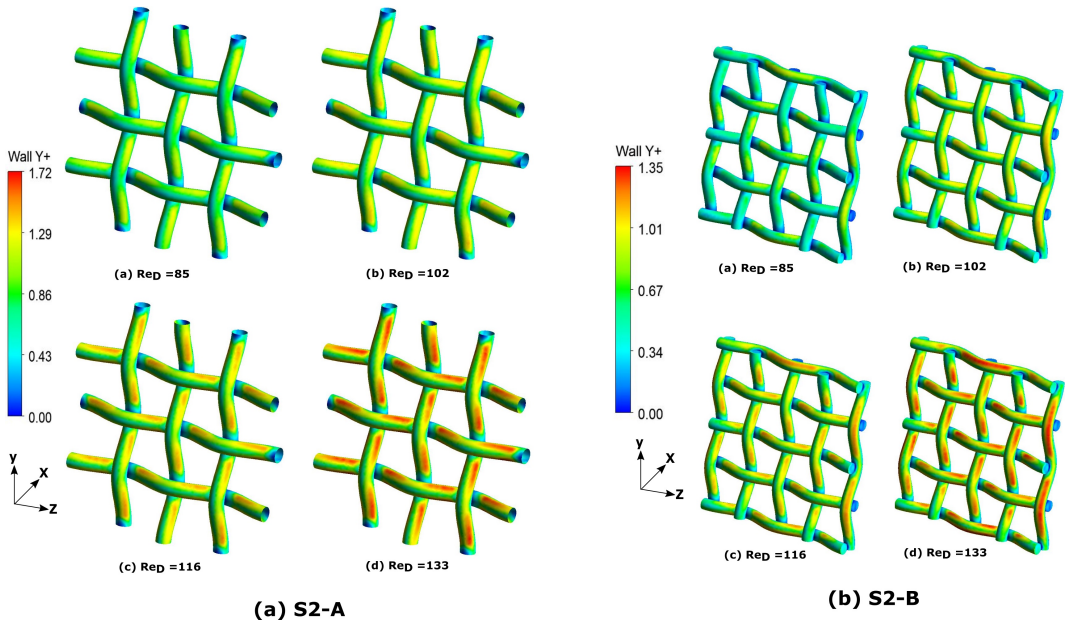

Figure C.8: Wall Y+ values for S2-A and S2-B

C.5 S2 Surface Pressure

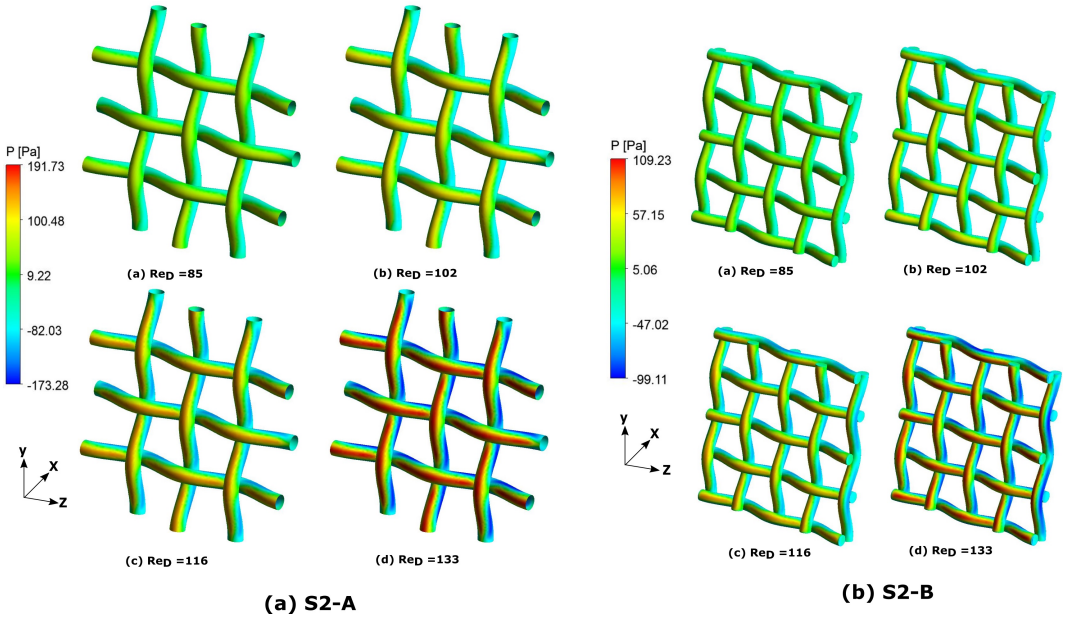

Figure C.9: Surface Pressure for S2-A and S2-B

C.6 S2 Wall Shear Stress

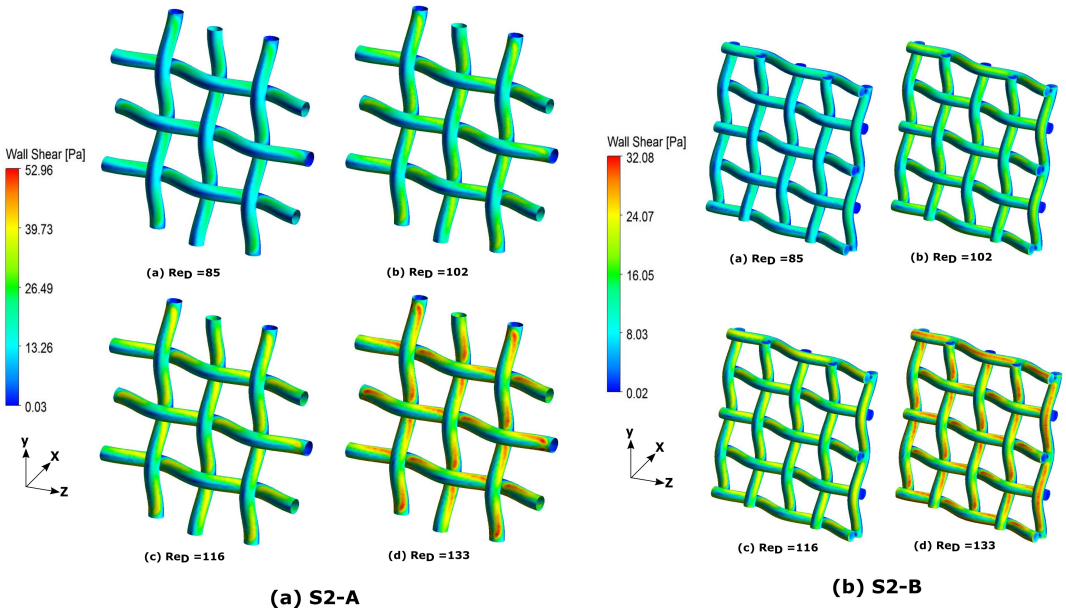

Figure C.10: Wall Shear Stress Magnitude for S2-A and S2-B

Appendix D

Screen S3 Contour Plots

D.1 S3 U_x Contours

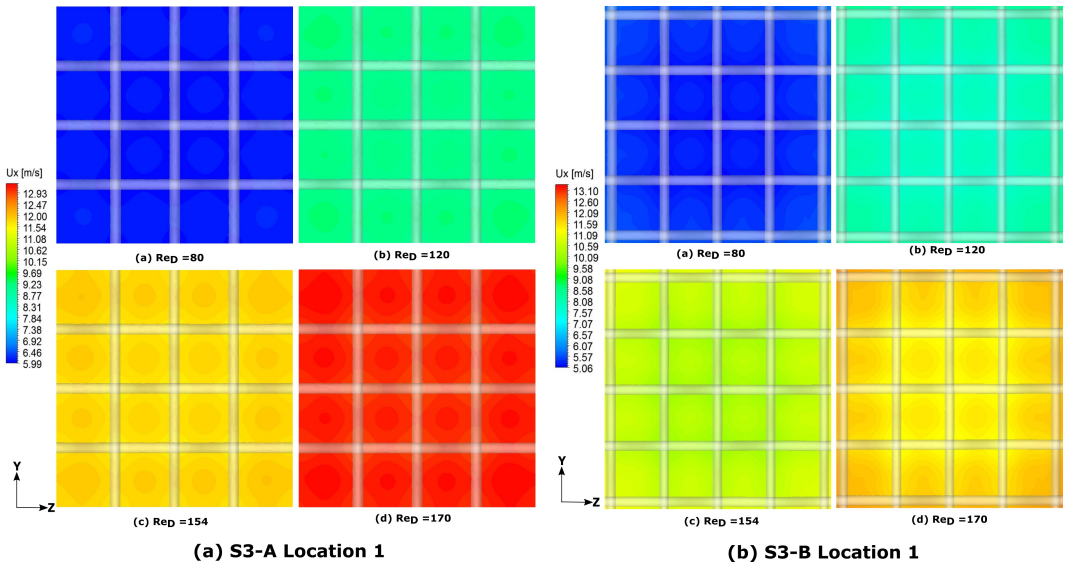

Figure D.1: U_x contour plots at location 1 for S3-A and S3-B

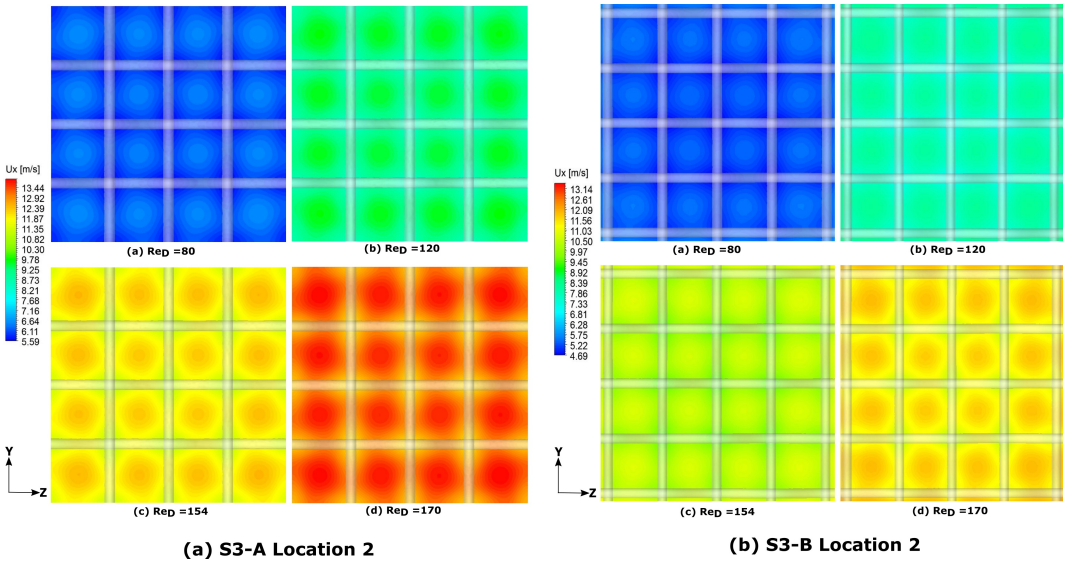

Figure D.2: U_x contour plots at location 2 for S3-A and S3-B

D.2 S3 U_y Contours

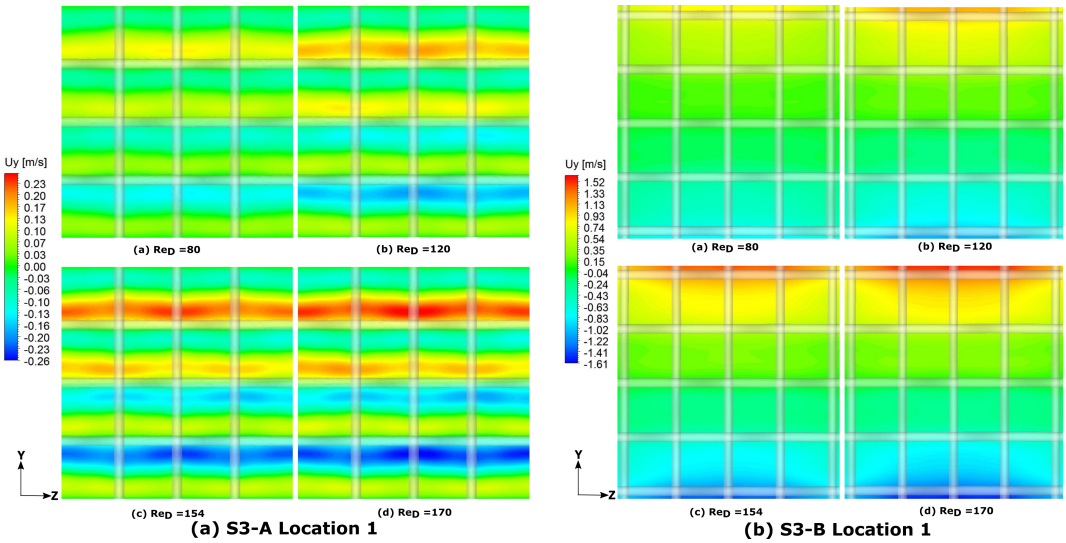

Figure D.3: U_y contour plots at location 1 for S3-A and S3-B

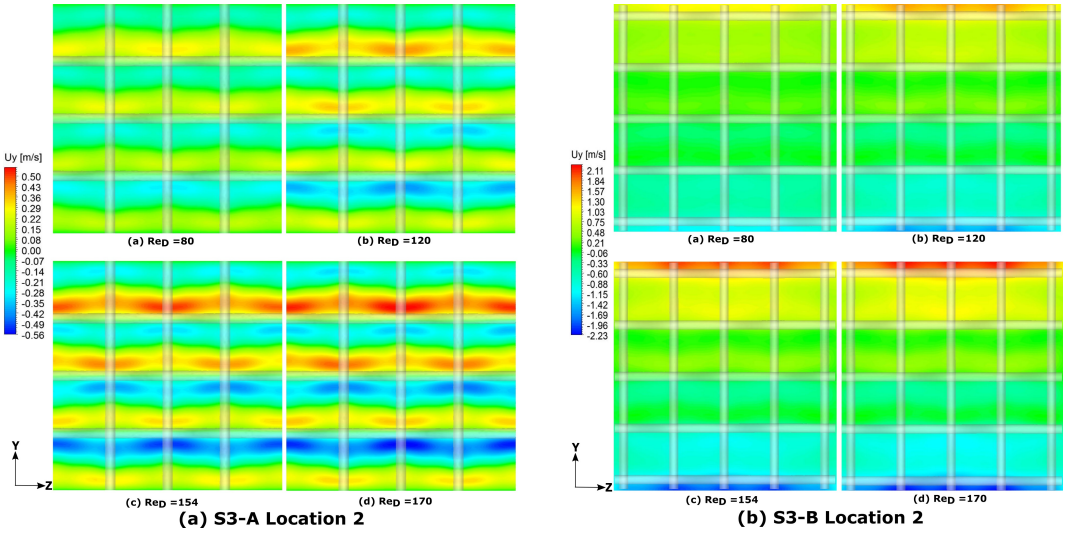

Figure D.4: U_y contour plots at location 2 for S3-A and S3-B

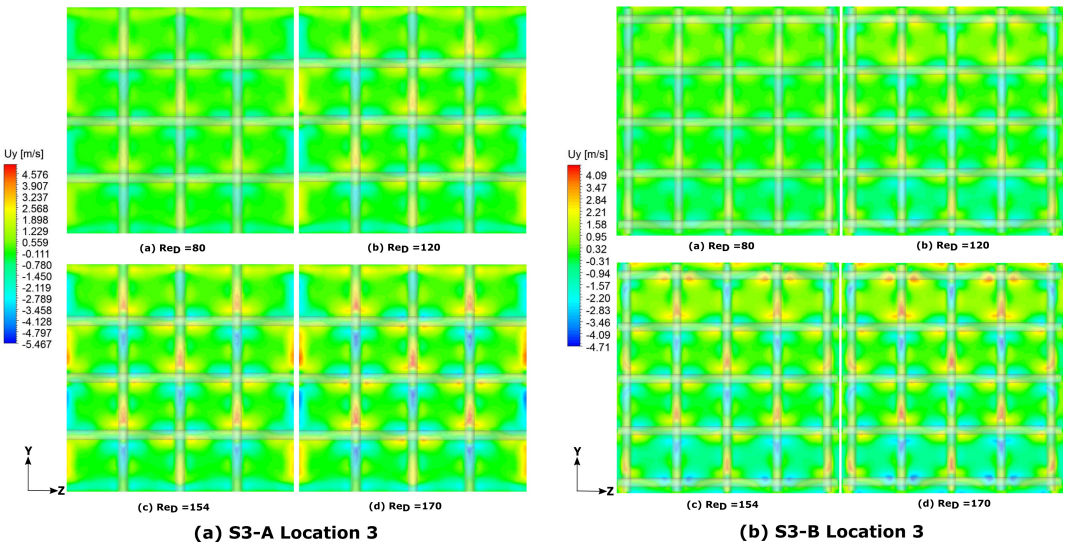

Figure D.5: U_y contour plots at location 3 for S3-A and S3-B

D.3 S3 TKE Contours

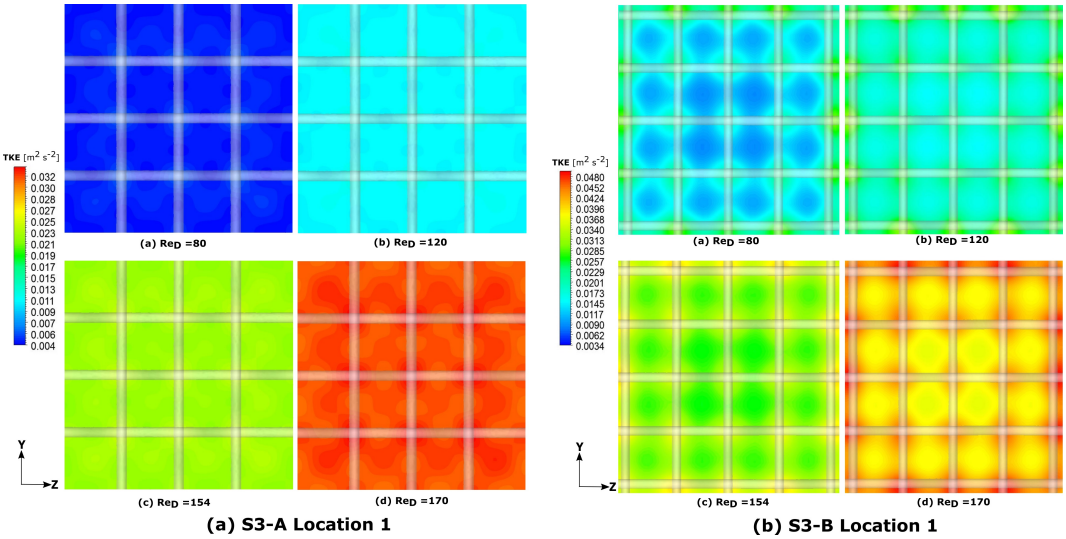

Figure D.6: TKE contour plots at location 1 for S3-A and S3-B

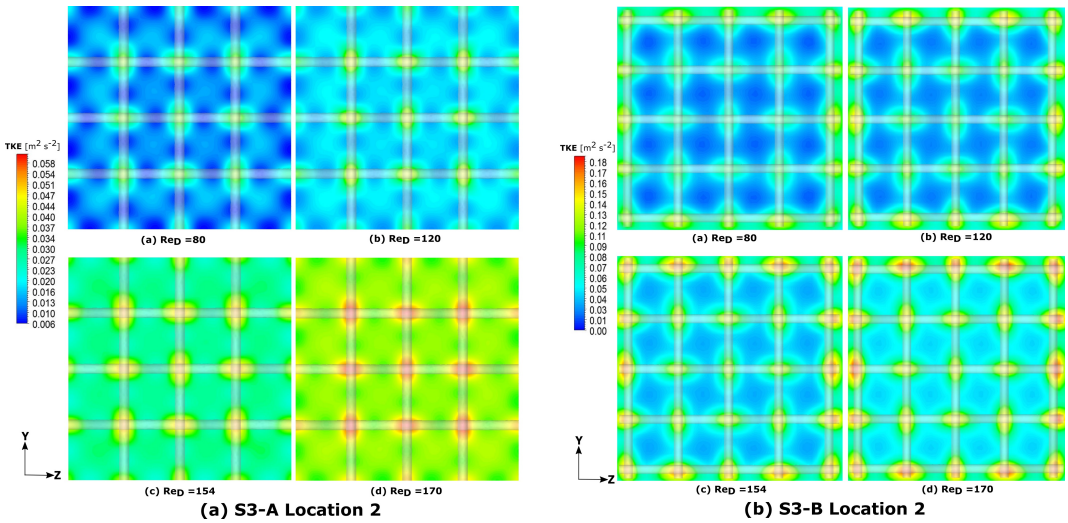

Figure D.7: TKE contour plots at location 2 for S3-A and S3-B

D.4 S3 Wall Y+

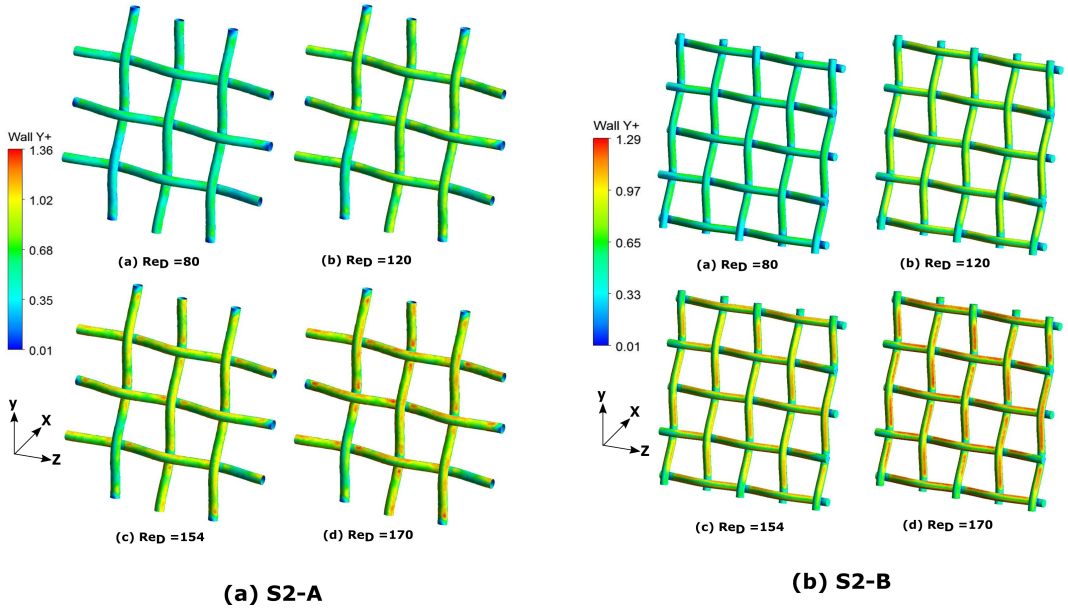

Figure D.8: Wall Y+ values for S3-A and S3-B

D.5 S3 Surface Pressure

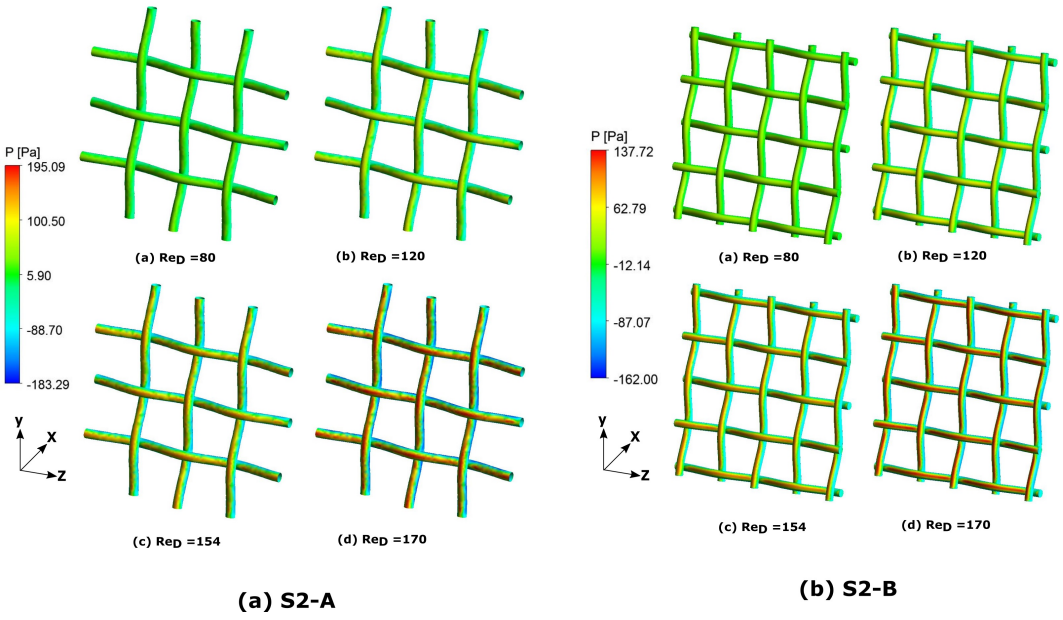

Figure D.9: Surface Pressure for S3-A and S3-B

D.6 S3 Wall Shear Stress

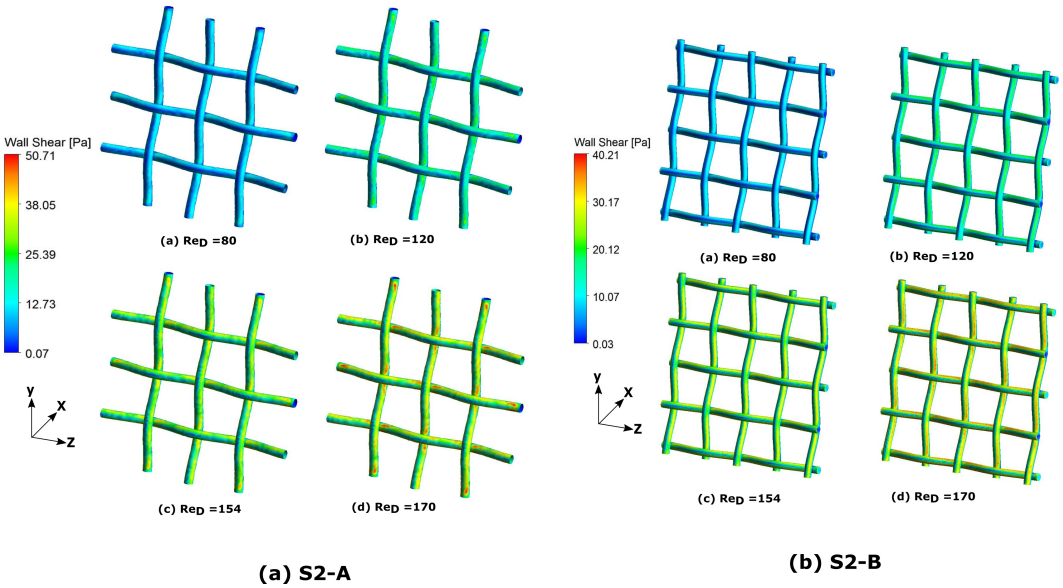

Figure D.10: Wall Shear Stress Magnitude for S3-A and S3-B